frontiers | Research Topics

Pre-interventional cardiac imaging

Edited by
Matthias Renker, Dominik Buckert and Maxim Avanesov

Published in
Frontiers in Cardiovascular Medicine

ISSN 1664-8714
ISBN 978-2-8325-6305-2
DOI 10.3389/978-2-8325-6305-2

About Frontiers

Frontiers is more than just an open access publisher of scholarly articles: it is a pioneering approach to the world of academia, radically improving the way scholarly research is managed. The grand vision of Frontiers is a world where all people have an equal opportunity to seek, share and generate knowledge. Frontiers provides immediate and permanent online open access to all its publications, but this alone is not enough to realize our grand goals.

Frontiers journal series

The Frontiers journal series is a multi-tier and interdisciplinary set of open-access, online journals, promising a paradigm shift from the current review, selection and dissemination processes in academic publishing. All Frontiers journals are driven by researchers for researchers; therefore, they constitute a service to the scholarly community. At the same time, the *Frontiers journal series* operates on a revolutionary invention, the tiered publishing system, initially addressing specific communities of scholars, and gradually climbing up to broader public understanding, thus serving the interests of the lay society, too.

Dedication to quality

Each Frontiers article is a landmark of the highest quality, thanks to genuinely collaborative interactions between authors and review editors, who include some of the world's best academicians. Research must be certified by peers before entering a stream of knowledge that may eventually reach the public - and shape society; therefore, Frontiers only applies the most rigorous and unbiased reviews. Frontiers revolutionizes research publishing by freely delivering the most outstanding research, evaluated with no bias from both the academic and social point of view. By applying the most advanced information technologies, Frontiers is catapulting scholarly publishing into a new generation.

What are Frontiers Research Topics?

Frontiers Research Topics are very popular trademarks of the *Frontiers journals series*: they are collections of at least ten articles, all centered on a particular subject. With their unique mix of varied contributions from Original Research to Review Articles, Frontiers Research Topics unify the most influential researchers, the latest key findings and historical advances in a hot research area.

Find out more on how to host your own Frontiers Research Topic or contribute to one as an author by contacting the Frontiers editorial office: frontiersin.org/about/contact

Pre-interventional cardiac imaging

Topic editors

Matthias Renker — Department of Cardiology, Kerckhoff Clinic, Germany

Dominik Buckert — Ulm University Medical Center, Germany

Maxim Avanesov — University Medical Center Hamburg-Eppendorf, Germany

Citation

Renker, M., Buckert, D., Avanesov, M., eds. (2025). *Pre-interventional cardiac imaging*. Lausanne: Frontiers Media SA. doi: 10.3389/978-2-8325-6305-2

Table of contents

frontiers | Frontiers in Cardiovascular Medicine

TYPE Editorial
PUBLISHED 23 April 2025
DOI 10.3389/fcvm.2025.1605768

OPEN ACCESS

EDITED AND REVIEWED BY
Christos Bourantas,
Queen Mary University of London,
United Kingdom

*CORRESPONDENCE
Matthias Renker
m.renker@kerckhoff-klinik.de

RECEIVED 03 April 2025
ACCEPTED 08 April 2025
PUBLISHED 23 April 2025

CITATION
Renker M, Avanesov M and Buckert D (2025) Editorial: Pre-interventional cardiac imaging. Front. Cardiovasc. Med. 12:1605768. doi: 10.3389/fcvm.2025.1605768

Editorial: Pre-interventional cardiac imaging

Matthias Renker[1,2]*, Maxim Avanesov[3] and Dominik Buckert[4]

[1]Department of Cardiology, Campus Kerckhoff of the Justus-Liebig-University Giessen, Bad Nauheim, Germany, [2]German Centre for Cardiovascular Research (DZHK), Partner Site RheinMain, Frankfurt am Main, Germany, [3]Department of Diagnostic and Interventional Radiology and Nuclear Medicine, University Hospital Hamburg Eppendorf, Hamburg, Germany, [4]Department of Cardiology, Ulm University Heart Center, Ulm, Germany

KEYWORDS

cardiac computed tomography (CCT), cardiac magnetic resonance (CMR), echocardiography, multimodality imaging, tissue characterization, preprocedural imaging, interventional guidance

Editorial on the Research Topic
Pre-interventional cardiac imaging

Cardiac imaging techniques are essential for ensuring optimal results and increasing patient safety in the context of invasive cardiac procedures. The field of cardiac imaging has undergone significant advancements primarily through enhanced diagnostic precision that allows for sophisticated peri-procedural evaluation. Among the most relevant imaging modalities, echocardiography, cardiac magnetic resonance imaging (CMR) and cardiac computed tomography (CCT) have revolutionized risk assessment, procedural guidance, and post-interventional assessment and are therefore emphasized here.

Echocardiography is the cornerstone of cardiac imaging as it is an easily accessible and portable modality for functional assessment offering dynamic visualization of cardiac motion, valve function, and also hemodynamics. While transthoracic echocardiography allows for immediate bedside evaluations in routine clinical practice, transesophageal echocardiography (TEE) also facilitates guidance of interventional procedures by way of further enhanced diagnostic accuracy and more particularly featuring high-resolution images of posterior cardiac structures (1).

CMR provides advanced tissue characterization with its ability to quantitatively assess focal and diffuse interstitial myocardial fibrosis, edema, perfusion, extracellular volume, and viability in a variety of different diseases (2–6). The ability to quantify cardiac ventricular volumes and function as well as characterize myocardial tissue composition by novel mapping techniques (7) and 4D flow dynamics (8) with high reproducibility, makes CMR the reference standard for comprehensive cardiac assessment without ionizing radiation.

CCT provides anatomical visualization with high spatial resolution, allowing for detailed assessment of coronary artery disease and cardiac anomalies (9). Based on its central role in the evaluation of patients prior to transcatheter aortic valve implantation and other structural heart interventions, CCT is nowadays essential for pre-procedural structural heart disease management (10, 11, 12).

Within this research collection, we present and discuss high-quality contributions from the field of cardiovascular imaging with focus on its pre-interventional role and beyond, aiming to cover recent advancements in the field, to familiarize readers with

the current state-of-the-art and to provide an outlook into the future. The featured articles include original research articles, reviews as well as case reports highlighting the wide area of application covered by cardiac imaging.

In the first of three selected case reports, Baltodano-Arellano et al. present a rare instance of a cardiac hematic cyst, detailing its imaging characteristics, differential diagnoses and surgical treatment. The accompanying literature review contextualizes the case within the broader spectrum of cardiac masses, offering valuable insights for clinicians encountering similar presentations. In their case report, Tian et al. describe an innovative approach to endoluminal removal of a superior vena cava filter, which was based on pre-interventional CT imaging. The findings provide practical insights for assessing and managing superior vena cava filter complications. In yet another case report, Kang et al. present a rare instance of mechanical hemolysis due to left ventricular (LV) outflow tract obstruction following aortic valve replacement. The successful resolution through transapical beating-heart septal myectomy underscores the role of advanced cardiac imaging in identifying and addressing procedural complications.

The original research study by Pan et al. examines the anatomical details of the mitral isthmus and its proximity to the esophagus, offering insights relevant to atrial fibrillation ablation procedures. Based on CCT, the authors provide a detailed assessment of spatial variations, which can inform procedural strategies to enhance safety and efficacy in catheter-based interventions.

Zheng et al. address the risk and prognostic significance of LV ejection fraction decline in asymptomatic patients with primary mitral regurgitation. Based on risk stratification with cardiac imaging, the study stresses the necessity of timely intervention before irreversible ventricular dysfunction develops.

The role of TEE in percutaneous closure of patent foramen ovale is the focus of a study by Luo et al. It introduces a novel method aimed at enhancing diagnostic accuracy and procedural safety, which has implications for reducing complications and optimizing outcomes in structural heart disease interventions.

In another interesting study, Zamani-Aliabadi et al. investigate the utility of 4D flow CMR in quantifying left-to-right shunting in pediatric ventricular septal defect. Comparing its accuracy with right heart catheterization, their research emphasized the potential of noninvasive cardiac imaging in congenital heart disease assessment and management including interventional closure.

The original research by Kong et al. evaluates the diagnostic performance of stress dynamic CT myocardial perfusion imaging in detecting myocardial ischemia. The study highlights the comparative efficacy of absolute and relative myocardial blood flow parameters in identifying hemodynamically significant coronary artery disease.

In the original research by Liu et al., investigators explore the implications of self-reported SARS-CoV-2 antibody positivity on cardiac morphology and function using CMR imaging. Their findings contribute to the growing body of knowledge on post-viral cardiac involvement, emphasizing the role of imaging surveillance in affected populations and their risk of LV hypertrophy potentially requiring medical intervention.

Finally, the elegant review by Stoiculescu et al. synthesizes current evidence on advanced imaging techniques in optimizing cardiac resynchronization therapy. It discusses the role of echocardiography, CMR and also nuclear imaging in patient selection, lead placement, and response prediction, highlighting how multimodality cardiac imaging refines therapeutic outcomes in interventional heart failure treatment.

All of the articles featured in this research collection exemplify the pivotal role of pre-interventional cardiac imaging for patient safety, procedural success and therapeutic outcomes. Moreover, imaging-based risk stratification, guidance of complex interventions and refined therapeutic decision-making are highlighted by each one of the contributions demonstrating the ongoing evolution of cardiovascular imaging in contemporary practice. As technological advancements continue to reshape the landscape of cardiac imaging, further adoption in clinical practice, standardization of image interpretation among cardiac imaging specialists and ongoing research focused on these advanced diagnostic modalities will be vital to ensure optimized patient care.

Author contributions

MR: Writing – review & editing, Writing – original draft. MA: Writing – original draft, Writing – review & editing. DB: Writing – original draft, Writing – review & editing.

Conflict of interest

The authors declare that the research was conducted in the absence of any commercial or financial relationships that could be construed as a potential conflict of interest.

The author(s) declared that they were an editorial board member of Frontiers, at the time of submission. This had no impact on the peer review process and the final decision.

Generative AI statement

The authors declare that no Generative AI was used in the creation of this manuscript.

Publisher's note

References

1. Thaden JJ, Malouf JF, Rehfeldt KH, Ashikhmina E, Bagameri G, Enriquez-Sarano M, et al. Adult intraoperative echocardiography: a comprehensive review of current practice. *J Am Soc Echocardiogr*. (2020) 33:735–55.e11. doi: 10.1016/j.echo.2020.01.012

2. Mandoli GE, D'Ascenzi F, Vinco G, Benfari G, Ricci F, Focardi M, et al. Novel approaches in cardiac imaging for non-invasive assessment of left heart myocardial fibrosis. *Front Cardiovasc Med*. (2021) 8:614235. doi: 10.3389/fcvm.2021.614235

3. Patel AR, Kramer CM. Role of cardiac magnetic resonance in the diagnosis and prognosis of nonischemic cardiomyopathy. *JACC Cardiovasc Imaging*. (2017) 10:1180–93. doi: 10.1016/j.jcmg.2017.08.005

4. Patel AR, Salerno M, Kwong RY, Singh A, Heydari B, Kramer CM. Stress cardiac magnetic resonance myocardial perfusion imaging: JACC review topic of the week. *J Am Coll Cardiol*. (2021) 78:1655–68. doi: 10.1016/j.jacc.2021.08.022

5. Avanesov M, Münch J, Weinrich J, Well L, Säring D, Stehning C, et al. Prediction of the estimated 5-year risk of sudden cardiac death and syncope or non-sustained ventricular tachycardia in patients with hypertrophic cardiomyopathy using late gadolinium enhancement and extracellular volume CMR. *Eur Radiol*. (2017) 27:5136–45. doi: 10.1007/s00330-017-4869-x

6. Buckert D, Kelle S, Buss S, Korosoglou G, Gebker R, Birkemeyer R, et al. Left ventricular ejection fraction and presence of myocardial necrosis assessed by cardiac magnetic resonance imaging correctly risk stratify patients with stable coronary artery disease: a multi-center all-comers trial. *Clin Res Cardiol*. (2017) 106:219–29. doi: 10.1007/s00392-016-1042-5

7. Ogier AC, Bustin A, Cochet H, Schwitter J, van Heeswijk RB. The road toward reproducibility of parametric mapping of the heart: a technical review. *Front Cardiovasc Med*. (2022) 9:876475. doi: 10.3389/fcvm.2022.876475

8. Zhuang B, Sirajuddin A, Zhao S, Lu M. The role of 4D flow MRI for clinical applications in cardiovascular disease: current status and future perspectives. *Quant Imaging Med Surg*. (2021) 11:4193–210. doi: 10.21037/qims-20-1234

9. Schoepf UJ, Zwerner PL, Savino G, Herzog C, Kerl JM, Costello P. Coronary CT angiography. *Radiology*. (2007) 244:48–63. doi: 10.1148/radiol.2441052145

10. Rudzinski PN, Leipsic JA, Schoepf UJ, Dudek D, Schwarz F, Andreas M, et al. CT in transcatheter-delivered treatment of valvular heart disease. *Radiology*. (2022) 304:4–17. doi: 10.1148/radiol.210567

11. Renker M, Korosoglou G. The role of computed tomography prior to transcatheter aortic valve implantation: preprocedural planning and simultaneous coronary artery assessment. *J Thorac Dis*. (2024) 16:833–8. doi: 10.21037/jtd-23-1384

12. Renker M, Kim WK. Choice of transcatheter heart valve: should we select the device according to each patient's characteristics or should it be "one valve fits all"? *Ann Transl Med*. (2020) 8(15):961. doi: 10.21037/atm.2020.04.13

frontiers | Frontiers in Cardiovascular Medicine

TYPE Case Report
PUBLISHED 02 July 2024
DOI 10.3389/fcvm.2024.1412571

OPEN ACCESS

EDITED BY
Matthias Renker,
Kerckhoff Clinic, Germany

REVIEWED BY
Vittorio Semeraro,
SS. Annunziata Hospital, Italy
Yung-Wei Chi,
University of California, Davis, United States

*CORRESPONDENCE
Jianlong Liu
✉ ljl_hy88@sina.com

RECEIVED 05 April 2024
ACCEPTED 03 June 2024
PUBLISHED 02 July 2024

CITATION
Tian X, Liu J, Li J, Liu X, Zhou M and Tian Y (2024) Case Report: Endoluminal removal of a conical retrievable superior vena cava filter with a retraction hook attached to the wall. Front. Cardiovasc. Med. 11:1412571. doi: 10.3389/fcvm.2024.1412571

Case Report: Endoluminal removal of a conical retrievable superior vena cava filter with a retraction hook attached to the wall

Xuan Tian[1], Jianlong Liu[1]*, Jinyong Li[1], Xiao Liu[1], Mi Zhou[1] and Yule Tian[2]

[1]Department of Vascular Surgery, Beijing Jishuitan Hospital, Capital Medical University, Beijing, China, [2]International Department, Experimental High School, Beijing Normal University, Beijing, China

We report the case of a 22-year-old male who underwent endoluminal surgery and was implanted an Option Elite filter in the superior vena cava (SVC) while the filter retraction hook was attached to the vessel wall. The patient requested to remove the filter after 155 days. Preoperative ultrasonography and CT examination revealed that the filter retraction hook was very likely to penetrate the SVC wall and its tip was very close to the right pulmonary artery. The SVC was not obstructed, and no thrombus was observed in either upper limb. After the filter retrieval device (ZYLOX, China) failed to capture the filter hook, we introduced a pigtail catheter with its tip partly removed and a loach guidewire, used a modified loop-snare technique to cut the proliferative tissues and free the hook, and finally removed the filter successfully by direct suspension of the guidewire. During this procedure, the patient experienced discomfort, such as chest pain and palpitations, but these symptoms disappeared when procedure completed. Repeated multiangle angiography revealed no contrast medium extravasation, no complications such as pericardial tamponade, pleural effusion, SVC haematoma formation, right pulmonary artery dissecting aneurysm, or intramural haematoma. We initially presented the modified loop-snare technique used to remove a conical superior vena cava filter (SVCF), so this method can be considered a practical and novel auxiliary technique for successful filter retrieval.

KEYWORDS

superior vena cava filter, filter retrieval, case report, loop-snare, superior vena cava (SVC)

Introduction

Vena cava filters are mainly used in patients with deep vein thrombosis (DVT) to prevent fatal pulmonary embolism (PE). The incidence of PE after DVT of lower extremities is as high as 45%–50% (1, 2), so inferior vena cava filters (IVCFs) are widely used. However, recent studies have shown that the incidence of PE after DVT in the upper limbs can reach 5%–10% (3). Some scholars have attempted to place the filter in the SVC, but this practice is controversial (4).

In view of the multiple complications associated with permanent filter implantation (5, 6), retrievable filters are dominant in trend, and timely removal is recommended once PE risk is reduced and the filter is no longer needed (7–9). At present,

endovascular surgery is preferred to remove IVCFs. However, open surgery is essential when filter removal is failed due to serious complications and can't be treated via endoluminal approach (10). Filter tilt is defined as an angulation of more than 15 degrees from the filter's long axis, which occurs in 3%–9% cases (11), resulting in hook attached to the vessel wall with proliferative tissue wrapping, failure to capture, thus increased damage of the hook or strut perforation to the vascular wall and adjacent tissues, and at last failure to retrieve the filter. Severe tilt is more common with IVCFs, while reports of tilt with SVCFs are rare. However, severe inclinations may result in permanent filter implantation into the SVC (4).

In this study, we report a case of endoluminal removal of a conical superior vena cava retrievable filter with the hook attached to the vessel wall.

Case report

The patient is a 22-year-old male who underwent the surgery to treat the thoracic outlet syndrome 155 days ago. Postoperative symptoms of left brachial plexus injury occurred with left upper limb DVT and PE. An Option Elite vena cava filter (ARGON, USA) was placed in the SVC, and anticoagulant therapy of 20 mg oral rivaroxaban QD was administered for 3 months. In the attempts to remove the SVCF, difficulties were encountered, and the filter could not be removed. The patient had repeated visits to two hospitals but still failed to remove the filter, so he was eventually transferred to our hospital for filter removal.

Preoperative examination

No PE was detected via computed tomographic pulmonary angiography (CTPA), the SVC was patent, and no haematoma formation. The filter retraction hook was likely to penetrate the SVC wall, and its tip was very close to the right pulmonary artery (Figures 1A,B). Colour Doppler ultrasound revealed no thrombus in the deep veins of either upper limb. No pericardial effusion was observed in echocardiography, nor arrhythmia in electrocardiogram. The surgical indications for filter removal were met, and the patient had strong desire for filter removal surgery. The procedure plan was designed as follows: the modified loop-snare technique (12) was firstly attempted to remove the filter; open surgery was a back-up when endoluminal therapy failed or complications occurred.

Device preparation

4Fr 100 cm pigtail catheter (Cordis, USA), a 4F catheter is recommended for its relative smaller outer diameter and easier advancement; 260 cm angled hydrophilic coated guidewire (Terumo Medical, Japan); filter retrieval kit (ZYLOX, China), a domestic manufactured device which is similar to Bard snare retrieval kit (BD, USA) in structure and function.

Angiographic imaging of the right common femoral vein showed that the inferior vena cava was unobstructed and no thrombus observed. Repeated multiangle angiography showed that the filter retraction hook had possibly entered the SVC wall (Figures 2A,B). ZYLOX filter retrieval kit was introduced but difficulties were encountered when attempting to capture the filter retraction hook. To solve this issue, we utilized a modified loop-snare technique (13) by introducing a pigtail catheter and a hydrophilic guidewire (Figure 2E). The pigtail catheter had its tip partially cut (Figures 2C,D) and was rotated to be guided into the interspace between the filter and the SVC wall (Figure 2B, red arrows). The guidewire was used to increase the catheter support and was advanced to free its end to be snared and externalized. A wire loop was formed across the proliferative tissue and was used to cut and destroy the proliferative tissue surrounding the retraction hook through the exertion of counteracting forces by the guidewire and retrieval sheath (Figures 3A,B), and the filter was successfully removed by directly suspension of the guidewire. It is worth noting that the patient experienced uncomfortable symptoms such as chest pain and palpitations during the removal process, but these symptoms disappeared once the operation was successfully completed. Repeated multiangle angiography showed no contrast medium spillage (Figure 3C). Finally, the filter was removed successfully and completely (Figure 3D). We also observed that the tip of the retrieval sheath was significantly deformed (Figures 3E,F).

CTPA (Figures 1C,D) was performed one week after the procedure. No pericardial effusion or pleural effusion was observed, no haematoma was found in the SVC, and no right pulmonary artery dissecting aneurysm or intramural haematoma was observed. PE did not occur in perioperative period, and anticoagulant therapy with 20 mg of rivaroxaban QD was recommended after the procedure (14). There was no recurrence of upper extremity DVT, no SVC thrombosis, and no symptoms related to PE during the 3-month follow-up.

Discussion

Compared with the inferior vena cava, SVC is short in length and small in diameter (15), so it is relatively difficult to place the filter. In particular for conical filters, inaccurate positioning and severe tilt are more likely to occur (4). This may lead to complications such as pericardial effusion, arrhythmia, aortic dissection, arteriovenous fistula, haemothorax, pneumothorax and air embolism (16–18). Especially in the case of hook attached to the vessel wall, the filter cannot be retrieved successfully and lead to permanent implantation in the body (4).

The surgical procedure in this case has the following characteristics and challenges: (1) the filter retraction hook is embedded in the SVC wall, it may be difficult to be captured by the conventional retrieval snare device, and the filter tip is close to the right pulmonary artery, so there are risks of collateral damage; (2) the occurrence of bleeding may result in complications such as pericardial tamponade, arrhythmia and pleural effusion, so it is vital to avoid the vascular injury during

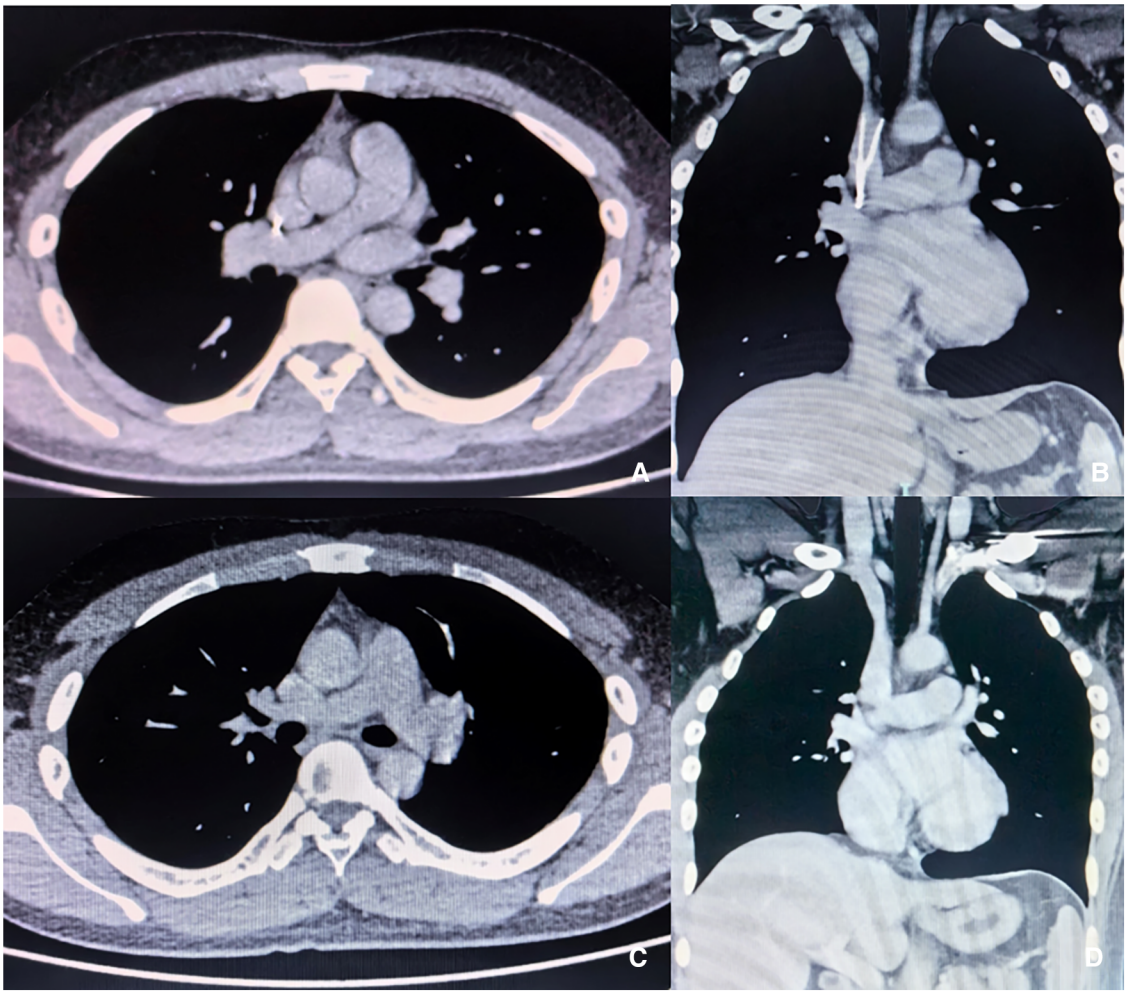

FIGURE 1
Enhanced CT images before and after procedure. (A,B) The filter retraction hook entered SVC wall, and the tip was close to the right pulmonary artery. (C,D) No haematoma, dissection or cardiac fluid accumulation in the superior vena cava or right pulmonary artery after filter removal.

the procedure; and (3) there are no reports on the use of the modified loop-snare technique to remove the attached SVCF.

When the filter is heavily tilt against the wall, the tissue proliferation around the retraction hook will result in the failure of capturing the retraction hook properly. The following methods can significantly increase the success rate of endoluminal filter removal: (1) loop-snare technique (19), which can pull the filter to correct its tilt angle; (2) the modified loop-snare technique (12), which is adopted in this study; (3) double wire lassoing technique (20), which corrects the tilt angle by pulling from both ends of the filter simultaneously; and (4) biopsy forceps technique (12), which grabs the filter retraction hook and struts into the catheter for filter removal.

We highlight the risk of central vein breakage during the removal of the conical filter with the retraction hook attached to the wall using various methods. When the inferior vena cava is injured, the bleeding risk is low due to the lower pressure of the central vein, and it's surrounded by the vascular sheath and adipose tissue. Once bleeding occurs, the haematoma can be absorbed by the posterior peritoneum quickly without major complications. However, if the injury occurs in the SVC, which is surrounded by the pericardium, the procedure risk increases significantly as the injury may cause pericardial effusion and other complications, such as hypotension and dyspnoea (18). When comparing the two loop-snare techniques, the modified loop-snare technique is safer to cut the proliferative tissue around the hook because it allows the filter retraction hook to re-enter the SVC. If the standard loop-snare technique is applied, pulling the filter may cause the hook to stab into the right pulmonary artery and cause serious complications. For this reason, the modified loop-snare technique is selected in this case.

Currently, the filter deployed in the superior vena cava is still controversial (4), but if the filter is needed, we recommend the following choices: (1) Denali filter (BD, USA), that it has good radial support in the vessel, and the risk of filter tilt with its hook attached to the wall is low (21); and (2) Non-conical filter, such as Optease (Cordis, USA), that it should be released in the direction of blood flow to avoid dislocation, and the filter should

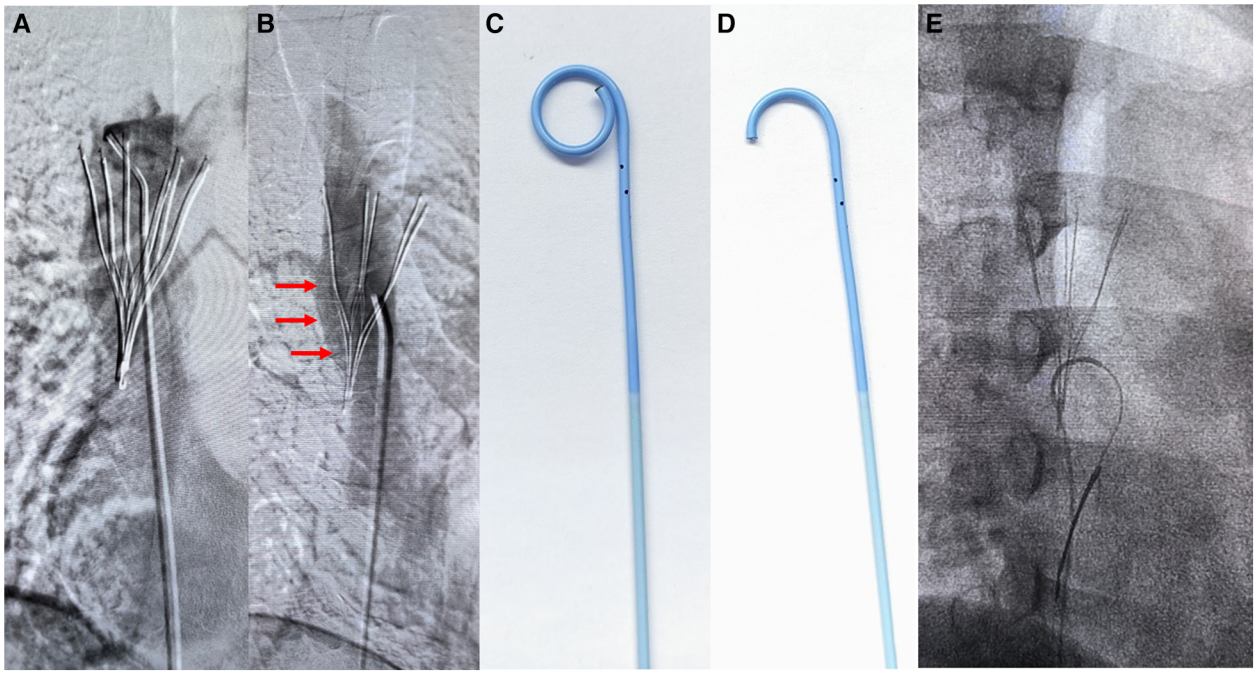

FIGURE 2
Images of the loop-snare technique steps. (**A**,**B**) Multiangle angiography of the superior vena cava. Red arrows marked the interspace between the filter and the SVC wall where the wire loop was formed. (**C**,**D**) The pigtail catheter shape with its tip partly cut. (**E**) Modified loop-snare technique using a decapitated pigtail catheter.

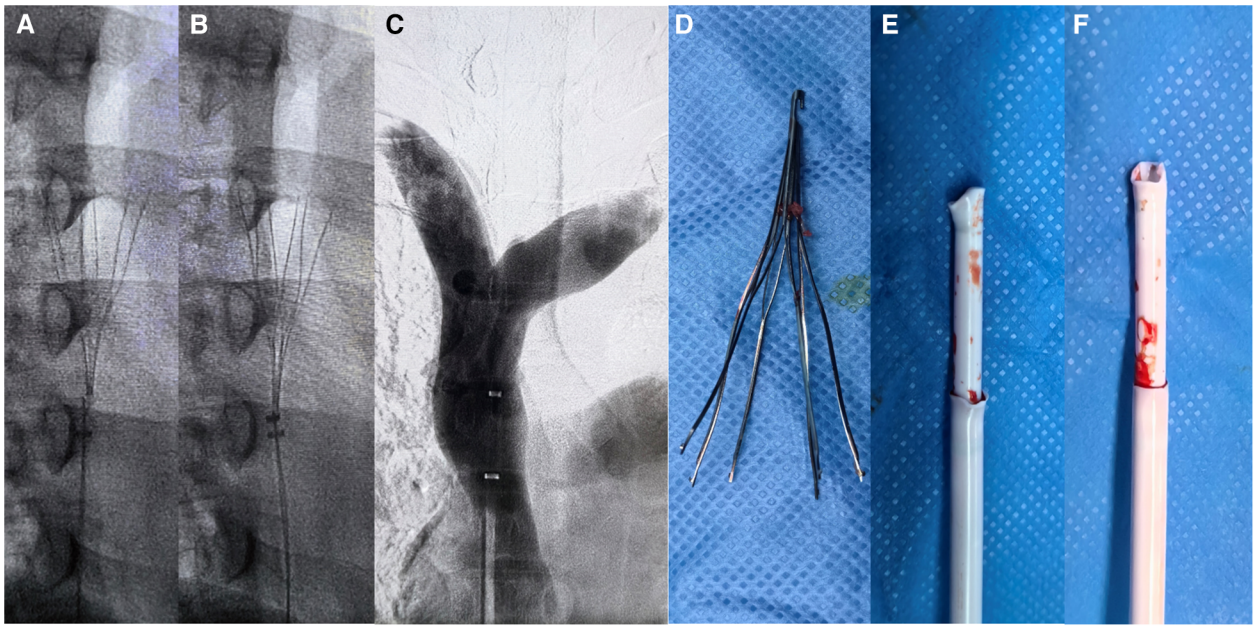

FIGURE 3
Filter removal process images. (**A**,**B**) Modified loop-snare technique for cutting the proliferated tissue around the retraction hook, with the guidewire directly suspending the retraction hook. (**C**,**D**) After the filter was successfully removed, no damage to the superior vena cava was observed by contrast imaging, and the filter was completely removed. (**E**,**F**) The deformed shape of the filter retrieval devices.

be retrieved at an early stage to avoid permanent placement; (3) Temperfilter II filter (B. Braun, Germany), the filter should be inverted via the femoral vein to the superior vena cava and should be avoided for long dwelling time.

Conclusion

Conical SVCF retraction hook attachment is a rare complication that can lead to permanent indwelling of the filter. However, the filter can be successfully removed with the modified loop-snare technique without any complications, thus avoiding severe trauma associated with open surgery. This new practical and auxiliary technique provides a valid method for the removal of SVCFs and has academic value and practical application prospects.

Data availability statement

The original contributions presented in the study are included in the article/Supplementary Material, further inquiries can be directed to the corresponding author.

Ethics statement

The studies involving humans were approved by the Ethics Committee of Beijing Jishuitan Hospital. The studies were conducted in accordance with the local legislation and institutional requirements. The participants provided their written informed consent to participate in this study. Written informed consent was obtained from the individual(s) for the publication of any potentially identifiable images or data included in this article.

Author contributions

XT: Writing – original draft, Writing – review & editing, Data curation, Formal Analysis, Funding acquisition. JL: Writing – original draft, Writing – review & editing, Conceptualization, Supervision. J-YL: Writing – original draft, Data curation, Formal Analysis. XL: Writing – original draft, Data curation. MZ: Writing – original draft, Writing – review & editing, Data curation. YT: Writing – review & editing.

Funding

The author(s) declare financial support was received for the research, authorship, and/or publication of this article.

Capital Funds for Health Improvement and Research, CFH2022-2-2074. Beijing Municipal Administration of Hospital Incubating Program, Code: PX2022015. Beijing Jishuitan Hospital Elite Young Scholar Program (XKGG202213).

Acknowledgments

The author thanks all the doctors and nurses of the Vascular Surgery Department of Beijing Jishuitan Hospital.

Conflict of interest

The authors declare that the research was conducted in the absence of any commercial or financial relationships that could be construed as a potential conflict of interest.

Publisher's note

References

1. Nutescu EA, Crivera C, Schein JR, Bookhart BK. Incidence of hospital readmission in patients diagnosed with DVT and PE: clinical burden of recurrent events. *Int J Clin Pract*. (2015) 69:321–7. doi: 10.1111/ijcp.12519

2. Tian X, Liu JL, Gu JP, Xu H, Ni FC, Li Z, et al. A multicenter clinical trial of safety and effectiveness of octoparms® vena cava filter in preventing pulmonary embolism. *Chin J Gen Surg*. (2021) 30(12):1395–402. doi: 10.7659/j.issn.1005-6947.2021.12.002

3. Rokosh RS, Ranganath N, Yau P, Rockman C, Sadek M, Berland T, et al. High prevalence and mortality associated with upper extremity deep venous thrombosis in hospitalized patients at a tertiary care center. *Ann Vasc Surg*. (2020) 65:55–65. doi: 10.1016/j.avsg.2019.10.055

4. Lopera JE, Barnes L. A single center 10-year clinical experience with superior vena cava retrievable filters. *Catheter Cardiovasc Interv*. (2019) 95(1):1–6. doi: 10.1002/ccd.28533

5. Moriarty JM, Steinberger JD, Bansal AK. Inferior vena cava filters: when to place and when to remove. *Semin Respir Crit Care Med*. (2017) 38(1):84–93. doi: 10.1055/s-0036-1597558

6. Quencer KB, Smith TA, Deipolyi A, Mojibian H, Ayyagari R, Latich I, et al. Procedural complications of inferior vena cava filter retrieval, an illustrated review. *CVIR Endovasc*. (2020) 3(1):23. doi: 10.1186/s42155-020-00113-6

7. Streiff MB, Agnelli G, Connors JM, Crowther M, Eichinger S, Lopes R, et al. Guidance for the treatment of deep vein thrombosis and pulmonary embolism. *J Thromb Thrombolysis*. (2016) 41(1):32–67. doi: 10.1007/s11239-015-1317-0

8. Interventional physicians branch of Chinese medical doctor association. Expert consensuses on the codes for the insertion and removal of inferior vena cava filters (2nd edition). *Nat Med J Chin*. (2020) 100(27):2092–101. doi: 10.3760/cma.j.cn112137-20200317-00804

9. Vascular surgery group, Gurgery branch, Chinese medical association. The interpretation of clinical application guidelines of vena cava filter. *Chin J Vasc Surg*. (2019) 4(3):145–53. doi: 10.3760/cma.j.issn.2096-1863.2019.03.005

10. Tian X, Liu J, Jet al L. Removal of inferior vena cava filter by open surgery after failure of endovenous retrieval. *Front Cardiovasc Med*. (2023) 10:1127886. doi: 10.3389/fcvm.2023.1127886

11. Li X, Haddadin I, McLennan G, Farivar B, Staub D, Beck A, et al. Inferior vena cava filter—comprehensive overview of current indications, techniques, complications and retrieval rates. *Vasa*. (2020) 49(6):449–62. doi: 10.1024/0301-1526/a000887

12. Desai KR, Pandhi MB, Seedial SM, Errea MF, Salem R, Ryu RK, et al. Retrievable IVC filters: comprehensive review of device-related complications and advanced retrieval techniques. *RadioFigureics*. (2017) 37:1236–45. doi: 10.1148/rg.2017160167

13. Tian X, Liu JL, Li JY, Liu X. Case report: endoluminal removal of a retrievable conical inferior vena cava filter with a ruptured retraction hook attached to the wall. *Front Surg*. (2022) 9:985060. doi: 10.3389/fsurg.2022.985060

14. Nunnelee JD. Review of an article: oral rivaroxaban for symptomatic venous thromboembolism. The EINSTEIN investigators et al. *N Engl J Med*. (2010) 363 (26):2499–510. doi: 10.1056/NEJMoa1007903

15. Murphy KD. Superior vena cava filters. *Tech Vasc Interv Radiol*. (2004) 7:105–9. doi: 10.1053/j.tvir.2004.02.007

16. Muriel A, Jimenez D, Aujesky D, Bertoletti L, Decousus H, Laporte S, et al. Survival effects of inferior vena cava filter in patients with acute symptomatic venous thromboembolism and a significant bleeding risk. *J Am Coll Cardiol*. (2014) 63:1675–83. doi: 10.1016/j.jacc.2014.01.058

17. Milovanovic L, Kennedy SA, Midia M. Procedural and indwelling complications with inferior vena cava filters: frequency, etiology, and management. *Semin Intervent Radiol*. (2015) 32:34–41. doi: 10.1055/s-0034-1396962

18. Zeng X, Zhou J, Zhou Q, Huang Z. Case report: pericardial tamponade and hemothorax after superior vena cava filter removal. *Front Cardiovas Med*. (2022) 9:863732. doi: 10.3389/fcvm.2022.863732

19. Kuyumcu G, Walker TG. Inferior vena cava filter retrievals, standard and novel techniques. *Cardiovasc Diagn Ther*. (2016) 6(6):642–50. doi: 10.21037/cdt.2016.09.07

20. Daye D, Walker TG. Novel and advanced techniques for complex IVC filter retrieval. *Curr Treat Options Cardiovasc Med*. (2017) 19(4):28. doi: 10.1007/s11936-017-0529-3

21. Liu J, Jiang P, Tian X, Jia W, Huang N-L, Zhan H, et al. Clinical outcomes of retrievable inferior vena cava filters for venous thromboembolic diseases. *J Comp Eff Res*. (2022) 11(6):437–49. doi: 10.2217/cer-2021-0291

frontiers | Frontiers in Cardiovascular Medicine

TYPE Case Report
PUBLISHED 11 July 2024
DOI 10.3389/fcvm.2024.1410222

OPEN ACCESS

EDITED BY
Matthias Renker,
Kerckhoff Clinic, Germany

REVIEWED BY
Kameel Kassab,
Yuma Regional Medical Center Cancer Center, United States
Jaroslav Januska,
Agel Podlesi Trinec Hospital, Czechia

*CORRESPONDENCE
Yani Liu
yani.liu@163.com

RECEIVED 31 March 2024
ACCEPTED 19 June 2024
PUBLISHED 11 July 2024

CITATION
Kang Q, Tian J, Zhu Y, Zhou W, Wei X and Liu Y (2024) Case Report: Mechanical hemolysis resulting from left ventricular outflow tract obstruction after aortic valve replacement relieved by transapical beating-heart septal myectomy.
Front. Cardiovasc. Med. 11:1410222.
doi: 10.3389/fcvm.2024.1410222

Case Report: Mechanical hemolysis resulting from left ventricular outflow tract obstruction after aortic valve replacement relieved by transapical beating-heart septal myectomy

Qingwen Kang[1], Jie Tian[1], Ying Zhu[1], Wei Zhou[1], Xiang Wei[2] and Yani Liu[1]*

[1]Department of Medical Ultrasound, Tongji Hospital, Tongji Medical College, Huazhong University of Science and Technology, Wuhan, Hubei, China, [2]Department of Cardiovascular Surgery, Tongji Hospital, Tongji Medical College, Huazhong University of Science and Technology, Wuhan, Hubei, China

Background: Aortic stenosis (AS) in combination with left ventricular outflow tract obstruction (LVOTO) has occasionally been reported. However, making a precise diagnosis and successfully treating this combination is challenging due to the hemodynamic interaction between the two conditions.
Case summary: A 56-year-old male patient who had been diagnosed with severe AS and asymmetric left ventricular hypertrophy underwent aortic valve replacement (AVR) and a conventional septal myectomy. Immediately after the procedure, significant systolic anterior motion and mitral regurgitation developed, necessitating a surgical mitral edge-to-edge repair. Ten days after the procedure, the patient developed hematuria and LVOTO, which was confirmed by echocardiography. Because the LVOTO might have been the cause of the hematuria, the patient underwent alcohol septal ablation, but this had little effect. Three months later, a transapical beating-heart septal myectomy (TA-BSM) was performed in our hospital. Postoperatively, the LVOTO had been significantly ameliorated and the hematuria had resolved.
Conclusion: For patients with AS and LVOTO due to a hypertrophic interventricular septum, inadequate amelioration of the LVOTO after AVR may lead to severe hemolytic hematuria. TA-BSM is a minimally invasive, safe, and effective surgical procedure for ameliorating LVOTO in patients with aortic valve prostheses.

KEYWORDS

left ventricular outflow tract obstruction, hematuria, transapical beating-heart septal myectomy, echocardiographic imaging, case report

Abbreviations

AV, aortic valve; AVR, aortic valve replacement; AS, aortic stenosis; BMD, beating-heart myectomy device; CPB, cardiopulmonary bypass; LV, left ventricle; LVEF, left ventricular ejection fraction; LVOT, left ventricular outflow tract; LVOTO, left ventricular outflow tract obstruction; MR, mitral regurgitation; MV, mitral valve; PG, pressure gradient; SM, septal myectomy; SAM, systolic anterior motion; TA-BSM, transapical beating-heart septal myectomy; TEE, transesophageal echocardiography; TTE, transthoracic echocardiography.

1 Case presentation

A 56-year-old man was admitted to our hospital due to left ventricular outflow tract obstruction (LVOTO) and hematuria that developed following an aortic valve replacement (AVR) and septal myectomy (SM) in another hospital. According to the previous hospitalization records of the patient, the initial preoperative transthoracic echocardiography (TTE) revealed severe stenosis of an aortic bicuspid valve [aortic valve (AV); area: 0.73 cm^2] and a high-pressure gradient (PG) across this AV (peak PG: 139 mmHg; mean PG: 78 mmHg). In addition, both TTE and enhanced computed tomography revealed asymmetrical left ventricular hypertrophy with a maximum septal thickness of 25 mm and posterior wall thickness of 13 mm. The left ventricular end-diastolic diameter was 58 mm, and the left ventricular ejection fraction (LVEF) was 52%. At rest, no accelerated blood flow signal was detected in the left ventricular outflow tract (LVOT), and only minimal mitral regurgitation (MR) was observed. On the basis of these comprehensive preoperative examinations, a replacement of the AV with a prosthetic AV (23# ON-X mechanical aortic valve) and a surgical SM (approximately 15 mm in width, 5 mm in depth, and 20–30 mm in length, toward the apex of the hypertrophied myocardium, and distal to the left coronary cusp and right coronary cusp) were performed on the patient under cardiopulmonary bypass (CPB). Immediately after the procedure, intraoperative transesophageal echocardiography (TEE) revealed systolic anterior motion (SAM) and severe MR, with an LVOT peak PG of 132 mmHg. Therefore, surgical mitral valve (MV) edge-to-edge repair was conducted to ameliorate the SAM and MR. Although the patient was returned to the ward without SAM, with a small amount of MR, an LVOT peak PG of 29 mmHg, and an AV peak PG of 12 mmHg immediately after surgery, he presented with nausea, fatigue, and gross hematuria on the 10th day following surgery. After ruling out unrelated urinary disease, repeated TTE revealed rapid systolic flow in LVOT, such that the prosthetic AV was exposed to a jet with a peak PG of 127 mmHg and severe MR, but there was no evidence of periprosthetic leakage. Considering the LVOTO might be the principal cause of the hematuria, and after medical therapy with β-receptor and calcium channel blockers failed to alleviate his LVOTO, an alcohol septal ablation was performed. Unfortunately, this procedure also did not significantly ameliorate LVOTO or the hematuria.

On admission to our hospital, a physical examination revealed the presence of a systolic murmur at the apical and left sternal margins of the patient, as well as a rapid respiratory rate and substantial breath sounds. A series of laboratory investigations were conducted, which yielded the following results: erythrocyte count 1.81×10^{12}/L (low), hemoglobin level 6.3 g/dl (low), free hemoglobin concentration >0.04 g/dl (high), haptoglobin concentration <0.006 g/dl (low), total bilirubin concentration 41.9 μmol/L (high), direct bilirubin concentration 7.2 μmol/L, indirect bilirubin concentration 34.7 μmol/L (high), urine occult blood 3+, NT-pro BNP concentration 1.0248×10^{-6} g/dl (high), and high-sensitivity cardiac troponin I concentration 1.8945×10^{-7} g/dl (high). Furthermore, coagulation and thromboelastography tests showed no abnormalities. These findings indicated the presence of hemolytic anemia.

TTE and TEE were both repeated in our hospital and revealed the following (Figure 1): contrast-enhanced echocardiography confirmed the presence of asymmetrical left ventricular hypertrophy, with the thicknesses of the basal and middle segments of the anterior interventricular septum of 23 and 17 mm, respectively. The thicknesses of the basal and middle segments of the posterior interventricular septum were found to be 16 and 19 mm, respectively. Compared with the initial preoperative echocardiography findings, the left ventricle (LV) end-diastolic internal diameter had decreased from 58 to 45 mm, and the LVEF had increased from 52% to 71%. The LVOT flow was directed into the prosthetic AV with a systolic peak velocity of 5.8 m/s and a peak PG of 136 mmHg. Thus, SAM and an associated MR of 4+ was indicated. TEE showed that the prosthetic AV was clear and opened normally, and there was no perivalvular leakage.

Because conventional SM through an aortotomy was no longer suitable for this patient, owing to his prosthetic AV, after a comprehensive discussion, a novel minimally invasive procedure, named transapical beating-heart septal myectomy (TA-BSM), was performed (Figure 2). For this procedure, the patient was anesthetized and placed in a supine position. TTE was used to identify the position of the apex within the fifth intercostal space,

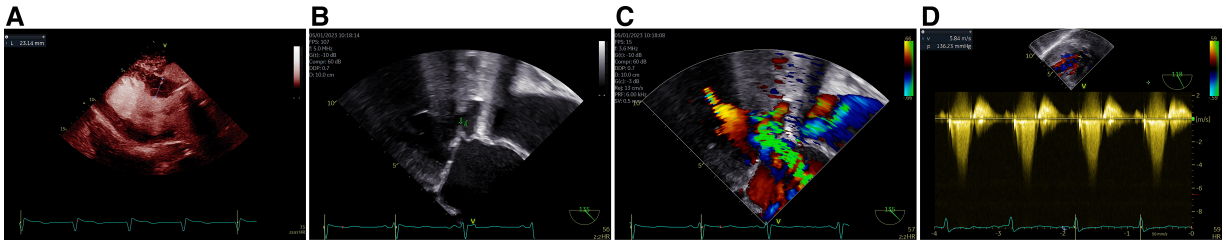

FIGURE 1
Asymmetric LV hypertrophy identified on the parasternal long-axis view using contrast-enhanced echocardiography (**A**), the anterior leaflet of the MV exhibiting prominent SAM (arrow, **B**), severe MR observed (**C**), and high systolic velocity flow in LVOT reached to 5.8 m/s with a corresponding peak PG of 136 mmHg (**D**).

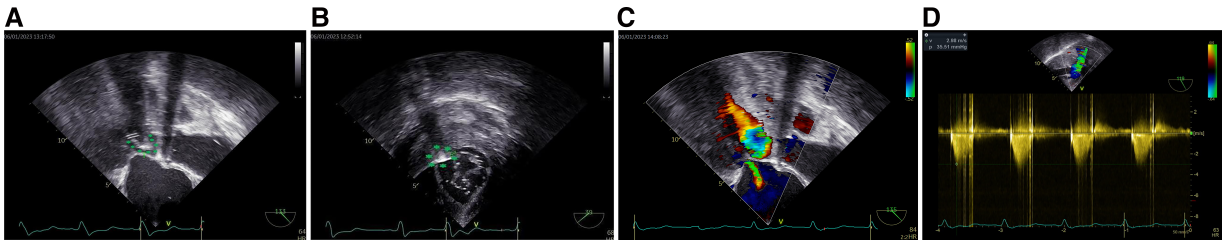

FIGURE 2
BMD tip visible on the mid-esophageal long-axis view of TEE (arrow, A). On the transgastric short-axis view, the BMD was shown close to the anterior interventricular septum (arrow, B). After the hypertrophied myocardium was resected, MR reduced to a mild degree (C) and the systolic peak velocity in the LVOT decreased to less than 3 m/s with a corresponding peak PG of 35 mmHg, indicating a favorable outcome (D).

and then the pericardium was incised and suspended. Subsequently, a double-layered pericardial purse was constructed in the apical avascular area using 3-0 prolene and a felt sheet. Once heparinization had been completed, an arterial manometric catheter was inserted through the purse string to measure the LV pressure. The systolic pressure gradient between the LV cavity and the peripheral artery, which reflects the LVOT gradient, was calculated. The manometric catheter was then withdrawn, and a guidewire was introduced to serve as a guide for the apical dissection. The apex was punctured inside the apical purse string, and then a beating-heart myectomy device (BMD), in the off state, was introduced into the LVOT, guided by TEE. The extent of advancement of the BMD was determined using the mid-esophageal LV long-axis view. The orientation of the resection was identified on the transgastric short-axis view at the basal level (Figure 2). Upon three-dimensional identification of the resection window using TEE, the first resection was performed at the midpoint of the basal anterior septum on the short-axis view, 5 mm away from the AV in the long-axis view. A second resection of the basal anterior septum was performed, parallel but slightly anterior to the first resection, which was achieved by rotating the BMD clockwise from the first resection on the short-axis. Subsequent resections were performed on the basis of a pre-procedure plan and real-time echocardiographic examination until the LVOT peak PG was <30 mmHg or the provoked LVOT gradient was <50 mmHg and the MR grade was ≤1+. A total of 7.8 g of the hypertrophied myocardium after 13 resections was successfully resected (Figure 3). After the incision had been completed, the BMD was extracted, and the apical purse strings were tightened and sutured to stop any bleeding. The entire procedure was performed in the absence of CPB.

The patient was transferred to the ward with an LVOT peak PG of 5 mmHg; his SAM and hematuria had disappeared, even though a small amount of MR persisted. There was no leakage around the aortic valve prosthesis. The patient was pathologically diagnosed as having hypertrophic cardiomyopathy following the procedure but was discharged from the hospital after his hemoglobin concentration had increased and his indirect/direct bilirubin and total bilirubin concentrations had decreased. Seven months later, the patient was found to be in

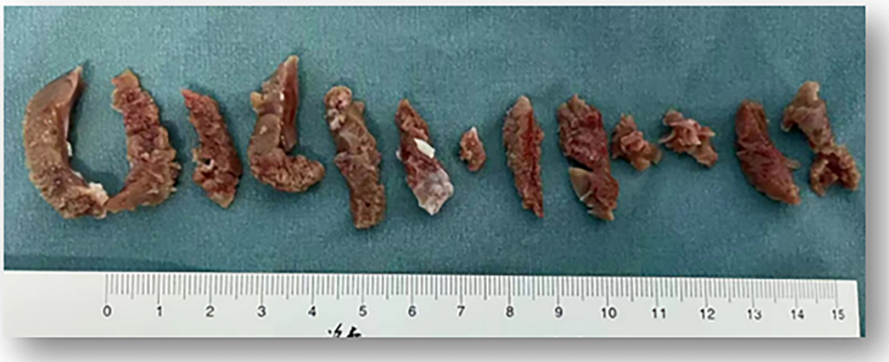

FIGURE 3
Myocardial tissue following 13 resections.

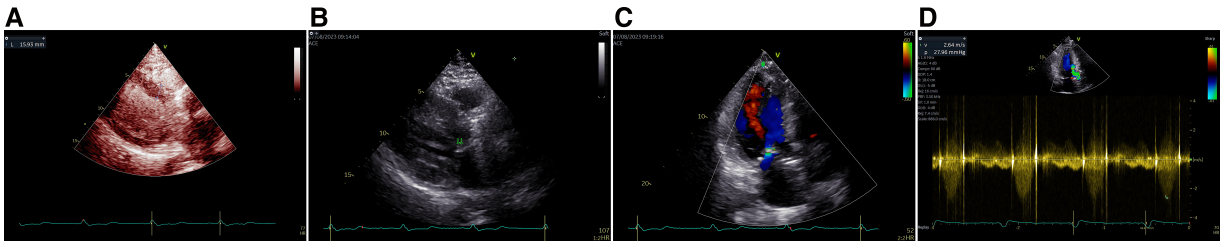

FIGURE 4
Upon a 7-month follow-up after surgery, the patient's septal thickness was notably thinner using contrast-enhanced echocardiography (**A**). SAM was no longer present (arrow, **B**). Only minimal MR remained (**C**). Systolic peak velocity in the LVOT decreased to 2.6 m/s with a corresponding peak PG of 28 mmHg, indicating a positive surgical outcome (**D**).

good health, with an LVOT peak PG of 28 mmHg (Figure 4) and no recurrence of the hematuria.

2 Discussion

Concomitant hypertrophic cardiomyopathy and aortic stenosis (AS) are common. Typical surgical treatment options include AVR in combination with drug therapy, SM, septal ablation, and mitral repair. Following technological advancements, most patients now experience superior outcomes. Hemolytic anemia caused by worsening LVOTO after AVR has been reported only once, in 2017, and was eventually ameliorated by dual-chamber pacing (1). Here, we report, for the first time, a case of hematuria in a patient with dual obstruction, which developed following AVR and SM and was ultimately alleviated using a novel, minimally invasive TA-BSM.

Accurately diagnosing AS and LVOT obstruction, as well as assessing their severity, presents a challenging task (2, 3). Some researchers have suggested using negative inotropic drugs to alleviate LVOTO before echocardiography to estimate AS (4). In the LV apical five-chamber or three-chamber views, a characteristic "dagger-shaped" envelope on the continuous-wave Doppler can be captured to determine dynamic LVOTO (5). Computed tomography and magnetic resonance imaging can provide precise cardiac structural information. Computed tomography is also a means of quantifying calcification and is increasingly recognized to be the gold-standard method of evaluating the severity of aortic stenosis. However, magnetic resonance imaging is the only non-invasive imaging modality that can be used to assess myocardial fibrosis, and therefore has a distinct advantage for the diagnosis of hypertrophic obstructive cardiomyopathy (3). The present patient underwent cardiac computed tomography, instead of magnetic resonance imaging, prior to the initial surgery. In addition, invasive hemodynamic assessment can be used to preoperatively evaluate the severity of dual obstructions (6). The interaction between AS and LVOTO makes it challenging to accurately assess their respective severities (7). Patients with severe AS have high afterloads, which mask the presence of LVOTO (5). Abnormally rapid intracavitary flow is associated with a small chamber and a hyperdynamic state in patients who have undergone AVR (8–10). In the present patient, the LV end-diastolic internal diameter decreased and LVEF increased after the initial surgery, resulting in the close proximity of the LV walls during systole, thereby reducing local pressure, causing SAM (+) and exacerbating LVOTO. The high-velocity blood flow that impinged on the mechanical aortic valve resulted in the rupture of red blood cells, leading to a high serum hemoglobin concentration and subsequent hemolytic anemia and hematuria.

Beyond the characterization of the double obstruction, the most distinctive aspect of this case study is that, to ameliorate LVOTO, the patient had undergone multiple unsuccessful procedures. Initially, drug therapy is typically used. Aggressive treatment with a β-receptor blocker and a calcium channel blocker is essential to avoid postoperative obstruction, but this was ineffective in the present patient. SM is generally considered to be the preferred treatment option for LVOTO, whether a transaortic, transmitral, or transapical route is used. Despite the risk of septal perforation, the incidence of mortality has decreased significantly with advancements in medical technology. A prospective study, published in 2021, showed that the 1-, 2-, and 5-year survival rates of 191 patients who underwent concomitant AV replacement and SM were 94%, 91%, and 83%, respectively, which are comparable to those of the general US population (11). However, there are some limitations that limit the widespread use of SM. First, stenosis of AV or MV reduces the size of the operative window, making it challenging to determine the extent and range of the septal resection required. Second, it is only after the heart resumes beating that the sufficiency of the myectomy can be assessed. Third, conventional SM is an effective treatment for sigmoid septal hypertrophy, but combined transaortic and transapical approaches are often needed to provide adequate exposure to resolve LVOTO, further increasing the complexity of the procedure and the risk of iatrogenic injury. Therefore, the technology required to perform SM is accessible only to a limited number of large heart research centers. Mitral leaflet edge-to-edge repair is an effective treatment for LVOTO caused by SAM (12). However, in the present patient, the LVOTO could not be solely attributed to SAM because it developed after combined AVR and SM. The obstruction persisted even after mitral leaflet edge-to-edge

repair was completed. Owing to its minimal invasiveness, septal ablation of the ventricular septum is more acceptable to patients (13). Prospective studies have shown that the mortality rate of patients within 30 days is 1%, and the survival rates after 1, 5, and 10 years are 98%, 89%, and 77%, respectively (14). However, this procedure is not suitable for patients with a septal thickness <15 mm, no suitable perforating artery of the ventricular septum, or prolonged occlusion of the collateral branches of the target perforating artery (15). There is also a 2% risk of left anterior descending branch stripping, coronary artery spasm, anterior wall infarction, cardiac perforation, and atrioventricular block, which is the most common complication, with 10.5% of patients requiring postoperative implantation of a permanent pacemaker (16).

In response to these limitations, our cardiac specialist team, under the leadership of Dr. Wei, pioneered the development of TA-BSM (17). This innovative approach involves the use of BMD through a mini-thoracotomy, guided by TEE, without the need for CPB. During TA-BSM, real-time TEE provides a comprehensive visualization of LV geometry, which aids the determination of the required extent and range of septal resection. In addition, it permits the measurement of hemodynamic and morphologic parameters after each resection, providing significant advantages over conventional methods. To prevent air and debris embolism, the BMD is flushed with saline to remove any trapped air during the procedure, and the resected myocardium is stored in a negative-pressure chamber until it is removed from the body. The versatility of different BMD models enables the treatment of various subtypes of hypertrophic obstructive cardiomyopathy. Moreover, the absence of CPB during surgery helps to maintain hemodynamic stability.

Data availability statement

The original contributions presented in the study are included in the article/**Supplementary Material**, further inquiries can be directed to the corresponding author.

Ethics statement

The studies involving humans were approved by the Ethics Review Board of Tongji Hospital, Tongji Medical College, Huazhong University of Science and Technology; TJ-IRB20230326; March 16, 2023. The studies were conducted in accordance with the local legislation and institutional requirements. The participants provided their written informed consent to participate in this study. Written informed consent was obtained from the individual(s) for the publication of any potentially identifiable images or data included in this article.

Author contributions

QK: Conceptualization, Data curation, Formal Analysis, Investigation, Methodology, Software, Validation, Visualization, Writing – original draft, Writing – review & editing. JT: Conceptualization, Data curation, Methodology, Validation, Visualization, Writing – original draft. YZ: Visualization, Writing – original draft, Conceptualization, Methodology, Supervision, Validation. WZ: Conceptualization, Methodology, Visualization, Writing – original draft, Validation. XW: Visualization, Writing – original draft, Investigation, Project administration, Resources. YL: Conceptualization, Methodology, Visualization, Writing – original draft, Investigation, Project administration, Resources, Supervision, Writing – review & editing.

Funding

The authors declare financial support was received for the research, authorship, and/or publication of this article.

The study was supported by Cardiovascular Ultrasound Innovation Team of Yunnan Province (202305AS350021).

Acknowledgments

The authors thank all of the doctors, nurses, technicians, and the patient involved at participating center for their dedication to the study.

Conflict of interest

The authors declare that the research was conducted in the absence of any commercial or financial relationships that could be construed as a potential conflict of interest.

Publisher's note

Supplementary material

The Supplementary Material for this article can be found online at: https://www.frontiersin.org/articles/10.3389/fcvm.2024.1410222/full#supplementary-material

References

1. Fukui S, Mitsuno M, Yamamura M, Tanaka H, Ryomoto M, Kajiyama T, et al. Left ventricular outflow tract obstruction masked by severe aortic stenosis. *Gen Thorac Cardiovasc Surg*. (2017) 65:160–3. doi: 10.1007/s11748-015-0586-z

2. Arain F, Nazemian R. Obstruction in parallel: a unique spectral Doppler pattern seen in concomitant left ventricular outflow tract obstruction and severe aortic stenosis. *A A Pract*. (2020) 14:e01352. doi: 10.1213/XAA.0000000000001352

3. Ben-Dor I, Rogers T, Medranda GA, Medvedofsky D, Weissman G, Case BC, et al. A word of caution before treating aortic stenosis in patients with concomitant LVOT obstruction. *JACC Case Rep*. (2022) 4:1162–8. doi: 10.1016/j.jaccas.2022.01.025

4. Dandel M, Hetzer R. Severe low-gradient aortic stenosis: impact of inadequate left ventricular responses to high afterload on diagnosis and therapeutic decision-making. *Heart Fail Rev*. (2022) 27:2017–31. doi: 10.1007/s10741-022-10240-y

5. Putra BE, Sukmawan R, Ariani R, Soesanto AM, Kuncoro AS. Two barricades in a row mixed lesion of dynamic left ventricular outflow tract obstruction and aortic stenosis: finding the culprit for decision making. *J Cardiovasc Echogr*. (2020) 30:104–9. doi: 10.4103/jcecho.jcecho_58_19

6. Harano Y, Kawase Y, Matsuo H. Unmasking the severity of aortic stenosis by pharmacological elimination of left ventricular outflow tract obstruction: a case report. *Eur Heart J Case Rep*. (2023) 7:ytad115. doi: 10.1093/ehjcr/ytad115

7. Bansal P, Lodhi H, Mathews A, Desai A, Morcos R, Maini B, et al. Haemodynamic interplay between concomitant left ventricular outflow tract obstruction and aortic stenosis. *Interv Cardiol*. (2021) 16:e11. doi: 10.15420/icr.2020.36

8. Aurigemma G, Battista S, Orsinelli D, Sweeney A, Pape L, Cuénoud H. Abnormal left ventricular intracavitary flow acceleration in patients undergoing aortic valve replacement for aortic stenosis. A marker for high postoperative morbidity and mortality. *Circulation*. (1992) 86:926–36. doi: 10.1161/01.cir.86.3.926

9. Hashimoto M, Kaneko M, Kasao M, Ueda K. An unusual case of left ventricular outflow tract obstruction after aortic valve replacement. *Int Heart J*. (2022) 63:639–41. doi: 10.1536/ihj.21-673

10. Saito T, Inohara T, Yoshijima N, Yashima F, Tsuruta H, Shimizu H, et al. Small left ventricle and clinical outcomes after transcatheter aortic valve replacement. *J Am Heart Assoc*. (2021) 10:e019543. doi: 10.1161/JAHA.120.019543

11. Desai MY, Alashi A, Popovic ZB, Wierup P, Griffin BP, Thamilarasan M, et al. Outcomes in patients with obstructive hypertrophic cardiomyopathy and concomitant aortic stenosis undergoing surgical myectomy and aortic valve replacement. *J Am Heart Assoc*. (2021) 10:e018435. doi: 10.1161/JAHA.120.018435

12. García-Villarreal OA. Transcatheter edge-to-edge valve repair in functional mitral regurgitation. *Eur J Cardiothorac Surg*. (2022) 62:ezab521. doi: 10.1093/ejcts/ezab521

13. Li Y, Feng Y, Li X, Zuo L, Gu T, Liu L, et al. Case report: minimally invasive therapy by transcatheter aortic valve replacement and percutaneous intramyocardial septal radiofrequency ablation for a patient with aortic stenosis combined with hypertrophic obstructive cardiomyopathy: two-year follow-up results. *Front Cardiovasc Med*. (2021) 8:735219. doi: 10.3389/fcvm.2021.735219

14. Sasahira Y, Yamada R, Doi N, Uemura S. Urgent percutaneous transluminal septal myocardial ablation for left ventricular outflow tract obstruction exacerbated after surgical aortic valve replacement. *Clin Case Rep*. (2021) 9:e04789. doi: 10.1002/ccr3.4789

15. Lv H, Fan Y, Yeerken M, Gao L, Tang B, Lu Y. Radiofrequency ablation of hypertrophic obstructive cardiomyopathy—a potential method for clinical application. *Int J Cardiol*. (2022) 368:36853–54. doi: 10.1016/j.ijcard.2022.08.003

16. Rigopoulos AG, Sakellaropoulos S, Ali M, Mavrogeni S, Manginas A, Pauschinger M, et al. Transcatheter septal ablation in hypertrophic obstructive cardiomyopathy: a technical guide and review of published results. *Heart Fail Rev*. (2018) 23:907–17. doi: 10.1007/s10741-018-9706-z

17. Fang J, Liu Y, Zhu Y, Li R, Wang R, Wang DW, et al. First-in-human transapical beating-heart septal myectomy in patients with hypertrophic obstructive cardiomyopathy. *J Am Coll Cardiol*. (2023) 82:575–86. doi: 10.1016/j.jacc.2023.05.052

frontiers | Frontiers in Cardiovascular Medicine

TYPE Original Research
PUBLISHED 12 July 2024
DOI 10.3389/fcvm.2024.1398635

OPEN ACCESS

EDITED BY
Matthias Renker,
Kerckhoff Clinic, Germany

REVIEWED BY
Sara Seitun,
San Martino Polyclinic Hospital IRCCS, Italy
Gitsios Gitsioudis,
Karl-Olga-Hospital Stuttgart, Germany

*CORRESPONDENCE
Hong Pu
ph196797@163.com
Guojin Zhang
zhanggj15@lzu.edu.cn
Lan Shang
shanglan8282@163.com

†These authors have contributed equally to this work and share first authorship

RECEIVED 10 March 2024
ACCEPTED 19 June 2024
PUBLISHED 12 July 2024

CITATION
Kong W, Long B, Huang H, Li F, He Y, Chen X, Pu H, Zhang G and Shang L (2024) Diagnostic efficacy of absolute and relative myocardial blood flow of stress dynamic CT myocardial perfusion for detecting myocardial ischemia in patients with hemodynamically significant coronary artery disease.
Front. Cardiovasc. Med. 11:1398635.
doi: 10.3389/fcvm.2024.1398635

Diagnostic efficacy of absolute and relative myocardial blood flow of stress dynamic CT myocardial perfusion for detecting myocardial ischemia in patients with hemodynamically significant coronary artery disease

Weifang Kong[1†], Bingzhu Long[2†], Hongyun Huang[1], Fang Li[1], Yuefeng He[1], Xinyue Chen[3], Hong Pu[1*], Guojin Zhang[1*] and Lan Shang[1*]

[1]Department of Radiology, Sichuan Provincial People's Hospital, School of Medicine, University of Electronic Science and Technology of China, Chengdu, China, [2]School of Medicine, University of Electronic Science and Technology of China, Chengdu, China, [3]Department of Diagnostic Imaging, CT Collaboration, Siemens Healthineers, Chengdu, China

Introduction: Stress dynamic computed tomography myocardial perfusion imaging (CT-MPI) is an accurate quantitative method for diagnosing myocardial ischemia in coronary artery disease (CAD). However, its clinical application has been limited, partly due to the varied cutoff values for absolute myocardial blood flow (MBFa) and the uncertain value of the relative myocardial blood flow ratio (MBF-ratio). This study aimed to compare the diagnostic efficacy of and investigate the optimal cutoff values for MBFa and the MBF-ratio in CT-MPI for diagnosing myocardial ischemia in patients with hemodynamically significant CAD.

Methods: Patients with suspected or known hemodynamically significant CAD who underwent CT-MPI + CT angiography and invasive coronary angiography (ICA)/fractional flow reserve (FFR) between October 2020 and December 2023 were retrospectively evaluated. ICA ≥80% or FFR ≤0.8 were set as the diagnostic standards for functional ischemia. The patients and vessels were categorized into ischemic and non-ischemic groups, and differences in MBFa and the MBF-ratio were compared between the groups. The area under the curve (AUC) and optimal cutoff values were calculated. Diagnostic efficacy parameters, such as sensitivity, specificity, and accuracy, were also compared. In addition, a consistency test was performed.

Results: A total of 46 patients (mean age: 65.37 ± 8.25 years; 120 vessels) were evaluated. Hemodynamically significant stenosis was detected in 30/46 patients (48%) and 81/120 vessels (67.5%). The MBFa and MBF-ratio values

Abbreviations
ATP, adenosine disodium triphosphate; AUC, area under the curve; CAD, coronary artery disease; CCTA, coronary computed tomography angiography; CT, computed tomography; CT-MPI, CT myocardial perfusion imaging; FFR, fractional flow reserve; ICA, invasive coronary angiography; MBF, myocardial blood flow; MBFa, absolute myocardial blood flow; MBF-ratio, relative myocardial blood flow ratio; MI, myocardial ischemia; ROC, receiver operating characteristic; CI, confidence interval.

were significantly lower in the ischemic than in the non-ischemic group; in the per-vessel analysis, the MBFa values were 73 vs. 128 ($P < 0.001$) and the MBF-ratio values were 0.781 vs. 0.856 ($P < 0.001$), respectively. The optimal cutoff values for MBFa and the MBF-ratio were 117.71 and 0.67, respectively. MBFa demonstrated a sensitivity, specificity, accuracy, AUC, positive predictive value, negative predictive value, and kappa value of 97.44%, 74.07%, 81.66%, 0.936 [95% confidence interval (CI): 0.876–0.973, $P < 0.001$], 63.33%, 98.36%, and 0.631 (95% CI: 0.500–0.762), respectively. The corresponding values for the MBF-ratio were 92.31%, 85.19%, 87.5%, 0.962 (95% CI: 0.911–0.989, $P < 0.001$), 75%, 95.83%, and 0.731 (95% CI: 0.606–0.857, $P < 0.001$), with no significant difference ($P = 0.1225$).

Conclusion: Both MBFa and the MBF-ratio exhibit excellent diagnostic performance for myocardial ischemia in patients with hemodynamically significant CAD. The MBF-ratio is more robust than MBFa for interpreting CT-MPI findings in clinical practice, which is useful for radiologists and clinicians implementing CT-MPI.

KEYWORDS

myocardial ischemia, coronary artery disease, relative MBF, absolute MBF, hemodynamically significant CAD, computed tomography perfusion

1 Introduction

Coronary artery disease (CAD) poses a substantial global, medical, and social burden. Coronary computed tomography angiography (CCTA) has definite diagnostic and prognostic value (IIA evidence level) in suspected CAD cases, as stipulated in the European Society of Cardiology (ESC) guidelines (1). However, CCTA offers solely anatomical information and does not present a linear correlation between the severity of coronary artery stenosis and myocardial ischemia (MI) (2). Assessing the presence and severity of myocardial ischemia is pivotal in guiding the choice between invasive or medical CAD treatment. Hence, the clinical evaluation of both coronary arteries and myocardial perfusion is essential.

Pharmacological stress dynamic computed tomography myocardial perfusion imaging (CT-MPI) is a relatively new, non-invasive functional imaging test (3). Several clinical trials have shown the usefulness of CT-MPI for diagnosing and evaluating hemodynamically significant CAD (moderate-to-severe coronary artery stenosis). Furthermore, there is a high level of expert consensus regarding its utility for determining the presence or absence of myocardial ischemia in CAD (4–6). However, the widespread adoption of CT-MPI in clinical practice faces challenges. This is partly due to the significant variation in absolute myocardial blood flow (MBFa) cutoff values—which range from 75 to 164 ml/100 ml/min—reported in studies employing diverse CT scanners and calculation algorithms (7–18). To mitigate the impact of algorithmic and individual differences on MBFa values, some studies have used the relative myocardial blood flow ratio (MBF-ratio) for diagnosing myocardial ischemia. However, the superiority of the MBF-ratio over MBFa remains inconclusive, and a standardized cutoff value has not been established (12–18). To address this challenge in applying CT-MPI to real-world settings, more clinical studies are needed.

Patients with hemodynamically significant CAD are more susceptible to myocardial ischemia and are recommended for CT-MPI (4). This study aimed to compare the diagnostic ability of two quantitative parameters—MBFa and MBF-ratio—for myocardial ischemia and explore their optimal cutoff values. To further this goal, the CT-MPI scans of patients with hemodynamically significant CAD were reviewed to acquire myocardial perfusion information.

2 Materials and methods

2.1 Study design and patients

This retrospective study was approved by the Ethics Committee of Sichuan Provincial People's Hospital (No. 2022-357). The requirement for informed consent was waived.

Adult patients with suspected or known hemodynamically significant CAD who underwent CT-MPI + CT angiography and invasive coronary angiography (ICA)/fractional flow reserve (FFR) between October 2020 and December 2023 were evaluated. The inclusion criteria were as follows: experiencing stable angina, having completed CT-MPI + CCTA, and having undergone ICA/FFR tests within 60 days and consented to participate. The exclusion criteria were as follows: myocardial infarction; postoperative coronary revascularization (e.g., stent placement or coronary artery bypass); other types of heart diseases, such as hypertrophic cardiomyopathy and hypertensive cardiomyopathy; and CT-MPI and CCTA image quality not meeting diagnostic and postprocessing requirements.

2.2 Preparation

CT examinations were performed using a third-generation dual-source CT scanner (SOMATOM Definition Force; Siemens Healthineers, Erlangen, Germany). The following medications

were discontinued 24–48 h before the examination: beta-blockers, nitrates, calcium antagonists, dipyridamole, and aminophylline. Caffeinated beverages and foods such as coffee and cola were also not consumed within the 24 h preceding the examination. Electrocardiogram monitoring leads were attached to monitor the patients throughout the examination. Blood pressure and heart rate were assessed, and breathing exercises were conducted. Two 18-gauge cannulas were inserted into the antecubital veins.

2.3 Scanning procedure in CT-MPI

A calcium score scan was initiated, and CT-MPI was performed as follows. The scan range was calculated based on the calcium score images to cover the entire left ventricle (LV). Tube voltage and current were automatically adjusted using CARE Dose 4D and CARE kV according to the following parameters: reference tube voltage, 80 kV; reference tube current, 300 mAs; rotation time, 0.25 s/cycle, collimation, 48 mm × 1.2 mm; kernel of reconstruction, Qr36; and slice thickness and increment, 3 and 2.9 mm, respectively. Adenosine disodium triphosphate (ATP) was intravenously injected at a rate of 0.14 mg/kg/min using a drug pump to induce vasodilation. After 3 min of injection, 40 ml of iodinated contrast agent (Iodophor, 400 mg/ml iodine; Bracco, Milan, Italy) was injected at a rate of 5 ml/s, followed by 40 ml of normal saline at the same rate. The scan trigger delay was 5 s, and scanning was conducted using the shuttle-mode acquisition technique at the end of systole (250 ms after the R-wave) for a total scan time of 32 s. The patients were closely monitored for their safety during scanning, and ATP injection was immediately stopped upon any complication in the procedure.

2.4 Scanning procedure in CCTA

Nitroglycerine was administered sublingually 5–10 min after CT-MPI, and retrospective ECG-gated CCTA scanning was then performed. An automatic triggering scan of the ascending aorta was conducted with a threshold of 100 HU and a 5-s delay. We injected 40–50 ml of iodinated contrast agent (Iodophor, 400 mg/ml iodine, Bracco) at a rate of 5 ml/s, followed by saline. The following parameters were used: reference tube voltage, 100 kV; CARE Dose 4D automatic current (reference tube current, 320 mAs); rotation time, 0.25 s/cycle; collimation, 192 mm × 0.6 mm; kernel of reconstruction, Bv40; and slice thickness and increment, 0.75 and 0.5 mm, respectively.

2.5 Postprocessing and interpretation of CT-MPI data

Initially, the original perfusion data were transmitted to the postprocessing workstation (syngo.via, Siemens Healthineers), where the myocardial perfusion analysis software generated multiple sets of LV perfusion-related sequences. These sequences underwent respiratory-related displacement correction, noise reduction, and myocardial segmentation. The perfusion images were automatically generated, and image quality was assessed based on Likert scoring of CT-MPI as follows: 4, ≥90% segments without artifact; 3, ≥80% segments without artifact; 2, ≥70% segments without artifact; 1, ≥60% segments without artifact; scores of 2–4 were considered qualified. The qualified perfusion images and CCTA image with systolic phase were transmitted to cardiac function analysis software (version 2.0.5; Siemens Healthineers) to generate automatically a polar map of MBF and a mixed-volume rendering image of CCTA combined with MBF. Subsequently, volumes of interest (VOIs) with a minimum size of 0.5 cm^2 were manually delineated in the lowest perfusion regions of 1–16 segments and in the highest perfusion regions of the LV. We used short-axis images with a color-coded scale for the delineation, guided by the visualization of the polar map and the mixed-volume rendering image. The VOIs were placed, allowing for only a minimal distance (1–2 mm) from the endocardial and epicardial layers to avoid contamination.

The lowest MBF values within the per-vessel territory and the highest MBF (MBF-hi) and average MBF (MBF-global) values of the LV were automatically calculated. The MBF-ratio was determined using the following equation: MBF-ratio = lowest MBF value/reference MBF value. In the per-patient analysis, the MBF-ratio was calculated as MBF-ratio = MBF-global value/MBF-hi value; in the per-vessel analysis, it was calculated as MBF-ratio = lowest MBFa value in the per-vessel territory/MBF-hi value. VOI processing is shown in Figure 1.

2.6 Postprocessing and interpretation of CCTA data

For CCTA images, coronary artery analysis software (syngo.via, Siemens Healthineers) was utilized. Initially, image quality was evaluated based on Likert scoring to determine the accessibility of CCTA. Subsequently, the coronary artery calcification score was automatically calculated. Thereafter, the degrees of stenosis of the left anterior descending artery, left circumflex artery, and right coronary artery were evaluated based on the Society of Cardiovascular Computed Tomography guidelines (6). Obstructive CAD and coronary stenosis were defined as ≥50%, and ≥70%, respectively. The CT-MPI and CCTA results were evaluated by two cardiac radiologists blinded to patient data. Disagreements were resolved by consulting a third senior cardiac radiologist (with >10 years of experience). Patient information—such as age, sex, body mass index, and CAD risk factors—were obtained from the picture archiving and communication system. Changes in heart rate, blood pressure, and the dose–length product of CT-MPI were documented. The effective radiation dose (mSv) was calculated as $\text{dose} - \text{length product} \times k$ ($k = 0.026$ mSv mGy^{-1} cm^{-1}).

2.7 ICA and FFR

An interventional cardiologist performed ICA or FFR within 60 days of CT-MPI + CCTA examination. ICA was performed

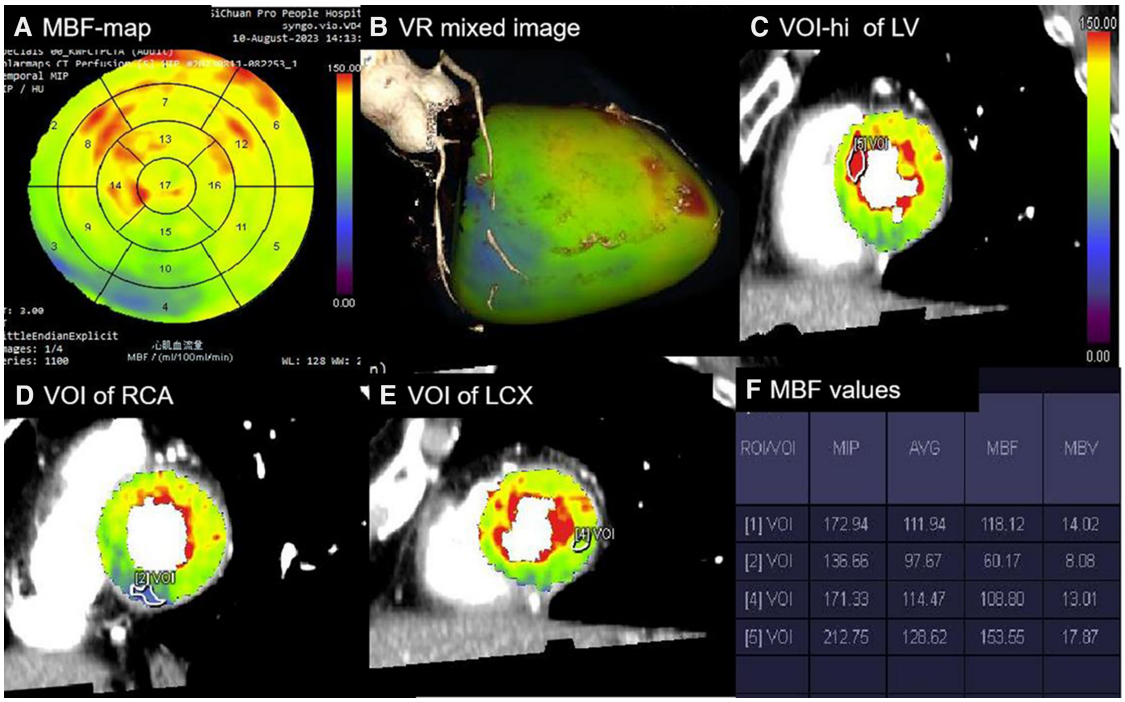

FIGURE 1
Processing of absolute and relative MBF values. (**A**) Polar map of MBF showing the MBF values in 1–17 segments with a color-coded scale. (**B**) Mixed-volume rendering image of CCTA combined with MBF showing the cardiac segments of three coronary artery territories. (**C**) VOI [5] with a minimum size of 0.5 cm^2 manually delineated in the highest perfusion regions of the LV in the short-axis images. (**D**) VOI [2] delineated in the lowest region of the RCA territory. (**E**) VOI [4] delineated in the lowest region of the LCX territory. (**F**) Perfusion parameters automatically calculated for all VOIs [1], referring to the average perfusion of the LV. The MBF-ratio values could then be determined using the following equation: MBF-ratio = lowest MBF value/reference MBF value. RCA, right coronary artery; LCX, left circumflex artery.

using the standard method, and at least two views were obtained and analyzed for each major vessel. Two cardiologists visually analyzed the images without knowledge of the CCTA and CT-MPI results, referring to quantitative coronary angiography when reaching an impasse regarding the degree of stenosis. If vessels presented with intermediate stenosis (i.e., a diameter reduction of between 50% and 80% on ICA), FFR measurements were performed. FFR was performed using a sensor-tipped 0.014-in. pressure wire in these lesions during rest and maximal myocardial hyperemia induced by the venous infusion of ATP (140 μg/kg/min). FFR values ≤0.80 were considered to indicate ischemic lesions. Lesions for which FFR measurements could not be obtained were classified based on ICA; the presence and absence of myocardial ischemic lesions were defined as those with ≥80% and <50% stenosis, respectively. Vessels with intermediate stenosis but without FFR measurements were excluded. Arteries with one or more ischemic lesions were identified as vessels causing ischemia, and the most severe stenosis was considered for analysis in the same perfusion territory.

2.8 Statistical analysis

All statistical analyses were conducted using SPSS (version 26.0, IBM) and the MedCalc software package (MedCalc 15.2.0). Categorical variables were presented as frequencies and composition ratios (%), while continuous variables were expressed as means ± standard deviations or medians with interquartile ranges. Normally and non-normally distributed data were analyzed using the variance or *t*-test and Mann–Whitney *U*-test, respectively. The Bonferroni correction was used for multiple comparisons. Each patient and vessel were studied individually. Differences in MBFa and the MBF-ratio between the myocardial ischemic and non-ischemic groups were compared. Using ICA/FFR as a standard, receiver operating characteristic (ROC) curves were generated for each analytical method, and the area under the curve (AUC) values were compared using the DeLong test. The optimal cutoff values were determined using the Youden test. Cohen's kappa statistic was used to compare the diagnostic utility of MBFa and the MBF-ratio with that of ICA/FFR for myocardial ischemia. A bilateral P-value < 0.05 was considered statistically significant.

3 Results

3.1 Patient characteristics

Among the 105 patients with suspected or known hemodynamically significant CAD, 94 underwent CT-MPI combined with CCTA examinations. We excluded 48 patients due to coronary artery stenting ($n = 6$), a history of myocardial infarction ($n = 5$), hypertrophic cardiomyopathy ($n = 3$), not

undergoing ICA ($n = 28$), and image quality not meeting postprocessing requirements ($n = 6$). Finally, the remaining 46 patients were evaluated; of these, 30 and 16 patients were diagnosed with the presence and absence of myocardial ischemia, respectively. Twenty-nine patients had moderate stenosis (50%–69%), while 17 patients had severe or occluded stenosis (≥70%) on CCTA. Of the 132 vessels initially evaluated, 12 vessels with 50%–80% stenosis not tested by FFR were excluded. Therefore, 120 vessels were analyzed, including 39 and 81 vessels with the presence and absence of myocardial ischemia, respectively. In total, 33, 27, 46, and 10 vessels had 0%–24%, 25%–49%, 50%–80%, and 80%–99% stenosis, respectively, and 4 vessels had chronic total occlusion on ICA. The flowchart is presented in Figure 2.

The mean age of the patients was 65.37 ± 8.25 years, and 32 patients (69.6%) were men. Compared with the non-ischemic group, the myocardial ischemic group exhibited a higher prevalence of multivessel stenosis (76.7% vs. 37.5%, $P = 0.032$) and a significantly higher calcification score ($P = 0.018$). Patients in the ischemic group were also older; however, there were no significant between-group differences in terms of sex or other high-risk factors for CAD. The results are presented in Table 1.

All participants tolerated the CT-MPI procedures well. The mean heart rate increased from 76.84 ± 12.77 bpm during rest to 90.87 ± 30.69 bpm during stress. The Likert scores for the image quality of CT-MPI were as follows: 4 for 30 patients, 3 for 12 patients, 2 for 4 patients, and 1 for 6 patients (who were excluded). The radiation exposure during CT-MPI was 297.44 ± 91.64 mGy cm, equivalent to 7.72 ± 2.38 mSv.

3.2 Differences between the ischemic and non-ischemic groups

In the per-patient analysis, both the MBF-global and MBF-ratio were significantly lower in the ischemic than in the non-ischemic group (127.35 ± 21.15 vs. 153.05 ± 28.15, $P = 0.004$, and 0.781 ± 0.075 vs. 0.856 ± 0.053, $P < 0.001$, respectively). The results are presented in Figure 3 and Table 2. Similar results were obtained in the per-vessel analysis. Both MBFa and the MBF-ratio were significantly lower in the ischemic group than in the non-ischemic group (73,47.66–106.83 vs. 128,116.44–151.51, $P < 0.001$, and 0.455 ± 0.169 vs. 0.775 ± 0.108, $P < 0.001$,

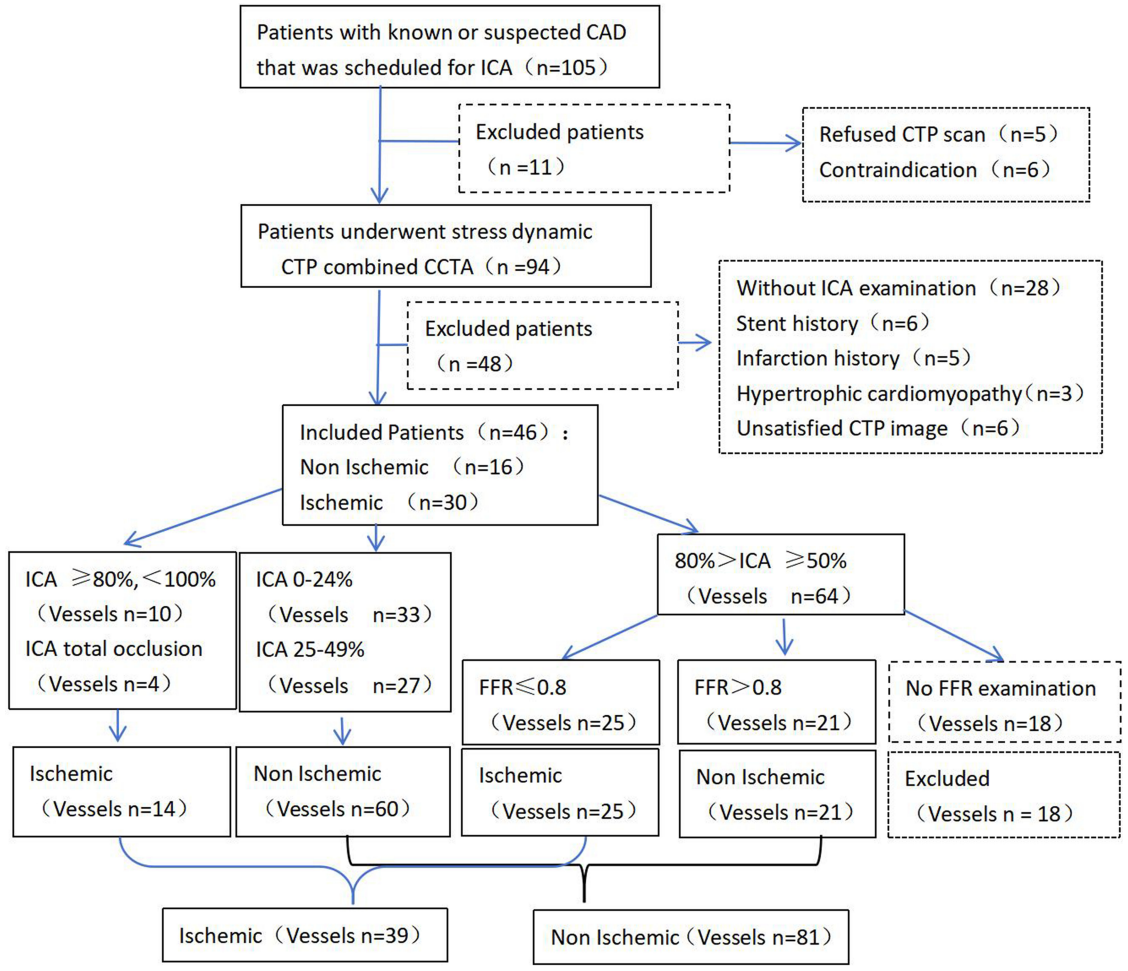

FIGURE 2
Patient inclusion flowchart.

TABLE 1 Patient characteristics.

Characteristic	Total ($n = 46$)	Ischemic group ($n = 30$, 65.22%)	Non-ischemic group ($n = 16$, 34.78%)	*P*-value
Age (years)	65.37 ± 8.25	67.67 ± 7.80	61.06 ± 7.50	0.008
Sex (male)	32 (69.60%)	22 (73.30%)	10 (62.50%)	0.447
BMI	24.17 ± 2.71	24.36 ± 2.82	23.66 ± 2.12	0.350
Hypertension (yes)	24 (52.20%)	18 (60%)	6 (37.50%)	0.146
Diabetes (yes)	19 (41.30%)	15 (78.93%)	74 (25.9%)	0.185
Hyperlipidemia (yes)	21 (45.70%)	14 (46.70%)	7 (43.80%)	0.623
Family history of CAD (yes)	9 (19.60%)	7 (23.33%)	2 (12.54%)	0.850
Number of vessel lesions				0.032
Three vessels	29 (63.00%)	23 (76.70%)	6 (37.50%)	
Two vessels	10 (21.70%)	4 (13.30%)	6 (37.50%)	
One vessel	7 (15.20%)	3 (10.00%)	4 (25.00%)	
Smoking (yes)	18 (39.10%)	12 (40.00%)	6 (37.50%)	0.869
Typical angina (yes)	23 (50%)	16 (53.3%)	7 (43.75%)	0.513
Resting HR (bpm)	71.2 ± 21.25	71.04 ± 25.94	71.5 ± 7.04	0.938
Stress HR (bpm)	86.00 ± 28.15	87.54 ± 29.56	83.14 ± 26.14	0.632
Calcification score	363.01 ± 495.31	585.66 ± 106.93	136.51 ± 34.13	0.018

BMI, body mass index; HR, heart rate; bpm, beats per minute.

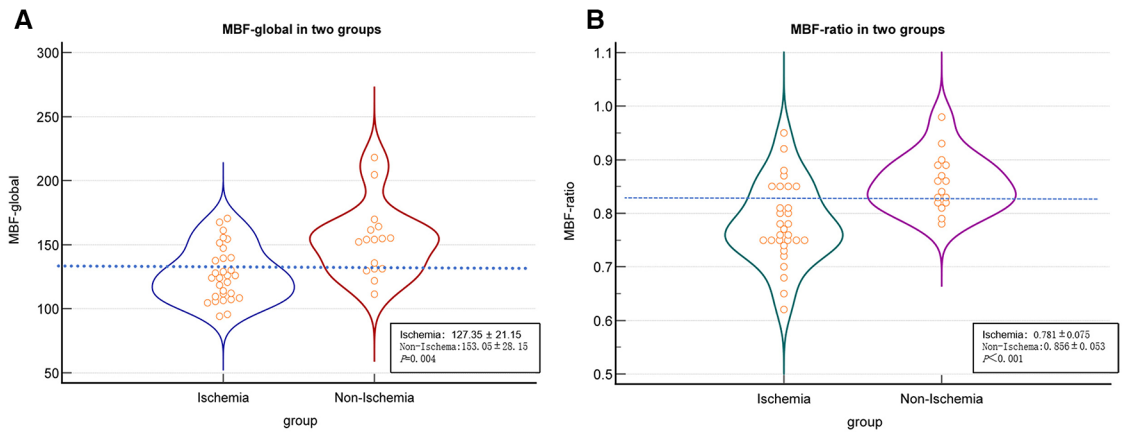

FIGURE 3
Comparison graphs of MBFa and the MBF-ratio in the ischemic and non-ischemic groups in the per-patient analysis. (A) Graph showing the distribution of the mean ± SD MBFa in the ischemic (blue) and non-ischemic (red) groups. The dotted line shows the optimal cutoff value (129.37 ml/100 ml/min). (B) Graph showing the mean ± SD MBF-ratio in the ischemic (green) and non-ischemic groups (pink). The dotted line shows the optimal cutoff value (0.81).

TABLE 2 MBF parameters in the per-patient analysis.

	Total ($n = 46$)	Ischemic group ($n = 30$, 65.22%)	Non-ischemic group ($n = 16$, 34.78%)	*P*-value
Highest MBF value (ml/100 ml/min)	168.70 ± 27.70	163.38 ± 25.30	178.66 ± 30.04	0.095
MBF-global value (ml/100 ml/min)	136.29 ± 26.57	127.35 ± 21.15	153.05 ± 28.15	0.004
MBF-ratio value	0.807 ± 0.076	0.781 ± 0.075	0.856 ± 0.053	<0.001

respectively). The degree of coronary artery stenosis was significantly more severe in the ischemic group ($P < 0.001$); approximately half of the patients in the non-ischemic group had only moderate stenosis. The results are presented in Figure 4 and Table 3.

3.3 Diagnostic efficacy of MBFa and MBF-ratio

In the per-patient analysis, the MBF-ratio had a higher AUC than the MBF-global for the diagnosis of myocardial ischemia;

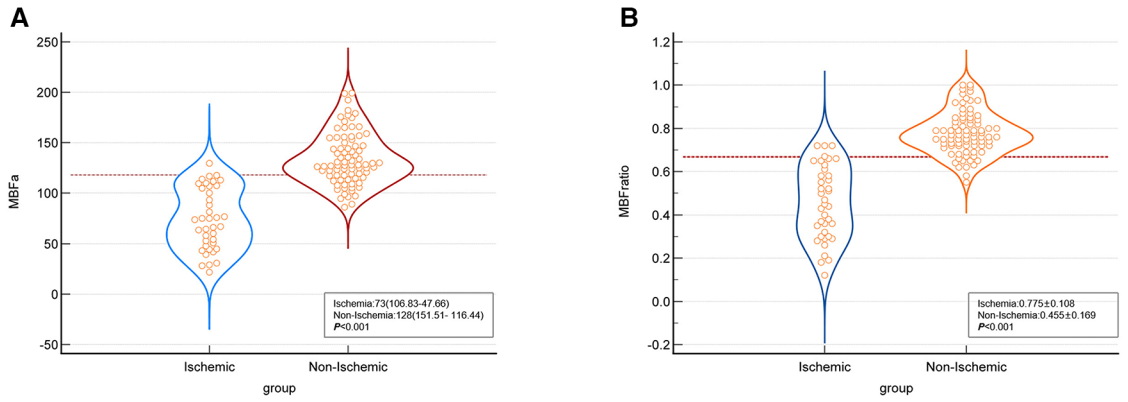

FIGURE 4
Comparison graphs of MBFa and the MBF-ratio in the ischemic and non-ischemic groups in the per-vessel analysis. (A) Graph showing the distribution of the mean ± SD MBFa in the ischemic (blue) and non-ischemic (red) groups. The dotted line shows the optimal cutoff value (117.71 ml/100 ml/min). (B) Graph showing the distribution of the mean ± SD MBF-ratio in the ischemic (blue) and non-ischemic groups (orange). The dotted line shows the optimal cutoff value (0.67).

TABLE 3 Comparison of quantitative parameters between the ischemic and non-ischemic groups in the per-vessel analysis.

	Total vessels ($n = 120$)	Ischemic vessels ($n = 39$, 32.5%)	Non-ischemic vessels ($n = 81$, 67.5%)	*P*-value
Diameter narrowing of coronary lesions by ICA (n, %)				<0.001
0: Negative (0%)	18 (15%)	0 (0%)	18 (22.2%)	
1: Minimal stenosis (1–24%)	15 (12.5%)	0 (0%)	15 (18.52%)	
2: Mild (25–49%)	27 (22.5%)	0 (0%)	27 (33.3%)	
3: Moderate (50–79%)	46 (38.33%)	25 (64.1%)	21 (25.93%)	
4: Severe (80–99%)	10 (8.33%)	10 (25.64%)	0 (0%)	
5: Occluded (100%)	4 (3.33%)	4 (10.26%)	0 (0%)	
Diameter narrowing of coronary lesions by CCTA (*n*, %)				<0.001
0: None	18 (15%)	0 (0%)	18 (22.2%)	
1: Minimal stenosis (1–24%)	14 (11.67%)	0 (0%)	14 (17.28%)	
2: Mild (25–49%)	24 (20%)	0 (0%)	24 (29.63%)	
3: Moderate (50–69%)	45 (37.5%)	22 (56.4%)	23 (28.40%)	
4: Severe (70–99%)	15 (12.5%)	13 (33.33%)	2 (2.47%)	
5: Occluded	4 (3.33%)	4 (10.26%)	0 (0%)	
Highest MBF (ml/100 ml/min)	164.5 (149–185)	160 (148–179)	165 (150.34–192)	0.079
MBF-ratio	0.722 (0.58–0.80)	0.775 ± 0.108	0.46 ± 0.17	<0.001
MBFa (ml/100 ml/min)	117.83 (95.05–138.97)	73 (47.66–106.83)	128 (116.44–151.51)	<0.001

however, the difference was not significant [0.807, 95% confidence interval (CI): 0.664–0.909, vs. 0.775, 95% CI: 0.628–0.885, $P = 0.633$]. Similarly, the MBF-ratio had a higher AUC than MBFa in the per-vessel analysis; the difference was still not significant [0.962 (95% CI: 0.911–0.989) vs. 0.936 (95% CI: 0.876–0.973), $P = 0.1225$]. The AUCs of ≥50% and ≥70% stenosis on CCTA were 0.846 (95% CI: 0.768–0.905) and 0.718 (95% CI: 0.629–0.797), respectively. Both MBFa and the MBF-ratio had higher AUCs than CCTA ($P < 0.005$). The results are presented in Figure 5 and Table 4.

The optimal cutoff value for the MBF-ratio was determined to be 0.67, with a sensitivity (high), specificity (good), accuracy, positive predictive value (PPV), and negative predictive value (NPV) of 92.31%, 85.19%, 87.5%, 75%, and 95.83%, respectively ($P < 0.001$). The MBF-ratio demonstrated strong consistency with ICA/FFR, exhibiting a kappa value of 0.731 (95% CI: 0.606–0.857, $P < 0.001$). For MBFa, the optimal cutoff value was 117.71 ml/100 ml/min, with a sensitivity (high), specificity (moderate), accuracy, PPV, and NPV of 97.44%, 74.07%, 81.66%, 63.33%, and 98.36%, respectively. The MBFa value was also strongly consistent with ICA/FFR, with a kappa value of 0.631 (95% CI: 0.500–0.762, $P < 0.001$). Stenosis ≥50% on CCTA demonstrated a sensitivity (high), specificity (moderate), accuracy, PPV, and NPV of 100%, 69.14%, 79.17%, 60.94%, and 100%, respectively; stenosis ≥70% on CCTA demonstrated higher specificity (97.53% vs. 69.14%) but lower sensitivity (46.15% vs. 100%) for the detection of hemodynamically significant CAD, and the accuracy, PPV, and NPV were 79.47%, 89.47%, and

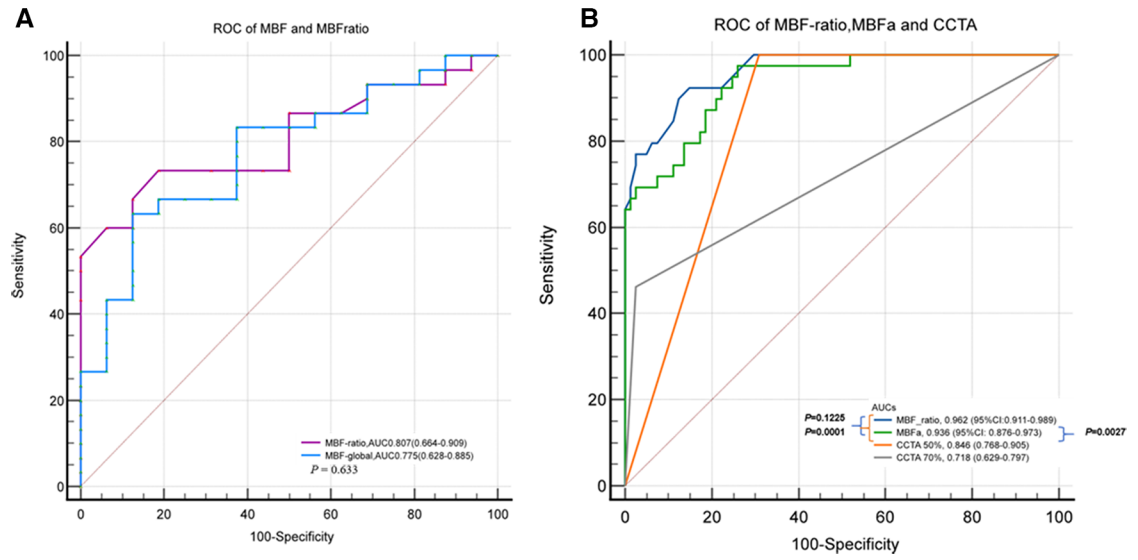

FIGURE 5
ROC curves of MBFa and the MBF-ratio for detecting MI. (**A**) ROC curves showing the AUCs of MBFa (0.705) and the MBF-ratio (0.807) for detecting MI (0.705 vs. 0.807, $P = 0.633$) in the per-patient analysis. (**B**) ROC curves showing that the AUCs of MBFa and the MBF-ratio are higher than that of CCTA for detecting MI with ≥50% and ≥70% stenosis (0.936 and 0.962 vs. 0.846 and 0.718, $P < 0.05$, respectively) in the per-vessel analysis.

TABLE 4 Diagnostic efficacy of MBFa and the MBF-ratio for myocardial ischemia.

	Sen (%)	Spe (%)	Acc (%)	PPV % (%)	NPV (%,	AUC (95% CI)	*P*-value	Cutoff value	Youden index	Kappa value (95% CI)
Per- patient										
MBFa	63.33 (19/30)	87.50 (14/16)	71.74 (33/46)	90.48 (19/21)	56.00 (14/25)	0.775 (0.628–0.885)	<0.001	129.37	0.508	
MBF-ratio	73.33 (22/30)	81.25 (13/16)	76.09 (35/46)	88.00 (22/25)	61.90 (13/21)	0.807 (0.664–0.909)	<0.001	0.81	0.546	
Per-vessel										
MBFa	97.44 (38/39)	74.07 (60/81)	81.66 (98/120)	63.33 (38/59)	98.36 (60/61)	0.936 (0.876–0.973)	<0.001	117.71	0.715	0.631 (0.500–0.762, $P < 0.001$)
MBF-ratio	92.31 (36/39)	85.19 (69/81)	87.50 (105/120)	75.00 (36/48)	95.83 (69/72)	0.962 (0.911–0.989)	<0.001	0.67	0.775	0.731 (0.606–0.857, $P < 0.001$)
CCTA (50%)	100.00 (39/39)	69.14 (56/81)	79.17 (95/120)	60.94 (25/64)	100 (56/56)	0.846 (0.768–0.905)	<0.001	50%	0.691	
CCTA (70%)	46.15 (17/39)	97.53 (79/81)	79.47 (96/120)	89.47 (17/19)	78.22 (79/101)	0.718 (0.629–0.797)	<0.001	70%	0.437	

The AUCs were compared using the DeLong test: CCTA (50%) vs. MBF-ratio, $P = 0.0001$; CCTA (50%) vs. MBFa, $P = 0.0027$; CCTA (70%) vs. MBF-ratio, $P < 0.0001$; CCTA (70%) vs. MBFa, $P < 0.0001$; MBF-ratio vs. MBFa, $P = 0.1225$; CCTA (50%) vs. CCTA (70%), $P = 0.0076$.
Sen, sensitivity; Spe, specificity, Acc, accuracy; NPV, negative predictive value; PPV, positive predictive value.

78.22%, respectively. The results are presented in Table 4. Two representative cases are presented in Figures 6, 7.

4 Discussion

4.1 Main findings

This study shows that both MBFa and the MBF-ratio have excellent diagnostic efficacy for myocardial ischemia; however, the MBF-ratio has more balanced diagnostic sensitivity and specificity and is more robust and reliable. Furthermore, in the per-vessel analysis, the optimal cutoff values for MBFa and the MBF-ratio for diagnosing myocardial ischemia were 117.71 ml/100 ml/min and 0.67, respectively.

4.2 Diagnostic performance of CT-MPI compared with CCTA

The ischemic group included more patients with multivessel lesions and severe calcification, and the degree of vessel stenosis

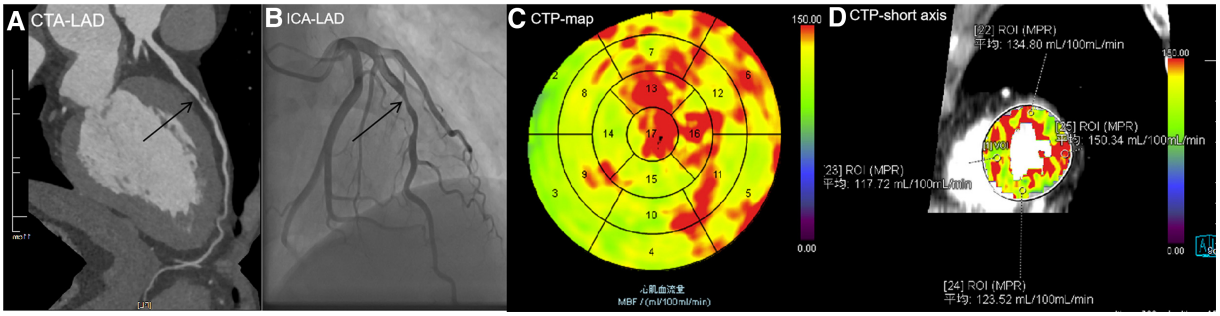

FIGURE 6
A 56-year-old man with type 2 diabetes for 1 year presented with chest pain. (**A**) CCTA image showing atherosclerotic plaques in the middle of the LAD with severe stenosis of 80%, indicating MI. (**B**) ICA showing 75% stenosis in the middle of the LAD, with an FFR value of 0.85. No revascularization therapy was performed. (**C**) CTP-MBF map image showing that the LAD territory (segment 14) was relatively lower than other areas. The MBF-global value was 131.15 ml/100 ml/min. (**D**) MBF short-axis image showing that all MBFa values were higher than the cutoff value (117.71 ml/100 ml/min), the lowest MBF-ratio value in segment 14 was 0.783 (117.72/150.34), and there was no evidence of MI. In this patient, moderate stenosis of the coronary artery did not cause MI, and MBFa and MBF-ratio values were consistent with FFR. LAD, left anterior descending artery; CTP, computed tomography perfusion.

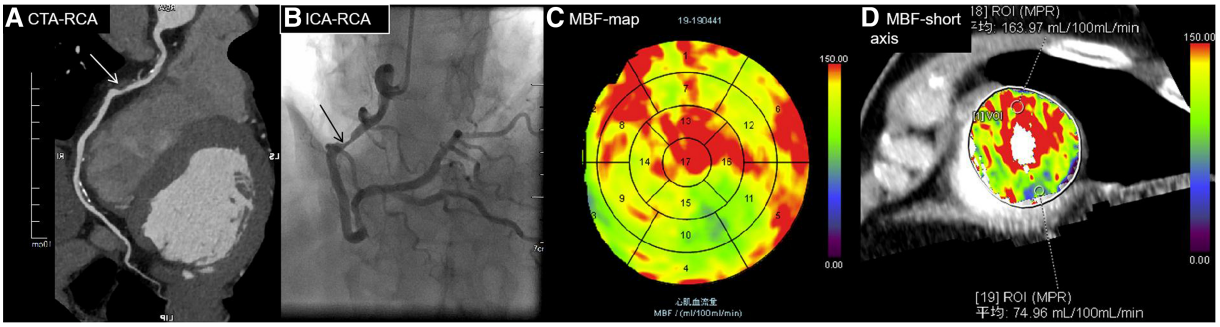

FIGURE 7
A 70-year-old man diagnosed with hypertension and diabetes for 7 years presented with chest pain. (**A**) CTA showing moderate stenosis of 75% in the middle RCA (white arrow), indicating MI. (**B**) ICA showing severe stenosis of 80% in the middle of the RCA (black arrow), with an FFR value of 0.7, indicating MI. (**C**) MBF map image showing decreased perfusion in the RCA territory (blue and green areas in segments 10, 11, and 15). (**D**) MBF short-axis image showing decreased perfusion in the inferior wall of the left ventricle, specifically at region of interest (ROI) 19. The MBFa value is 74.96 ml/100 ml/min, and the MBF-ratio is 0.46 (74.96/163.97) (highest MBF, ROI 18). The MBFa and MBF-ratio values were consistent with FFR.RCA, right coronary artery.

was more severe than in the non-ischemic group. Conversely, approximately half of the vessels had moderate stenosis in the non-ischemic group. This confirmed that the degree of stenosis was not completely proportional to myocardial ischemia in moderately stenotic vessels. Thus, further functional examinations are necessary for vessels with moderate stenosis. CT-MPI is helpful for the diagnosis of myocardial ischemia. Compared with CCTA alone, CT-MPI combined with CCTA has demonstrated significantly better accuracy for myocardial ischemia diagnosis (7–9, 16, 17). Kitagawa et al. (17) found that, compared with CCTA alone (≥50% stenosis), CT-MPI combined with CCTA had significantly higher diagnostic specificity (36% vs. 75%, $P < 0.001$) and accuracy (64% vs. 74%, $P < 0.001$), especially in the diagnosis of moderate stenosis (44% vs. 71%, $P < 0.001$). Our study demonstrated similar results: compared with CCTA (≥50% stenosis), CT-MPI using the MBF-ratio had significantly higher diagnostic specificity (69.14% vs. 85.1%, $P < 0.001$) and accuracy (79.17% vs. 87.5%, $P < 0.001$). Furthermore, MBFa had better diagnostic accuracy (79.17% vs. 81.6%, $P < 0.001$) in the per-vessel analysis. Compared with CCTA (≥70% stenosis), CT-MPI using both the MBF-ratio and MBFa had significantly higher sensitivity (46.15% vs. 97.55% and 92.31%, $P < 0.001$); this is similar to the results of a previous study (16). Furthermore, CT-MPI also demonstrated a better balance between sensitivity and specificity than CCTA. Yu et al. (19) also reported that, compared with CCTA alone, CCTA combined with CT-MPI is associated with a lower incidence of ICAs without vascular revascularization; thus, unnecessary ICA examinations can be avoided, especially in patients with moderate stenosis.

4.3 Diagnostic efficacy and optimal cutoff value of MBFa

MBFa values were significantly lower in the ischemic group than in the non-ischemic group in both per-patient and per-vessel analyses. In the per-vessel analysis, the MBFa value had an excellent AUC value of 0.936 (95% CI: 0.876–0.973), a high sensitivity of 97.44%, and a moderate specificity of 74.07%. It also had good consistency with the standard (0.631, 95% CI: 0.50–0.762). These results were consistent with those of previous studies. In a meta-analysis, the AUC of CT-MPI reached 0.911, and the sensitivity and specificity were 85% and 81%, respectively (20). The optimal cutoff value for MBFa varies substantially from 75 to 164 ml/100 ml/min (12–18); in our study, it was 117.71 ml/100 ml/min, consistent with the results of studies that used the same CT scanner and standards (20). It was also consistent with the lower limit of the normal range found by a Chinese study (116 ml/100 ml/min) (21). The main reason for the wide variation in the optimal cutoff value for MBFa may be due to differences in the degree of myocardial ischemia among patients. For example, in studies (7, 12) that included patients with myocardial ischemia and a history of revascularization, the optimal cutoff value for MBFa was significantly lower. By contrast, the optimal cutoff value was higher in studies that involved a relatively lower proportion of lesions in three vessels and severe stenosis (13, 16).

4.4 Diagnostic efficacy and optimal cutoff value for the MBF-ratio

Given the substantial variation in the optimal cutoff value for MBFa in previous studies, we tried to use the MBF-ratio; still, the results were inconsistent. Wichmann et al. (12) and Kono et al. (18) reported that the AUCs of the MBF-ratio were significantly higher than those of MBFa (0.925 vs. 0.882, $P = 0.0022$, and 0.85 vs. 0.75, $P = 0.02$, respectively). By contrast, Yi et al. (14) reported a significantly higher AUC value of MBFa (0.955 vs. 0.906, $P = 0.02$). Several studies (13, 15, 16) also reported higher AUCs for the MBF-ratio compared with those for MBFa for detecting ischemia. Specifically, the AUCs were 0.90 vs. 0.87, 0.956 vs. 0.942, and 0.82 vs. 0.79, respectively, in these studies; however, the difference was not statistically significant ($P > 0.05$). The current study showed that the MBF-ratio was significantly lower in the ischemic than in the non-ischemic group in both per-patient ($P = 0.02$) and per-vessel analysis ($P < 0.01$). The AUC value of the MBF-ratio in the per-vessel analysis was higher than that of the MBFa, albeit without a significant difference (0.936 vs. 0.962, $P = 0.1225$). However, the MBF-ratio showed a trend of a better balance between sensitivity (92.31%) and specificity (85.19%) than MBFa (sensitivity, 97.44%; specificity, 74.07%). In addition, the MBF-ratio exhibited better consistency with the diagnostic standards for functional ischemia (ICA ≥80% or FFR ≤0.8). Collectively, these results indicated that the MBF-ratio demonstrated equal or superior diagnostic efficacy compared with the MBFa for myocardial ischemia diagnosis.

The optimal cutoff values for the MBF-ratio range from 0.675 to 0.85 (12–18), with an optimal value of 0.67 in the current study. These values align closely with the pressure drop for myocardial ischemia diagnosis by FFR (0.75–0.8). The highest MBF can be selected as a reference to simulate the maximum initial normal state of the coronary artery. Overall, compared with MBFa, the MBF-ratio exhibits a relatively smaller range of variation, making it more robust and reliable in real-world clinical applications. One possible reason for the different performance of the MBF-ratio is the difference in study design (12–18, 22), particularly the different denominators (remote myocardium of reference) used as reference MBF values. These included the highest segmental MBF value without artifacts (12, 18) and the highest automatic segmental value of the endocardium (14), the third quartile of the average segmental value (13), and the average MBF value of the LV (23, 24) and all the myocardial segments supplied by vessels with <30% stenosis (14). These MBF values were all used as reference MBF values for calculating the MBF-ratio. Theoretically, using the MBF-hi as a reference MBF value should yield lower cutoff values than other MBF values. Using the third quartile or average MBF value as a reference may result in an underestimation of the identified reference value to some extent, especially in patients with multivessel stenosis. This results in an amplification of relative proportions and an increase in false-negative results; thus, the MBF-hi may be a better reference to simulate the maximum initial normal state of the coronary artery (22). Another reason for different performance is a different numerator (endocardial, epicardial, or transmural perfusion). Endocardial analysis makes perfusion defects more apparent than transmural and epicardial assessments (18). For predicting ischemia, the MBF-ratio of the endocardial myocardium layer as a numerator performs better than the ratio from the transmural layer (13, 22). In our study, we drew VOIs in the transmural layers to avoid artifacts related to myocardial displacement of the LV.

Given the different perfusion between the endocardium and epicardia, the transmural perfusion ratio (TPR) and endocardial-to-epicardial MBF-ratio are also used to detect myocardial ischemia. The TPR has a lower AUC than a visual analysis of myocardial perfusion (0.759 vs. 0.877, $P = 0.002$) (25) while exhibiting comparable performance to that of the absolute MBF value (26). In previous studies, the AUC of the TPR was significantly higher than that of the MBF for the detection of flow-limiting CAD (0.833 vs. 0.711, $P = 0.0273$) (27). However, the diagnostic utility of the TPR for detecting myocardial ischemia still needs to be further explored.

4.5 Radiation dose

The disadvantages of dynamic CT-MPI include the radiation dose. However, this study used a third-generation dual-source CT system with radiation exposure of 7.72 ± 2.38 mSv, a nearly 30% reduction in dose from previous studies utilizing a second-generation

dual-source CT system wherein the radiation exposure ranged from 588 to 757 mGy cm, i.e., 8.23–10.6 mSv (3, 5). One study attempted to reduce the radiation dose of CT perfusion to 3.8 ± 1.4 mSv by lowering the tube voltage to 70 kV (22).

4.6 Limitations

First, this was a retrospective, single-center, small-sample study; thus, the findings may apply only to similar examination protocols using third-generation dual-source CT. Second, diagnosing myocardial ischemia requires reference to the normal range in healthy individuals. Third, MBF was measured semiautomatically on the axial images, which may have resulted in interobserver differences and long postprocessing times. Fourth, FFR was performed using a visual analysis of ICA with 50%–80% stenosis, which may have influenced the results of the study. Finally, the study included patients with non-ischemic and chronic occlusion, which may have led to an overevaluation of the performance of CT-MPI. Multicenter prospective trials are needed to investigate further automated methods for measuring the relative MBF. The diffusion and clinical use of automatic software offering standardization of CT-MPI quantitative data will help define the best approach in different clinical settings in the future. The application of new techniques, such as the use of deep learning to remove motion artifacts of the LV, will also help improve the effectiveness of quantitative parameters for diagnosing myocardial ischemia.

4.7 Conclusions

In conclusion, stress dynamic CT-MPI offers high spatial resolution, complete left ventricle coverage, and the ability to correlate perfusion abnormalities with coronary CCTA results, thus seamlessly integrating anatomy and function. Importantly, the MBFa and MBF-ratio have excellent diagnostic efficacy in diagnosing myocardial ischemia, and the relative MBF-ratio has a more balanced diagnostic sensitivity and specificity. The result is particularly useful for radiologists and clinicians, addressing a common challenge in applying CT-MPI in real-world settings and thus potentially impacting the accurate diagnosis and management of CAD.

Data availability statement

The original contributions presented in the study are included in the article/Supplementary Material, further inquiries can be directed to the corresponding authors.

Ethics statement

The studies involving humans were approved by the Ethics Committee of the Sichuan Provincial People's Hospital (No.2022-357). The studies were conducted in accordance with the local legislation and institutional requirements. The Ethics Committee/institutional review board waived the requirement of written informed consent for participation from the participants or the participants' legal guardians/next of kin because it is a retrospective study of clinical data without naming or privacy.

Author contributions

WK: Conceptualization, Data curation, Funding acquisition, Methodology, Writing – original draft, Writing – review & editing. BL: Formal Analysis, Investigation, Validation, Writing – original draft, Methodology, Software. HH: Writing – review & editing, Conceptualization, Investigation, Methodology, Software. FL: Conceptualization, Writing – review & editing, Data curation, Investigation, Methodology, Software. YH: Investigation, Methodology, Software, Writing – original draft, Conceptualization, Data curation. XC: Conceptualization, Methodology, Software, Writing – review & editing, Formal Analysis. HP: Writing – review & editing, Project administration, Resources, Supervision. GZ: Conceptualization, Project administration, Supervision, Writing – review & editing. LS: Conceptualization, Formal Analysis, Writing – review & editing, Funding acquisition, Investigation, Validation.

Funding

The authors declare financial support was received for the research, authorship, and/or publication of this article.

This work was supported by the Sichuan Science and Technology Program (No. 2022YFS0075), the Sichuan Provincial Cadre Health Research Project (Nos. 2020-225, 2021-230), and the Liang Shan Science and Technology Bureau (No. 21ZDY0069).

Conflict of interest

Author XC was employed by company Siemens Healthineers.

The remaining authors declare that the research was conducted in the absence of any commercial or financial relationships that could be construed as a potential conflict of interest.

Publisher's note

References

1. Knuuti J, Wijns W, Saraste A, Capodanno D, Barbato E, Funck-Brentano C, et al. 2019 ESC guidelines for the diagnosis and management of chronic coronary syndromes. *Eur Heart J*. (2020) 41(3):407–77. doi: 10.1093/eurheartj/ehz425

2. Ciccarelli G, Barbato E, Toth GG, Gahl B, Xaplanteris P, Fournier S, et al. Angiography versus hemodynamics to predict the natural history of coronarystenoses: fractional flow reserve versus angiography in multivessel evaluation 2substudy. *Circulation*. (2018) 137:1475–85. doi: 10.1161/CIRCULATIONAHA.117.028782

3. Seitun S, Castiglione Morelli M, Budaj I, Boccalini S, Galletto Pregliasco A, Valbusa A, et al. Stress computed tomography myocardial perfusion imaging: a new topic in cardiology. *Rev Esp Cardiol*. (2016) 69:188–200. doi: 10.1016/j.rec.2015.10.018

4. Patel AR, Bamberg F, Branch K, Carrascosa P, Chen M, Cury RC, et al. Society of Cardiovascular Computed Tomography expert consensus document on myocardial computed tomography perfusion imaging. *J Cardio Vasc Comput Tomogr*. (2020) 14:87–100. doi: 10.1016/j.jcct.2019.10.003

5. Sliwicka O, Sechopoulos I, Baggiano A, Pontone G, Nijveldt R, Habets J, et al. Dynamic myocardial CT perfusion imaging—state of the art. *Eur Radiol*. (2023) 33 (8):5509–25. doi: 10.1007/s00330-023-09550-y

6. Cury RC, Leipsic J, Abbara S, Achenbach S, Berman D, Bittencourt M, et al. CAD-RADS^{TM} 2.0—2022 coronary artery disease-reporting and data system: an expert consensus document of the Society of Cardiovascular Computed Tomography (SCCT), the American College of Cardiology (ACC), the American College of Radiology (ACR), and the North America Society of Cardiovascular Imaging (NASCI). *J Cardiovasc Comput Tomogr*. (2022) 16(6):536–57. doi: 10.1016/j.jcct.2022.07.002

7. Bamberg F, Becker A, Schwarz F, Marcus RP, Greif M, von Ziegler F, et al. Detection of hemodynamically significant coronary artery stenosis: incremental diagnostic value of dynamic CT-based myocardial perfusion imaging. *Radiology*. (2011) 260:689–98. doi: 10.1148/radiol.11110638

8. Pontone G, Andreini D, Guaricci AI, Baggiano A, Fazzari F, Guglielmo M, et al. Incremental diagnostic value of stress computed tomography myocardial perfusion with whole-heart coverage CT scanner in intermediate- to high-risk symptomatic patients suspected of coronary artery disease. *JACC Cardiovasc Imaging*. (2019) 12:338–49. doi: 10.1016/j.jcmg.2017.10.025

9. Pontone G, Baggiano A, Andreini D, Baggiano A, Fazzari F, Guglielmo M, et al. Dynamic stress computed tomography perfusion with a whole-heart coverage scanner in addition to coronary computed tomography angiography and fractional flow reserve computed tomography derived. *JACC Cardiovasc Imaging*. (2019) 12:2460–71. doi: 10.1016/j.jcmg.2019.02.015

10. Huber AM, Leber V, Gramer BM, Muenzel D, Leber A, Rieber J, et al. Myocardium: dynamic versus single-shot CT perfusion imaging. *Radiology*. (2013) 269(2):378–86. doi: 10.1148/radiology.13121441

11. Rossi A, Merkus D, Klotz E, Mollet N, de Feyter PJ, Krestin GP. Stress myocardial perfusion: imaging with multidetector CT. *Radiology*. (2014) 270:25–46. doi: 10.1148/radiol.13112739

12. Wichmann JL, Meinel FG, Schoepf UJ, Lo GG, Choe YH, Wang Y, et al. Absolute versus relative myocardial blood flow by dynamic CT myocardial perfusion imaging in patients with anatomic coronary artery disease. *Am J Roentgenol*. (2015) 205:W67–72. doi: 10.2214/AJR.14.14087

13. Rossi A, Wragg A, Klotz E, Pirro F, Moon JC, Nieman K, et al. Dynamic computed tomography myocardial perfusion imaging comparison of clinical analysis methods for the detection of vessel-specific ischemia. *Circ Cardiovasc Imaging*. (2017) 10(4):e005505. doi: 10.1161/CIRCIMAGING.116.005505

14. Yi Y, Xu C, Wu W, Wang Y, Li YM, Ge YQ, et al. Stress dynamic myocardial CT perfusion for symptomatic patients with intermediate- or high-risk of coronary artery disease: optimization and incremental improvement between the absolute and relative myocardial blood flow analysis. *J Cardiovasc Comput Tomogr*. (2020) 14(5):437–43. doi: 10.1016/j.jcct.2020.01.010

15. Li YH, Dai X, Lu ZG, Shen CX, Zhang JY. Diagnostic performance of quantitative, semi-quantitative, and visual analysis of dynamic CT myocardial perfusion imaging: a validation study with invasive fractional flow reserve. *Eur Radiol*. (2021) 31(1):525–34. doi: 10.1007/s00330-020-07145-5

16. Nous FMA, Geisler T, Kruk MBP, Alkadh H, Kitagawa K, Vliegenthart R, et al. Dynamic myocardial perfusion CT for the detection of hemodynamically significant coronary artery disease. *JACC Cardiovasc Imaging*. (2022) 15(1):75–87. doi: 10.1016/j.jcmg.2021.07.021

17. Kitagawa K, Nakamura S, Ota H, Ogawa CR, Shizuka DK, Kubo T, et al. Diagnostic performance of dynamic myocardial perfusion imaging using dual-source computed tomography. *J Am Coll Cardiol*. (2021) 78(20):1937–49. doi: 10.1016/j.jacc.2021.08.067

18. Kono AK, Coenen A, Lubbers M, Kurata A, Rossi A, Dharampal A, et al. Relative myocardial blood flow by dynamic computed tomographic perfusion imaging predicts hemodynamic significance of coronary stenosis better than absolute blood flow. *Invest Radiol*. (2014) 49(12):801–7. doi: 10.1097/RLI.0000000000000087

19. Yu M, Shen C, Dai X, Lu Z, Wang YN, Lu B, et al. Clinical outcomes of dynamic computed tomography myocardial perfusion imaging combined with coronary computed tomography angiography versus coronary computed tomography angiography-guided strategy. *Circ Cardiovasc Imaging*. (2020) 13(1):e009775. doi: 10.1161/CIRCIMAGING.119.009775

20. Lu M, Wang S, Sirajuddin A, Arai AE, Zhao S. Dynamic stress computed tomography myocardial perfusion for detecting myocardial ischemia: a systematic review and meta-analysis. *Int J Cardiol*. (2018) 258:325–31. doi: 10.1016/j.ijcard.2018.01.095

21. Lyu LJ, Pan JC, Li DM, Li XH, Yang W, Dong M, et al. Knowledge of hyperemic myocardial blood flow in healthy subjects helps identify myocardial ischemia in patients with coronary artery disease. *Front Cardiovasc Med*. (2022) 3(9):817911. doi: 10.3389/fcvm.2022.817911

22. Yi Y, Xu C, Wu W, Wang Y, Li YM, Dong M, et al. Myocardial blood flow analysis of stress dynamic myocardial CT perfusion for hemodynamically significant coronary artery disease diagnosis: the clinical value of relative parameter optimization. *J Cardiovasc Comput Tomogr*. (2020) 14(4):314–21. doi: 10.1016/j.jcct.2019.10.001

23. Yi Y, Xu C, Wu W, Shen ZJ, Lee W, Yun CH, et al. Low-dose CT perfusion with combined use of CTP and CTP-derived coronary CT angiography at 70 kVp: validation with invasive fractional flow reserve. *Eur Radiol*. (2021) 31(2):1119–29. doi: 10.1007/s00330-020-07096-x

24. Wichmann JL, Meinel FG, Schoepf UJ, Szemes AV, Muscogiuri G, Cannaò PM, et al. Semiautomated global quantification of left ventricular myocardial perfusion at stress dynamic CT: diagnostic accuracy for detection of territorial myocardial perfusion deficits compared to visual assessment. *Acad Radiol*. (2016) 23(4):429–37. doi: 10.1016/j.acra.2015.12.005

25. Yang DY, Kim YH, Roh JH, Kang JW, Han DJ, Jung H, et al. Stress myocardial perfusion CT in patients suspected of having coronary artery disease: visual and quantitative analysis—validation by using fractional flow. *Radiology*. (2015) 276 (3):715–23. doi: 10.1148/radiol.2015141126

26. Coenen A, Lubbers MM, Kurata A, Kono A, Dedic A, Chelu RG, et al. Diagnostic value of transmural perfusion ratio derived from dynamic CT-based myocardial perfusion imaging for the detection of haemodynamically relevant coronary artery stenosis. *Eur Radiol*. (2017) 27(6):2309–16. doi: 10.1007/s00330-016-4567-0

27. Goto Y, Kitagawa K, Uno M, Nakamori S, Ito T, Nagasawa N, et al. Diagnostic accuracy of endocardial-to-epicardial myocardial blood flow ratio for the detection of significant coronary artery disease with dynamic myocardial perfusion dual-source computed tomography. *Circ J*. (2017) 81(10):1477–83. doi: 10.1253/circj.CJ-16-1319

frontiers | Frontiers in Cardiovascular Medicine

TYPE Original Research
PUBLISHED 22 July 2024
DOI 10.3389/fcvm.2024.1399110

OPEN ACCESS

EDITED BY
Maxim Avanesov,
University Medical Center Hamburg-Eppendorf, Germany

REVIEWED BY
Datta Singh Goolaub,
University of Toronto, Canada
Takashi Fujiwara,
University of Colorado Denver, United States

*CORRESPONDENCE
Ahmad Bitarafan-Rajabi
✉ bitarafan@hotmail.com
Hojjat Mortezaeian
✉ mehranmortezaeian@yahoo.com
Kiara Rezaei-Kalantari
✉ rkkiara@gmail.com

RECEIVED 11 March 2024
ACCEPTED 10 July 2024
PUBLISHED 22 July 2024

CITATION
Zamani-Aliabadi SM, Qanadli SD, Fatehi-Feyzabad SH, Ghasemnezhad M, Ghaemi H, Azarine A, Mohammadzadeh A, Bitarafan-Rajabi A, Mortezaeian H and Rezaei-Kalantari K (2024) Assessment of 4D flow MRI for quantification of left-to-right shunt in pediatric patients with ventricular septal defect: comparison with right heart catheterization.
Front. Cardiovasc. Med. 11:1399110.
doi: 10.3389/fcvm.2024.1399110

Assessment of 4D flow MRI for quantification of left-to-right shunt in pediatric patients with ventricular septal defect: comparison with right heart catheterization

Seyed Mohammad Zamani-Aliabadi[1], Salah D. Qanadli[2], Seyed Hasan Fatehi-Feyzabad[3], Mohsen Ghasemnezhad[4], Hamidreza Ghaemi[4], Arshid Azarine[5], Ali Mohammadzadeh[3], Ahmad Bitarafan-Rajabi[1]*, Hojjat Mortezaeian[4]* and Kiara Rezaei-Kalantari[3]*

[1]Department of Medical Physics, School of Medicine, Iran University of Medical Sciences, Tehran, Iran, [2]Cardiothoracic and Vascular Division, Department of Diagnostic and Interventional Radiology, Lausanne University Hospital and University of Lausanne, Lausanne, Switzerland, [3]Department of Radiology, Rajaie Cardiovascular Medical and Research Center, Iran University of Medical Sciences, Tehran, Iran, [4]Department of Pediatric Cardiology, Rajaie Cardiovascular Medical and Research Center, Iran University of Medical Sciences, Tehran, Iran, [5]Department of Radiology, Hôpital Marie Lannelongue, Groupe Hospitalier Paris Saint-Joseph, Université Paris-Saclay, Paris, France

Objectives: The percentage of shunt fraction significantly impacts the management of patients with congenital shunts, influencing strategic choices such as surgical or interventional procedures. This study compared the estimated shunt fraction (the ratio of pulmonary-to-systemic flow, Qp/Qs) for quantifying the left-to-right shunt in children with ventricular septal defect (VSD) using heart catheterization, four-dimensional (4D) flow, and two-dimensional (2D) flow magnetic resonance imaging (MRI). The goal was to establish a non-invasive and reliable measurement ratio between pulmonary and systemic blood flow in these patients.
Methods: Between July 2022 and June 2023, patients scheduled to undergo invasive right heart catheterization were included in this study. MRI was performed one hour before the catheterization procedure. The correlation of shunt fraction was assessed between all methods after calculating the Qp/Qs ratio from 2D and 4D flow MRI and catheterization.
Results: A total of 24 patients (aged 3–15 years, eight females) were ultimately included in the study. The Qp/Qs ratios obtained from 4D flow had a robust correlation (correlation coefficient $r = 0.962$) compared to those obtained during catheterization. Cardiac catheterization recorded the mean shunt fraction at 1.499 ± 0.396, while 4D flow measured it at 1.403 ± 0.344, with no significant difference between the two techniques. Moreover, there was a reasonable correlation ($r = 0.894$) between 2D flow measurements of Qp/Qs and the results obtained from catheterization, with a mean shunt fraction of 1.326 ± 0.283.
Conclusion: 4D flow MRI has the potential to be a non-invasive method for accurately measuring the left-to-right shunt in children with VSD.

KEYWORDS

right heart catheterization, cardiac magnetic resonance imaging, four-dimensional (4D) flow, two-dimensional (2D) flow, shunt fraction, ventricular septal defect (VSD), congenital heart disease (CHD)

1 Introduction

Congenital heart disease (CHD) affects about 1 in every 110 births, making it the most common congenital disorder (1–3). This condition encompasses functional problems and anatomical anomalies, including atypical dimensions, irregular connections, and structural abnormalities within the heart chambers, blood vessels, and adjacent veins. The physiological implications of CHD span a wide range, from asymptomatic cases detected only in adulthood to critical complications requiring immediate surgical intervention in infancy (4). Ventricular septal defect (VSD) is children's most common congenital heart defect and the second most frequent congenital anomaly in adults. VSD is a condition with communication between the right and left ventricles, leading to shunt formation, the primary mechanism of hemodynamic compromise. This process gives rise to pulmonary arterial hypertension (PAH), ventricular dysfunction, and an increased susceptibility to arrhythmias (5, 6). Nevertheless, remarkable progress in diagnosing, managing, and treating CHD has enhanced survival rates, leading to a growing population of individuals with CHD who are now reaching adulthood (7).

Measurement of the shunt fraction is crucial in guiding management and decisions for surgical or interventional approaches for patients with congenital shunts such as VSD (8, 9). Shunt quantification includes evaluating systemic flow (Qs) and pulmonary flow (Qp), which can be done through invasive or non-invasive techniques. An invasive approach for assessing pulmonary and systemic blood flow involves using right heart catheterization with oximetry. This method has long been recognized as the gold standard and allows calculating the shunt fraction using the Fick equation (10, 11). Transthoracic and transesophageal Doppler echocardiography and cardiac magnetic resonance imaging (MRI) constitute non-invasive approaches to assess flow. However, it is essential to note that there are limitations in quantifying shunt volumes through Doppler echocardiography. Reliable and reproducible Doppler shunt measurements depend on the presence of well-acoustic windows and the expertise of highly qualified operators, both of which are essential (12–14).

Cardiovascular evaluation with MRI is widely used to evaluate cardiovascular disease based on morphological and functional information. 2D (two-dimensional) planar phase-contrast cine imaging within cardiac MRI (PC-MRI) has been established as a reliable method for shunt quantification. However, as blood flow volume and velocity must be measured on a predetermined plane, the presence of an expert physician or highly qualified technologist during the scan is necessary (15, 16). Recently, the emergence of four-dimensional (4D) flow MRI has significantly advanced the field of flow imaging, enabling a thorough investigation of blood flow in arteries and the heart (17). Therefore, the application of this procedure has increased for visualization and quantification of blood flow in CHD patients (7). 4D flow MRI falls under the category of PC-MRI, involving three-dimensional (3D) anatomical coverage, velocity encoding along all three flow directions, and time-resolved relative to the dimension throughout the cardiac cycle. This modality allows for a comprehensive evaluation of intricate blood flow patterns by making it possible to visualize them in 3D and enabling adaptable retrospective quantification of flow parameters that can be performed in any plane within the acquisition volume (17–19).

While previous studies have compared the shunt fraction between invasive catheterization and 2D flow MRI in both childhood and adulthood (15, 16) and have directly compared 4D flow MRI and catheterization in adults (20, 21), there is a notable gap in comparing shunt fraction data from 4D flow MRI with catheterization in the pediatric age group. This gap is significant because effectively managing these patients during childhood is crucial. The objective of this study was to conduct a comparative analysis of shunt fraction measurements using 4D flow MRI and catheterization, concurrently with 2D flow MRI, in a specific pathology (VSD), focusing on patients with an average age of 10 years.

2 Materials and methods

2.1 Study plan

This prospective study was conducted at a single cardiovascular medical research center from July 2022 to June 2023. Thirty-one patients were recruited from those already scheduled for invasive right heart catheterization as part of their clinical care. Three patients were excluded due to claustrophobia, as we did not intend for patients to undergo general anesthesia (GA) for MRI. Two patients had their catheterizations canceled following consultation with an anesthesiologist for GA. Additionally, two patients were excluded due to technical problems with the MRI scan. Consequently, 24 patients remained in the study.

The primary objective was to compare shunt fraction measurements (Qp/Qs) between 4D flow MRI and right heart catheterization in patients. Concurrently, we aimed to perform a similar comparison using 2D flow MRI.

2.2 Cardiac MRI

All patients underwent cardiac MRI using a 1.5T Philips scanner [MR Systems Ingenia Ambition X, Release 5.7 2021-10-04 SRN = 47525 Nominal Main Magnetic Field (B0) = 1.5T, equipped with a 32-channel phased-array coil]. Cardiovascular magnetic resonance imaging (CMR) was performed without administering contrast agents or sedation, with retrospective electrocardiogram (ECG)-gating. It was scheduled one hour before catheterization over approximately 17–20 min, including the following scan items: [Q-4D flow, sQ-2D flow aorta, sQ-2D flow pulmonary and functional assessments of short axis (SA), left ventricle (LV), right ventricle (RV), two-chamber (2CH), three-chamber (3CH), and four-chamber (4CH)].

The analysis of 4D and 2D flow MRI was carried out after catheterization, following the guidelines provided by the software's owning company. Subsequently, a radiologist with over 10 years of expertise reevaluated the results (K.R-K).

2.3 4D flow MRI

4D flow was carried out using the same protocol for all patients, which included phase contrast without breath control (free-breathing) and compressed sensing, with each scan taking approximately 4–6 min. The average scan parameters were as follows: [Voxel Cor = 2.52 × 2.50 × 2.50; Rel SNR = 1.00; TE = 2.3; TR = 4.1—Geometry: FOV: FH = 333 mm, RL = 333 mm, AP = 110 mm; ACO voxel size: FH = 2.5 mm, RL = 2.5 mm, AP = 2.5 mm; Slice thickness = 2.5 mm; Recon voxel size: FH = 1.48 mm, RL = 1.48 mm, AP = 2.5 mm; Reconstruction matrix = 224; reduction = 8; slices = 44—Contrast: Contrast enhancement = T1; Flip angle = 8 deg—Dyn/Ang: Anglo/ Contrast enhancement = phase contrast; Quantitative flow = yes; PC flow directions = RL-AP-FH; uniform velocity = yes; PC velocity = 150 cm/s]. Following previous research findings, for patients with confirmed or suspected venous shunting conditions, such as atrial septal defects (ASD) or VSD, a lower velocity encoding speed was recommended. In all our cases, this approach was adopted due to ventricular septal defects (VSD), necessitating a velocity-encoded value of 150 cm/s (20). The post-processing of data and calculation of the shunt fraction in 4D flow MRI were conducted using CAAS MR solutions software developed by Pie Medical Imaging company. Aliasing correction and window of interest with offset correction were employed as post-processing techniques. We used functional images to position a valve plane for visualizing and quantifying blood flow throughout the cardiac cycle. Functional LV and RV images were utilized for the aortic and pulmonary valves, respectively, while the 4CH view was employed for the mitral and tricuspid valves (Supplementary Figure S1). Blood flow was visualized by streamlines over the heart valves, which resulted from overlapping functional images on 4D flow (Figure 1). The results included forward and backward flow and the shunt fraction.

2.4 2D flow MRI

Cardiac MRI with 2D planar phase-contrast cine imaging was performed using a retrospective gating technique on both the ascending aorta and the main pulmonary artery, with the following scan parameters:[Voxel Tra = 2.52 × 2.47 × 8.00; Rel SNR = 1.00; TE = 2.8; TR = 4.4—Geometry: FOV: RL = 262 mm, AP = 223 mm; ACQ voxel size: RL = 2.5 mm, AP = 2.5 mm; Slice thickness = 8 mm; Recon voxel size: RL = 1.09 mm, AP = 1.09 mm; Reconstruction matrix = 240—Contrast: Contrast enhancement = T1; Flip angle = 12 deg—Dyn/Ang: Anglo/ Contrast enhancement = phase contrast; Quantitative flow = yes; PC flow directions = FH; PC velocity = 150 cm/s]. Slice position for aortic (Qs) and pulmonary (Qp) flow was approximately 2–3 cm distal to the aortic and pulmonary valves in the proximal ascending aorta and main pulmonary artery. Data post-processing in 2D flow MRI, akin to 4D flow, was accomplished using CAAS MR Solutions (Pie Medical Imaging) software. The calculation of the shunt fraction involved manual drawing of the cross-sectional areas of the pulmonary trunk and ascending aorta for each time frame on either the magnitude or phase images (Figure 2).

2.5 Right heart catheterization

Invasive oximetry was performed under sedation using the femoral vein method to obtain blood samples from the inferior vena cava (IVC), superior vena cava (SVC), right atrium (RA), right ventricle (RV), left ventricle (LV), pulmonary artery (PA), and ascending aorta (AO) before occluding the VSD (Figure 3). Subsequently, these blood samples were placed in an

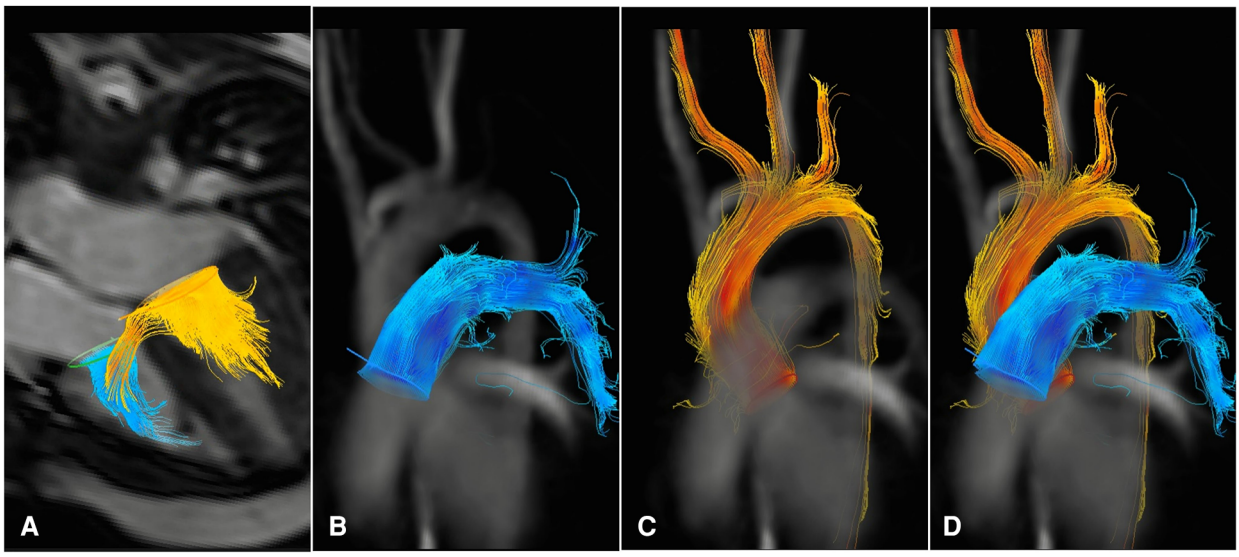

FIGURE 1
4d flow MRI images from a patient with VSD. The blood flow connection between the left and right ventricles can be visualized as yellow streamlines traversing through the ventricular septum during diastole (A) Blood flow measurements during systole are shown in the main pulmonary artery (B–D) and the ascending aorta (C–D).

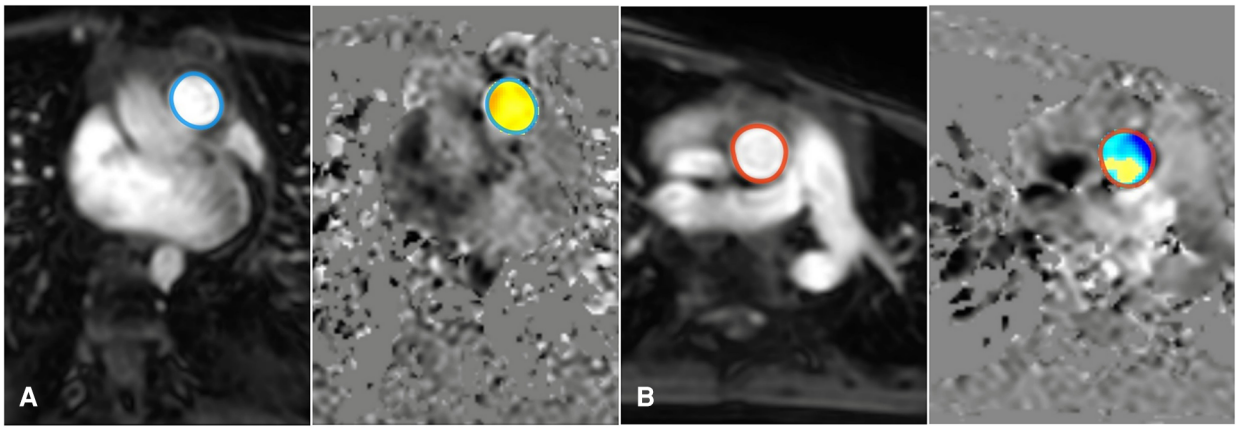

FIGURE 2
Measurement of the shunt fraction in 2D flow MRI: Add an ROI on the pulmonary artery (A), and ascending aorta artery (B).

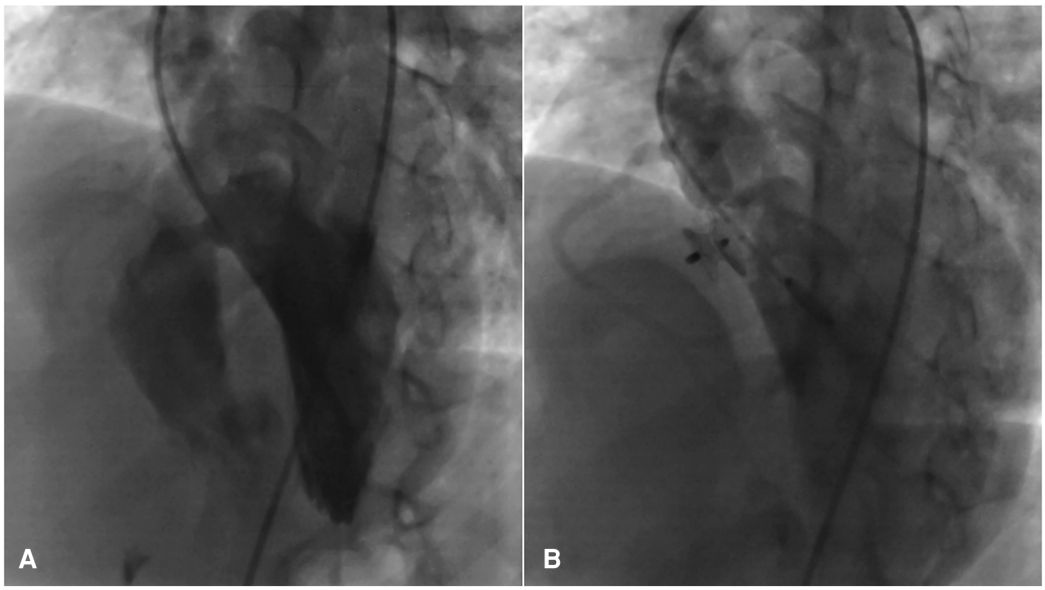

FIGURE 3
Significant peri membranous VSD extended to the sub-aortic septum, for which the 4D flow image was also displayed in (A), that was occluded by an 8 mm amplatzer asymmetric septal occluder (B).

AVOXimeter device (a tool designed for measuring oxygen saturation) to measure oxygen saturation (SatO2). In the context of invasive oximetry, the shunt fraction was determined using the Fick equation as outlined below (22):

$$Qp/Qs = \frac{\text{Ao sat} - \text{Mv}* \text{ sat}}{\text{Pv sat} - \text{Pa sat}}$$

$$*Mv = 3\text{SVC sat} + \frac{IVC\ sat}{4}$$

Ao sat and Mv sat represent arterial and mixed venous oxygen saturation, while Pv sat and Pa sat indicate pulmonary venous and pulmonary arterial oxygen saturation. SVC sat and IVC sat refer to oxygen saturation in the superior vena cava and inferior vena cava, respectively.

2.6 Statistical analysis

The correlation between shunt fraction measurements obtained through 4D flow MRI analysis and catheterization data was evaluated using linear regression analysis with Pearson correlation, and their agreement was assessed using the Bland-Altman method. Statistical analyses, Bland-Altman plots, and

scatter plots were performed using Prism GraphPad software. Similar statistical tests were conducted to compare Qp/Qs ratios derived from 2D flow data and catheterization, as well as between 4D and 2D flow (Supplementary Figure S2). A P value <0.05 was considered statistically significant for all analyses.

3 Results

3.1 Patients

Twenty-four patients were included in the final analysis. These patients had a mean age of ten years, with a standard deviation of ±4 years. Sixteen (67%) of the participants were male. All studied patients had a VSD with left-to-right shunt and no other cardiac abnormalities. Among them, 8 (33%) displayed Qp/Qs ratios lower than 1.3 (Qp/Qs<1.3), while 16 (67%) demonstrated ratios exceeding 1.3 (Qp/Qs>1.3). These assessments were based on catheterization data obtained using the Fick equation. Notably, among the entire cohort, diagnostic catheterization was performed without the need for immediate interventions in 4 cases. In contrast, VSDs were effectively occluded during the catheterization procedure in 15 cases using different types of VSD occluders, while 5 patients were subsequently referred for surgical treatment. Six patients were diagnosed with pulmonary hypertension, characterized by a pulmonary arterial pressure exceeding 20 mm Hg. Furthermore, eighteen individuals exhibited pulmonary pressures within the normal range, registering at 20 mmHg or below (Table 1).

TABLE 1 Patient characteristics.

Variables	Overall ($N = 24$)
Female	$N = 8$
Male	$N = 16$
Mean age (years)	10 ± 4
Height (cm)	136 ± 23
Weight (kg)	35 ± 21
Cardiac shunt	Left-to-right
Mean PAP (mm Hg) >20	$N = 6$
Mean PAP (mm Hg) ≤20	$N = 18$

Cardiac shunt and pulmonary artery pressure (PAP) were determined through a catheterization procedure.

3.2 Assessing shunt fraction: a comparative analysis of MRI and catheterization data

The Qp/Qs ratios derived from 4D flow strongly correlated with those determined through catheterization (R = 0.962; 95% CI: 0.9133–0.9838; $P < 0.0001$). The mean shunt fraction was 1.403 ± 0.344 when evaluated using 4D flow, while it measured 1.499 ± 0.396 through cardiac catheterization, revealing no significant difference between the two methods. The bias was 0.096, and the limits of agreement ranged from −0.127 to 0.319 (Table 2). Bland-Altman plots also displayed strong agreement between the two methods (Figure 4). In 21% of the patients, the shunt fraction obtained from 4D and 2D flow exceeded the values observed in catheterization. In contrast, 79% of the cases demonstrated lower values when compared to the shunt fraction obtained through catheterization.

Analysis of 2D flow yielded Qp/Qs ratios that exhibited a fair correlation with those calculated through catheterization using the Fick equation (R = 0.894; 95% CI: 0.7687 to 0.9538; $P < 0.0001$). The mean shunt fraction was 1.326 ± 0.283 when measured through 2D flow. At the same time, the Bland-Altman analysis indicated excellent agreement between the Qp/Qs ratios obtained through 2D flow and catheterization; this level of correlation was lower than the results obtained between 4D flow and catheterization (Figure 4 and Table 2).

TABLE 2 Comparison of shunt fraction 4D flow MRI, catheterization, and 2D MRI.

Parameters Procedures	Pearson correlation coefficient	Mean difference (point value)	Upper limit	Lower limit
4D flow vs. catheterization	R = 0.962	0.096	0.319	−0.127
2D flow vs. catheterization	R = 0.894	0.172	0.546	−0.201
4D flow vs. 2D flow MRI	R = 0.969	0.049	0.199	−0.099

The mean difference (point value) and the upper and lower limits were derived from the Bland-Altman (BA) analysis. The correlation coefficient (R) was obtained using the Pearson method.

4 Discussion

For effective management and choosing the best treatment for patients with cardiac shunts, accurate measurement of shunt severity is imperative (23–29). While the conventional approach often involves invasive catheterization, this study advocates the utilization of 4D flow as a non-invasive alternative for assessing shunt-related issues or as a valuable preliminary step in the assessment process before considering catheterization. Furthermore, it suggests that invasive catheterization can be postponed in specific cases until additional information about the heart's structure or function is required to conduct a more comprehensive evaluation. Data obtained through invasive oximetry for Qp/Qs ratios (shunt fraction) demonstrated high consistency and correlation when employing 2D and 4D flow MRI techniques. Despite the time-consuming nature of 4D flow compared to 2D flow in terms of data acquisition and measurement of hemodynamic parameters, the Qp/Qs ratio obtained from invasive catheterization aligned more consistently with the results from 4D flow MRI than those from 2D phase contrast. Additionally, 4D flow MRI offers other advantages, such as comprehensive anatomical assessment and the potential for future post-processing analysis of evolving hemodynamic indices. Moreover, respiratory motion does not adversely affect measurement accuracy in 4D flow MRI, thanks to advanced techniques like compressed sensing and free-breathing protocols (30, 31). Therefore, our research demonstrates that measuring

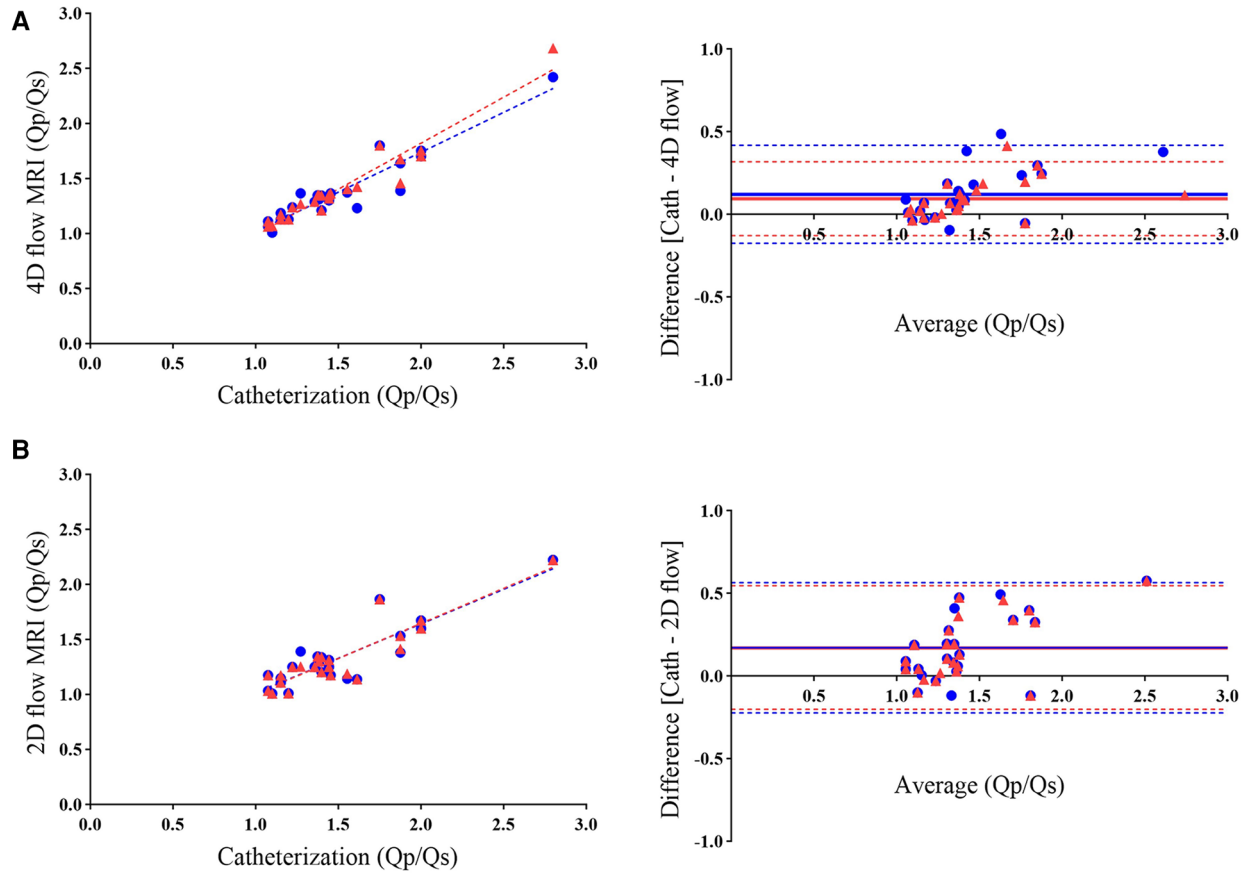

FIGURE 4
Scatterplots (left) and bland-altman analysis (right) illustrate the agreement between Qp/Qs measurements obtained using 4D flow MRI (A) and 2D flow MRI (B) with catheterization. The comparison reveals higher agreement in shunt fraction measurements with 4D flow than with 2D flow when referenced against catheterization. Blue circles represent initial data points from the analysis (R = 0.936; bias = 0.122), while red triangles indicate rechecked 4D flow measurements by an independent observer (R = 0.962; bias = 0.096). As mentioned in the manuscript, the overlapping of both colors in scatterplots and bias lines in Figure B demonstrates the lack of recheck ability in 2D flow.

pediatric left-to-right shunts using 4D flow is feasible and reliable. Consequently, in some cases, 4D flow can replace invasive testing, resulting in cost savings, reduced patient discomfort, and the prevention of severe but uncommon consequences associated with catheterization.

Our study specifically focused on calculating the shunt fraction from pulmonary and systemic flow. This emphasis stemmed from previous research, which indicated that the Qp/Qs ratio obtained from blood flow measurements is more accurate in clinical settings than ventricular volumetry (20).

Hemodynamic assessment through cardiac catheterization is a valuable diagnostic tool for evaluating various cardiovascular conditions. However, it is not without its complexities and potential complications. These complications encompass ventricular arrhythmias, temporary right bundle branch block, and complete heart block. Additionally, air embolism is risky if air enters the catheters or pressure transducers, leading to sudden chest pain, dyspnea, and hypotension. Pulmonary artery perforation, although infrequent, can occur during extended catheter placement, especially in patients with prior pulmonary hypertension and those undergoing anticoagulation therapy (32, 33). Indwelling pulmonary artery catheters are associated with various potential issues, including infections, pulmonary infarctions, perforations, and arrhythmias. Furthermore, there is a risk of allergic reactions to contrast agents and radiation exposure during x-ray fluoroscopy. Vein thrombosis is another potential complication. Additionally, sedation, agitation, and breathing issues can negatively impact venous and arterial blood oxygenation. Nevertheless, a recent study found no difference in Qp/Qs regardless of the sedation method employed, although it did note lower values for PAP and PVRI under general anesthesia (34). It is important to note that genuine mixed venous saturation is computed rather than directly measured by taking upper and lower vena cava samples (35, 36). Given these drawbacks, discussing the continued use of invasive oximetry as the gold standard compared to non-invasive techniques is imperative.

Addressing the complexities of MRI scans and the limitations that existed in our study is very important. Conducting MRI scans in pediatric patients presents unique challenges, as anatomical structures are minor, necessitating higher spatial resolution. Additionally, pediatric patients often have higher

heart rates, demanding superior temporal resolution to mitigate motion artifacts. Some patients may require sedation due to uncooperative behavior and claustrophobia (37, 38). Moreover, it's essential to note that this study was conducted for research purposes, and there was no significant time delay between imaging and invasive catheterization in all cases. However, if a delay were to occur between these two methods, it could potentially impact the agreement between catheterization and 4D flow measurements, possibly due to changes in medication or other environmental conditions. Furthermore, the study was conducted at a single location using a single MRI scanner, with the same technologist, protocols, and software for analysis. The successful application of the more recent 4D flow technique requires a certain level of expertise, including a comprehensive understanding of potential imaging challenges, such as errors related to vortical flow and the identification of various artifacts, including those arising from turbulence, dephasing and aliasing (39, 40). Despite these complications and the ethical imperative that prohibited the use of contrast agents and anesthesia during cardiac imaging, we observed a marginally higher correlation between the shunt fraction obtained from 4D flow MRI and catheterization compared to the study conducted in adults, where contrast agents were used in CMR (20, 21). Therefore, the present study demonstrates that 4D flow MRI in pediatrics, even without contrast media, could feasibly measure the left-to-right shunt in children with VSD using standard scan settings (18).

In conclusion, this study underscores the potential of 4D flow MRI as a non-invasive method for measuring left-to-right shunts in children with VSD, providing a comparable alternative to invasive cardiac catheterization with oximetry for these patients. These findings support the use of Qp/Qs results obtained through 4D flow MRI in assessing and managing such patients.

Data availability statement

The raw data supporting the conclusions of this article will be made available by the authors, without undue reservation.

Ethics statement

The studies involving humans were approved by the Research Ethics Committees of the School of Medicine at Iran University of Medical Sciences [Approval ID: IR.IUMS.FMD.REC.1401.064]. The patients/participants provided their written informed consent to participate in this study.

Author contributions

SZ-A: Conceptualization, Data curation, Formal Analysis, Investigation, Methodology, Project administration, Software, Visualization, Writing – original draft. SQ: Funding acquisition, Supervision, Validation, Writing – review & editing. SF-F: Data curation, Formal Analysis, Writing – original draft. MG: Data curation, Formal Analysis, Writing – review & editing. HG: Conceptualization, Data curation, Formal Analysis, Writing – original draft. AA: Validation, Writing – review & editing. AM: Formal Analysis, Writing – review & editing. AB-R: Formal Analysis, Supervision, Writing – original draft. HM: Data curation, Formal Analysis, Methodology, Writing – original draft. KR-K: Conceptualization, Data curation, Formal Analysis, Investigation, Methodology, Project administration, Resources, Supervision, Validation, Visualization, Writing – original draft.

Funding

The author(s) declare financial support was received for the research, authorship, and/or publication of this article. This research was made possible by the generous support of the Rajaie Cardiovascular, Medical, and Research Center and the Iran University of Medical Sciences. We acknowledge their pivotal role in our study.

Acknowledgments

We acknowledge the invaluable contributions of the Pediatric Angiography and Medical Imaging Department staff at Rajaie Hospital. We extend our gratitude to Pie Medical Imaging company for their support with the advanced medical imaging software used in this research.

Conflict of interest

The authors declare that the research was conducted in the absence of any commercial or financial relationships that could be construed as a potential conflict of interest.

The author(s) declared that they were an editorial board member of Frontiers, at the time of submission. This had no impact on the peer review process and the final decision.

Publisher's note

Supplementary material

The Supplementary Material for this article can be found online at: https://www.frontiersin.org/articles/10.3389/fcvm.2024.1399110/full#supplementary-material

References

1. Shabana N, Shahid SU, Irfan U. Genetic contribution to congenital heart disease (CHD). *Pediatr Cardiol.* (2020) 41:12–23. doi: 10.1007/s00246-019-02271-4

2. Hoffman JI, Kaplan S. The incidence of congenital heart disease. *J Am Coll Cardiol.* (2002) 39(12):1890–900. doi: 10.1016/S0735-1097(02)01886-7

3. Van Der Linde D, Konings EE, Slager MA, Witsenburg M, Helbing WA, Takkenberg JJ, et al. Birth prevalence of congenital heart disease worldwide: a systematic review and meta-analysis. *J Am Coll Cardiol.* (2011) 58(21):2241–7. doi: 10.1016/j.jacc.2011.08.025

4. Vasanawala SS, Hanneman K, Alley MT, Hsiao A. Congenital heart disease assessment with 4D flow MRI. *J Magn Reson Imaging.* (2015) 42(4):870–86. doi: 10.1002/jmri.24856

5. Dakkak W, Oliver T. *Ventricular Septal Defect. StatPearls.* Treasure Island, FL: StatPearls Publishing (2020).

6. Kalayinia S, Mahdavi M, Maleki M, Mazloumzadeh S, Rabbani B, Mahdieh N. Regional distribution of congenital heart disease in Iran; A study on 1000 Iranian hospitalized patients in three years. *Int Cardiovasc Res J.* (2020) 14(4):e108858.

7. Rizk J. 4D flow MRI applications in congenital heart disease. *Eur Radiol.* (2021) 31:1160–74. doi: 10.1007/s00330-020-07210-z

8. Minette MS, Sahn DJ. Ventricular septal defects. *Circulation.* (2006) 114 (20):2190–7. doi: 10.1161/CIRCULATIONAHA.106.618124

9. Webb G, Gatzoulis MA. Atrial septal defects in the adult: recent progress and overview. *Circulation.* (2006) 114(15):1645–53. doi: 10.1161/CIRCULATIONAHA.105.592055

10. Warnes CA, Williams RG, Bashore TM, Child JS, Connolly HM, Dearani JA, et al. ACC/AHA 2008 guidelines for the management of adults with congenital heart disease: a report of the American College of Cardiology/American Heart Association task force on practice guidelines (writing committee to develop guidelines on the management of adults with congenital heart disease): developed in collaboration with the American society of echocardiography, heart rhythm society, international society for adult congenital heart disease, society for cardiovascular angiography and interventions, and society of thoracic surgeons. *Circulation.* (2008) 118(23):e714–833.

11. Antman EM, Marsh JD, Green LH, Grossman W. Blood oxygen measurements in the assessment of intracardiac left to right shunts: a critical appraisal of methodology. *Am J Cardiol.* (1980) 46(2):265–71. doi: 10.1016/0002-9149(80)90068-5

12. Dittmann H, Jacksch R, Voelker W, Karsch K-R, Seipel L. Accuracy of Doppler echocardiography in quantification of left to right shunts in adult patients with atrial septal defect. *J Am Coll Cardiol.* (1988) 11(2):338–42. doi: 10.1016/0735-1097(88)90099-X

13. Gabbour M, Schnell S, Jarvis K, Robinson JD, Markl M, Rigsby CK. 4-D flow magnetic resonance imaging: blood flow quantification compared to 2-D phase-contrast magnetic resonance imaging and Doppler echocardiography. *Pediatr Radiol.* (2015) 45:804–13. doi: 10.1007/s00247-014-3246-z

14. Boehrer JD, Lange RA, Willard JE, Grayburn PA, Hillis LD. Advantages and limitations of methods to detect, localize, and quantitate intracardiac left-to-right shunting. *Am Heart J.* (1992) 124(2):448–55. doi: 10.1016/0002-8703(92)90612-Y

15. Debl K, Djavidani B, Buchner S, Heinicke N, Poschenrieder F, Feuerbach S, et al. Quantification of left-to-right shunting in adult congenital heart disease: phase-contrast cine MRI compared with invasive oximetry. *Br J Radiol.* (2009) 82 (977):386–91. doi: 10.1259/bjr/18500608

16. Beerbaum P, Körperich H, Barth P, Esdorn H, Gieseke J, Meyer H. Noninvasive quantification of left-to-right shunt in pediatric patients: phase-contrast cine magnetic resonance imaging compared with invasive oximetry. *Circulation.* 2001;103 (20):2476–82. doi: 10.1161/01.CIR.103.20.2476

17. Markl M, Frydrychowicz A, Kozerke S, Hope M, Wieben O. 4D flow MRI. *J Magn Reson Imaging.* (2012) 36(5):1015–36. doi: 10.1002/jmri.23632

18. Bissell MM, Raimondi F, Ait Ali L, Allen BD, Barker AJ, Bolger A, et al. 4D flow cardiovascular magnetic resonance consensus statement: 2023 update. *J Cardiovasc Magn Reson.* (2023) 25(1):1–24. doi: 10.1186/s12968-023-00942-z

19. Azarine A, Garçon P, Stansal A, Canepa N, Angelopoulos G, Silvera S, et al. Four-dimensional flow MRI: principles and cardiovascular applications. *Radiographics.* (2019) 39(3):632–48. doi: 10.1148/rg.2019180091

20. Horowitz MJ, Kupsky DF, El-Said HG, Alshawabkeh L, Kligerman SJ, Hsiao A. 4D flow MRI quantification of congenital shunts: comparison to invasive catheterization. *Radiology: Cardiothoracic Imaging.* (2021) 3(2):e200446. doi: 10.1148/ryct.2021200446

21. Valdeolmillos E, Sakhi H, Tortigue M, Audié M, Isorni M-A, Lecerf F, et al. 4D flow cardiac MRI to assess pulmonary blood flow in patients with pulmonary arterial hypertension associated with congenital heart disease. *Diagn Interv Imaging.* (2024) 105(7):266–72.

22. Baim DS, Grossman W. Grossman's cardiac catheterization, angiography, and intervention. (No Title). (2006).

23. Valente AM, Cook S, Festa P, Ko HH, Krishnamurthy R, Taylor AM, et al. Multimodality imaging guidelines for patients with repaired tetralogy of fallot: a report from the American society of echocardiography: developed in collaboration with the society for cardiovascular magnetic resonance and the society for pediatric radiology. *J Am Soc Echocardiogr.* (2014) 27(2):111–41. doi: 10.1016/j.echo.2013.11.009

24. Silvestry FE, Cohen MS, Armsby LB, Burkule NJ, Fleishman CE, Hijazi ZM, et al. Guidelines for the echocardiographic assessment of atrial septal defect and patent foramen ovale: from the American society of echocardiography and society for cardiac angiography and interventions. *J Am Soc Echocardiogr.* (2015) 28(8):910–58. doi: 10.1016/j.echo.2015.05.015

25. Campbell RM, Douglas PS, Eidem BW, Lai WW, Lopez L, Sachdeva R. ACC/AAP/AHA/ASE/HRS/SCAI/SCCT/SCMR/SOPE 2014 appropriate use criteria for initial transthoracic echocardiography in outpatient pediatric cardiology: a report of the American College of Cardiology appropriate use criteria task force, American academy of pediatrics, American Heart Association, American society of echocardiography, heart rhythm society, society for cardiovascular angiography and interventions, society of cardiovascular computed tomography, society for cardiovascular magnetic resonance, and society of pediatric echocardiography. *J Am Coll Cardiol.* (2014) 64(19):2039–60. doi: 10.1016/j.jacc.2014.08.003

26. Quiñones MA, Otto CM, Stoddard M, Waggoner A, Zoghbi WA. Recommendations for quantification of Doppler echocardiography: a report from the Doppler quantification task force of the Nomenclature and standards committee of the American society of echocardiography. *J Am Soc Echocardiogr.* (2002) 15 (2):167–84. doi: 10.1067/mje.2002.120202

27. Stout KK, Daniels CJ, Aboulhosn JA, Bozkurt B, Broberg CS, Colman JM, et al. 2018 AHA/ACC guideline for the management of adults with congenital heart disease: executive summary: a report of the American College of Cardiology/American Heart Association task force on clinical practice guidelines. *J Am Coll Cardiol.* (2019) 73 (12):1494–563. doi: 10.1016/j.jacc.2018.08.1028

28. Vincent J-L. Understanding cardiac output. *Critical Care.* (2008) 12:1–3.

29. Christodorescu R, Corrado D, D'Alto M. 2020 ESC guidelines for the management of adult congenital heart disease. *Eur Heart J.* (2021) 42:563À645.

30. Panayiotou HR, Mills LK, Broadbent DA, Shelley D, Scheffczik J, Olaru AM, et al. Comprehensive neonatal cardiac, feed and wrap, non-contrast, non-sedated, free-breathing compressed sensing 4D flow MRI assessment. *J Magn Reson Imaging.* (2023) 57(3):789–99. doi: 10.1002/jmri.28325

31. Sjöberg P, Hedström E, Fricke K, Frieberg P, Weismann CG, Liuba P, et al. Comparison of 2D and 4D flow MRI in neonates without general anesthesia. *J Magn Reson Imaging.* (2023) 57(1):71–82. doi: 10.1002/jmri.28303

32. Manda YR, Baradhi KM. Cardiac catheterization risks and complications. (2018).

33. Mehta R, Lee KJ, Chaturvedi R, Benson L. Complications of pediatric cardiac catheterization: a review in the current era. *Catheter Cardiovasc Interv.* (2008) 72 (2):278–85. doi: 10.1002/ccd.21580

34. Go K, Kato T, Kito M, Morimoto Y, Kawai S, Yamamoto H, et al. Effects of general anesthesia on the results of cardiac catheterization in pediatric patients with ventricular septal defect. *Congenit Heart Dis.* (2023) 18(2):235–43.

35. Li Q, Zhang X, Xu Y, Zhou L, Li J, Zhang Z. Progression of aortic regurgitation following transcatheter closure of intracristal ventricular septal defects in children: a mid-to long-term follow-up study. *Front Cardiovasc Med.* (2023) 10:1190013. doi: 10.3389/fcvm.2023.1190013

36. Cigarroa RG, Lange RA, Hillis LD. Oximetric quantitation of intracardiac left-to-right shunting: limitations of the QpQs ratio. *Am J Cardiol.* (1989) 64(3):246–7. doi: 10.1016/0002-9149(89)90471-2

37. Simonetti OP, Cook S. Technical aspects of pediatric CMR. *J Cardiovasc Magn Reson.* (2006) 8(4):581–93. doi: 10.1080/10976640600713715

38. Secinaro A, Ait-Ali L, Curione D, Clemente A, Gaeta A, Giovagnoni A, et al. Recommendations for cardiovascular magnetic resonance and computed tomography in congenital heart disease: a consensus paper from the CMR/CCT working group of the Italian society of pediatric cardiology (SICP) and the Italian college of cardiac radiology endorsed by the Italian society of medical and interventional radiology (SIRM) part I. *Radiol Med.* (2022) 127(7):788–802. doi: 10.1007/s11547-022-01490-9

39. Contijoch FJ, Horowitz M, Masutani E, Kligerman S, Hsiao A. 4D flow vorticity visualization predicts regions of quantitative flow inconsistency for optimal blood flow measurement. *Radiology: Cardiothoracic Imaging.* (2020) 2(1):e190054. doi: 10.1148/ryct.2020190054

40. Callaghan FM, Burkhardt B, Geiger J, Valsangiacomo Buechel ER, Kellenberger CJ. Flow quantification dependency on background phase correction techniques in 4D-flow MRI. *Magn Reson Med.* (2020) 83(6):2264–75. doi: 10.1002/mrm.28085

frontiers | Frontiers in Cardiovascular Medicine

TYPE Case Report
PUBLISHED 30 July 2024
DOI 10.3389/fcvm.2024.1417074

OPEN ACCESS

EDITED BY
Matthias Renker,
Kerckhoff Clinic, Germany

REVIEWED BY
Ionut Donoiu,
University of Medicine and Pharmacy of Craiova, Romania
Marcello Chiocchi,
University of Rome Tor Vergata, Italy

*CORRESPONDENCE
Kevin Velarde-Acosta
✉ kevin_velarde.93@hotmail.com

RECEIVED 14 April 2024
ACCEPTED 18 July 2024
PUBLISHED 30 July 2024

CITATION
Baltodano-Arellano R, Alvarez-Tiburcio E, Barriales-Revilla L, Bellido-Yarlequé D, Cachicatari A, Cupe-Chacalcaje K, La Torre-Zuñiga A and Velarde-Acosta K (2024) Case report and literature review: cardiac hematic cyst.
Front. Cardiovasc. Med. 11:1417074.
doi: 10.3389/fcvm.2024.1417074

Case report and literature review: cardiac hematic cyst

Roberto Baltodano-Arellano[1,2], Eduardo Alvarez-Tiburcio[3], Lucia Barriales-Revilla[4], David Bellido-Yarlequé[3], Angela Cachicatari[1], Kelly Cupe-Chacalcaje[1], Alan La Torre-Zuñiga[5] and Kevin Velarde-Acosta[4]*

[1]Cardiac Imaging Area of Cardiology Service, Hospital Guillermo Almenara Irigoyen – EsSalud, Lima, Peru, [2]School of Medicine, Universidad Nacional Mayor de San Marcos, Lima, Peru, [3]Cardiac Surgery Unit, Hospital Guillermo Almenara Irigoyen - EsSalud, Lima, Peru, [4]Clinical Cardiology Service, Hospital Guillermo Almenara Irigoyen - EsSalud, Lima, Peru, [5]Pathological Anatomy Service, Hospital Edgardo Rebagliati Martins - EsSalud, Lima, Peru

A 49-year-old female patient, asymptomatic, presented to the cardiology office for a right atrial mass, identified incidentally in a non-electrocardiogram (ECG)-gated contrast-enhanced computed tomography, performed for follow-up of pulmonary tuberculosis. Echocardiography, surprisingly, showed an anechogenic ovoid mass in the right atrium measuring 40×40 mm^2, implanted in the interatrial septum without affecting the tricuspid valve. ECG-gated computed tomography angiography (CTA), confirmed the dimensions of the mass, which presented homogeneous content, calcified areas, and a 12-mm pedicle implanted near the ostium of the coronary sinus. Additionally, contrast uptake and infiltration of adjacent structures were ruled out. In the surgical field, an encapsulated mass with blood content was found, which pathology reported as a hematic endocardial cyst (HEC). These are rare cardiac masses, constituting 1.5% of all primary cardiac tumors. It is usually an incidental finding, and its clinical presentation will depend on its dimensions and the intracardiac hemodynamic impact. A highlighting feature is its anechogenic content on ultrasound, however, multimodality imaging allows for making diagnostic assumptions, discerning between primary cardiac tumors, and provides morphological and hemodynamic information useful for therapeutic decision making. The age of the patient, the large size of the HEC, and its location in the interatrial septum make up a completely atypical presentation of this rare disease, which motivated this report.

KEYWORDS

right atrium, cardiac hematic cyst, echocardiography, computed tomography angiography, multimodality imaging

Case report

Clinical presentation

A 49-year-old woman from the Peruvian Andes presented to the cardiology office due to an incidental tomographic finding of a mass in the right atrium. In the anamnesis, the patient reported being asymptomatic, while the cardiorespiratory physical examination did not show relevant findings. Her medical history was notable for a tuberculous pulmonary nodule removed 2 years previously, for which she received complete treatment for 6 months and required subsequent computed tomography (CT) controls. She had no

cardiovascular risk factors or relevant family or socioeconomic history. Laboratory tests were within normal ranges, while the electrocardiogram showed no pathological alterations.

Differential diagnosis

In the presence of a right atrial mass implanted in the interatrial septum, a myxoma should be considered due to its frequency (1–3). Echocardiography and magnetic resonance imaging (MRI) determine structural and tissue characteristics that bring the diagnosis closer. On some occasions, the finding of a thrombus trapped in the foramen ovale has been described in transesophageal echocardiography (TEE) (4, 5). This mass's cystic appearance guides the diagnosis of rarer pathologies such as cardiac hydatid, bronchogenic or endocardial hematic cyst, which are usually diagnosed in pathological anatomy (6–8).

Diagnostic workup

A cardiologic study plan was initiated with transthoracic echocardiography (TTE), which confirmed the presence of an anechogenic ovoid mass in the right atrium measuring 40 mm × 40 mm^2, implanted in the interatrial septum without affecting the tricuspid valve (Figure 1A; Supplementary Video S1). In the study with agitated saline solution, echogenicity of the blood-like mass was evident (Figures 1B,D, Supplementary Video S2). No additional relevant findings were found.

The TEE showed a homogeneous mass covered by a thin layer, implanted in the mid-low septum, and exhibited pendulum movement (Figure 1C, Supplementary Video S3). Furthermore, the previous dimensions were confirmed and no signs suggestive of vascularization were found. Given these findings, the diagnosis work-up was complemented with an ECG-gated CTA, displaying an ovoid, mobile mass of 35 mm in diameter with homogeneous content and calcified areas with a 12-mm pedicle adhered to the lower atrial septum near the coronary sinus ostium (Figure 2).

Treatment

With these findings, the patient underwent an open surgical resection of the mass. After the right atriotomy, a violaceous,

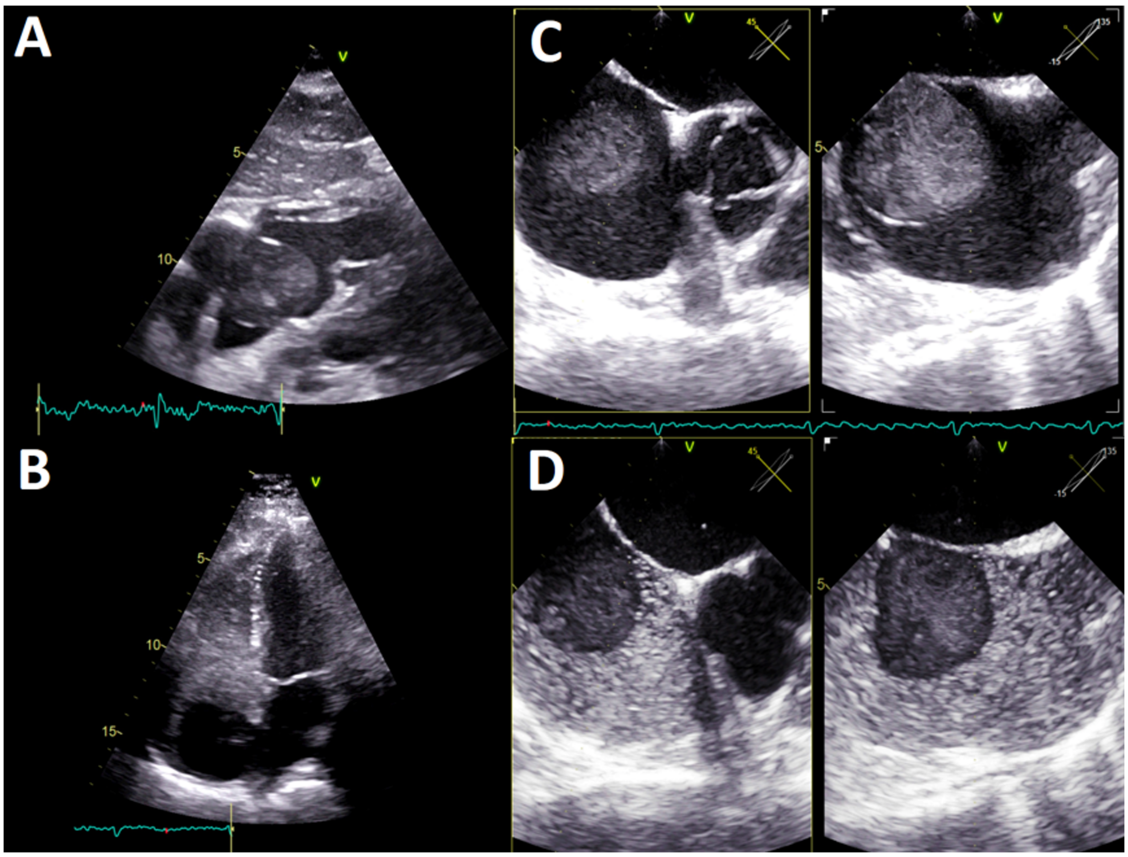

FIGURE 1
(A) TTE, four-chamber subcostal view. Ovoid mass in the right atrium, with echogenicity almost blood-like and calcification areas. (B) TTE, four-chamber apical view. The agitated saline test shows an anechogenic, 40 × 40 mm^2, mass in the right atrium implanted in the interatrial septum. No tricuspid valve compromise was observed. (C) TEE, multiplanar image of the interatrial septum (45°; 135°). A homogeneous pedunculated mass with a thin covering was implanted in the middle-low interatrial septum with pendulum movement. (D) TEE, multiplanar image of the interatrial septum (45°; 135°). The agitated saline test depicts anechogenicity of the hematic mass. TTE, transthoracic echocardiography; TEE, transesophageal echocardiography.

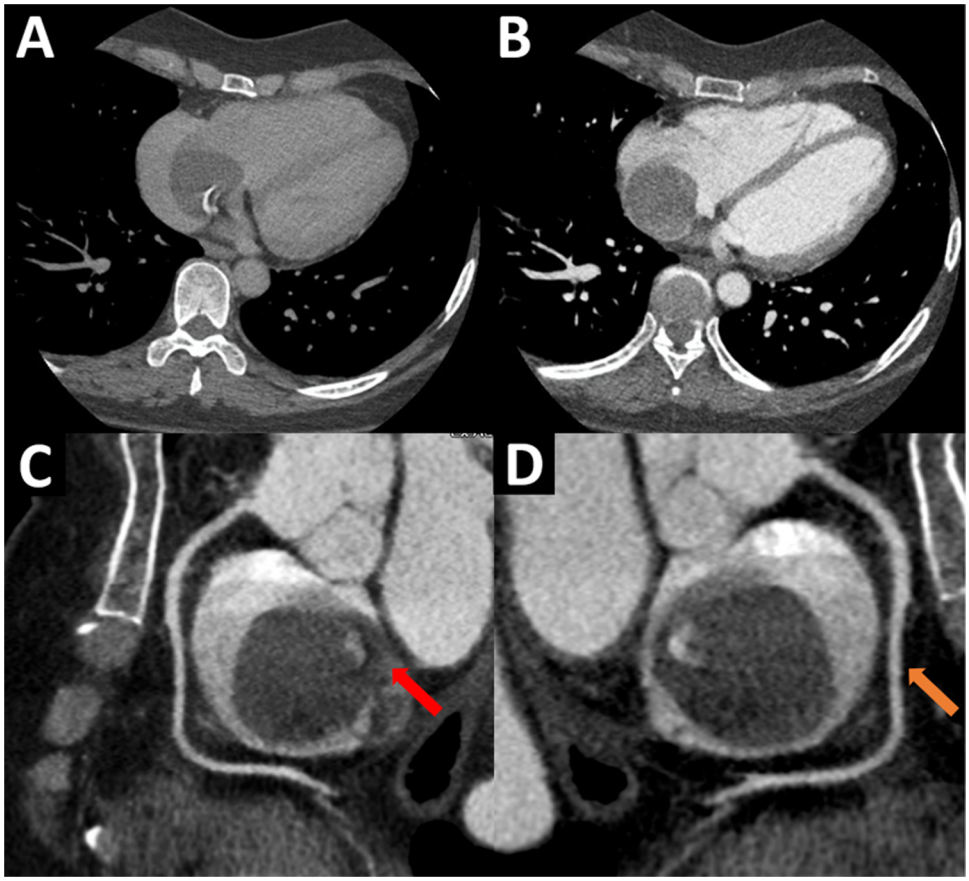

FIGURE 2
(A,B) ECG-gated CTA, four-chamber view. A mobile, round, homogenous mass is seen adhered to the right lower interatrial septum. (C,D) ECG-gated CTA, sagittal views of the right atrium. A homogeneous, non-contrast-enhancing mass with calcified areas and defined edges is seen in the right atrium. Note the 12 mm pedicle (red arrow) that attaches it to the interatrial septum, near the fossa ovalis. Likewise, the right coronary artery (orange arrow) is seen, which does not provide collateral to the mass. ECG, electrocardiogram; CTA, computed tomography angiography.

smooth, tense, and shiny mass was found, suggesting a cyst with bloody content (Figure 3A). The pathological study described a fibrous (collagenous) wall devoid of epithelium and with few inflammatory cells. Furthermore, fibrin content with areas of calcification was reported (Figures 3B,C), confirming the diagnosis of HEC (8–10).

Follow-up

At one year of follow-up, the patient did not present relevant symptoms, except for a nonspecific chest pain in the healed surgical wound. Due to a suboptimal acoustic window, TEE was performed, which excluded mass recurrence.

Discussion

HEC constitutes 1.5% of all cardiac tumors (8). It occurs mainly in infants and its preferential location is the heart valves (8, 9, 11). Its origin is still unknown, but two hypotheses are suggested: the first describes ectatic vessels evolving into a hematic cyst, and the second describes local inflammation that develops into a hematoma and transforms into a hematic cyst (8, 9).

To learn about clinical and therapeutic features in adults affected by this rare entity, we did an extensive search of the medical literature in Medline for articles published up to January 2022 (Table 1). Our search revealed that this disease occurs indistinctly in both sexes and the main location of this mass is the mitral valve, as it occurs in infants. Likewise, it allowed us to know that, in our case, the magnitude of the mass, located in an uncommon site, is the largest published in the literature.

The set of symptoms depends on the mass dimensions and its impact on intracardiac hemodynamics. As cysts may involve the free edges of the valves, patients can present with dyspnea or heart murmurs due to valve regurgitation. Other clinical manifestations described are systemic embolism, syncope, or even sudden death (8, 9). Despite the multiple possibilities of clinical manifestations, the vast majority of findings of this tumor are incidental, as seen in our patient in whom the tumor was discovered in a tomographic control for pulmonary tuberculosis.

Within cardiac imaging studies, echocardiography is essential for the initial examination of intracardiac masses (1–3, 35, 36). It

10.3389/fcvm.2024.1417074

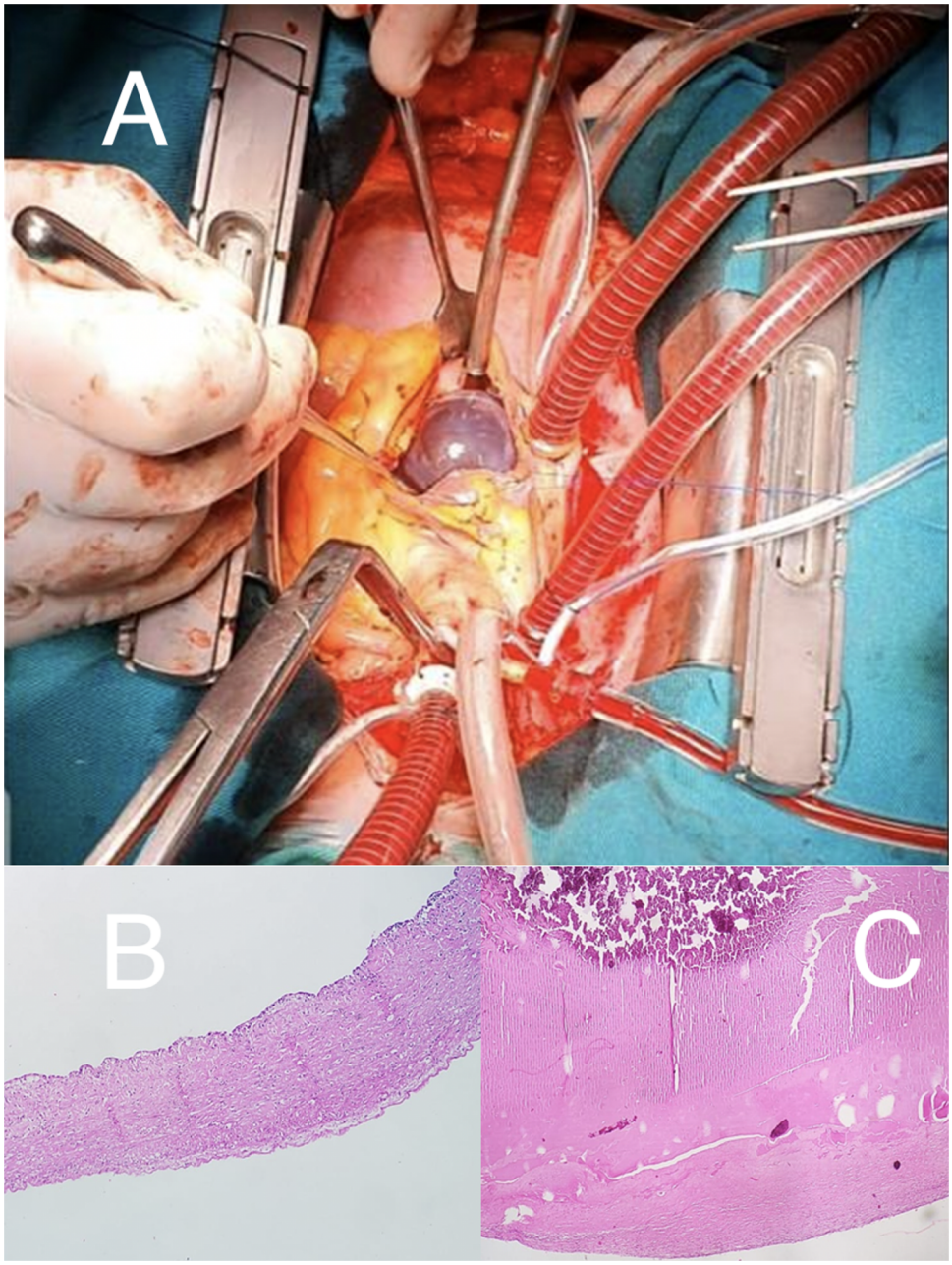

FIGURE 3
(A) Surgical field. Right atriotomy, with exposure of violaceous, smooth, and shiny mass. (B) Microscopy: fibrous (composed of collagenous layers) cyst wall without epithelial cells. Presence of some lymphocytes. (C) Microscopy: uniform fibrin content with calcification areas (upper region with more intense staining).

provides morphological information, data on the anatomical relationship, and determines the hemodynamic impact of the HEC. The cysts have particular ultrasound characteristics such as a thin reflective layer and an echolucent content, which could go unnoticed by novice explorers (9, 11). A meticulous analysis of our patient images confirmed these findings. The agitated saline solution study was useful because it highlighted the magnitude and dynamics of the mass, in addition to ruling out interatrial shunts. TEE describes with high precision anatomical aspects of atrial masses and defines carefully the components of a cyst, including the absence of vascularization, as seen in the images of this case (8, 9).

ECG-gated CTA reported a homogeneous mass with calcified areas and defined edges, mobile, without contrast-enhancing or infiltration. Also, it excluded the presence of additional intracardiac masses, contributing to better surgical planning (37). Cardiac MRI is an important technique to define contrast uptake in masses. In particular, hematic cysts do not capture medium contrast, because they are not vascularized, unlike a malignant neoplasm (9). Due to the cystic structure, hydatid disease must

TABLE 1 Reported cases of hematic cyst in adult patients.

Patient	Year of publication	Age	Gender	Size	Anatomical location	Sign and symptoms	Time course	Complications	Treatment	Reference
1	1983	27-year old	Male	25 mm	Mitral valve anterior leaflet Anterolateral papillary muscle	Acute right-sided Hemiparesis Expressive Aphasia	NR	None	Surgical excision Median sternotomy	(12)
2	1990	46- year old	Male	30 × 25 mm	Mitral valve anterior Leaflet	Chest tightness on exertion	5 years	None	Surgical excision Median sternotomy	(13)
3	1992	41-year-old	Female	13 × 10 mm 2 × 3 mm	Mitral valve posterior leaflet	Dyspnea on exertion	NR	None	Surgical excision of BC (13 × 10 mm) Median sternotomy	(14)
4	1995	16-year-old	Female	13 mm	Right aortic valve leaflet Free margin	Systolic ejection murmur left sternal border	2 years	None	Surgical excision Median sternotomy	(10)
5	1996	59-year-old	Female	20 × 20 mm	Interatrial septum	Substernal Pressure Systolic Murmur	NR	None	Surgical excision Median sternotomy	(15)
6	1999	50-year-old	Male	21 × 22 mm	Mitral valve anterior leaflet	Left Parasternal Systolic Murmur	NR	None	Conservative	(16)
7	2000	45-year-old	Female	20 × 20 mm	Mitral valve anterior leaflet	Asymptomatic	NR	None	Surgical excision Median sternotomy	(17)
8	2003	52-year-old	Male	40 × 30 mm	Interatrial septum	Asymptomatic	NR	None	Surgical excision Median sternotomy	(18)
9	2004	44-year-old	Female	20 mm	Mitral valve anterior leaflet	Dyspnea on exertion	NR	None	Surgical excision Median sternotomy	(19)
10	2005	25-year-old	Female	23 × 25 mm	Mitral valve anterior leaflet	Asymptomatic	NR	None	Surgical excision Median sternotomy	(20)
11	2005	35-year-old	Male	15 × 21 mm	Mitral valve anterior leaflet	NR	NR	None	Surgical excision	(21)
12	2006	65-year-old	Female	44 × 20 mm	Interatrial septum	Headache	NR	None	Surgical excision	(22)
13	2007	29-year-old	Male	30 mm	Mitral valve anterior leaflet	Chest pain	9 months	None	Surgical excision Median sternotomy	(23)
14	2008	62-year-old	Male	30 mm	Interatrial septum	Syncope Headache	NR	None	Surgical excision Median sternotomy	(11)
15	2008	62-year-old	Female	NR	Mitral valve anterior leaflet	Dyspnea on exertion Systolic Murmur	7 days	None	Surgical excision Median sternotomy	(24)
16	2009	65-year old	Female	10 × 10 mm 10 × 10 mm	Mitral valve anterior leaflet Mitral valve posterior leaflet	Chest pain	4 months	None	Surgical excision Median sternotomy Mitral valvuloplasty	(25)
17	2011	28-year-old	Female	19 mm	Mitral valve posterior leaflet	NR	NR	None	Surgical excision Median sternotomy	(26)
18	2011	69-year-old	Male	40 × 25 mm	Interatrial septum	Asymptomatic	NR	None	Surgical excision Median sternotomy	(8)
19	2012	55-year-old	Male	20 × 18 mm	Mitral valve sub valvular apparatus Posterior papillary muscle	NR	NR	None	Surgical excision Myocardial revascularization Median sternotomy	(27)
20	2012	47-year-old	Male	16 × 14 mm	Mitral valve anterior leaflet Anterolateral papillary muscle	Asymptomatic	3 weeks	None	Surgical excision Mitral valvuloplasty Median sternotomy	(28)
21	2013	25-year old	Male	NR	Mitral valve anterior leaflet	Dyspnea on exertion	NR	NR	NR	(29)

(*Continued*)

10.3389/fcvm.2024.1417074

10.3389/fcvm.2024.1417074

TABLE 1 Continued

Patient	Year of publication	Age	Gender	Size	Anatomical location	Sign and symptoms	Time course	Complications	Treatment	Reference
22	2015	23-year-old	Male	20 mm	Mitral valve anterior leaflet	Shortness of breath	NR	None	Surgical excision Trans-septal approach Mitral valvuloplasty Ring Annuloplasty	(30)
23	2015	70-year-old	Female	16 mm	Mitral valve anterior leaflet	Dyspnea on exertion	NR	None	Surgical excision Median sternotomy	(31)
24	2016	85-year-old	Female	30 × 30 mm 25 × 25 mm	Interatrial septum	Asymptomatic	NR	None	Surgical excision Median sternotomy	(32)
25	2019	47-year-old	Female	10 mm	Mitral valve sub valvular apparatus	Chest pain	3 days	None	Conservative	(33)
26	2020	57- year old	Female	10 × 10 mm	Mitral valve anterior leaflet (A1–A2 segment)	Chest pain Fever	NR	None	None	(34)

be ruled out through specific MRI sequences that differentiate it from the hematic cyst. In the former the T1 signal is hypointense and T2 signal hyperintense, while in the latter the T1 and T2 signals are isointense (11). Despite the usefulness of cardiac MRI for the differential diagnosis of cardiac masses, it was not performed in our patient because the magnetic resonator was inoperative during that period; likewise, surgical resection of the cyst had already been decided by the Heart Team based on ultrasound and tomographic features.

The decision to surgically remove an asymptomatic cardiac mass is based on avoiding embolic phenomena and ruling out malignancy. If the nature of this tumor is specified with imaging tests, the surgical time will depend on the speed of growth, hemodynamic impact, and the risks of rupture and embolization (8, 9, 38, 39). Although our patient did not present cardiac symptoms, the intervention was based on age, the low risk of malignancy, the dimensions of the mass and the prevention of embolisms, as occurred in the vast majority of cases reported in the literature.

Conclusions

The HEC is an extremely rare mass that usually affects the heart valves of infants. The characteristics of this report, such as the adult age of the patient, the anatomical location in the interatrial septum, and the gigantic dimensions of the mass, are unprecedented in the medical literature.

Multimodality imaging allows differential diagnosis between primary cardiac tumors and provides useful morphological and hemodynamic information for therapeutic decision making. Surgical removal avoids embolic phenomena and hemodynamic disturbances. Finally, the purplish, smooth, shiny, blood-bag-like surgical piece is a distinguishable feature of this cardiac mass.

Data availability statement

The original contributions presented in the study are included in the article/Supplementary Material, further inquiries can be directed to the corresponding author.

Ethics statement

Written informed consent was obtained from the individual(s) for the publication of any potentially identifiable images or data included in this article.

Author contributions

RB-A: Conceptualization, Data curation, Formal Analysis, Software, Supervision, Visualization, Writing – original draft, Writing – review & editing. EA-T: Writing – original draft. LB-R: Conceptualization, Data curation, Software, Validation, Visualization, Writing – original draft, Writing – review &

editing. DB-Y: Writing – original draft. AC: Software, Writing – review & editing. KC-C: Software, Writing – original draft, Writing – review & editing. AL: Writing – original draft. KV-A: Conceptualization, Formal Analysis, Supervision, Visualization, Writing – review & editing.

Funding

The author(s) declare that no financial support was received for the research, authorship, and/or publication of this article.

Conflict of interest

The authors declare that the research was conducted in the absence of any commercial or financial relationships that could be construed as a potential conflict of interest.

Publisher's note

Supplementary material

The Supplementary Material for this article can be found online at: https://www.frontiersin.org/articles/10.3389/fcvm.2024.1417074/full#supplementary-material

SUPPLEMENTARY VIDEO S1
TTE, subcostal view. Evidence of ovoid mass in the right atrium with mainly hypoechoic contents.

SUPPLEMENTARY VIDEO S2
TTE, apical view 4 chambers. Agitated saline demonstrates a mass in the right atrium with echogenicity similar to blood.

SUPPLEMENTARY VIDEO S3
TEE, X-plane. Saline solution test highlights pear morphology of mass implanted in the interatrial septum.

SUPPLEMENTARY DATA SHEET 1
Timeline of patient evolution.

References

1. Tyebally S, Chen D, Bhattacharyya S, Mughrabi A, Hussain Z, Manisty C, et al. Cardiac tumors: *JACC CardioOncology* state-of-the-art review. *JACC CardioOncol.* (2020) 2(2):293–311. doi: 10.1016/j.jaccao.2020.05.009

2. Basso C, Rizzo S, Valente M, Thiene G. Cardiac masses and tumours. *Heart.* (2016) 102(15):1230–45. doi: 10.1136/heartjnl-2014-306364

3. Bussani R, Castrichini M, Restivo L, Fabris E, Porcari A, Ferro F, et al. Cardiac tumors: diagnosis, prognosis, and treatment. *Curr Cardiol Rep.* (2020) 22(12):169. doi: 10.1007/s11886-020-01420-z

4. Seo WW, Kim SE, Park MS, Lee JH, Park DG, Han KR, et al. Systematic review of treatment for trapped thrombus in patent foramen Ovale. *Korean Circ J.* (2017) 47 (5):776–85. doi: 10.4070/kcj.2016.0295

5. Zoltowska DM, Agrawal Y, Kalavakunta JK. Serpentine thrombus in the heart: a rare case of trapped thrombus in patent foramen ovale. *BMJ Case Rep.* (2018) 2018: bcr2017223469. doi: 10.1136/bcr-2017-223469

6. Oraha AY, Faqe DA, Kadoura M, Kakamad FH, Yaldo FF, Aziz SQ. Cardiac hydatid cysts; presentation and management. A case series. *Ann Med Surg (Lond).* (2018) 30:18–21. doi: 10.1016/j.amsu.2018.04.001

7. Fukudome Y, Hieda M, Masui S, Yokoyama T, Futami S, Moriyama S, et al. Case report: bronchogenic cyst in the right atrium of a young woman. *Front Cardiovasc Med.* (2022) 9:915876. doi: 10.3389/fcvm.2022.915876

8. Mori F, Oddo A, Fabbri V, Perini AP, Stefano PL, Taddei GL. Endocardial blood cyst: a rare site and age of presentation. *Echocardiography.* (2011) 28(3):E50–2. doi: 10.1111/j.1540-8175.2010.01306.x

9. Bortolotti U, Vendramin I, Lechiancole A, Sponga S, Pucci A, Milano AD, et al. Blood cysts of the cardiac valves in adults: review and analysis of published cases. *J Card Surg.* (2021) 36(12):4690–98. doi: 10.1111/jocs.15992

10. DeGroff C, Silberbach M, Sahn DJ, Droukas P. Giant blood cyst of the aortic valve. *J Am Soc Echocardiogr.* (1995) 8(4):543–5. doi: 10.1016/s0894-7317(05)80343-8

11. Centella T, Moya JL, Muñoz M, Reguero EM. Images in cardiovascular medicine. Giant endocardial blood cyst in the right atrium: echocardiographic and magnetic resonance imaging features. *Circulation.* (2008) 117(25):3250–1. doi: 10.1161/CIRCULATIONAHA.107.734814

12. Hauser AM, Rathod K, McGill J, Rosenberg BF, Gordon S, Timmis GC. Blood cyst of the papillary muscle. Clinical, echocardiographic and anatomic observations. *Am J Cardiol.* (1983) 51(3):612–3. doi: 10.1016/s0002-9149(83)80109-x

13. Arnold IR, Hubner PJ, Firmin RK. Blood filled cyst of the papillary muscle of the mitral valve producing severe left ventricular outflow tract obstruction. *Br Heart J.* (1990) 63(2):132–3. doi: 10.1136/hrt.63.2.132

14. Xie SW, Lu OL, Picard MH. Blood cyst of the mitral valve: detection by transthoracic and transesophageal echocardiography. *J Am Soc Echocardiogr.* (1992) 5(5):547–50. doi: 10.1016/s0894-7317(14)80047-3

15. Niinami H, Ishihara S, Hara S, Tanaka S, Yamaguti E, Takase S. Blood cyst with a calcium stone originating from the right atrial septum. *Cardiovasc Surg.* (1996) 4 (2):260–2. doi: 10.1016/0967-2109(96)82329-5

16. Pelikan HM, Tsang TS, Seward JB. Giant blood cyst of the mitral valve. *J Am Soc Echocardiogr.* (1999) 12(11):1005–7. doi: 10.1016/s0894-7317(99)70157-4

17. Kuvin J, Saha P, Rastegar H, Salomon RN, Pandian N, Denofrio D. Blood cyst of the mitral valve apparatus in a woman with a history of orthotopic liver transplantation. *J Am Soc Echocardiogr.* (2004) 17(5):480–2. doi: 10.1016/j.echo.2004.01.013

18. Tanaka H, Ebato M, Narisawa T, Mori T, Masuda M, Suzuki T, et al. Atrial blood cyst with ischemic heart disease. *Circ J.* (2003) 67(1):91–2. doi: 10.1253/circj.67.91

19. Minneci C, Casolo G, Popoff G, Sulla A, Comin CE, Pedemonti E. A rare case of left ventricular outflow obstruction. *Eur J Echocardiogr.* (2004) 5(1):72–5. doi: 10.1016/s1525-2167(03)00041-6

20. Yamamoto H, Nakatani S, Niwaya K, Ohnishi T, Uematsu M, Kitakaze M. Images in cardiovascular medicine. Giant blood cyst of the mitral valve: echocardiographic and intraoperative images. *Circulation.* (2005) 112(22):e341. doi: 10.1161/CIRCULATIONAHA.105.546390

21. Kurtoğlu N, Yildirim T, Uzunlar B, Cevik C, Incedere O, Dindar I. A rare case: blood cyst of the mitral valve. *Anadolu Kardiyol Derg.* (2005) 5(4):346.

22. Seebacher G, Binder T, Frank H, Wolner E, Mohl W. Cystic formation of the foramen ovale mimicking a right atrial myxoma. *Ann Thorac Surg.* (2006) 82 (6):2296–8. doi: 10.1016/j.athoracsur.2006.04.051

23. Zhang C, Hu J, Ni YM, Jiang ZN, Xu HY. Giant blood cyst tumor in the left ventricular outflow tract. *Chin Med J (Engl).* (2007) 120(12):1109–10. doi: 10.1097/00029330-200706020-00015

24. Mandegar MH, Roshanali F, Rayatzadeh H. Cyst-like lesion on mitral valve. *J Card Surg.* (2008) 23(1):97. doi: 10.1111/j.1540-8191.2007.00554.x

25. Dencker M, Jexmark T, Hansen F, Tydén P, Roijer A, Lührs C. Bileaflet blood cysts on the mitral valve in an adult. *J Am Soc Echocardiogr*. (2009) 22 (9):1085.e5–8. doi: 10.1016/j.echo.2009.04.002

26. Kühn A, Schreiber C, Weirich G, Vogt M. Intracardiac blood cyst: rare finding in a complex congenital heart lesion. *Eur Heart J*. (2012) 33(2):229. doi: 10.1093/eurheartj/ehr222

27. Donndorf P, Bermaoui B, Westphal B, Steinhoff G. Asymptomatic blood cyst of the papillary muscle in an adult undergoing coronary bypass surgery. *Interact Cardiovasc Thorac Surg*. (2013) 16(3):402–4. doi: 10.1093/icvts/ivs495

28. Park MH, Jung SY, Youn HJ, Jin JY, Lee JH, Jung HO. Blood cyst of subvalvular apparatus of the mitral valve in an adult. *J Cardiovasc Ultrasound*. (2012) 20(3):146–9. doi: 10.4250/jcu.2012.20.3.146

29. Sun F, Ren W, Bi W, Zhang Y, Guo B. A "balloon" on the mitral valve. *J Am Coll Cardiol*. (2013) 62(1):81. doi: 10.1016/j.jacc.2012.12.062

30. Halim J, van Schaagen FR, Riezebos RK, Lalezari S. Giant intracardiac blood cyst: assessing the relationship between its formation and previous cardiac surgery. *Neth Heart J*. (2015) 23(7-8):392–4. doi: 10.1007/s12471-015-0707-4

31. Madhavan S, Jayaprakash K, Jayaprasad N, Sathish G, George R. Blood cyst of the anterior mitral leaflet causing severe mitral regurgitation. *Proc (Bayl Univ Med Cent)*. (2015) 28(3):363–4. doi: 10.1080/08998280.2015.11929275

32. Otsuka H, Arinaga K, Fukuda T, Takaseya T, Shojima T, Takagi K, et al. Double right atrial blood cysts. *Ann Thorac Surg*. (2016) 101(5):e147–9. doi: 10.1016/j.athoracsur.2015.10.021

33. Ludhwani D, Sheikh B, Sheikh Y. Evaluation of mitral apparatus blood cyst: a case report and review of literature. *Cureus*. (2019) 11(10):e5812. doi: 10.7759/cureus.5812

34. Ramírez-Mesías DC, Contreras-Valero JF, Pinilla-Monsalve GD, Vesga-Reyes CE. Blood cyst of the mitral valve diagnosed in an adult after systemic thrombolysis. *Case Rep Cardiol*. (2020) 2020:4320269. doi: 10.1155/2020/4320269

35. Mitchell C, Rahko PS, Blauwet LA, Canaday B, Finstuen JA, Foster MC, et al. Guidelines for performing a comprehensive transthoracic echocardiographic examination in adults: recommendations from the American society of echocardiography. *J Am Soc Echocardiogr*. (2019) 32(1):1–64. doi: 10.1016/j.echo.2018.06.004

36. Baltodano-Arellano R, Falcón-Quispe L, Cupe-Chacalcaje K, Meléndez-Ramírez G, Cachicatari-Beltran A, Patrón-Chi S, et al. Collection of cardiac masses. Up-to-date echocardiography and cardiac MRI tools. *Echocardiography*. (2024) 41(2):e15757. doi: 10.1111/echo.15757

37. Sheng C, Yang C, Cheng Y, Li YM. Current status of diagnosis and treatment of primary benign cardiac tumors in children. *Front Cardiovasc Med*. (2022) 9:947716. doi: 10.3389/fcvm.2022.947716

38. Imai A, Enomoto Y, Shigeta O, Suzuki Y. Right atrial blood cyst in elderly patient: the timing of surgery. *Asian Cardiovasc Thorac Ann*. (2020) 28(8):500–03. doi: 10.1177/0218492320949406

39. Higuchi K, Furukawa K, Nakamura E, Nakamura E, Asada Y, Nakada H, et al. Right atrial blood cyst incidentally detected by computed tomography for metastatic breast cancer in an adult female patient: a case report. *World J Cardiovasc Surg*. (2019) 9:47–51. doi: 10.4236/wjcs.2019.95006

frontiers | Frontiers in Cardiovascular Medicine

TYPE Original Research
PUBLISHED 31 July 2024
DOI 10.3389/fcvm.2024.1428380

OPEN ACCESS

EDITED BY
Matthias Renker,
Kerckhoff Clinic, Germany

REVIEWED BY
Roberto Spina,
Gosford Hospital, Australia
Weichieh Lee,
Chi Mei Medical Center, Taiwan
Tiziana Attisano,
Ospedali Riuniti San Giovanni di Dio e Ruggi d'Aragona, Italy

*CORRESPONDENCE
Limin Luo
aniu2008.hi@163.com
Yongshi Wang
wang.yongshi@zs-hospital.sh.cn
Xianhong Shu
shu.xianhong@zs-hospital.sh.cn

RECEIVED 06 May 2024
ACCEPTED 24 July 2024
PUBLISHED 31 July 2024

CITATION
Luo L, Xie Z, Wu Q, Liu Q, Hou H, Wang Y and Shu X (2024) Transesophageal echocardiography guidance for percutaneous closure of PFO and a new method to improve the diagnosis and safety during the procedures.
Front. Cardiovasc. Med. 11:1428380.
doi: 10.3389/fcvm.2024.1428380

Transesophageal echocardiography guidance for percutaneous closure of PFO and a new method to improve the diagnosis and safety during the procedures

Limin Luo[1]*, Zehan Xie[1], Qiaoyan Wu[1], Qiang Liu[1], Huiping Hou[1], Yongshi Wang[1,2]* and Xianhong Shu[1,2]*

[1]Department of Echocardiography, Zhongshan Hospital (Xiamen), Fudan University, Xiamen, Fujian, China, [2]Department of Echocardiography, Zhongshan Hospital, Fudan University, Shanghai, China

Purpose: Percutaneous patent foramen ovale (PFO) closure is becoming more and more common for the treatment or prevention of PFO-associated right-to-left shunt (RLS). This study aims to investigate the value of transesophageal echocardiography (TEE) in percutaneous PFO closure, and to explore a new method that can improve intraoperative diagnosis and surgical safety.

Materials and methods: Based on our inclusion and exclusion criteria, we enrolled 73 patients between 16 and 70 years old (average age 43.25 ± 14.87 years) who underwent percutaneous PFO closure at the Department of Cardiac Surgery, Zhongshan Hospital (Xiamen), Fudan University, from January 2022 to December 2023. Out of the 73 enrolled patients, there were 28 males (38.36%) and 45 females (61.64%), 29 migraine patients (39.73%), 14 patients (19.19%) with headache and dizziness, 14 patients (19.18%) with a history of cerebral infarction (CI), and 25 patients (34.25%) with CI, lacunar infarction or ischemic focus on magnetic resonance imaging (MRI). All patients received routine transthoracic echocardiography (TTE) and agitated saline contrast echocardiography (ASCE) before operations. Percutaneous closure of PFO was completed under the guidance of TEE. In 12 patients, the method of "injection of heparinized sterile saline through the delivery sheath" was used to observe their RLS, and the anatomical characteristics of the PFO according to the shunt path were monitored and evaluated. This method was also applied to some patients to guide the conveyor to pass through the foramen ovale (FO) channel safely and effectively, thereby improving the success rate of PFO closure.

Results: The application of TEE during the procedure of percutaneous PFO closure, including preoperative evaluation, intraoperative guidance, and postoperative reevaluation, can offer further details about the anatomical and shunt characteristics of PFO, improve the diagnosis rate, and confirm the safety of the surgical path. It ensures the safety and reliability of the whole operation, greatly improving the success rate and reducing postoperative complications.

Abbreviations

3D, three-dimensional; ASA, atrial septal aneurysm; ASCE, agitated saline contrast echocardiography; ASD, atrial septal defect; CI, cerebral infarction; CS, cryptogenic stroke; FO, fossa ovale; LA, left atrial; LRS, left-to-right shunt; LSPV, left superior pulmonary vein; MB, micro-bubble; MRI, magnetic resonance imaging; PFO, patent foramen ovale; RA, right atrial; TEE, transesophageal echocardiography; TIA, transient ischemic attack.

Conclusions: TEE guidance of percutaneous PFO closure has the advantages of minimal trauma, no radiation and real-time visualization, while injecting heparinized sterile saline through the delivery sheath is safer and more effective in improving the success rate and reducing postoperative complications.

KEYWORDS

echocardiography, transesophageal echocardiography, PFO, percutaneous PFO closure, cryptogenic stroke, migraine atrial septal defect, cerebral infarction (CI), cryptogenic stroke (CS)

1 Introduction

Fossa ovale (FO) is the pore located between the septum primary and secondary septum during fetal development, an important structure to maintain normal fetal circulation. After birth, as a baby cries and the pleural pressure drops, the left atrial (LA) pressure increases, pushing the primary septum to the secondary septum and making the two septums adhere and fuse. This process gradually forms a permanent atrial septum. Failing to complete this process leads to an interatrial slit-like channel called patent foramen ovale (PFO) (1, 2). The global prevalence of PFO is approximately 27% (2). An autopsy study showed the incidence of PFO was 30% in the age group of 1–29 years, 25% in the age group of 30–79 years, and 20.2% in the age group of over 80 years (3). As a common congenital cardiac abnormality, the incidence of PFO ranges from 20% to 34% (4). In general, the primary septum is thin and long, and the secondary septum is thick and muscular. Under normal circumstances, because the LA pressure is higher than the right atrial (RA) pressure, the primary septum and secondary septum are closely attached, and the FO is in a closed state. The FO may remain persistently open in the presence of a PFO or may open when the thin, long primary septum is pushed apart as the RA pressure becomes higher than LA (e.g., coughing, sneezing, or constipation). Blood, thrombus, or any substance in the blood (including vasoactive substances such as 6-tibiottryptamine and platelet-derived factor) from the right heart system can enter the arterial system through the open FO to form an embolism (paradoxical embolism). The long-standing concept of PFO is that it has no special clinical significance, so it has not been paid much attention. In fact, however, PFO is associated with a variety of clinical symptoms, including ischemic stroke, transient ischemic attack (TIA), migraine, systemic or coronary embolism, and so on. PFO closure is a way to alleviate or prevent the related symptoms, especially for those young patients (under 60 years old) who have had cerebral infarction and PFO complications. When other causes of cerebral infarction are excluded, PFO closure plays an important role in successfully preventing the recurrence of cerebral infarction.

At present, percutaneous PFO closure can be performed under the guidance of x-ray or TEE-guided ultrasound. While many of the procedures are still under the guidance of x-ray, the TEE-guided percutaneous PFO closure is more widely used in recent years. This study aims to investigate the value of TEE in percutaneous closure of PFO, and to explore a new method that can be used to improve the intraoperative diagnosis and safety of the operation.

2 Material and methods

2.1 Patient population and study design

We enrolled 73 patients between 16 and 70 years old (average age 43.25 ± 14.87 years) who underwent percutaneous PFO closure at the Department of Cardiac Surgery, Zhongshan Hospital (Xiamen), Fudan University, from January 2022 to December 2023, including 28 males (38.36%) and 45 females (61.64%), 29 patients with migraine (39.73%),14 patients (19.19%) with headache and dizziness, 14 patients (19.18%) with a history of cerebral infarction, 25 patients (34.25%) with cerebral infarction, lacunar infarction or ischemic focus on MRI, 21 patients (28.77%) with PFO detected by TTE color flow Doppler presenting left-to-right shunt (LRS) at the FO, 66 patients (90.41%) with PFO confirmed by TEE before admission(there are both gaps and shunts), and 7 patients (9.59%) with PFO showing a small gap yet inevident shunt by TEE before admission but right-to-left shunt (RLS) suggested by ASCE. According to the 2019 SCAI guidelines (5), although some patients did not have strong indications for PFO closure, they were also clinically included in the cohort because of the strong demand of these patients or their families. All patients had significant clinical symptoms, including migraine, dizziness or vertigo, and syncope that could not be controlled by medications. Some patients experienced these symptoms accompanied by nausea and vomiting, while severe patients were accompanied by loss of consciousness—the most serious was cerebral infarction. The course of the disease ranged from 1 month to 40 years, and other causes that could cause related symptoms or cerebral infarction were excluded before surgery.

Inclusion criteria:

1. Age between 16 and 70 years old, including 16 and 70 years old;
2. Combined PFO and clinically excluded other causes of related diseases: (1) cryptogenic stroke (CS) or transient ischemic attack (TIA); (2) refractory migraine with no response to medications;
3. Large PFO (channel inner >4 mm);

4. Complex PFO: PFO with multiple shunts; long channel PFO (≥8 mm); combined with atrial septal aneurysm (ASA); accompanied by a lengthy Eustachian valve; hypertrophic secondary atrial septum (>10 mm), and with complicated atrial septal defect (ASD);
5. Patients or their authorized proxy agree to have the PFO closure performed under general anesthesia.
6. Patients or their authorized proxy agreed to sign the informed consent before surgery.

Exclusion criteria:

1. Patients with other cardiac diseases requiring surgical treatment;
2. Patients combined with esophageal stenosis or perforation, esophagotracheal fistula, active esophageal or gastric bleeding and other patients who are not suitable for TEE monitoring.

2.2 Methods

2.2.1 TTE

TTE was conducted using a Philips EPIQ 7C ultrasound system equipped with an S5-1 1–5 MHz transducer (Philips Ultrasound, Holland). All patients underwent a complete TTE examination by an experienced sonographer. Patients were scanned in the left lateral decubitus position and connected to an electrocardiogram. All two-dimensional (2D) and Doppler recordings and measurements were performed according to American Society of Echocardiography guidelines (6). We mainly observed the atrial septum in the parasternal aortic short-axis view, parasternal 4-chamber view, and subcostal biatrial view. The presence of PFO was considered if two or more views confirmed a thin bundle of oblique LRS at the FO. In addition to focusing on the PFO, it is also important to rule out the presence of other structural lesions, the presence of thrombosis, and other intracardiac diseases that may be related to the clinical symptoms, because it will affect the clinical management decisions.

2.2.2 ASCE

ASCE was also performed by an experienced sonographer using a Philips EPIQ 7C ultrasound system equipped with an S5-1 1–5 MHz transducer (Philips Ultrasound, Holland). Patients were also scanned in the left lateral decubitus position and connected to an electrocardiogram. Every patient was cannulated in the right antecubital with an 18-gauge cannula. The cannula was connected with an extension tube, to which is connected a three-way tap and two ten 10 ml syringes, respectively 8 ml of sterile saline, one 1 ml of air and 1 ml of the patient's blood. They were thoroughly exchanged at least 10 times to produce an air suspension. During this time the patient was asked to do the Valsalva maneuver (VM) for around 10 s. If the VM was effective we can find that the interatrial septum was pushed to the LA by the improving pressure of the RA. Then, the air suspension was injected into the patient immediately. When the micro-bubble (MB) can be seen in the RA, the patient was asked to exhale quickly. If any MB was observed in the LA immediately or in 3–5 cardiac cycles, PFO was diagnosed.

2.2.3 TEE

TEE were performed by using a Philips EPIQ 7C ultrasound system equipped with an X7-2t 2-7MHz transducer (Philips Ultrasound, Holland). If there was a "slit-like" channel between the primary septum and secondary septum and color Doppler showed LRS, PFO was confirmed. Because the shunt was impacted by the pressure between left and right atrial, sometimes the shunt was not obvious. In this case, the patient's medical history and the result of the ASCE may be important to the diagnosis of PFO.

2.3 Intraoperative TEE-guided percutaneous PFO closure

All patients underwent TEE-guided percutaneous PFO closure under routine anesthesia in the operating room. The right femoral vein was the first choice to establish venous access. The whole TEE-guided procedure was divided into three steps:

(1) **Preoperative TEE** (Figure 1) A comprehensive preoperative TEE was necessary, including evaluations of cardiac function, the presence of pericardium, and most importantly, the exclusion of other cardiac conditions requiring surgical treatment. The observation content was the anatomical characteristics of the FO, including the size and length of the FO, the thickness and mobility of the primary septum, the presence of thrombosis in the FO, the size and direction of the FO shunt and the number of shunt tracts. In addition, it would be necessary to observe whether there was an atrial septal aneurysm (ASA) and excluded the presence of a thrombus within the aneurysm sac, the existence of a long Eustachian valve, and the presence of an atrial septal defect (ASD), which could provide reference for the selection of occlusion path, size and number of occluder.

(2) **Intraoperative guidance** (Figure 2): This is the main step. First of all, for patients without obvious shunt in preoperative TEE, we needed to further clarify the shunt before occlusion. At the view showing the "slit-like" channel of the FO, the head end of the delivery sheath was placed at the RA side of the FO, and 20 ml sterile saline was quickly injected. At this moment, the sonographer should observe the flow of the liquid. If it was shown in the LA with crystal reflection (appearance on ultrasound is a punctate hyperechoic), it indicated the existence of PFO. If not, the presence of a PFO was excluded.

This step is especially important for patients with a small gap: first, we can confirm the existence of the PFO, the size and length of the FO; second, we can confirm the path of the occlusion, which can reduce the procedure time, improve the occlusion efficiency and reduce complications. For patients with a clear gap and

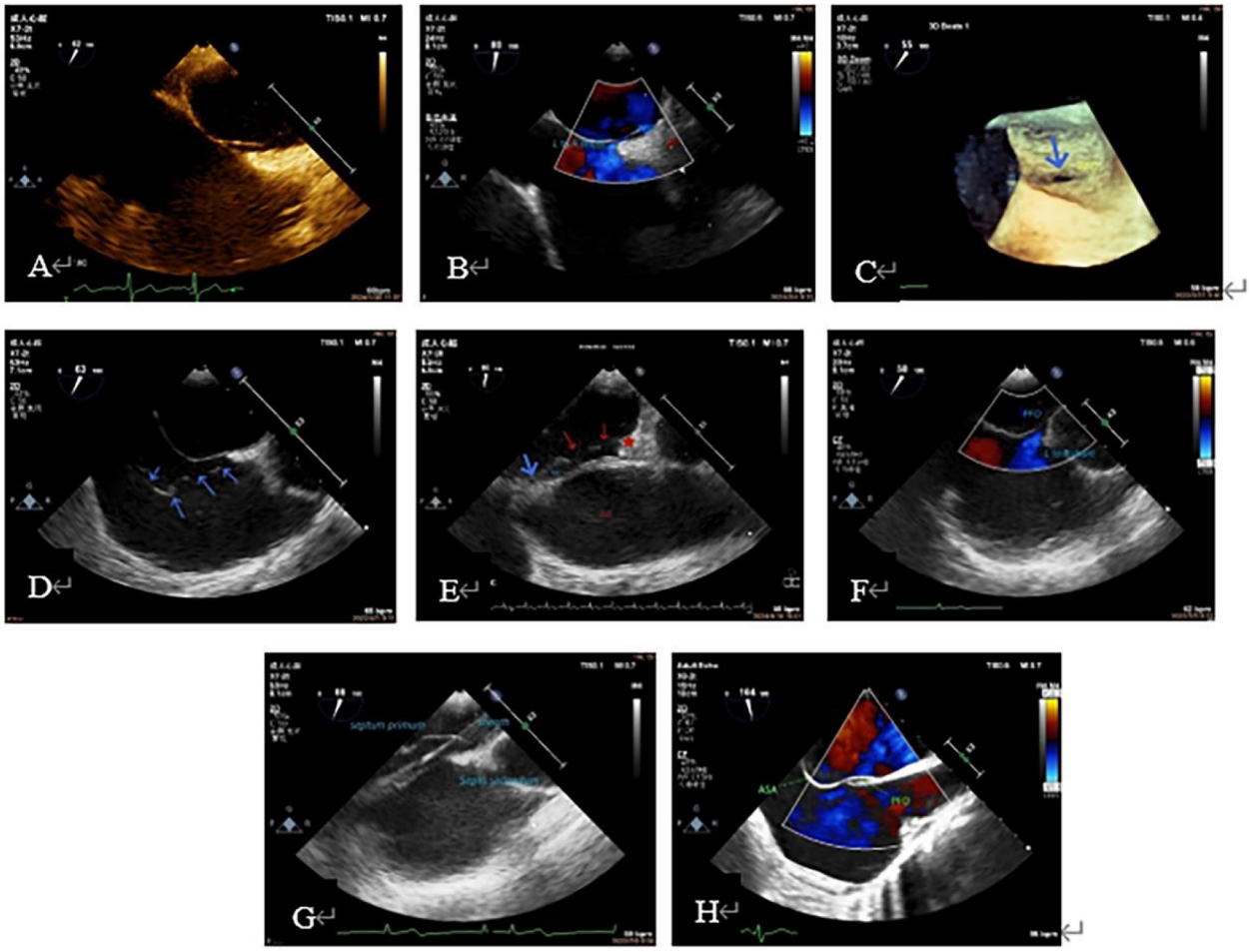

FIGURE 1
Preoperative TEE to understand PFO shape, size, shunt, thickness and mobility of the primary septum, whether it is combined with ASA, excessive eustachian valve, and whether it is combined with other structural problems that need to be treated. (**A**): PFO tunnel showed a small RA opening and a large LA opening. (**B**): LRS of PFO; (**C**): PFO under 3D ultrasound (blue arrow); (**D**): excessive Eustachian valve; (**E**): the primary septum of the PFO (shown by blue arrow) was connected with the coumadin ridge (shown by red star). The PFO was continuously open, and two continuous interruptions were observed on the primary septum (shown by red arrow). (**F**): Preoperative diagnosis of ASD, intraoperative TEE showed a large PFO; (**G**): primary septum with large mobility. (**H**): TEE showe ASA. 3D, three-dimensional; ASA, atrial septal aneurysm; ASD, atrial septal defect; LA, left atrial; LRS, left-to-right shunt; PFO, patent foramen ovale; RA, right atrial; TEE, transesophageal echocardiography.

shunt, it is necessary to choose a view that can clearly show the gap of the FO (if there is a shunt, it is better to show the shunt and the gap together).

The procedure included the following steps: ① the guide wire was guided through the FO to the left superior pulmonary vein (LSPV). ② Guide the delivery sheath (if the gap is large enough) to follow the wire into the LSPV. If the gap is too small to directly pass through the delivery sheath, the inner core should be used for a certain auxiliary expansion. Because the tip of the inner core is sharp, the cooperation between the sonographer and the operator is very important during this process. The operator should push the inner core forward very slowly until the tip is exposed. This process does not need to expose the inner core head end completely: 5–10 mm in length is enough. Then, under the close observation of the sonographer, the whole delivery sheath was slowly advanced along the gap of the FO into the LA. The inner core was then returned to the sheath, and finally the delivery sheath was delivered to the LSPV. When the FO is too small, the guide wire occasionally accidentally breaks the secondary septum and enters under the capsule of the left atrial surface of the secondary septum when trying to enter the gap. At this time, it is difficult to identify whether the guide wire is in the channel of the FO or under the capsule, because the capsule is too thin to distinguish from the primary septum. In order to determine the position of the guide wire, we also took the method of injecting heparinized sterile saline (1,000 ml sterile saline + 100 mg heparin) through the delivery sheath. In contrast to the previous, this process requires a slow injection. Before this step, we withdrew the sheath to ensure that no gas remains inside (i.e., the evacuation process), thus avoiding the occurrence of air embolism. If the guide wire is in the FO channel, this process will be very smooth, and the crystals in the LA can be reflected at the same time. If not, there will be resistance during the injection process, and there is no crystal reflection in the LA.

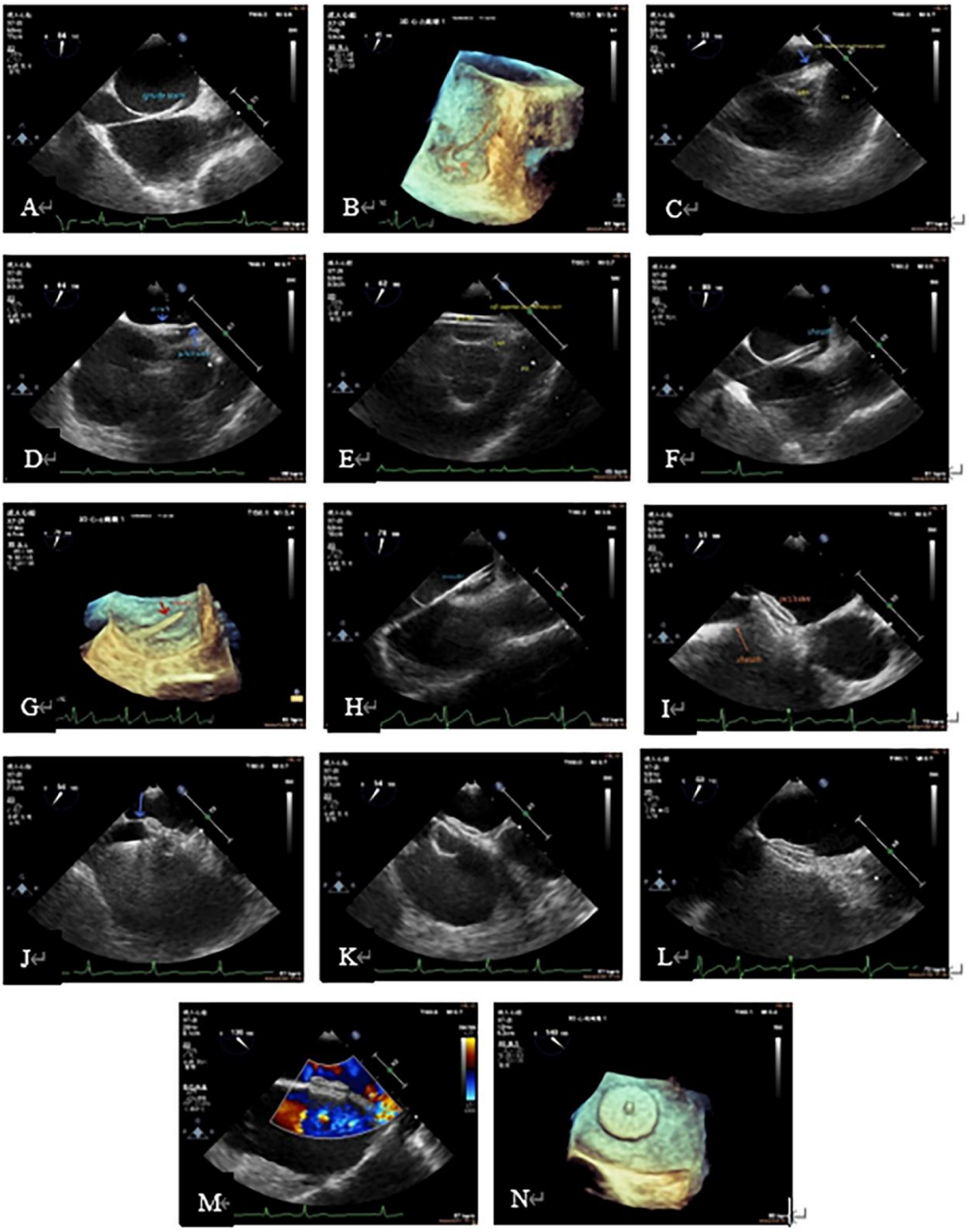

FIGURE 2
Procedure demonstration during TEE-guided percutaneous PFO closure. (**A**): Guide wire through PFO tunnel; (**B**): 3D visualization of the guidewire reaching the LA through the PFO. (**C**): Guidewire leading to LSPV (blue arrow); (**D**): the sheath (short blue arrow) passed through the PFO into the LA via the guide wire (long blue arrow). (**E**): Sheath entering the LSPV; (**F**): the sheath in the LA; (**G**): three-dimensional image showing the delivery sheath reaching the LA via the PFO; (**H**): occlude in the delivery sheath (echogenic part in the sheath); (**I**): after completely releasing of the two discs of the occlude, the atrial septum was located between the two discs, when the delivery sheath was still connected to the right atrial disc (arrow). (**J**): With the help of the sheath tube, the occlude was "pushed" to the LA, and the primary septum was pushed up (arrow). (**K**): The whole occlude was "pulled" to the RA, and the slight deformation of the right atrial disc could be seen. (**L**): State after the complete release of the occlude (complete detachment of the sheath from the right atrial disc). (**M**): Color Doppler showed no residual shunt. (**N**): Left atrial disc showed in 3D. 3D, three-dimensional; LA, left atrium; LSPV, left superior pulmonary vein; PFO, patent foramen ovale; TEE, transesophageal echocardiography.

On the contrary, a raised capsular and a dark area of crystal reflection can be seen, which can become larger with the injection. In this case, the operator needs to withdraw the guide wire and re-adjust the access until it enters the correct FO gap. During this process, the method of injecting heparinized sterile saline can be used repeatedly to determine the position of the guide wire to ensure the safety and feasibility of the occlusion process. ③ Guide the release of the occluder: after the occluder was installed, the operator completely withdrew the inner core of the delivery sheath from the sheath, exhausted the sheath tube (exhaust is a very important step, otherwise coronary artery gas embolism is likely to occur), placed the occluder device in the delivery sheath, and slowly pushed it. When the occluder can be identified by the ultrasound screen, the sonographer should closely follow the position of the occluder. When the occluder came out of the sheath, the delivery sheath was withdrawn to the LA as a whole, and the operator synchronously slowly released the occluder until the left atrial disc was completely released. The transport sheath continued to withdraw. When the left atrial disc was close to the atrial septum, the right atrial disc was quickly and completely released. When this step was completely done, the delivery device was still connected to the right atrial disc. The sonographer needs to observe the position of the occluder, whether the two discs are on both sides of the atrial septum, whether there is residual shunt at the atrial level, and whether there is pericardial effusion. After confirming the two discs were completely separated and were located on either side of the atrial septum, thereby no residual shunt and pericardial effusion, the operator needed to conduct the "push" (push the occluder to the LA, if the atrial septum is shown to be jacked up, means in the correct position) and "pull" (pull the occluder backward to the RA; if the position is correct, it is visible that the disc is deformed by pulling) tests on the occluder to ensure the occluder is located on either side of the atrial septum. One should repeat the tests 2–3 times to ensure the stability of the occluder. After the completion of "push" and "pull" tests, the sonographer reconfirmed the position of the occluder and the shunt at the atrial level. If the occluder position is fixed and there is no shunt at the atrial level, the delivery sheath can be removed from the occluder device. The whole process of occlusion was completed. ④ After transcatheter closure, the main observations were whether the position of the occluder was fixed, and whether there was residual shunt at the atrial level, thrombosis, pericardial effusion and cardiac function.

2.4 Follow-up

All patient underwent a routine echocardiography examination before discharge. We conducted telephone follow-up or face-to-face follow-up at the patient's 1-month, 3-month, 6-month, 1-year, and 2-year postoperative visits. The follow-up included the clinical symptoms improved conditions, any thrombotic events happened, whether presented atrial fibrillation, whether there was residual shunting on echocardiography, and re-intervention.

2.5 Statistical analysis

Statistical analysis was performed using IBM SPSS software (version 26.0; IBM Corp.). Data was represented by (mean ± SD) for continuous variables and as frequency (*n*) and percentage (%) for categorical variables.

3 Results

3.1 **Baseline Information of patients** (Table 1): The average age of the subjects was 43.25 ± 14.87 years old. There were 45 females (61.64%), 29 patients with migraine (39.73%), 14 patients (19.19%) with headache and dizziness, 14 patients (19.18%) with a history of cerebral infarction, and 25 patients (34.25%) with cerebral infarction, lacunar infarction or ischemic focus on MRI. The duration of migraine and dizziness ranged from 1 month to 40 years. Among the subjects enrolled, 11 (15.07%) had a history of hypertension, 3 (4.11%) had a history of diabetes, and 4 (5.48%) had a history of coronary heart disease. There were 21 patients (28.77%) with PFO on TTE color Doppler, 66 patients (90.41%) with PFO confirmed by TEE before admission, and the average size of PFO was 1.48 ± 0.86 mm and the average length of PFO was 11.87 ± 5.44 mm. There were 16 cases (21.92%) of complex PFO. Preoperative ASCE showed that there were RLS, including 7 cases of grade 1 (9.59%), 12 cases of grade 2 (16.44%), and 35 cases of grade 3 (47.95%).

TABLE 1 Baseline data of patients undergoing percutaneous PFO closure. Grade 1 (few RLS): 1–10 MBs/frame in LA; Grade 2 (moderate RLS): 11–30 MBs/frame in LA; Grade 3 (massive RLS): >30 MBs/frame in the LA, or the LA was almost filled with MBs with significantly reduced sound transmission.

Patients' baseline data (χ±s, *n* (%)		
Basic information		
Age (year)		43.25 ± 14.87
Female		45 (61.64)
Migraine		45 (61.65)
Dizziness		23 (31.51)
History of CI		14 (19.18)
HBP		11 (15.07)
DM		3 (4.11)
CHD		4 (5.48)
Auxiliary examination		
MRI		25 (34.25)
TTE		21 (28.77)
ASCE	Grade 1	7 (9.59)
	Grade 2	12 (16.44)
	Grade 3	35 (47.95)
TEE		66 (90.41)
Characteristics of PFO		
Size (mm)		1.48 ± 0.86
Length (mm)		11.87 ± 5.44
Complex PFO		16 (21.92)

ASA, atrial septal aneurysm; ASCE, agitated saline contrast echocardiography; CHD, coronary heart disease; CI, cerebral infarction; DM, diabetes mellitus; LA, left atrial; MB, microbubbles; MRI, magnetic resonance imaging; PFO, patent foramen ovale; RLS, right-to-left shunt; TEE, transesophageal echocardiography; TTE, transthoracic echocardiography.

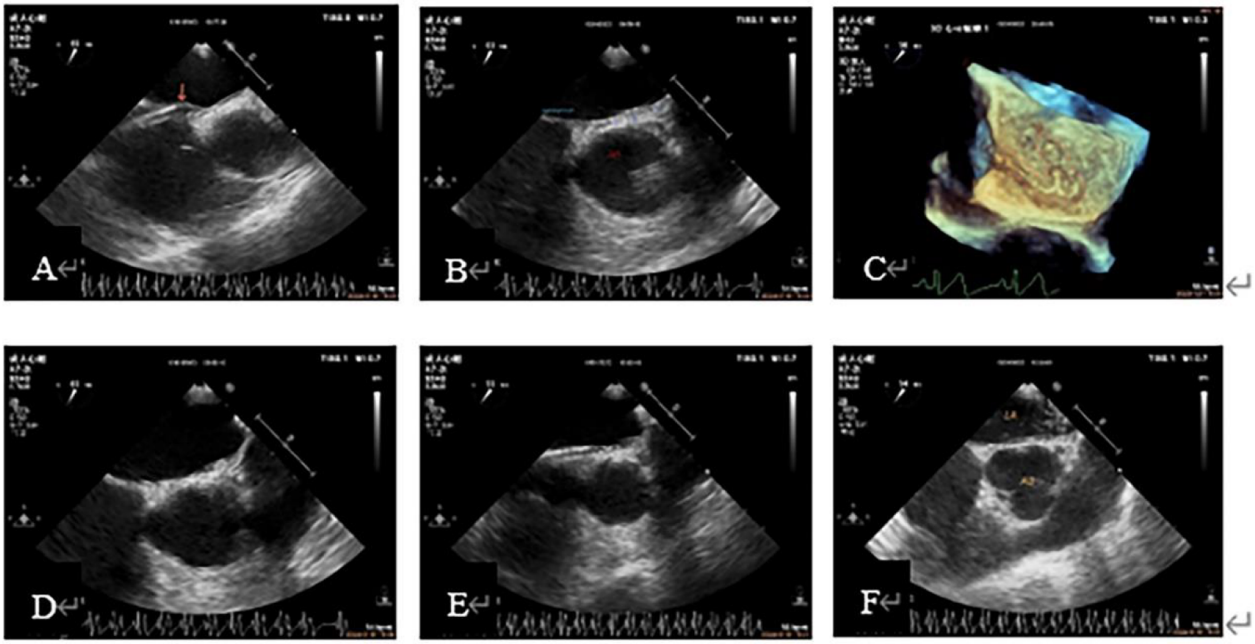

FIGURE 3
Case 1 A 53-year-old woman with migraine for more than 10 years had a grade 2 result by ASCE and preoperative TEE showed a PFO about 1 mm wide. (**A**): The head end of the delivery sheath was placed at the RA opening of the PFO, and the primary septum was pushed up (arrow). (**B**): Guidewire walking under the capsular of the secondary septum. (**C**): The tortuous guidewire shadow under the capsular of the secondary septum was shown in the 3D view of the LA surface. (**D**, **E**): The secondary septum was lifted after a slow injection of saline through the delivery sheath, and the hyperechoic subcapsule was observed, which proved that the sheath tube was under the secondary septum capsule and not in the LA. (**F**): Strong crystal echo in the LA after readjusting the path of the guidewire, indicating that the path was correct and the patient successfully completed PFO closure. 3D, three-dimensional; ASCE, agitated saline contrast echocardiography; LA, left atrial; RA, right atrial; PFO, patent foramen ovale; TEE, transesophageal echocardiography.

3.2 **"Injection of heparinized sterile saline through the delivery sheath" has a good value in assisting the diagnosis of PFO and confirming the closure path** (Figures 3, 4): Two cases were used to demonstrate the application of this method in path confirmation and PFO diagnosis.

3.3 All patients completed at least 3-months clinical and echocardiography follow-up, the longest follow-up being 2 years and 6 months (mean average 14 ± 10months; median time 14 months.). There were 2 patients with recurrent cerebral infarction at 1 month and 7 months post-operation respectively, and were relieved after corresponding treatment, and no embolic events occurred within 2-year follow-up. Among the patients with migraine and other symptoms, 3 patients felt that their symptoms did not improve at all after the operation, and their follow-up time was 3 months to 6 months. 11 patients had complete symptom relief, and 57 patients had symptom improvement. All patients had no atrial fibrillation after the operation, and no residual shunts or re-interventions were found on echocardiography follow-up (Table 2).

4 Discussion

In recent years, with the continuous improvement of interventional technology and biomaterials, the treatment of structural heart disease has gradually transformed from open surgery to interventional surgery. PFO, as a common disease, is closely related to a variety of clinical conditions. In 1992, Bridge et al. described the first transcatheter closure of PFO with the use of Bard Clamshell atrial septal umbrella after presumed retrograde embolization (7). Since then, the treatment of structural heart disease has entered a new era of intervention. The subsequent results of four randomized controlled trials in 2017 and 2018 (8–11) improved the management of PFO in patients with unexplained stroke/TIA, and substantially revised and updated the global guidelines (12, 13).

Migraine, a paroxysmal disorder characterized by complex sensory dysfunction and headache, is the second leading cause of disability worldwide (14). It is also a common disease in young people, and one-third of these patients have migraine aura (15, 16). Moreover, studies have proved that PFO is closely related to migraine (17), and migraine aura is related to RLS including PFO (18, 19). The mechanism of migraine caused by PFO is believed to be the transfer of vasoactive substances, which are usually filtered by the pulmonary circulation and enter the systemic circulation (18). Studies have shown that interventional closure of PFO can effectively reduce the frequency and duration of headache attacks compared to medications (4). And a large number of meta-analyses have shown that percutaneous PFO closure can effectively improve the duration and frequency of

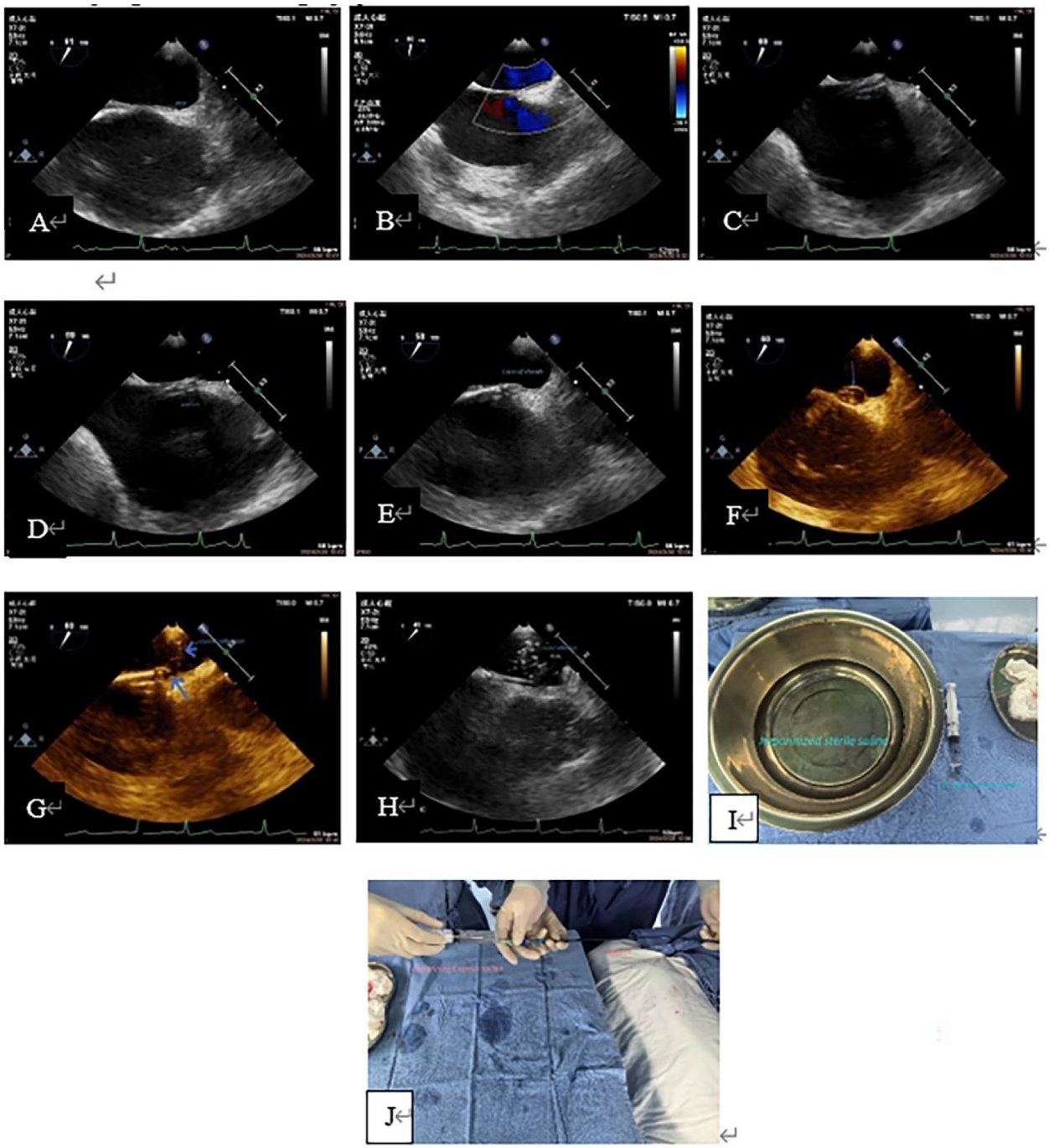

FIGURE 4
Case 2 A 31-year-old man with a history of cerebral infarction who had a positive result by ASCE (grade 3) and a 12 mm PFO tunnel width on preoperative TEE. (**A**, **B**): Preoperative TEE showed a small PFO channel and minimal LRS. (**C**): The delivery sheath was capped at the RA opening of the PFO. (**D**, **E**): The inner core was slowly sent into the PFO tunnel. (**F**): Saline was slowly injected through the sheath and the primary septum was lifted; the PFO appeared as a balloon (arrow). (**G**): Showed a pore in the primary septum and secondary septum (long blue arrow), and hyperechoic crystal was seen entering the LA through the pore (short blue arrow), which indicated the existence of PFO channel and correct delivery path of the sheath canal. H: showed that a large number of crystal echoes appear in the LA, indicating that the delivery sheath was entirely in the LA. (**I**): Showed the heparinized normal saline solution and a 20 ml syringe needed for the test. (**J**): Showed "injection of heparinized sterile saline through the delivery sheath", this process was carried out jointly by nurses and doctors. This patient also underwent a successful occlusion. ASCE, agitated saline contrast echocardiography; LA, left atrium; LRS, left-to-right shunt; PFO, patent foramen ovale; TEE, transesophageal echocardiography.

migraine symptoms in patients with migraine (20–23). Therefore, more and more migraine patients with PFO are suggested to choose percutaneous PFO closure as their treatment plans.

Cryptogenic stroke (CS) refers to stroke after exclusion of other identifiable stroke mechanisms, such as large-artery atherosclerotic disease, established cardiac embolic source, small-vessel occlusive

TABLE 2 Short-term and middle-term follow-up. Symptom relief includes a decrease in the frequency and/or severity of symptoms.

		n = 73	
Complications of the procedure (case/%)	Anesthesia-related complications	0	0
	Pericardial effusion	1	1.37
	Vessel rupture	0	0
	Pericardial tamponade	0	0
	Hepatic vein injury	0	0
	Embolic events	0	0
Complications of the TEE (case/%)	Mucosal bleeding	3	4.11
	Esophageal and gastric perforation	0	
Follow-up (case/%)	Embolic events	2	2.74
	Symptom completely disappeared	11	15.07
	Symptom relief	57	78.82
	No improvement in the symptoms at all	3	4.11
	Atrial fibrillation	0	0
	Residual shunt	0	0
	Re-intervention	0	0

disease (lacunar stroke), hypercoagulation disorder requiring anticoagulant therapy, or arterial dissection. Up to 40% of patients have unknown etiology (24), and PFO is present in 50% of CS patients <60 years old (25, 26), which is almost twice the prevalence in the general population (25). The mechanisms of CS caused by PFO include paradoxical thrombosis, *in situ* thrombosis, and arrhythmia (27), while paradoxical embolism is considered the most common mechanism, in which venous thrombosis enters the systemic circulation through the open PFO. There has been data suggesting that percutaneous PFO closure is superior to antiplatelet therapy in reducing the risk of recurrent stroke in selected patients under 60 years of age (8–11). And several meta-analyses also have confirmed that PFO closure reduced the risk of ischemic stroke in cryptogenic stroke patients with concomitant PFO (28, 29). According to the European Stroke Organization (ESO) guidelines, in adults under 60 years of age with cryptogenic stroke/transient ischemic attack and high-risk PFO features (moderate or severe shunt, ASA, atrial septal overactivity), percutaneous PFO closure plus medical therapy are recommended over antiplatelet therapy alone (30). Many clinical observations have confirmed PFO closure as a safe and effective treatment method to prevent recurrent cerebral embolism events (31, 32).

Since 1974, King and Mills performed the first successful percutaneous closure of ASD with the assistance of x-ray (33), tremendous intervention and innovation have occurred in the field of percutaneous

ASD closure using a transcatheter-based device during the last 70 years. Because closure devices for ASD can also be used for preventing paradoxical embolism in transcatheter closure of PFO, a subtype of secondary septal defect, percutaneous closure techniques have also been used in the treatment of PFO. Percutaneous PFO closure is similar to ASD closure except for the difference in occluder.

Although the guidance of x-ray can observe the whole process of delivery and occlusion, it also has its limitations including ① it is radioactive; ② it has certain risks of carcinogenesis, chromosome malformation and blood diseases; ③ lipiodol contrast agent also has a certain effect on the patient's body; ④ more importantly, the intracardiac structures and adjacent anatomical relationships could not be shown; ⑤ for some small PFO or complex PFO, the operation can not be performed or takes a long time, which will cause certain mental stress to the patients in the alert state. Meanwhile, due to the limitation of the fluoroscopy-guided PFO closure, the PFO cannot be further clarified during the procedure, and a comprehensive evaluation of the PFO cannot be performed, which also means that the appropriate occluder cannot be selected preoperatively. In addition, it is impossible to exclude whether there are small atrial septal defect (ASD) that cannot be identified in TTE examination, especially those that are very close to the PFO. It is impossible to identify and confirm whether exist thrombus in the PFO tunnel pre-operation and whether the closure device surface has thrombus post-operation. These reasons can easily lead to residual shunts and untreated atrial communication after the closure, thereby increasing the post-closure reintervention rate and also lead to thrombotic events during and after the procedure.

TEE has become an indispensable application in cardiac surgery (34, 35); especially, in valve surgery, it has become the standard intraoperative monitoring. Compared to only fluoroscopy-guided PFO closure, TEE not only improves the success rate of surgery (36), reduces the mortality of patients, but also reflects the hemodynamic changes in real-time. It is also increasingly used and plays an important role in coronary artery and other structural cardiac surgery, and is an important tool for intraoperative evaluation of regional ventricular wall motion or structural abnormalities (37). Percutaneous PFO closure has become the first choice for patients with indications due to its high success rate, minimal trauma and rapid postoperative recovery. TEE-guided PFO closure has the following characteristics and advantages: ① no radiation. ② Minimum injury: esophageal mucosal injury is the most common complication, but it usually recovers soon after esophageal probe evacuation. ③ Does not affect the surgical operation. ④ Real-time visualization: the TEE probe is located behind the LA, which allows close observation of the intracardiac structure. The anatomical characteristics of the PFO can be observed before the operation, and if necessary, the sterile saline injection test can be used to confirm whether an RLS is present or whether the intervention path is correct. It can provide more preoperative information and effective evidence for clinicians to make surgical decisions. In addition, it can assist the exhaust, closely observe the coronary artery gas embolism or not, dynamically observe the changes in cardiac function, and reduce the malignant complications such as cardiac arrest caused by coronary artery gas embolism. The position of the occluder, residual shunt and thrombosis could be observed after operation. ⑤ Less surgical complications and high safety: due to the real-time visualization of TEE, the incidence of cardiac injury or rupture

and malignant complications such as cardiac arrest can be reduced. ⑥ Intraoperative " heparinized sterile saline injection test" can improve the intraoperative diagnosis rate of PFO and the success rate of operation, and reduce surgical trauma. Clinically, there are quite a number of patients, including those with a history of stroke, whose primary septum is relatively thin, even though they show strong positive results in ASCE, but there is no obvious gap or shunt visible on TEE. TTE is more difficult to observe the gap and shunt in these patients, so we chose the method to further confirm the evidence of communication between the left and right atria during surgery.

In summary, TEE is essentially the operating surgeon's eyes. TEE can monitor the position, movement direction, and speed of the delivery device in the heart throughout the procedure. The serious complication of pericardial tamponade is mostly due to improper operation, such as excessive force applied by the operating surgeon, excessive speed, or heart ear rupture caused by these factors, under TEE guidance it can be prevented by providing timely feedback to the operating surgeon and communicate in real-time. During the procedure, we often encounter changes in the patient's heart rhythm, which are related to the operation, but with TEE, we can provide real-time feedback on the position of the delivery device, which can prevent improper operation from continuing and reduce or avoid the occurrence of serious complications.

5 Conclusions

TEE, a real-time visualization examination technology, has the characteristics of small injuries, no radiation, and no influence on surgical operation, which can reduce surgical complications and is highly safe. It has a high clinical application value in PFO closure. Intraoperative " heparinized sterile saline injection test" can improve the intraoperative diagnosis rate of PFO and the success rate of operation, and reduce surgical trauma. This method is innovative, simple, and easy to operate and popularized in clinical practice.

6 Limitations

The main limitation of this study was not a randomized controlled trial, the sample size was not sufficient and the follow-up time was not long enough to provide more convincing evidences. Moreover percutaneous PFO closure was performed by different operators, due to their varying experience had different surgical techniques and operation times. Additionally, the choice of occluder by different patients based on their economic ability also varies.

TEE is to monitor the whole process of the operation by placing the probe in the middle of the esophagus and behind the LA, and it cannot observe the process of the guide wire and delivery sheath from the femoral vein to the right atrium, which may lead to: ① when the guide wire crosses the iliac vein confluence and enters the contralateral iliac vein, it cannot be detected in real-time. Its detection depends on the operators' and sonographers' experience; for instance, sonographers paying specific attention to the detection when not finding the guide wire in the RA; ②. The sharp inner core of the delivery sheath may damage the vessel wall or perforate during the push process, leading to retroperitoneal hematoma. In order to avoid this situation, our experience is that the delivery sheath with the inner core is pulled into the outer sheath about 2 cm after the femoral vein travels.

Data availability statement

The original contributions presented in the study are included in the article/Supplementary Material, further inquiries can be directed to the corresponding authors.

Ethics statement

The protocol was approved by the Institutional Ethics Committee of Zhongshan Hospital (Xiamen), Fudan University (B-2021-027), and all subjects provided written informed consent before undergoing examinations.

Author contributions

LL: Writing – original draft, Methodology, Investigation. ZX: Writing – review & editing, Investigation, Formal Analysis, Data curation. QW: Writing – review & editing, Investigation, Data curation. QL: Writing – review & editing, Software, Investigation, Data curation. HH: Writing – review & editing, Investigation, Data curation. YW: Writing – review & editing, Project administration, Methodology, Conceptualization. XS: Writing – review & editing, Validation, Project administration, Methodology, Conceptualization.

Funding

The author(s) declare that no financial support was received for the research, authorship, and/or publication of this article.

Conflict of interest

The authors declare that the research was conducted in the absence of any commercial or financial relationships that could be construed as a potential conflict of interest.

Publisher's note

References

1. Naqvi N, McCarthy KP, Ho SY. Anatomy of the atrial septum and interatrial communications. *J Thorac Dis*. (2018) 10(Suppl 24):S2837–47. doi: 10.21037/jtd.2018.02.18

2. Hagen PT, Scholz DG, Edwards WD. Incidence and size of patent foramen ovale during the first 10 decades of life: an autopsy study of 965 normal hearts. *Mayo Clin Proc*. (1984) 59(1):17–20. doi: 10.1016/s0025-6196(12)60336-x

3. McKenzie JA, Edwards WD, Hagler DJ. Anatomy of the patent foramen ovale for the interventionalist. *Catheter Cardiovasc Interv*. (2009) 73(6):821–6. doi: 10.1002/ccd.21889

4. Calvert PA, Rana BS, Kydd AC, Shapiro LM. Patent foramen ovale: anatomy, outcomes, and closure. *Nat Rev Cardiol*. (2011) 8(3):148–60. doi: 10.1038/nrcardio.2010.224

5. Horlick E, Kavinsky CJ, Amin Z, Konstantinos DB, John DC, Ziyad MH, et al. SCAI expert consensus statement on operator and institutional requirements for PFO closure for secondary prevention of paradoxical embolic stroke: the American academy of neurology affirms the value of this statement as an educational tool for neurologists. *Catheter Cardiovasc Interv*. (2019) 93(5):859–74. doi: 10.1002/ccd.28111

6. Lang RM, Badano LP, Mor-Avi V, Afilalo J, Armstrong A, Ernande L, et al. Recommendations for cardiac chamber quantification by echocardiography in adults: an update from the American society of echocardiography and the European association of cardiovascular imaging. *J Am Soc Echocardiogr*. (2015) 28(1):1–39. doi: 10.1016/j.echo.2014.10.003

7. Akagi T. Transcatheter closure of patent foramen ovale: current evidence and future perspectives. *J Cardiol*. (2021) 77(1):3–9. doi: 10.1016/j.jjcc.2020.09.005

8. Saver JL, Carroll JD, Thaler DE, Smalling RW, MacDonald LA, Marks DS, et al. Long-term outcomes of patent foramen ovale closure or medical therapy after stroke. *N Engl J Med*. (2017) 377(11):1022–32. doi: 10.1056/NEJMoa1610057

9. Sondergaard L, Kasner SE, Rhodes JF, Andersen G, Iversen HK, Nielsen-Kudsk JE, et al. Patent foramen ovale closure or antiplatelet therapy for cryptogenic stroke. *N Engl J Med*. (2017) 377(11):1033–42. doi: 10.1056/NEJMoa1707404

10. Mas JL, Derumeaux G, Guillon B, Massardier E, Hosseini H, Mechtouff L, et al. Patent foramen ovale closure or anticoagulation vs. antiplatelets after stroke. *N Engl J Med*. (2017) 377(11):1011–21. doi: 10.1056/NEJMoa1705915

11. Lee PH, Song JK, Kim JS, Heo R, Lee S, Kim DH, et al. Cryptogenic stroke and high-risk patent foramen ovale: the DEFENSE-PFO trial. *J Am Coll Cardiol*. (2018) 71(20):2335–42. doi: 10.1016/j.jacc.2018.02.046

12. Mas JL, Derex L, Guerin P, Guillon B, Habib G, Juliardet JM, et al. Reprint of: transcatheter closure of patent foramen ovale to prevent stroke recurrence in patients with otherwise unexplained ischaemic stroke: expert consensus of the French neurovascular society and the French Society of Cardiology. *Rev Neurol (Paris)*. (2020) 176(1–2):53–61. doi: 10.1016/j.neurol.2019.10.002

13. Kleindorfer DO, Towfighi A, Chaturvedi S, Cockroft KM, Gutierrez J, Lombardi-Hill D, et al. 2021 guideline for the prevention of stroke in patients with stroke and transient ischemic attack: a guideline from the American Heart Association/American stroke association. *Stroke*. (2021) 52(7):e364–467. doi: 10.1161/STR.0000000000000375

14. Krause DN, Warfvinge K, Haanes KA, Edvinsson L. Hormonal influences in migraine—interactions of oestrogen, oxytocin and CGRP. *Nat Rev Neurol*. (2021) 17(10):621–33. doi: 10.1038/s41582-021-00544-2

15. Burch RC, Loder S, Loder E, Smitherman TA. The prevalence and burden of migraine and severe headache in the United States: updated statistics from government health surveillance studies. *Headache*. (2015) 55(1):21–34. doi: 10.1111/head.12482

16. Lipton RB, Liberman JN, Kolodner KB, Bigal ME, Dowson A, Stewart WF. Migraine headache disability and health-related quality-of-life: a population-based case-control study from England. *Cephalalgia*. (2003) 23(6):441–50. doi: 10.1046/j.1468-2982.2003.00546.x

17. Tariq N, Tepper SJ, Kriegler JS. Patent foramen ovale and migraine: closing the debate–a review. *Headache*. (2016) 56(3):462–78. doi: 10.1111/head.12779

18. Finocchi C, Del SM. Migraine with aura and patent foramen ovale: myth or reality? *Neurol Sci*. (2015) 36(Suppl 1):61–6. doi: 10.1007/s10072-015-2163-8

19. Schwerzmann M, Nedeltchev K, Lagger F, Mattle HP, Windecker S, Meier B, et al. Prevalence and size of directly detected patent foramen ovale in migraine with aura. *Neurology*. (2005) 65(9):1415–8. doi: 10.1212/01.wnl.0000179800.73706.20

20. Elbadawi A, Barssoum K, Abuzaid AS, Rezq A, Biniwale N, Alotaki E, et al. Meta-analysis of randomized trials on percutaneous patent foramen ovale closure for prevention of migraine. *Acta Cardiol*. (2019) 74(2):124–9. doi: 10.1080/00015385.2018.1475027

21. Zhang Y, Wang H, Liu L. Patent foramen ovale closure for treating migraine: a meta-analysis. *J Interv Cardiol*. (2022) 2022:6456272. doi: 10.1155/2022/6456272

22. Zhang QQ, Lu JJ, Yan MY, Hu XW, Qin YR, Wang DP, et al. The efficacy of percutaneous patent foramen ovale closure on migraine: a meta-analysis of randomized controlled trials and observational studies. *Biomed Res Int*. (2021) 2021:6643266. doi: 10.1155/2021/6643266

23. Shi YJ, Lv J, Han XT, Luo GG. Migraine and percutaneous patent foramen ovale closure: a systematic review and meta-analysis. *BMC Cardiovasc Disord*. (2017) 17(1):203. doi: 10.1186/s12872-017-0644-9

24. Giblett JP, Abdul-Samad O, Shapiro LM, Rana BS, Calvert PA. Patent foramen ovale closure in 2019. *Interv Cardiol*. (2019) 14(1):34–41. doi: 10.15420/icr.2018.33.2

25. Mojadidi MK, Zaman MO, Elgendy IY, Mahmoud AN, Patel NK, Agarwal N, et al. Cryptogenic stroke and patent foramen ovale. *J Am Coll Cardiol*. (2018) 71(9):1035–43. doi: 10.1016/j.jacc.2017.12.059

26. Kent DM, Dahabreh IJ, Ruthazer R, Furlan AJ, Reisman M, Carroll JD, et al. Device closure of patent foramen ovale after stroke: pooled analysis of completed randomized trials. *J Am Coll Cardiol*. (2016) 67(8):907–17. doi: 10.1016/j.jacc.2015.12.023

27. Hanley PC, Tajik AJ, Hynes JK, Edwards WD, Reeder GS, Hagler DJ, et al. Diagnosis and classification of atrial septal aneurysm by two-dimensional echocardiography: report of 80 consecutive cases. *J Am Coll Cardiol*. (1985) 6(6):1370–82. doi: 10.1016/s0735-1097(85)80228-x

28. Turc G, Calvet D, Guerin P, Sroussi M, Chatellier G, Mas JL. Closure, anticoagulation, or antiplatelet therapy for cryptogenic stroke with patent foramen ovale: systematic review of randomized trials, sequential meta-analysis, and new insights from the CLOSE study. *J Am Heart Assoc*. (2018) 7(12):1–38. doi: 10.1161/JAHA.117.008356

29. Darmoch F, Al-Khadra Y, Soud M, Fanari Z, Alraies MC. Transcatheter closure of patent foramen ovale versus medical therapy after cryptogenic stroke: a meta-analysis of randomized controlled trials. *Cerebrovasc Dis*. (2018) 45(3–4):162–9. doi: 10.1159/000487959

30. Ahmed N, Audebert H, Turc G, Cordonnier C, Christensen H, Sacco S, et al. Consensus statements and recommendations from the ESO-Karolinska stroke update conference, Stockholm 11–13 November 2018. *Eur Stroke J*. (2019) 4(4):307–17. doi: 10.1177/2396987319863606

31. Gafoor S, Franke J, Boehm P, Lam S, Bertog S, Vaskelyte L, et al. Leaving no hole unclosed: left atrial appendage occlusion in patients having closure of patent foramen ovale or atrial septal defect. *J Interv Cardiol*. (2014) 27(4):414–22. doi: 10.1111/joic.12138

32. Hornung M, Bertog SC, Franke J, Id D, Taaffe M, Wunderlich N, et al. Long-term results of a randomized trial comparing three different devices for percutaneous closure of a patent foramen ovale. *Eur Heart J*. (2013) 34(43):3362–9. doi: 10.1093/eurheartj/eht283

33. King TD, Mills NL. Nonoperative closure of atrial septal defects. *Surgery*. (1974) 75(3):383–8.

34. MacKay EJ, Neuman MD, Fleisher LA, Patel PA, Gutsche JT, Augoustides JG, et al. Transesophageal echocardiography, mortality, and length of hospitalization after cardiac valve surgery. *J Am Soc Echocardiogr*. (2020) 33(6):756–62. doi: 10.1016/j.echo.2020.01.014

35. Nicoara A, Skubas N, Ad N, Finley A, Hahn RT, Mahmood F, et al. Guidelines for the use of transesophageal echocardiography to assist with surgical decision-making in the operating room: a surgery-based approach: from the American Society of Echocardiography in collaboration with the society of cardiovascular anesthesiologists and the society of thoracic surgeons. *J Am Soc Echocardiogr*. (2020) 33(6):692–734. doi: 10.1016/j.echo.2020.03.002

36. Wang S, Zhu G, Liu Z, Zhou J, Zang W. Only transesophageal echocardiography guided patent foramen ovale closure: a single-center experience. *Front Surg*. (2022) 9:977959. doi: 10.3389/fsurg.2022.977959

37. Lawton JS, Tamis-Holland JE, Bangalore S, Bates ER, Beckie TM, Bischoff JM, et al. 2021 ACC/AHA/SCAI guideline for coronary artery revascularization: executive summary: a report of the American College of Cardiology/American Heart Association joint committee on clinical practice guidelines. *Circulation*. (2022) 145(3):e4–17. doi: 10.1161/CIR.0000000000001039

frontiers | Frontiers in Cardiovascular Medicine

TYPE Original Research
PUBLISHED 14 October 2024
DOI 10.3389/fcvm.2024.1410859

OPEN ACCESS

EDITED BY
Maxim Avanesov,
University Medical Center Hamburg-Eppendorf, Germany

REVIEWED BY
Lucia La Mura,
Federico II University Hospital, Italy
Sunil Mankad,
Mayo Clinic, United States
Andreea Calin,
Carol Davila University of Medicine and Pharmacy, Romania

*CORRESPONDENCE
Louis J. Dell'Italia
louis.dellitalia@va.gov

RECEIVED 01 April 2024
ACCEPTED 27 September 2024
PUBLISHED 14 October 2024

CITATION
Zheng J, Huang S-w, Ahmed MI, Pat B, Lloyd SG, Sharifov OF, Denney TS Jr and Dell'Italia LJ (2024) Imminent risk of LVEF decline in asymptomatic patients with primary mitral regurgitation.
Front. Cardiovasc. Med. 11:1410859.
doi: 10.3389/fcvm.2024.1410859

Imminent risk of LVEF decline in asymptomatic patients with primary mitral regurgitation

Jingyi Zheng[1], Shao-wei Huang[1], Mustafa I. Ahmed[2], Betty Pat[2,3], Steven G. Lloyd[2,3], Oleg F. Sharifov[2], Thomas S. Denney Jr[4] and Louis J. Dell'Italia[2,3]*

[1]Department of Mathematics and Statistics, Auburn University, Auburn, AL, United States, [2]Division of Cardiovascular Disease, University of Alabama at Birmingham, Birmingham, AL, United States, [3]Research & Development Service, Birmingham Veterans Affairs Health Care System, Birmingham, AL, United States, [4]Department of Electrical and Computer Engineering, Samuel Ginn College of Engineering, Auburn University, Auburn, AL, United States

Background: 2020 American College of Cardiology/American Heart Association (ACC/AHA) Guidelines state that the ideal time for mitral valve surgery in primary mitral regurgitation (PMR) is when the LV approaches but has not yet reached echocardiographic LV ejection fraction (EF) < 60% or LV end-systolic dimension (ESD) > 40 mm. However, it is difficult to know the imminent risk of crossing this threshold when the surgical outcome is less optimal.
Objective: Using machine learning and statistical models, we have shown that cardiac magnetic resonance (CMR) LV sphericity index (SI) and LV mid circumferential strain rate (SR_{circ}) added to LVEF and LVESD predict LVEF < 50% after mitral valve surgery. Here we test the hypothesis that these CMR features predict LVEF < 60% in asymptomatic PMR patients at 18 months.
Methods: 33 asymptomatic PMR patients with moderate to severe mitral regurgitation had CMR with tissue tagging at baseline and every 6 months for 18 months. Two types of models were employed to predict LVEF < 60% at 18 months: a model using CMR features at a single time point (e.g., baseline) and a model utilizing repeated measurements over time.
Results: CMR LVEF decreased below 60% in 13 patients over 18 months. LVEF varied over time with an inverse relation to mean arterial pressure and mean end-systolic wall stress. Random Forest models utilizing LV SI, LV mid SR_{circ}, LVESD, and LVEF at a single time point (baseline) had a predictive accuracy of 64%. LV SI, LV mid SR_{circ}, LVESD and LVEF at baseline, 6, and 12 months achieved a higher predictive accuracy of 79%, improved sensitivity from 57% to 85% than baseline alone and identified a threshold of CMR LVEF 63%–64% signaling LVEF < 60%.
Conclusion: The variability of LVEF due to blood pressure dependence may require a longitudinal study that incorporates LVEF, LVESD, SR_{circ} at multiple time points to identify the threshold at which LVEF is at risk for decline to less than 60%.

KEYWORDS

machine learning, predictive longitudinal modeling, asymptomatic primary mitral regurgitation, cardiac MRI, LVEF decline, LV circumferential strain rate

10.3389/fcvm.2024.1410859

Introduction

It is well recognized that outcomes remain suboptimal in primary mitral regurgitation (PMR) patients (1). Despite guidelines recommending earlier surgical intervention there is a wide disparity in adoption across centers (2). Furthermore parameters for intervention remain crude; for example, guidelines recommend the 60% left ventricular ejection fraction (LVEF) cutoff, in an era where more refined measures of function and geometry are becoming increasingly available. It is imperative to refine models for earlier intervention given the fact that despite pre-operative LVEF > 60%, approximately 20% of PMR patients develop post-operative LV dysfunction and long term outcomes are poor (3–5). In the evaluation of asymptomatic PMR patients with LVEF > 60%, it is difficult to know the ***imminent risk*** of LVEF < 60% in the ensuing 6-18 months.

According to 2020 ACC/AHA Guidelines the ideal time for mitral valve surgery is when the LV approaches but has not yet reached echocardiographic LVEF < 60% or LV end-systolic dimension (ESD) > 40 mm. The uncertainty of this threshold has fueled early surgical intervention for asymptomatic PMR patients (2). As a result of these uncertain guidelines, over 75% of 37,000 PMR patients from 2011 to 2016 present with symptoms or LV dysfunction and only 10% are asymptomatic (6), with the additional caveat that preoperative LVEF < 60% is associated with late mortality (7).

In PMR, LV dimensions and geometry-based volumes belie true LV and left atrial (LA) volumes and LV spherical remodeling obtained with geometry independent cardiac magnetic resonance (CMR) imaging (8, 9). The assessment of PMR is further confounded by a spuriously elevated LVEF due to increased adrenergic drive (10) and ejection into a low-pressure LA. We have shown that even in patients with LVEF > 60%, there is severe cardiomyocyte mitochondrial and cytoskeletal damage, excessive oxidative stress, and interstitial collagen loss, resulting in a decrease in the LV mass/volume ratio and a spherically remodeled LV (11–13).

We recently reported that machine learning models using LVEF, mid LV circumferential strain rate (SR_{circ}), LV end-systolic dimension (LVESD), and LV sphericity (SI) predict LVEF < 50% after mitral valve surgery (14). When applying these markers to asymptomatic PMR LVEF > 60% with moderate to severe PMR, 30% of patients were predicted to have post-surgery LVEF < 50% if they had mitral valve surgery (14). The advantages of machine learning models are their ability to integrate predictors extracted from multiple sources and model both linear and nonlinear interactions amongst them (15). The purpose of this study is to identify LV functional and geometric markers that herald a decrease in LVEF < 60% in asymptomatic PMR patients with moderate to severe PMR over 18 months with CMR exams every six months. Using both statistical and machine learning models, we will explore two types of models that employ CMR LVEF, mid LV mid SR_{circ}, LVESD, and LV SI features at a single time point (e.g., baseline) and a model utilizing repeated measurements over time.

Materials and methods

Study population

This single-center study includes 33 asymptomatic PMR patients recruited between 2006 and 2010 under NHLBI Specialized Centers of Clinically Oriented Research grant (16). Primary degenerative mitral valve prolapse has echocardiographic evidence of thickened, redundant leaflets with excessive motion and prolapse. Patients were excluded for evidence of: (1) aortic valve > trace aortic regurgitation or mean gradient of > 10 mmHg, (2) mitral stenosis (mean gradient > 5 mmHg, valve area < 1.5 cm2), (3) endocarditis, (4) iatrogenic MR (ergot, radiation induced), (5) hemodialysis, (6) pregnancy, (7) presence of coronary artery disease (stenosis > 50%), (8) positive exercise tolerance test with myocardial perfusion. None of the patients were surgical candidates upon entering this study. All patients were asymptomatic and had no history or evidence of coronary artery disease, ruled out by a maximum exercise tolerance test with nuclear imaging. The Institutional Review Boards of the University of Alabama at Birmingham and Auburn University approved the study protocol. All participants gave written informed consent.

All data from patients' baseline and return visits were obtained prospectively and recorded in electronic health data records. Asymptomatic PMR patients had Class I status, with moderate/severe PMR by color flow Echo/Doppler, LVEF > 60%, LVESD < 40 mm, leaflet thickening and prolapse, and normal maximal exercise myocardial perfusion imaging (16).

Cardiac magnetic resonance imaging

Magnetic resonance imaging was performed on a 1.5-T MRI scanner (Signa GE, Milwaukee, Wisconsin) optimized for cardiac application. Electrocardiographically gated breath-hold steady-state free precision technique was used to obtain standard (2-, 3-, and 4-chamber short-axis) views using the following parameters: slice thickness of the imaging planes 8 mm, field of view 44 44, scan matrix 256 128, flip angle 45°, repetition/echo times 3.8/1.6 ms. Three-dimensional LV geometric parameters were measured from endocardial and epicardial contours manually traced on cine-MR images acquired near end diastole and end systole. The contours were traced to exclude the papillary muscles. Cubic B-spline surfaces were fit to the endocardial and epicardial contours for each time frame (8–13). The severity of mitral regurgitation (regurgitant volume and regurgitant fraction) was obtained by: Regurgitant volume = LV – RV stroke volume and Regurgitant fraction = LV – RV stroke volume/LV stroke volume.

Tagged magnetic resonance images were acquired with repetition/echo times 8/44 ms, and tag spacing 7 mm (10, 11). Three-dimensional LV strain was measured from tagged images at end systole, which was defined by visual inspection of the image data as the time frame with maximum contraction. Strain computations were conducted using an in-house software

package. Two-dimensional strain rates were measured using harmonic phase analysis. Harmonic phase analysis measures the local, 2-dimensional strain of the myocardium based on the local spatial frequency of the tag lines. During myocardial contraction, the tag lines become closer to each other and the tag frequency increases in proportion to that contraction. Strain rates were computed at mid LV segment as defined by Cerqueira et al. (17)

Calculations

Three-dimensional wall thickness was computed at the same segments by measuring the distance from a point on the endocardial surface to the closest point on the endocardial surface along a line perpendicular to the epicardial surface. The radius to wall thickness ratio was computed as the reciprocal of the product of the endocardial circumferential curvature (κ) and wall thickness (T). End-systolic wall stress was computed according to the formula (10):

$$\text{Wall stress} = 0.133\frac{P}{2kT\left(1+\frac{\kappa T}{2}\right)}$$

where P is mean arterial LV blood pressure measured by a cuff measurement at the time of the MR scan. Mean arterial pressure was calculated as: MAP = DP + 1/3(SP – DP) or MAP = DP + 1/3(PP) [systolic blood pressure 2(diastolic pressure)]/3.

Model development in asymptomatic PMR

The objective of this preliminary study is to develop models for predicting LVEF < 60% in the subsequent (6 month) CMR examination. Due to the limited number of patients, the study employed four features selected from our previous study (14): LVEF, LVESD, LV SI, and mid LV SR_{circ} measured at four time points: baseline, 6, 12, and 18 months. Predictive models were constructed to investigate the following questions: (1) Compared with the model using CMR at a single time point, does the inclusion of features recorded at multiple time points improve the prediction of LVEF < 60%? and (2) What is the optimal number of time points required for accurate prediction in this context?

The final goal of this preliminary study is to develop a predictive model for predicting LVEF < 60% in the subsequent (6 month) CMR examination. Statistical models that model repeated measurements (e.g., mixed-effect model, marginal model) require at least three time points. Thus, we utilized machine learning models to investigate the two questions. After finalizing how many time points to be included in the predictive model, both statistical and machine learning model were fitted for predicting LVEF < 60% at 18 months.

Random Forest for repeated measures

Since Random Forest (RF) showed superior performance in our previous study (14), we utilized RF to construct three predictive models to investigate the inclusion of features measured at multiple time points. RF is a nonparametric and tree-based approach that operates without assuming a specific distribution of the data. It effectively models complex relationships between variables without assuming a specific function form and is less prone to overfitting especially when dealing with high-dimensional data (18). Three RF models were used to predict whether LVEF is less than 60% at 18 month using CMR features from a) baseline only, b) baseline + 6 months, and c) baseline + 6 month + 12 month. For each model, we performed feature selection and hyperparameter tuning, and assessed the model performance via repeated cross-validation. The metrics used for model assessment include accuracy, sensitivity, specificity, and Area under the ROC curve (AUC) values.

$$Accuracy = \frac{TP+TN}{TP+TN+FP+FN}$$

$$Sensitivity = \frac{TP}{TP+FN}$$

$$Specificity = \frac{TN}{TN+FP}$$

Where *TP, TN, FP*, and *FN* are short for true positive, true negative, false positive, and false negative.

In addition to assessing the performance of the predictive models, the SHapley Additive exPlanations (SHAP) (14, 19) value was used to investigate the importance of each feature and the directional impact of each feature on predicting the drop in LVEF (i.e., a positive or negative impact on LVEF < 60% at 18 months).

Statistical models

With the four CMR parameters (LVEF, LVESD, LV SI, and mid LV SR_{circ}) obtained at baseline, 6 month, and 12 month, we also fitted the Generalized Linear Mixed-effect Model (GLMM) (20) and the Generalized Estimating Equations (GEE) (21) model, which is the marginal model, for the prediction and inference at the patient and population level, respectively. Different from RF models, the response variable in the GLMM and GEE is a length 3 vector, with each element indicating whether LVEF > 60% (coded as 0) or < 60% (coded as 1) at 6, 12, and 18 months and the predictors are the four CMR parameters recorded at baseline, 6, and 12 months.

With GLMM, the effect of the longitudinal features on individual patients is assessed (i.e., subject-level inference). To account for repeated measures within each patient, the GLMM is fitted with a random intercept. The model incorporates follow-up time as a discrete variable and interactions between the features and time to estimate the rate of progression for each feature. The

determination of significant predictors and interactions are based on likelihood ratio tests, comparing the coefficient of a predictor being zero vs. non-zero.

The GEE is fitted with a similar model structure and the correlation structure being autoregressive lag 1. Different from GLMM, GEE enables group-level inference, investigating the fixed effects of the longitudinal CMR parameters on a broader population of asymptomatic PMR patients. Due to the scale differences among the four parameters, each parameter was standardized. GLMM and GEE models are assessed by the marginal R squared, which describes the proportion of variance explained by the fixed effects, and conditional R squared, which describes the proportion of variance explained by both the fixed and random effects. GLMM is not applicable to cross validation. Thus, only GEE performance was assessed via repeated cross validation and compared with the RF model. The final model was retrained using all the data, allowing for a comprehensive understanding of the model's coefficients.

Statistical methods

Data in Table 1 are presented as number/total (%) in group or median with 25% and 75% interquartile range in parentheses.

Results

Demographics and cardiac magnetic resonance imaging data

Demographics, CMR-derived LV and LA volumes, and LV strains in 33 asymptomatic PMR patients are listed in Table 1.

TABLE 1 Demographics and CMR in asymptomatic PMR patients at baseline.

	PMR (n = 33)
Age (years)	53 (45, 62)
Female/male	16 (52%)/15 (48%)
BMI (kg/m^2)	25.5 (22.0, 27.1)
BSA (m^2)	1.83 (1.68, 2.06)
LVEF (%)	61.9 (59.0, 67.0)
LVED volume (ml/m^2)	176.8 (145.6, 204.3)
LVES volume (ml/m^2)	63.5 (51.5, 78)
LV stroke volume (ml/m^2)	110.5 (85.8, 129)
LVED diameter (mm)	54 (51.5, 58.5)
LVES diameter (mm)	40.8 (36, 44.7)
LVED mass/volume (g/ml)	0.6 (0.5, 0.7)
LV sphericity index (SI)	1.6 (1.5, 1.7)
LVED radius/wall thickness	4.7 (4.2, 5.4)
LA max volume(ml/m^2)	42.3 (35.6, 55.9)
LA min volume (ml/m^2)	20.3 (15.4, 26.9)
Regurgitant volume (ml)	38.6 (26.3, 56.5)
Regurgitant fraction (%)	38.6 (28.7, 51.1)
LV Syst. Circ. strain rate (1/ms)	−0.0007 (−0.0007, −0.0006)
LVES circumferential strain	−0.14 (−0.15, −0.13)
LVES longitudinal strain	−0.14 (−0.16, −0.12)
LVES maximal strain	−0.20 (−0.21, −0.19)

Importance of mid LV in PMR

The mid LV is an important point of spherical transition as LV diameter increases to a greater extent than LV length decreasing sphericity index and wall thickness/radius producing an increase in LV wall stress. LV biopsies taken at mid LV from our previous studies (10–12) demonstrate this point in our PMR patients, showing a decrease in LV SI and LV wall thickness (Figure 1A) along with a decrease in mid LV endocardial curvature (Figure 1B). The green arrow in Figure 1A at the location of our myocardial biopsies is coincident with myofibril lysis, sarcomere breakdown, and disorganized mitochondria with cristae lysis (Figure 1C). LVEDD and LVESD (Figure 1D) is the sum of 32 radially directed vectors at mid LV that is close to measurement of mid LV SR_{circ}. It is important to note that the location of the myocardial biopsies from our previous studies of PMR patients is in the same location of the CMR derived LVEDD and LVESD (10–12).

Asymptomatic PMR 18 month time course

The 18-month outcome of 33 PMR patients with CMR baseline LVEF > 60% (n = 21) or baseline LVEF < 60% (n = 12) is presented in Figure 2. Of 21 patients with baseline LVEF > 60%, 6 patients had LVEF < 60% and 15 had LVEF > 60% at 18 months. Of 12 patients with baseline LVEF < 60%, 5 patients had an increase in LVEF > 60% at 18 months and 7 patients were asymptomatic with LVEF < 60% at 18 months. Of the 33 PMR patients, 13 had CMR LVEF < 60% by 18 months despite all presenting with a median baseline CMR-derived LVEF > 60% (Table 1) and Echo-derived LVEF >60%.

There is a wide variability of LVEF, LVESD, and mid LV SR_{circ} at each time point over the 18-month period (Figure 3). These indices of LV shortening are load dependent as demonstrated by the inverse relation of LVEF to mean arterial pressure at the time of imaging and a calculated LV end-systolic wall stress (Figure 4). This demonstrates the inherent physiological variability of LVEF to a changing afterload, militating for repeated measures at the four time points.

Random Forest models single vs. repeated measures

All patients had four scans (baseline, 6 month, 12 month, and 18 month). To predict the LVEF decline at 18 months, we considered using CMR features measured at baseline only (type 1 model) compared to repeated CMR features measured at two or three time points (type 2 model). In the type 2 model, we considered using baseline + 6 month CMR features and baseline + 6 month + 12 month CMR features respectively. The purpose

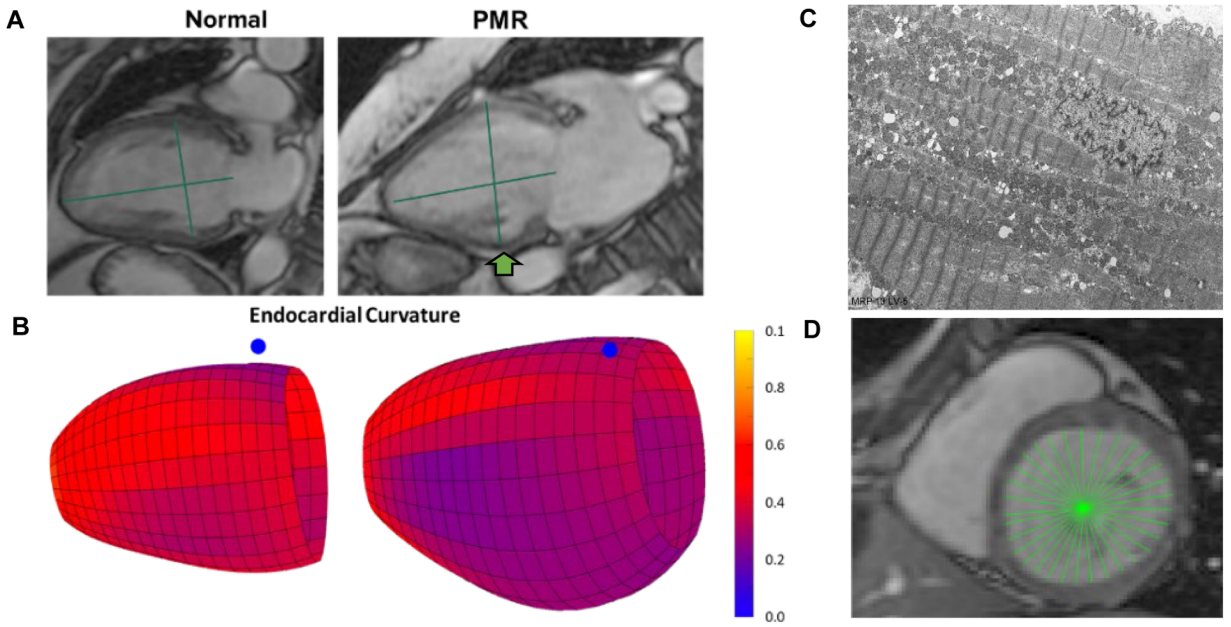

FIGURE 1
Importance of mid LV remodeling in PMR. **(A)** CMR images of a normal subject and PMR patient demonstrate LV wall thinning and decrease in sphericity index (green lines length/width). **(B)** Color-coded LV maps demonstrating decrease in endocardial curvature (**bluer**) at mid LV (blue dot marks interventricular septum). **(C)** TEM of endomyocardial biopsies from mid LV lateral wall (**green arrow in A**) depicting extensive myofibrillar lysis, and breakdown of sarcomere structure with disorganized and damaged mitochondria. **(D)** CMR LVESD measurement as the sum of 32 radially directed vectors measured at the tips of the papillary muscles in the mid LV near measurement of mid LV circumferential strain rate.

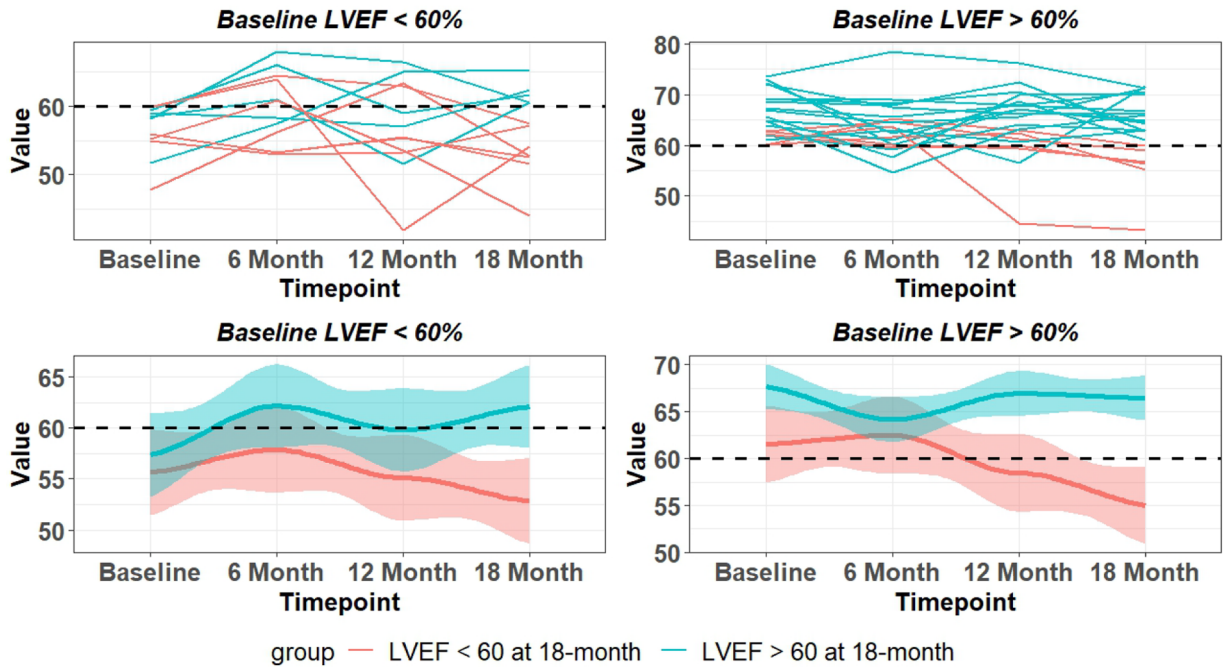

FIGURE 2
LVEF changes over 18 months in asymptomatic patients with moderate to severe PMR with baseline CMR LVEF < 60% and LVEF > 60%. Top panel are individual patients and bottom panel indicates mean and 95% CI (shaded area). Blue lines – LVEF remains > 60% at 18 months. Red lines LVEF < 60% at 18 months.

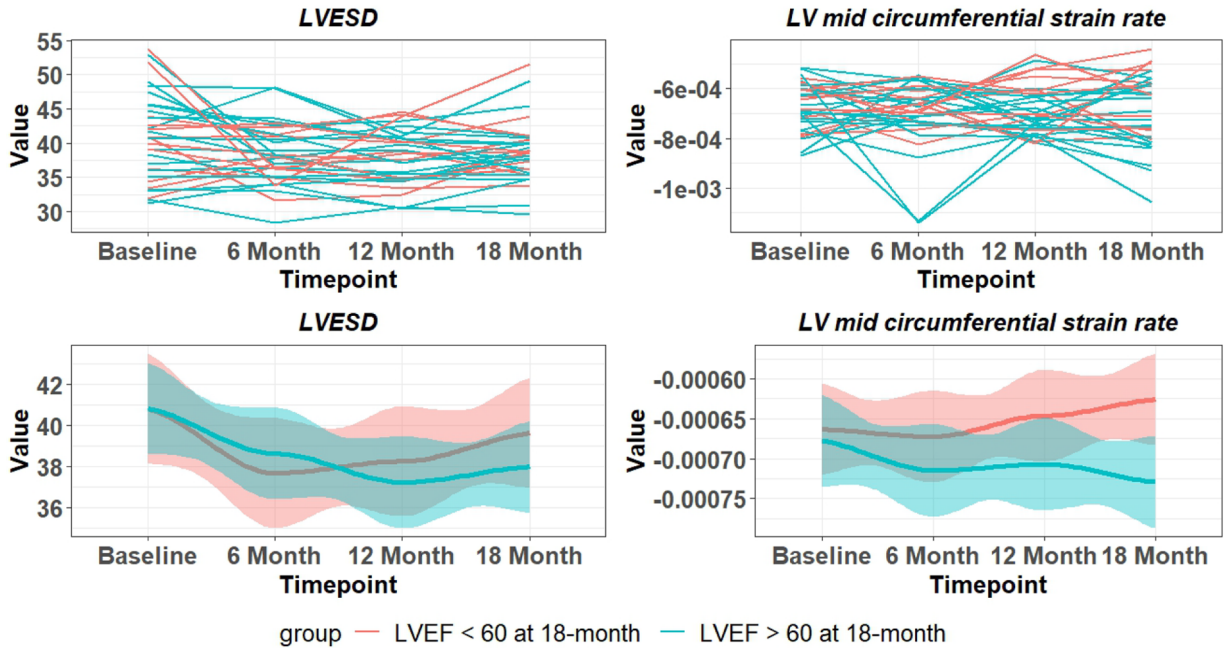

FIGURE 3
Variability of LVESD and mid LV SR_{circ} over 18 months in PMR patients. Top panel are individual patients and bottom panel indicates mean and 95% CI (shaded area). Blue lines – LVEF remains > 60% at 18 months. Red lines LVEF < 60% at 18 months.

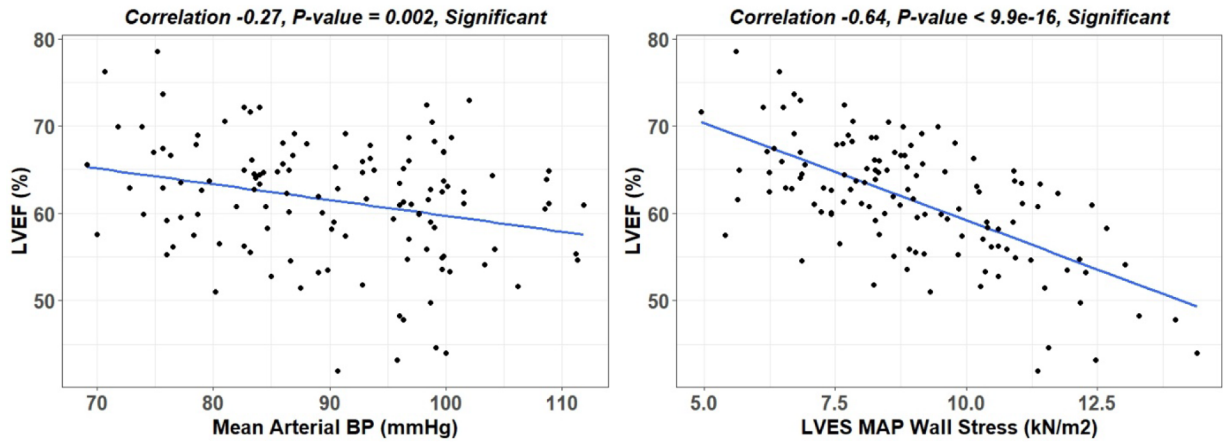

FIGURE 4
Linear regression of LVEF to mean arterial pressure (MAP) and LVES MAP wall stress. LV end-systolic wall stress provides a more accurate means of defining afterload than MAP, which considers wall thickness and diameter thereby allowing for comparison of different hearts.

of constructing these two types of models is to address two questions: (1) if including repeated CMR measurements can improve the prediction of the decline in LVEF at 18 months, compared with a model only using baseline measurements; (2) how many repeated measurements are needed to best predict LVEF decline at 18 months, or in other words, is it necessary to have a CMR scan every six months.

Random Forest models were constructed to predict LVEF < 60% at 18 months. The first model incorporated the four CMR features (LVEF, LVESD, LV SI, and mid LV SR_{circ}) identified from our previous study (14) at a single time point (i.e., baseline). The second model integrated the four features measured at two consecutive time points—baseline and 6 months. The third model encompassed the four features measured at baseline, 6, and 12 months. The RF model utilizing the four features at baseline achieved a low prediction accuracy of 64% and sensitivity of 57%, which slightly improved with the second model (72% and 63% respectively) (Table 2).

TABLE 2 Random Forest model performance in predicting LVEF < 60% at 18 months comparing single vs. repeated measures over time.

Model Performance	Single	Repeated measures	
	Baseline	Baseline + 6 month	Baseline + 6 month + 12 month
Accuracy	0.64	0.72	0.79
Sensitivity	0.57	0.63	0.85
Specificity	0.69	0.79	0.75
AUC	0.75	0.80	0.88

Incorporating the four features (measured at baseline, 6, and 12 months) in the third model achieved highest prediction accuracy (79%) and sensitivity (85%) (Table 2).

Random Forest vs. statistical models for the prediction of LVEF < 60% at 18 months

Random Forest model was compared to GLMM and GEE statistical models for prediction of LVEF < 60% at 18 months using the same four features measured at baseline, 6, and 12 months. The coefficients of GEE and GLMM are summarized in Table 3. GEE is a marginal model that focuses on estimating the population level effects; while GLMM is the conditional model that focuses on estimating subject-specific effects. For GLMM, the marginal R squared is 0.673 and the conditional R squared is 0.673, and the variance of the subject effect is close to zero. This implies that fixed effects rather than random effects largely explain the drop in LVEF. The GEE marginal R square and conditional R square are 0.736, implying that the GEE population-averaged correlation structure fits the data better and explains more variation in the data providing a better final statistical model for the prediction of LVEF < 60%. A comparison between GEE and RF model performance (using repeated measures of the four features at baseline, 6 months and 12 months) shows that the RF model has a higher prediction accuracy and sensitivity (Table 4).

Random Forest captures the non-linear relationship between features and the response variables, and further identifies important features that have a strong impact on the LVEF < 60% in a non-linear way. The GEE model assumes a linear relationship between the features and log odds, while RF captures the interactions and combinations among features. Thus, the GEE linear model may not capture such complex relationships; while the data-driven RF model relies heavily on the patterns and information present in the provided data.

Feature importance in the repeated measures Random Forest model

The RF model computes the importance of each variable using the four CMR features repeatedly measured at baseline, 6, and 12 months (4 features × 3 time points = 12 features) to predict LVEF < 60% at 18 months (Figure 5). The Random Forest model performance used 4 features measured at 3 time points. The RF model utilizing the top 3 features: 12 month LVEF, baseline LVEF, and 12 month mid LV SR_{circ} gave the best model performance in predicting 18 month LVEF < 60% with 79% accuracy and 85% sensitivity (Table 5).

TABLE 3 Coefficients of GEE and GLM using repeated measures.

Coefficients	GEE	GLM
	Estimate (SE)	Estimate (SE)
Month 6	1.309 (1.09)	1.466 (1.09)
Month 12	1.364 (1.116)	1.548 (1.107)
LVEF	−2.202*** 0.753)	−1.999** 0.894)
LVESD	1.633*** (0.552)	1.518** (0.750)
Sphericity index (SI)	0.103 (0.395)	0.440 (0.678)
LV SR_{circ}	−1.502* (0.826)	−1.547* (0.913)
Month 6 × LVEF	0.477 (0.912)	1.022 (1.100)
Month 12 × LVEF	−0.637 (1.52)	0.085 (1.177)
Month 6 × LVESD	−1.538** (0.628)	−1.193 (0.957)
Month 12 × LVESD	−1.858* (0.948)	−1.758* (0.971)
Month 6 × LV SI	−0.771 (0.814)	−1.073 (0.890)
Month 12 × LV SI	0.393 (0.716)	−0.068 (0.787)
Month 6 × LV SR_{circ}	2.037* (1.083)	2.608** (1.110)
Month 12 × LV SR_{circ}	2.629** (1.137)	2.508** (1.112)

*$p < 0.1$
**$p < 0.05$
**$p < 0.01$.

TABLE 4 Comparison of model performance in predicting LVEF < 60% at 18 months using repeated measures (baseline, 6 months, 12 months).

	GEE	Random Forest
Accuracy	0.65	0.79
Sensitivity	0.50	0.85
Specificity	0.76	0.75
AUC	0.78	0.88

Interpretation of Random Forest models

The Shapley Additive exPlanations (SHAP) value (19), inspired by the Shapley value in cooperative game theory, assigns an importance value to each feature in machine learning models to explain the decision made by the model. The SHAP value constructed an overall interpretation of the RF model with the three most important features (12 month LVEF, baseline LVEF, and 12 month mid LV SR_{circ}) and its directional impact on prediction (a positive or negative impact on probability of LVEF < 60% at 18 months), and how each feature contributes to a prediction in each patient.

The SHAP value calculated for each patient for the top three features (y-axis) is presented in Figure 6. SHAP values quantify the contribution of each feature to model prediction on the x-axis. The sign of the SHAP value represents the directed impact on probability of LVEF < 60% at 18 months. A positive SHAP indicates high probability while a negative value indicates low

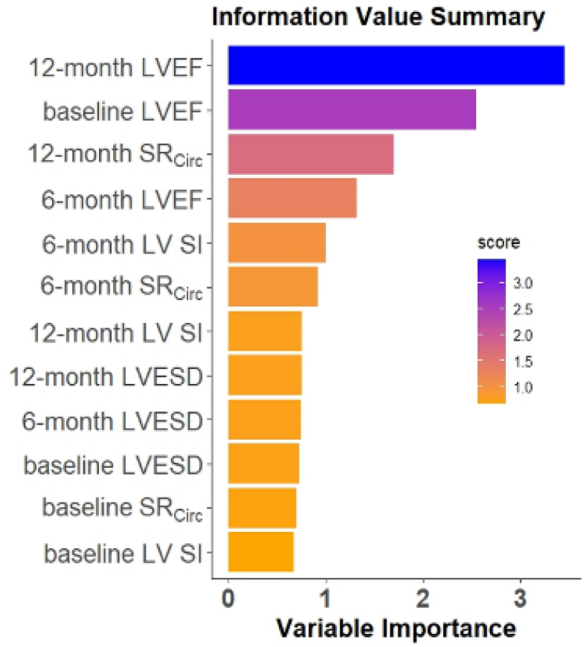

FIGURE 5
Ranking of feature importance in the repeated measures RF model. The RF model computes the importance of each variable using the four CMR features at baseline, 6, and 12 months (4 features×3 time points) to predict the LVEF < 60% at 18 months.

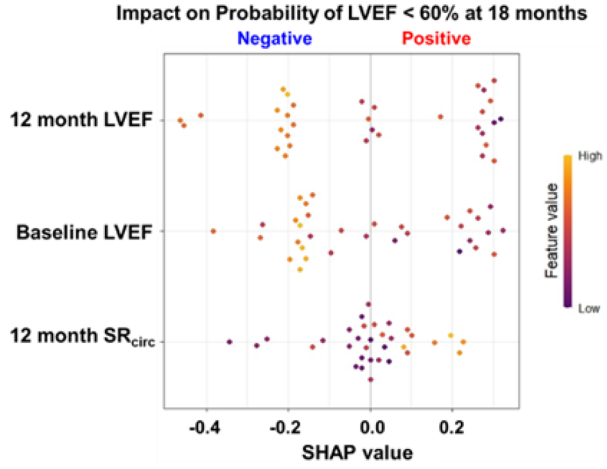

FIGURE 6
SHAP value for probability for LVEF < 60% at 18 months for the top 3 features in the RF model for asymptomatic PMR. SHAP values quantify the contribution of each feature to model prediction on the *x*-axis. The sign (+/-) of the SHAP value represents the directed impact on probability of LVEF < 60% at 18 months. A positive SHAP indicates high probability while a negative value indicates low probability for LVEF < 60% at 18 months. The magnitude of the SHAP value on the *x*-axis represents the strength of the contribution. Each dot represents an individual patient (n = 33), and the color of the dot represents the feature value (color scale), high (orange) and low (purple).

TABLE 5 RF model performance based on 3–12 features in predicting LVEF < 60% at 18 months.

Prediction of LVEF < 60% at 18 months				
Model performance	Total number of features in RF Model			
	3	4	5	12
Accuracy	0.794	0.791	0.766	0.668
Sensitivity	0.850	0.823	0.770	0.565
Specificity	0.753	0.768	0.763	0.746
AUC	0.883	0.886	0.846	0.774

The RF model utilizing the top 3 most important features (Figure 5) has the best model performance.

probability for LVEF < 60% at 18 months. The magnitude of the SHAP value on the *x*-axis represents the strength of the contribution. Each dot represents an individual patient, and the color of the dot represents the feature value, high (orange) and low (purple). For baseline and 12 month LVEF, the orange-yellow dots (high LVEF) are located on the left side of the 0 SHAP (i.e., negative SHAP), indicating less probability of LVEF < 60% at 18 months. For 12 month mid LV SR_{circ}, the high value (orange-yellow dots) are located on the right side of the 0 (positive SHAP), therefore, a higher 12 month mid LV SR_{circ} (i.e., less negative), the higher chance of developing LVEF < 60% at 18 months.

To better visualize the top three features (12 month LVEF, baseline LVEF, and 12 month mid LV SR_{circ}), the actual value of each feature on the *x* axis and the likelihood of developing LVEF < 60% (red dot) or LVEF > 60% (blue dot) at 18 months is presented in Figure 7. Our data indicates that a higher absolute baseline CMR derived LVEF (> 63%), the less likely for LVEF < 60% at 18 months (negative SHAP values and mostly blue circles). Mid LV SR_{circ} is a negative quantity; thus, more negative values represent a greater LV SR_{circ} and therefore less likely to develop LVEF < 60% at 18 months.

Discussion

We have previously reported that a combination of statistical methods and machine learning models show that LV SR_{circ}, LVESD, LVEF, and LV sphericity index (SI) predict LVEF < 50% after surgery in patients with baseline LVEF > 60% (14). We utilized these same four features to predict the drop in LVEF < 60% over 18 months in 33 asymptomatic patients with moderate to severe PMR with CMR obtained every 6 months. Random Forest models at a single time point (baseline) had a predictive accuracy of 64%. Using repeated measures at baseline, 6, and 12 months achieved a higher predictive accuracy of 79%, improved sensitivity from 57% to 85%, and identified a threshold of CMR LVEF 63%–64% for LVEF < 60%. This pilot longitudinal study in PMR patients provides a stimulus for a longitudinal study that utilizes a more nuanced combination of LV functional parameters that will better inform the clinician of the need for surgery in PMR (including Echo/Doppler derived).

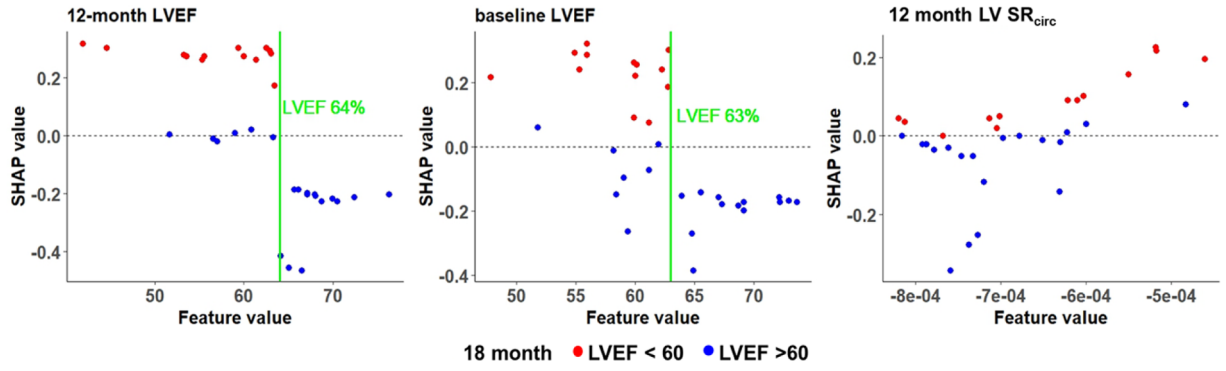

FIGURE 7
SHAP values for the top 3 features in the RF model for asymptomatic PMR. Manual cutoff values for LVEF (green vertical line) indicate the impact on the likelihood of LVEF < 60% at 18 months. Each dot is an individual patient and colored based on whether the patient has a negative SHAP value indicating lower probability of LVEF < 60% (blue dots) or a positive SHAP value indicating a higher probability of LVEF < 60% (red dots) at 18 months.

Many studies of PMR have identified predictors of survival or heart failure and death. They include extracellular volume (22–26), regurgitant volume (27), longitudinal strain (28, 29), BNP (30–32), exercise capacity (33), pulmonary artery pressure (34), LA volume (35, 36) and LA emptying fraction (37–39). These studies are largely retrospective, provide just one snapshot in time, and have not addressed the short-term risk for LVEF < 60% in a prospective "***watchful waiting approach***" (40) thus limiting clinical applicability. In the evaluation of asymptomatic PMR patients with LVEF > 60%, it is difficult to know the imminent danger for progression to LVEF < 60%, because surgery in patients with LVEF < 60% has a less favorable outcome. Given the unreliability of LVEF alone, we questioned whether our previous interactive predictors of LV remodeling (LV SI) and LV shortening (LVEF, LVESD, mid LV SR_{circ}) features can identify an impending LVEF < 60% in the asymptomatic PMR patient.

The interactive power of machine learning captures the LV spherical remodeling in PMR (8, 9) and its relation to mid LV SR_{circ} affected by the decrease in LV endocardial curvature and LV wall thickness that increases wall stress at the mid LV (Table 1). This is further compounded by severe myofibril lysis, sarcomere breakdown, and disorganized mitochondria with cristae lysis (Figure 1C) — all of which contribute to decreased mid LV SR_{circ}. In models that determine the effect of LV shape on LVEF, circumferential strain is significantly more important than longitudinal strain in maintaining a normal LVEF in the spherically dilated LV (41). The connection to mid LV SR_{circ} underscores the decrease in contractile velocity that stems not only from myofibril breakdown but also derangement of calcium-handling proteins despite LVEF > 55% in PMR patients (42–45). We have also demonstrated sarcolipin protein upregulation from LV endo-myocardial biopsies in PMR patients (10). Sarcolipin functions as a regulator of SERCA2a by lowering its Ca^{2+} affinity and its inhibitory function is independent of phospholamban (46), both of which control extent and rate of sarcomere shortening.

Based on the coefficients of GEE model in Table 3, there is a predictive variability of LVEF, LVESD, mid LV, SR_{circ} over time. For example, baseline LVEF and 12 month LVEF have a negative while 6 month LVEF has a positive impact. For LVESD, baseline coefficient is positive while 6 and 12 month coefficients are both negative. For mid LV SR_{circ}, the baseline coefficient is negative while 6 and 12 month coefficients are both positive. The variability in these indices of LV shortening could be due to the variable blood pressures at each imaging session and also to the small number of patients in this pilot study. This may also explain the higher predictability of three vs. one-time point for predicting LVEF < 60%. LVEF negatively correlated with mean arterial pressure and end-systolic wall stress (Figure 4), which more accurately estimates afterload by incorporating LV radius of curvature and wall thickness. In a stepwise discriminate multivariate analysis of PMR surgery patients, Carabello et al. reported LVES stress/ESV index ratio as the only independent predictor of outcome (47). Future longitudinal studies should include LVES stress/ESV index to normalize effects of afterload on LVEF and other indices of shortening (LVESD and LV mid SRcirc).

The SHAP value identified a CMR LVEF threshold of 63%-64% at baseline, 6 and 12 months. The SHAP value provides an overall interpretation of the machine learning models including a directional positive or negative impact on the probability of LVEF < 60% and a local interpretation at the patient level on how each feature contributes to an individual prediction for each patient. This provides cutoff values that in a larger sample size can comprise a risk score. The SHAP cutoff of 63%-64% is consistent with a study of 300 PMR patients with echo at baseline and within 9-12 months' post-surgery. The occurrence of post-operative LV dysfunction was 9% when LVEF was ≥ 64% and LVESD < 37 mm and 33% with LVEF < 64% and LVESD ≥ 37 mm (48). Taken together, these results militate for a higher LVEF threshold for mitral valve surgery in PMR.

Limitations

The obvious limitation of this study is the small number of patients. In this preliminary study, we utilized the classic RF model instead of the Mixed Effects Random Forest (MERF) to model the longitudinal features. Unfortunately, we do not have blood pressure at all time points. In future studies, adding the blood pressure or end-systolic wall stress may provide additive predictive value in normalizing effects of afterload on LVEF. Compared with the classic RF, MERF considers the correlation structure within repeated measurements by incorporating random effects providing accurate predictions for each patient. However, the computational and model complexity of MERF is higher than that of RF due to the inclusion of random effects, which requires more patients. In this preliminary study with the small sample size ($n = 33$) classic RF is preferred over MERF.

Conclusions

In this pilot study, we identify key LV shortening indices that are widely variable due to the prevailing blood pressures at the time of imaging, which may in part explain the need for more frequent observations. Future studies with a larger number of patients that include blood pressure and end systolic wall stress may improve the predictability of a single study. Taken together, the uncertainty of knowing when the LV approaches but has not yet reached LVEF < 60% calls for a longitudinal study in a larger patient population to test whether a combination of functional features derived from both CMR and Echo/Doppler provides a better indicator for timing of surgical intervention in PMR.

Data availability statement

The raw data supporting the conclusions of this article will be made available by the authors, without undue reservation.

Ethics statement

The studies involving humans were approved by University of Alabama at Birmingham and Auburn University IRB. The studies were conducted in accordance with the local legislation and institutional requirements. The participants provided their written informed consent to participate in this study.

Author contributions

JZ: Conceptualization, Data curation, Formal Analysis, Funding acquisition, Investigation, Methodology, Project administration, Resources, Software, Supervision, Validation, Visualization, Writing – original draft, Writing – review & editing. S-wH: Data curation, Formal Analysis, Investigation, Methodology, Software, Writing – original draft, Writing – review & editing. MA: Investigation, Writing – original draft, Writing – review & editing, Conceptualization, Supervision. BP: Conceptualization, Investigation, Supervision, Writing – original draft, Writing – review & editing, Data curation, Methodology, Project administration, Validation. SL: Data curation, Investigation, Methodology, Supervision, Validation, Writing – original draft, Writing – review & editing, Formal Analysis, Resources, Software, Visualization. OS: Data curation, Investigation, Methodology, Software, Writing – original draft, Writing – review & editing. TD: Data curation, Investigation, Methodology, Software, Writing – original draft, Writing – review & editing, Conceptualization, Formal Analysis, Funding acquisition, Resources, Supervision, Validation, Visualization. LD: Conceptualization, Data curation, Formal Analysis, Funding acquisition, Investigation, Methodology, Resources, Software, Supervision, Validation, Visualization, Writing – original draft, Writing – review & editing, Project administration.

Funding

The author(s) declare financial support was received for the research, authorship, and/or publication of this article. This work was supported by the National Heart, Lung, and Blood Institute and Specialized Centers of Clinically Oriented Research grant [P50HL077100 to L.J.D] in cardiac dysfunction; Department of Veteran Affairs for Merit Review grant [1CX000993-01 to L.J.D]; and National Institutes of Health Grant [P01 HL051952 to L.J.D]. VHA 2021 John Blair Barnwell Award [to LJD]; No relationships to industry.

Conflict of interest

The authors declare that the research was conducted in the absence of any commercial or financial relationships that could be construed as a potential conflict of interest.

Publisher's note

References

1. David TE, David CM, Tsang W, Lafreniere-Roula M, Manlhiot C. Long-term results of mitral valve repair for regurgitation due to leaflet prolapse. *J Am Coll Cardiol*. (2019) 74:1044–53. doi: 10.1016/j.jacc.2019.06.052

2. Otto CM, Nishimura RA, Bonow RO, Carabello BA, Erwin JP, Gentile F, et al. 2020 ACC/AHA guideline for the management of patients with valvular heart disease: executive summary: a report of the American College of Cardiology/American Heart Association joint committee on clinical practice guidelines. *J Am Coll Cardiol*. (2021) 77(4):450–500. doi: 10.1016/j.jacc.2020.11.035

3. Miller JD, Suri RM. Left ventricular dysfunction after degenerative mitral valve repair: a question of better molecular targets or better surgical timing? *J Thorac Cardiovasc Surg*. (2016) 152(4):1071–4. doi: 10.1016/j.jtcvs.2016.07.018

4. Enriquez-Sarano M, Suri RM, Clavel M, Mantovani F, Michelena HI, Pislaru S, et al. Is there an outcome penalty linked to guideline-based indications for valvular surgery? Early and long-term analysis of patients with organic mitral regurgitation. *J Thorac Cardiovasc Surg*. (2015) 150(1):50–8. doi: 10.1016/j.jtcvs.2015.04.009

5. Quintana E, Suri RM, Thalji NM, Daly RC, Dearani JA, Burkhart HM, et al. Left ventricular dysfunction after mitral valve repair-the fallacy of "normal" preoperative myocardial function. *J Thorac Cardiovasc Surg*. (2014) 148:2752–62. doi: 10.1016/j.jtcvs.2014.07.029

6. Gammie JS, Chikwe J, Badhwar V, Thibault DP, Vemulapalli S, Thourani VH, et al. Isolated mitral valve surgery: the society of thoracic surgeons adult cardiac surgery database analysis. *Ann Thorac Surg*. (2018) 106(3):716–27. doi: 10.1016/j.athoracsur.2018.03.086

7. Desai A, Thomas JD, Bonow RO, Kruse J, Andrei AC, Cox JL, et al. Asymptomatic degenerative mitral regurgitation repair: validating guidelines for early intervention. *J Thorac Cardiovasc Surg*. (2021) 161(3):981–994.e5. doi: 10.1016/j.jtcvs.2020.11.076

8. Schiros CG, Dell'Italia LJ, Gladden JD, Clark D 3rd, Aban I, Gupta H, et al. Magnetic resonance imaging with 3-dimensional analysis reveals important LV remodeling in isolated mitral regurgitation: implications beyond dimensions. *Circulation*. (2012) 125:2334–42. doi: 10.1161/CIRCULATIONAHA.111.073239

9. Schiros CG, Ahmed MI, Sanagala T, Zha W, McGiffin DC, Bamman MM, et al. Importance of three-dimensional geometric analysis in the assessment of the athlete's heart. *Am J Cardiol*. (2013) 111(7):1067–72. doi: 10.1016/j.amjcard.2012.12.027

10. Zheng J, Yancey D, Ahmed M, Chiros CG, Wei CC, Gladden JD, et al. Increased sarcolipin expression and adrenergic drive in patients with chronic isolated mitral regurgitation. *Circulation Heart Failure*. (2014) 7(1):194–202. doi: 10.1161/CIRCHEARTFAILURE.113.000519

11. Ahmed M, Gladden JD, Litovsky S, McGiffin D, Gupta H, Lloyd S, et al. Myofibrillar degeneration, oxidative stress and post-surgical systolic dysfunction in patients with isolated mitral regurgitation and pre surgical left ventricular ejection fraction >60%. *J Am Coll Cardiol*. (2009) 55:671–9. doi: 10.1016/j.jacc.2009.08.074

12. Ahmed MI, Guichard JL, Rajasekaran NS, Ahmad S, Mariappan N, Litovsky S, et al. Disruption of desmin-mitochondrial architecture in patients with regurgitant mitral valves and preserved ventricular function. *J Thorac Cardiovasc Surg*. (2016) 152(4):1059–70. With Accompanying Editorial. doi: 10.1016/j.jtcvs.2016.06.017

13. Ahmed MI, Andrikopoulou E, Zheng J, Ulasova E, Pat B, Kelley EE, et al. Interstitial collagen loss, myocardial remodeling, and function in primary mitral regurgitation. *JACC Basic Transl Sci*. (2022) 7(10):973–81. doi: 10.1016/j.jacbts.2022.04.014

14. Zheng J, Li Y, Billor N, Ahmed MI, Fang Y-HD, Pat B, et al. Understanding post-surgical decline in left ventricular function in primary mitral regurgitation using regression and machine learning models. *Front Cardiovasc Med*. (2023) 10:1112797. doi: 10.3389/fcvm.2023.1112797

15. Goldstein BA, Navar AM, Carter RE. Moving beyond regression techniques in cardiovascular risk prediction: applying machine learning to address analytic challenges. *Europ Heart J*. (2017) 38:1805–14. doi: 10.1093/eurheartj/ehw302

16. Ahmed MI, Aban I, Lloyd SG, Gupta H, Howard G, Inusah S, et al. A randomized controlled phase IIb trial of Beta-1 receptor blockade in isolated degenerative mitral regurgitation. *J Am Coll Cardiol*. (2012) 60:833–8. doi: 10.1016/j.jacc.2012.04.029

17. Cerqueira MD, Weissman NJ, Dilsizian V, Jacobs AK, Kaul S, Laskey WK, et al. Standardized myocardial segmentation and nomenclature for tomographic imaging of the heart: a statement for healthcare professionals from the cardiac imaging committee of the council on clinical cardiology of the American Heart Association. *Circulation*. (2002) 105:539–42. doi: 10.1161/hc0402.102975

18. Breiman L. Random forests. *Mach Learn Arch*. (2001) 45(1):5–32. doi: 10.1023/A:1010933404324

19. Lundberg SM, Lee S-I. *A unified approach to interpreting model predictions. Proceedings of the 31st International Conference on Neural Information Processing Systems (NIPS'17) Curran Associates Inc.*; Long Beach, CA, USA (2017). p. 4768–77

20. Jiang J, Nguyen T. *Linear and Generalized Linear Mixed Models and Their Applications. Vol. 1*. New York: Springer (2007).

21. Zeger SL, Liang K-Y, Albert PS. Models for longitudinal data: a generalized estimating equation approach. *Biometrics*. (1988) 44:1049–60. doi: 10.2307/2531734

22. Kitkungvan D, Yang EY, Tallawi KC, Nagueh SF, Nabi F, Khan MA, et al. Extracellular volume in primary mitral regurgitation. *JACC Cardiovasc Imaging*. (2021) 14(6):1146–60. doi: 10.1016/j.jcmg.2020.10.010

23. Constant Dit Beaufils AL, Huttin O, Jobbe-Duval A, Senage T, Filippetti L, Piriou N, et al. Replacement myocardial fibrosis in patients with mitral valve prolapse relation to mitral regurgitation, ventricular remodeling, and arrhythmia. *Circulation*. (2021) 143(18):1763–74. doi: 10.1161/CIRCULATIONAHA.120.050214

24. Kitkungvan D, Nabi F, Kim RJ, Khan MA, Xu J, Little SH, et al. Myocardial fibrosis in patients with primary mitral regurgitation with and without prolapse. *J Am Coll Cardiol*. (2018) 72(8):823–34. doi: 10.1016/j.jacc.2018.06.048

25. Liu B, Neil DAH, Premchand M, Bhabra M, Patel R, Barker T, et al. Myocardial fbrosis in asymptomatic and symptomatic chronic severe primary mitral regurgitation and relationship to tissue characterisation and left ventricular function on cardiovascular magnetic resonance. *J Cardiovasc Magn Reson*. (2020) 22(1):86. doi: 10.1186/s12968-020-00674-4

26. Kitkungvan D, Yang EY, El Tallawi KC, Nagueh SF, Nabi F, Khan MA, et al. Prognostic implications of diffuse interstitial fibrosis in asymptomatic primary mitral regurgitation. *Circulation*. (2019) 140(25):2122–4. doi: 10.1161/CIRCULATIONAHA.119.043250

27. Myerson SG, d'Arcy J, Christiansen JP, Mohiaddin R, Francis JM, Prendergast B, et al. Determination of clinical outcome in mitral regurgitation with cardiovascular magnetic resonance quantification. *Circulation*. (2016) 133(23):2287–96. doi: 10.1161/CIRCULATIONAHA.115.017888

28. Kislitsina ON, Thomas JD, Crawford E, Michel E, Kruse J, Liu M, et al. Predictors of left ventricular dysfunction after surgery for degenerative mitral regurgitation. *Ann Thorac Surg*. (2020) 109(3):669–77. doi: 10.1016/j.athoracsur.2019.10.044

29. Alashi A, Mentias A, Patel K, Gillinov AM, Sabik JF, Popović ZB, et al. Synergistic utility of BNP and left ventricular global longitudinal strain in asymptomatic patients with significant primary mitral regurgitation and preserved systolic function undergoing mitral valve surgery. *Circ Cardiovasc Imaging*. (2016) 5(1):e002561. doi: 10.1161/CIRCIMAGING.115.004451

30. Detaint D, Messika-Zeitoun D, Chen HH, Scott C, Chen H, Burnett JC Jr, et al. B-type natriuretic peptide in organic mitral regurgitation: determinants and impact on outcome. *Circulation*. (2005) 111:2391–7. doi: 10.1161/01.CIR.0000164269.80908.9D

31. Magne J, Mahjoub H, Pibarot P, Pirlet C, Pierard LA, Lancellotti P. Prognostic importance of brain natriuretic peptide and left ventricular longitudinal function in asymptomatic degenerative mitral regurgitation. *Heart*. (2012) 98:584–91. doi: 10.1136/heartjnl-2011-301128

32. Pizarro R, Bazzino OO, Oberti PF, Falconi ML, Arias AM, Krauss JG, et al. Prospective validation of the prognostic usefulness of brain natriuretic peptide in asymptomatic patients with chronic severe mitral regurgitation. *J Am Coll Cardiol*. (2009) 54:1099–106. doi: 10.1016/j.jacc.2009.06.013

33. Naji P, Griffin BP, Barr T, Asfahan F, Gillinov AM, Grimm RA, et al. Importance of exercise capacity in predicting outcomes and determining optimal timing of surgery in significant primary mitral regurgitation. *J Am Heart Assoc*. (2014) 3(5):e001010. doi: 10.1161/JAHA.114.001010

34. Mentias A, Patel K, Patel H, Gillinov AM, Sabik JF, Mihaljevic T, et al. Effect of pulmonary vascular pressures on long-term outcome in patients with primary mitral regurgitation. *J Am Coll Cardiol*. (2016) 67(25):2952–61. doi: 10.1016/j.jacc.2016.03.589

35. Le Tourneau T, Messika-Zeitoun D, Russo A, Detaint D, Topilsky Y, Mahoney DW, et al. Impact of left atrial volume on clinical outcome in organic mitral regurgitation. *J Am Coll Cardiol*. (2010) 56(7):570–8. doi: 10.1016/j.jacc.2010.02.059

36. Rusinaru D, Tribouilloy C, Grigioni F, Avierinos JF, Suri RM, Barbieri A, et al. Mitral regurgitation international DAtabase (MIDA) investigators. Left atrial size is a potent predictor of mortality in mitral regurgitation due to flail leaflets: results from a large international multicenter study. *Circ Cardiovasc Imaging*. (2011) 4(5):473–81. doi: 10.1161/CIRCIMAGING.110.961011

37. Cameli M, Pastore MC, Righini FM, Mandoli GE, D'Ascenzi F, Lisi M, et al. Prognostic value of left atrial strain in patients with moderate asymptomatic mitral regurgitation. *Int J Cardiovasc Imaging*. (2019) 35(9):1597–604. doi: 10.1007/s10554-019-01598-6

38. Yang LT, Tsai WC, Luo CY, Li YH, Tsai LM. Role of left atrial reservoir strain rate in left atrial remodeling in severe mitral regurgitation. *J Med Ultrasound*. (2017) 25(1):16–23. doi: 10.1016/j.jmu.2016.09.003

39. Ring L, Rana BS, Wells FC, Kydd AC, Dutka DP. Atrial function as a guide to timing of intervention in mitral valve prolapse with mitral regurgitation. *JACC Cardiovasc Imaging*. (2014) 7(3):225–32. doi: 10.1016/j.jcmg.2013.12.009

40. Goldstone AB, Patrick WL, Cohen JE, Aribeana CN, Popat R, Woo YJ. Early surgical intervention or watchful waiting for the management of asymptomatic mitral regurgitation: a systematic review and meta-analysis. *Ann Cardiothorac Surg*. (2015) 4(3):220–9. doi: 10.3978/j.issn.2225-319X.2015.04.01

41. Stokke TM, Hasselberg NE, Smedsrud MK, Sarvari SI, Haugaa KH, Smiseth OA, et al. Geometry as a confounder when assessing ventricular systolic function. Comparison between ejection fraction and strain. *J Am Coll Cardiol*. (2017) 70 (8):942–54. doi: 10.1016/j.jacc.2017.06.046

42. Mulieri LA, Leavitt BJ, Martin BJ, Haeberle JR, Alpert NR. Myocardial force-frequency defect in mitral regurgitation heart failure is reversed by forskolin. *Circulation*. (1993) 88:2700–4. doi: 10.1161/01.CIR.88.6.2700

43. Mulieri LA, Tischler MD, Martin BJ, Leavitt BJ, Ittleman FP, Alpert NR, et al. Regional differences in the force-frequency relation of human left ventricular myocardium in mitral regurgitation: implications for ventricular shape. *Am J Physiol Heart Circ Physiol*. (2005) 288:H2185–91. doi: 10.1152/ajpheart.00905.2003

44. Leszek P, Korewicki J, Klisiewicz A, Biederman A, Browarek A, Charlemagne D, et al. Reduced myocardial expression of calcium handling protein in patients with severe chronic mitral regurgitation. *Eur J Cardiothorac Surg*. (2006) 30:737–43. doi: 10.1016/j.ejcts.2006.07.008

45. Leszek P, Szperl M, Klisiewicz A, Janas J, Biederman A, Rywik T, et al. Alteration of myocardial sarcoplasmic reticulum Ca2+-ATPase and na+-Ca2 + exchanger expression in human left ventricular volume overload. *Eur J Heart Fail*. (2007) 9:579–86. doi: 10.1016/j.ejheart.2007.01.011

46. Shaikh S, Sahoo S, Periasamy M. Phospholamban and sarcolipin: are they functionally redundant or distinct regulators of sarco(endo)Plasmic Reticulum calcium ATPase? *J Mol Cell Cardiol*. (2016) 91:81–91. doi: 10.1016/j.yjmcc.2015.12.030

47. Carabello BA, Nolan SP, McGuire LB. Assessment of preoperative left ventricular function in patients with mitral regurgitation: value of the end-systolic wall stress-end-systolic volume ratio. *Circulation*. (1981) 64(6):1212–7. doi: 10.1161/01.cir.64.6.1212

48. Tribouilloy C, Rusinaru D, Szymanski C, Mezghani S, Fournier A, Lévy F, et al. Predicting left ventricular dysfunction after valve repair for mitral regurgitation due to leaflet prolapse: additive value of left ventricular end-systolic dimension to ejection fraction. *Eur J Echocardiogr*. (2011) 12(9):702–10. doi: 10.1093/ejechocard/jer128

frontiers | Frontiers in Cardiovascular Medicine

TYPE Review
PUBLISHED 18 December 2024
DOI 10.3389/fcvm.2024.1406899

OPEN ACCESS

EDITED BY
Dominik Buckert,
Ulm University Medical Center, Germany

REVIEWED BY
Alexander H. Maass,
University Medical Center Groningen, Netherlands
Dan Octavian Nistor,
Târgu Mureș Emergency Institute for Cardiovascular Diseases and Transplantation (IUBCVT), Romania

*CORRESPONDENCE
Călin-Dinu Hădăreanu
✉ calin.hadareanu@yahoo.com

†These authors have contributed equally to this work and share first authorship

RECEIVED 25 March 2024
ACCEPTED 02 December 2024
PUBLISHED 18 December 2024

CITATION
Stoiculescu F-M, Hădăreanu D-R, Hădăreanu C-D, Donoiu I and Florescu C (2024) Refining cardiac resynchronization therapy: a comprehensive review on the role of advanced multimodality imaging. Front. Cardiovasc. Med. 11:1406899. doi: 10.3389/fcvm.2024.1406899

Refining cardiac resynchronization therapy: a comprehensive review on the role of advanced multimodality imaging

Flavia-Mihaela Stoiculescu[1,2†], Diana-Ruxandra Hădăreanu[2,3†], Călin-Dinu Hădăreanu[1,4*], Ionuț Donoiu[2,3] and Cristina Florescu[3,5]

[1]Doctoral School, University of Medicine and Pharmacy of Craiova, Craiova, Romania, [2]Department of Cardiology, Clinical Emergency County Hospital of Craiova, Craiova, Romania, [3]Department of Cardiology, University of Medicine and Pharmacy of Craiova, Craiova, Romania, [4]Department of Cardiovascular Surgery, Clinical Emergency County Hospital of Craiova, Craiova, Romania, [5]Department of Cardiology, Filantropia Clinical Hospital of Craiova, Craiova, Romania

Cardiac resynchronization therapy (CRT) offers significant benefits in symptom alleviation, reduction of rehospitalization rates, and overall survival of patients with heart failure (HF) with reduced ejection fraction (rEF). However, despite its proven efficacy, precisely identifying suitable CRT candidates remains a challenge, with a notable proportion of patients experiencing non-response. Accordingly, many attempts have been made to enhance patient selection, and to identify the best imaging parameters to predict the response and survival after CRT implantation. This review article provides a comprehensive overview on the role of multi-modality cardiac imaging in selecting, optimizing, and predicting CRT response and outcomes in HFrEF patients, beginning with an exploration of dyssynchrony types and their impact on HF progression, and an emphasis on the utility of echocardiography in assessing cardiac dyssynchrony. Subsequently, the role of advanced techniques such as speckle tracking and three-dimensional echocardiography, as well as the visual assessment of apical rocking (ApRock) and septal flash (SF) are highlighted. Finally, cardiac magnetic resonance (CMR) scar data, and novel modalities like four-dimensional flow CMR, together with single-photon emission computed tomography offer additional insights, emerging as valuable predictors of CRT response, and potentially refining the identification of suitable CRT candidates.

KEYWORDS

cardiac resynchronization therapy (CRT), heart failure, multi-modality cardiac imaging, cardiac resynchronization therapy optimization, advanced echocardiography, cardiac magnetic resonance, cardiac dyssynchrony

1 Introduction

Cardiac resynchronization therapy (CRT) is a cornerstone in the management of patients with heart failure with reduced ejection fraction (HFrEF), and numerous clinical trials have demonstrated the effects of CRT implantation in reducing HF symptoms, decreasing hospitalization rates, and improving patients' survival (1). CRT implantation is recommended in patients with left ventricular (LV) ejection fraction (EF) ≤35% who remain symptomatic despite optimal medical therapy for at least 3

months, and who are in sinus rhythm with either a class IA in patients with a QRS duration ≥150 ms and left bundle branch (LBBB) morphology, or IIaB indication if the QRS duration is 130–149 ms or in case of a non-LBBB morphology (2). Furthermore, significant attempts were made in order to appropriately select the ideal candidates for CRT implantation, and to predict HFrEF patients' outcomes after CRT implantation based on electrocardiographic parameters and different imaging techniques (mainly echocardiography). However, the number of CRT non-responders remains high, with a notable 30%–40% non-responder rate (3), and with a high variability of the response as well (4), and none of these measures increased the responder rate (5) or predict major adverse cardiovascular events (MACEs). Nevertheless, the suggested parameters were deemed insufficiently sensitive or specific (6) to decrease non-response, resulting in unnecessary pacing and elevated mortality rates in HFrEF patients. Consequently, the aim of this article is to provide a state-of-the-art review on the role of cardiac imaging for selecting, optimizing and predicting CRT response and outcome in HFrEF patients, from the basic principles of evaluating cardiac dyssynchrony, to the role of advanced multi-modality imaging.

2 Pathophysiology and types of dyssynchrony

The main determinant of the CRT response is the degree of LV dyssynchrony (7), playing a crucial role in the development and progression of HF due to its effects on the systolic and diastolic LV function, and right ventricular (RV) and left atrial (LA) function as well (8–10). Cardiac dyssynchrony encompasses both electrical and mechanical dyssynchrony. The electrical component is characterized by prolonged conduction time in the ventricles, manifesting as an increased QRS duration. In contrast, the mechanical one involves the discordant mechanical coordination, often marked by simultaneous contraction and stretching in various segments of the LV, with delays in the time to peak contraction from one segment to another. From another point of view, cardiac dyssynchrony types cand be classified in atrioventricular, interventricular, and intraventricular (11). The atrioventricular dyssynchrony impacts ventricular diastolic filling, because of the initiation of the ventricular contraction while still in the diastolic period, resulting in mitral regurgitation (12), a shortened ventricular filling time, and ultimately, atrial systole occurring during the early passive filling phase (13). The interventricular and intraventricular dyssynchrony have a greater impact on the ventricular pump function, and characterize the electro-mechanical alterations found in patients with LBBB, and their hemodynamic consequences manifest as a reduction in stroke volume, diminished stroke work, higher LV pressure, and an increase in LV end-systolic wall stress (14). The presence and degree of echocardiographic mechanical dyssynchrony before CRT proved to be a significant predictor of long-term survival, and patients who experienced resolution of mechanical dyssynchrony within the 12 months following CRT exhibited the most favorable outcome (15).

3 Definition, types and sex differences in CRT response

While CRT non-responders display some of the worst outcomes in the HF population, the concept of a CRT responder should be applied with caution. While response typically refers to an improvement in cardiac size or function and/or clinical improvement based on symptoms, the specific measures used assess it vary across studies, and there is no universal consensus on a clear definition to what CRT response is (16, 17). Several clinical endpoints such as New York Heart Association (NYHA) functional class, quality of life scores, and exercise capacity measured by the 6-minute walking distance, along with the hemodynamic response and echocardiographic increase in LVEF or reduction in LV size, and outcome measures assessment have been used to assess the effectiveness of CRT and define responders (18). However, while a 15% reduction in LV end-systolic volume (ESV) and an increase in LVEF of 5% are commonly accepted markers of CRT success (19), it may not uniformly apply across patients subgroups, because of the underlying myocardial damage and limited potential for reverse remodeling in ischaemic cardiomyopathies, in which it might represent a clinically significant improvement, in contrast to patients with a non-ischaemic etiology of HF where greater reversibility is often expected. This highlights the need for a more nuanced approach to evaluating CRT response that incorporated factors such as etiology of HF, sex differences, baseline ventricular function, and other clinical conditions, as a one-size-fits-all criterion may not be appropriate for every patient (20). Moreover, while certain conditions such as ischemic cardiomyopathy, atrial fibrillation, non-LBBB QRS morphology are linked to poorer clinical outcomes or less favorable LV reverse remodeling (20), the influence of sex on CRT response has only been hypothesized until recently. Cheng et al. performed a meta-analysis on 72 studies comprising 33,434 patients and found that women experienced greater reduction in the risk of all-cause mortality, cardiac death, HF hospitalization after CRT compared to men, along with consistently stronger echocardiographic evidence of reverse remodeling (21). The possible explanation of why women with LBBB QRS morphology, particularly if the QRS duration is 130–149 ms, show a significantly better response to CRT than men (22), is represented by the sex differences in LV size, as smaller LV size in women accounts for a lower QRS duration threshold in women for CRT benefit (23). Moreover, the presence of LBBB and non-ischemic cardiomyopathy is higher in women, while the prevalence of an ischemic etiology is higher in men, together with non-LBBB conduction abnormalities, a history of atrial tachyarrhythmias, several comorbidities such as chronic pulmonary obstructive disease (24), diabetes and renal dysfunction (25).

4 Electrocardiography

The use of 12-lead electrocardiograms (ECGs) has greatly enhanced the understanding of ventricular conduction abnormalities,

and represents the basis of electrical dyssynchrony evaluation. Currently, the CRT implantation in HF class I and II indications according to clinical practice guidelines are established based on the QRS duration and morphology (2). However, one of the main limitations in selecting the CRT recipients based on the ECG is a large variability of LBBB definition depending on the criteria used (26). Moreover, the prevalence of LBBB morphology identification in the general CRT population differs widely—from 29% according to the American Heart Association/American College of Cardiology/Heart Rhythm Society (AHA/ACC/HRS) definitions (27), to 47% using European Society of Cardiology (ESC) criteria (28), and to 61% according to Strauss et al. (29). The robustness of the association between LBBB morphology of the QRS and outcomes after CRT varies based on the ECG classification used for defining it, with the simplest ones showing the strongest correlations with the clinical endpoints (30). Yet, even more notable is the absence of a significant correlation between QRS complex morphology and CRT outcomes as reported by a meta-analysis of 3,782 patients including five major randomized CRT trials (CARE-HF, RAFT, MIRACLE, MIRACLE-ICD, and LBBB REVERSE) (31). These findings contrast with the previously held belief that patients with LBBB were most favorable candidates for CRT, a view supported by the results of a large meta-analysis that included 6,523 patients from five trials (COMPANION, CARE-HF, MADIT-CRT, RAFT and REVERSE) which further emphasized that CRT did not improve the outcome of death and/or hospitalization for HF in non-LBBB morphology (32).

On the other hand, vectorcardiography offers a three-dimensional view of the heart's electrical vectors, providing additional information on the direction and magnitude of electrical forces. This can be particularly useful in cases where the standard ECG morphology is ambiguous or when assessing complex conduction disturbances (33). Another difficulty is represented by the non-LBBB patients since they cannot be treated as a single, homogenous group, other ECG parameters being particularly useful in this group of CRT candidates. The QRS area measured on the baseline 12-lead ECG was strongly associated with the clinical response and LV reverse-remodeling after CRT in both LBBB and non-LBBB patients with QRS ≥150 ms, and had better prognostic value compared to QRS morphology and duration (34). Finally, a reduction in QRS area after CRT is linked to lower mortality rates (35).

5 Echocardiography

Echocardiography remains the main imaging method used for selecting the patients that might benefit the most from CRT implantation, and for device optimization (36). However, the use of cardiac imaging to assess mechanical dyssynchrony is recommended only in patients with large QRS (>130 ms) as the Echo-CRT trial indicated potential harm when used as a criterion for CRT in patients with a QRS duration <130 ms (37). Table 1 provides a summary of the main echocardiographic

TABLE 1 The main echocardiographic parameters used for the evaluation of cardiac dyssynchrony.

Index	Method	Advantages	Disadvantages	Prognostic value
SPWMD ≥130 ms	M-mode color TDI	• No need for advanced technical specifications • Easy to apply • Widely available	• Influenced by passive movements or wall tethering • Affected by akinetic segments	• Predictive of reverse remodeling and improvement in heart failure status
DFT/RR ≤40%	PW Doppler	• Marker of global myocardial performance	• Significantly influenced by heart rate	• Its increase after CRT reflects favorable reverse remodeling and is associated with better clinical outcomes
IVMD ≥40 ms	PW Doppler	• No need for advanced technical equipment or software • Widely available • High reproducibility	• Influenced by both LV and RV contraction and relaxation	• Good feasibility and reproducibility • Predicts survival and CRT response
Basal septal-to lateral wall delay ≥65 ms	Color DTI Ts	• Easy to apply • Analysis can be conducted offline	• Influenced by passive movements or wall tethering	• Highly predictive for both clinical and echocardiographic response after CRT
Maximum difference in Ts ≥100 ms	Color DTI Ts	• Analysis can be conducted offline • Enhanced identification of longitudinal dyssynchrony	• Influenced by passive movements or wall tethering	• Highly predictive for both clinical and echocardiographic response after CRT
Dyssynchrony index/Yu index ≥33 ms	Color DTI	• Analysis can be conducted offline • Enhanced identification of longitudinal dyssynchrony	• Influenced by passive movements or wall tethering	• Independently associated with long-term prognosis after CRT • Useful risk-stratification tool
SDI ≥8.3%	RT3DE	• Angle-independent assessment of regional and global deformation • Assesses dyssynchrony with a single aquisition	• Lower spatial resolution • Longer learning curve and the need for an experienced user • Requires offline analysis • Not widely available	• Conflicting data regarding its prognostic value

CRT, cardiac resynchronization therapy; DFT, diastolic filling time; IVMD, inter-ventricular mechanical delay; LV, left ventricle; PW, pulsed-wave; RR, cardiac cycle duration; RT3DE, real-time three-dimensional echocardiography; RV, right ventricle; SDI, systolic dyssynchrony index; SPWMD, septal to posterior wall delay; TDI, tissue doppler imaging; Ts, time to peak systolic velocities in the slowest of 6 basal LV segments.

parameters used for the evaluation of cardiac dyssynchrony, as well as their advantages, disadvantages and clinical usefulness.

5.1 M-mode, Doppler and two-dimensional echocardiography

LV intraventricular dyssynchrony can be evaluated by M-mode echocardiography using a simple index of septal to posterior wall motion delay (SPWMD), with a cut-off value of >130 ms identifying the patients with a more favorable outcome after CRT (38). The value of SPWMD was first demonstrated by Pitzalis et al. more than 20 years ago in a study on 20 patients, showing that a SPWMD of >130 ms and a QRS duration of >150 ms correlated with a positive response to CRT, defined as a >15% reduction in LV ESV index in 79% of the patients (39). A SPWMD of ≥130 ms furthermore predicted the improvement in LVEF and was associated with a lower risk of clinical worsening after CRT (40). This led to SPWMD emerging as a reliable prognosticator of LV reverse remodeling following CRT implantation. However, the feasibility and reproducibility of SPWMD measurements are limited according to a retrospective analysis of the CONTAK-CD trial which included 79 patients with HFrEF (EF 22 ± 7%, QRS duration 159 ± 27 ms). Furthermore, greater SPWMD values did not correlate neither with the six-month change in LV end-diastolic volume (EDV) and ESV index or LVEF, nor with any markers of clinical improvement, and no significant differences in SPWMD values were found between CRT responders and non-responders (41). Therefore, the utility of M-mode evaluation of LV dyssynchrony is supplemental to other echocardiographic modalities, and should not be used alone.

Pulsed-wave (PW) Doppler echocardiography is used for the assessment of all atrioventricular, inter- and intra-ventricular dyssynchronies. Atrioventricular (AV) dyssynchrony is objectivated by a reduced diastolic ventricular filling time, measured by PW Doppler at the level of the mitral valve leaflets' tips between the onset of the E wave and the end of the A wave, and normalized as a percentage of the cardiac cycle (Figure 1A). A LV filling time <40% indicated significant AV dyssynchrony (42). It can be used only in sinus rhythm and results either from an abnormal delay between the end of atrial systole and onset of ventricular systole in case of a long PR interval, or from a prolonged and abnormal intraventricular conduction (43). Parsai et al. hypothesized that the identification of all types of dyssynchrony would better determine the CRT responders, and conducted a study on 161 patients investigated before and after CRT. They propose an algorithm that includes the identification of 4 subgroups of mechanisms: the presence of true dyssynchrony as SF, impaired diastolic filling with either short or long AV delay, and exaggerated LV-RV interaction. The CRT clinical response depended on correcting the underlying mechanisms involved in the development of HF, and solely relying on the assessment of LV dyssynchrony failed to identify 40% of responders (44).

Empirically, the interventricular dyssynchrony was considered the interventricular mechanical delay (IVMD), calculated as a difference between LV pre-ejection interval (Figure 1B), and RV

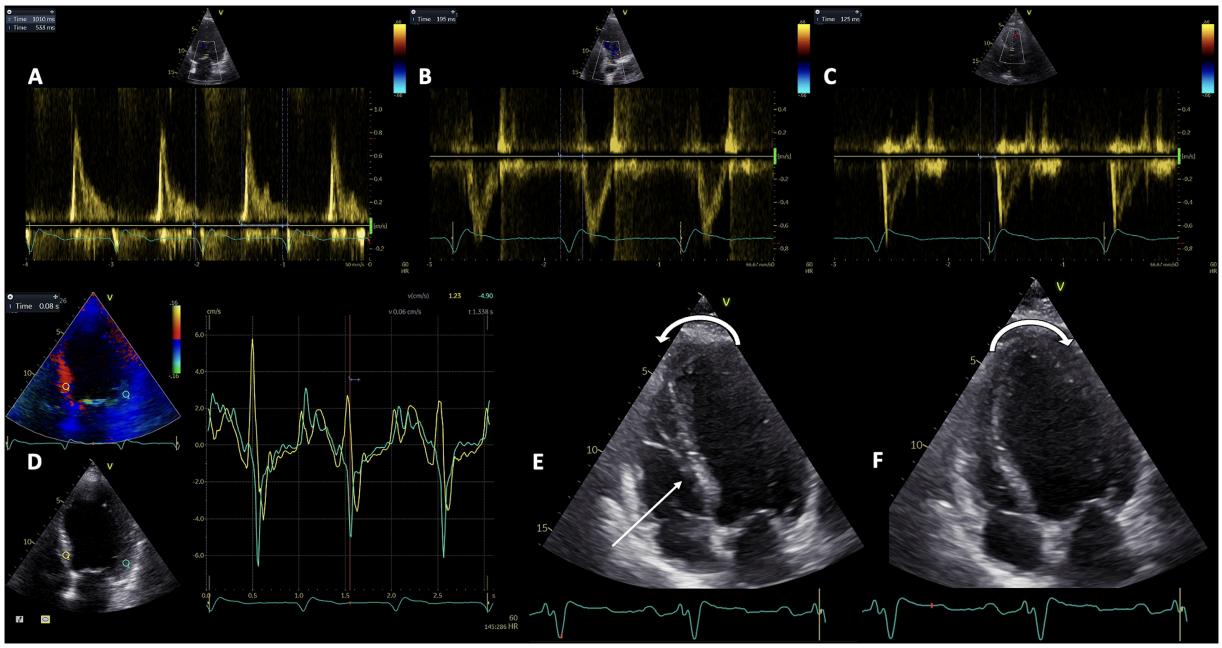

FIGURE 1
The evaluation of the three types of mechanical dyssynchrony by Doppler echocardiography. Pulsed-wave Doppler assessment of atrioventricular dyssynchrony as the diastolic filling time relative to cardiac cycle duration (**A**); and interventricular dyssynchrony as the difference between LV pre-ejection time (**B**), and RV pre-ejection time (**C**) Tissue Doppler Imaging evaluation of intraventricular dyssynchrony as the basal septal to lateral wall delay (**D**) Representation of septal flash and apical rocking (**E** and **F**). LV, left ventricle; RV, right ventricle.

pre-ejection interval (Figure 1C) of more than 40 ms. LV and RV pre-ejection intervals are measured by PW Doppler, from the onset of the QRS complex and, respectively, the initiation of aortic and pulmonary ejection flows (45). Several studies confirmed the association between the IVMD and a favorable response to CRT. In the SCART Study Achilli et al. found that an IVMD >44 ms independently predicted the response (46), while patients with IVMD >49 ms benefited significantly from CRT in an analysis by Richardson et al. of the CARE-HF trial (47). However, the IVMD is considered to lack sufficient accuracy to be used for CRT reponse in clinical practice according to the PROSPECT study (6). More recently, as part of the CAVIAR response score developed by the investigators of the MARC study, the vectorcardiographic QRS area, IVMD and ApRock were strongly associated to LV reverse remodeling after CRT (48). The MARC study, which is the only prospective multi-modality biomarker study on CRT response, provided significant insights into the effectiveness of various echocardiographic criteria used, underscoring the importance of combining different parameters to improve the accuracy of CRT response prediction.

Intraventricular dyssynchrony can be evaluated by measuring the prolongation of the LV pre-ejection interval, as well as that of the contraction of either the septum or the left lateral wall after aortic valve closure (49).

Similarly, RV dyssynchrony indices in CRT patients were retrospectively evaluated. Adding the measurement of RV indices provides incremental prognostic value compared to LV parameters, with the highest sensitivity and specificity for RV deformation synchrony and RV isovolumic contraction dyssynchrony. However, they did not predict reverse remodeling after CRT (50). In contrast, the non-invasive estimation of RV to pulmonary artery coupling measured as the ratio between tricuspid annulus systolic excursion and systolic pulmonary artery pressure (TAPSE/sPAP) predicted both the response to CRT and LV reverse remodelling, andCRT responders also had improved TAPSE/sPAP at follow-up (51, 52). Moreover, in a large study on 807 CRT recipients followed-up for a median time of 8 years, the rates of survival at 3 and 5 years were significantly lower in patients with a TAPSE/sPAP <0.45 mm/mmHg, showing poorer long-term outcomes in CRT patients with RV to pulmonary artery uncoupling (53).

While the impact of CRT on the diastolic function remains a topic of debate (54), certain prospective studies have indicated that a favorable filling pattern and a less enlarged LA at baseline are more likely to correlate with positive LV remodeling following CRT (55). Moreover, a lack of reduction in mean LV filling pressures after CRT was associated with a negative response (56). Grade I LV diastolic dysfunction lead to a better prognosis compared to grade II or III (54). Nonetheless, a smaller LA volume index per one unit of standard deviation below the mean predicted LVEF super-response after CRT (57).

Tissue Doppler Imaging (TDI) is essential for the accurate determination of the amplitude, timing of onset, and peak systolic and diastolic velocities in correlation with the ECG signal. PW TDI is useful for measuring the electromechanical delay (58, 59), and the electro-systolic delay (60), from the beginning of the QRS interval to S wave onset, and to peak systolic contraction, respectively. Additionally, color TDI loops can be recorded and subsequently analyzed offline as reconstructed signals, in order to overcome the well-known limitations of PW TDI. The color-coded TDI has been the method of choice for assessing dyssynchrony by echocardiography for many years (61). The dyssynchrony indices obtained by color TDI are basal septal to lateral wall delay (Figure 1D), maximum time to peak systolic velocity in the slowest of 6 basal LV segments, as well as the Yu index which integrates data from the 3 apical LV views and represents a 12-segment model (62). While Bax et al. elegantly demonstrated that the degree of LV dyssynchrony predicted the clinical response and LV remodeling after CRT, with a cut-off value of 65 ms for the opposite wall delay (63), a Yu index or mechanical dyssynchrony index ≥33 ms managed to predict LV remodeling in patients with a QRS duration >150 ms with a sensitivity of 100% and specificity of 78% (64). An alternative approach to the Yu index is calculating the time to peak systolic velocity in all the segments, for which a value ≥100 ms is predictive of the CRT response (61). However, the 12-segment model has higher variability and the disadvantage of being more technically challenging (65).

Myocardial strain imaging derived by TDI offers widely-used diagnostic tools, potentially enhancing patient selection for CRT. Currently, several strain parameters are used as clinical indicators of CRT response, the most frequently used parameter being the delayed longitudinal contraction or post-systolic shortening, defined as more than 30% of 12 LV segments contracting after aortic valve closure (62). Also, recent data showed that end-systolic septal strain strongly correlates with favorable reverse remodeling following CRT, regardless of the assessment technique employed. Utilizing any strain imaging technique to measure end-systolic septal strain offers additional predictive value beyond existing guideline criteria (66), yet TD strain imaging poses the well-known limitations of Doppler angle dependency and technical difficulties in patients with spherical LV geometry. Nonetheless, Yu et al. identified time to peak myocardial contraction as the strongest predictor of LV reverse remodeling (67) Finally, TD strain-imaging derived mechanical dispersion refers to the variation in the timing of myocardial contraction across the different LV segments. It is calculated as the standard deviation of time-to-peak contraction of these segments, with a higher mechanical dispersion index indicating more dyssynchrony. While newer techniques (i.e., speckle-tracking echocardiography) are increasingly used for assessing mechanical dispersion due to their higher spatial resolution and ability to provide more detailed, angle-independent measurements, the TDI-derived mechanical dispersion index remains a reliable and widely accessible parameter, and a strong predictor of outcomes in CRT recipients (67).

Echocardiographic and Doppler imaging methods remain the foundation of mechanical dyssynchrony assessment as a key factor for determining CRT eligibility, even though the results of the PROSPECT study taught that the complexity of the technical issues impact their feasibility and reproducibility, and no ideal method exists (65). However, since PROSPECT, several advancements in cardiac imaging (speckle-tracking echocardiography, three-dimensional echocardiography, cardiac magnetic resonance) have

improved the accuracy and reliability of assessing dyssynchrony and overall cardiac function, reinforcing the expanding role of cardiac imaging in CRT.

5.2 Visual assessment of apical rocking and septal flash

Both ApRock and SF occur as a consequence of the mechanical dyssynchrony secondary to the LBBB (15), and their superiority over conventional parameters has already been demonstrated in several prospective observational studies (68, 69). ApRock (Figures 1E,F) is characterized as an initial septal contraction in the LV isovolumic contraction period which results in a short inward motion of the septum and causes the apex to move septally. Next, the delay in the activation of the lateral wall pulls the apex laterally during the ejection time while stretching the septum (68, 70). SF is caused by an initial thickening/thinning of the septum during isovolumic systole (Figure 1E). This phenomenon can also be easily identified using M-mode echocardiography in the parasternal long-axis view or tissue Doppler imaging in both the short and long parasternal long-axis views (71), while a low-dose dobutamine administration may help unmasking the SF in a minority of challenging cases (72).

The visual assessment of ApRock and SF is relatively easy and reproducible, and they should be used frequently in selecting CRT candidates because of their prognostic value. However, while their presence is associated with a favorable outcome in patients who undergo an upgrade from regular pacing to CRT, as well in patients with a QRS duration of less than 150 milliseconds (42), also having additional value in predicting long term major cardiac events (73), the accurate recognition of SF and ApRock in candidates for CRT is heavily dependent on the expertise of the echocardiographer (74).

5.3 Speckle tracking echocardiography (STE) and LV myocardial work

Mechanical dyssynchrony, rather than electrical dyssynchrony, serves as the primary predictor of responsiveness to CRT. On one hand, electrical dyssynchrony, evaluated by QRS duration on an ECG, may be less reliable due to scar-related moderate QRS enlargements that may not correspond to significant mechanical dyssynchrony. This phenomenon is especially noticeable among patients with an ischemic etiology of HF, in which several myocardial segments have delayed contraction, often attributed to scar tissue formation. On the other hand, scar tissue or fibrosis, resulting in reduced or lack of contractile reserve, influence CRT response. However, relying solely on time-delay indexes for identifying responders is inherently limited since it does not consider residual myocardial contraction. Accordingly, comprehensive echocardiographic evaluations of both LV mechanical dyssynchrony (Figures 2A–C) and contractile function, providing insights into myocardial viability and scar tissue burden, can now be conducted reliably and independently of imaging angles through the application of STE (75, 76). Delgado et al. proved that combining the LV radial dyssynchrony with the radial strain of the LV segment corresponding to the LV lead placement (with values <16.5% indicating a myocardial scar with >50% transmurality as validated by cardiac magnetic resonance), and placing the LV lead in the latest activated segment defined as concordant lead position predicted the long-term survival in a large cohort of ischemic HF patients (77). These three parameters provided additional prognostic value beyond that offered by clinical parameters alone. However, radial dyssynchrony cannot be used in patients with a history of septal infarction.

LV global longitudinal strain (GLS) is a more reliable indicator of LV systolic performance compared to LV EF, simultaneously predicting cardiac events in CRT recipients (75). Greater baseline LV GLS values, and significantly higher LV GLS values at follow-up were found in CRT responders compared to non-responders (76). Moreover, 2D STE can identify the significant activation delay typical of a true LBBB, patients without the typical LBBB contraction pattern facing a threefold increase in the risk of adverse outcomes following CRT implantation (78). Another important index derived from STE is LV mechanical dispersion. Van der Bijl et al. demonstrated that greater LV mechanical dispersion at 6 months post-CRT predicted all-cause mortality and higher arrhythmic risk, independent of the clinical response and LV reverse remodeling, while baseline dispersion did not impact the outcome (79). However, LV mechanical dispersion does not differentiate between an ischaemic and conduction disturbance substrate, since it is common to observe the reduced systolic shortening and post-systolic shortening in the scarred myocardium (80, 81), and accordingly, mechanical dispersion is not currently recommended to be used for dyssynchrony assessments (42).

Adding LA reservoir strain (Figure 2E) measurement to LV GLS calculation is an useful tool for selecting CRT candidates, and could potentially improve the risk stratification in patients undergoing CRT implantation. Furthermore, higher LA reservoir strain at baseline correlates with a more significant LV remodeling after CRT (82, 83). Nevertheless, although frequently overlooked, right atrial (RA) remodeling, assessed as either RA volume or RA strain (Figure 2F), has important prognostic value in HF patients, including in those undergoing CRT (84, 85).

Strain delay index derived from longitudinal strain amplitude measurements by two-dimensional STE is another reliable predictor of CRT response, regardless of whether patients have an ischemic or nonischemic etiology of HF (86).

Moreover, the non-invasive echocardiographic LV myocardial work (Figure 2D) evaluation prior to CRT implantation has emerged as a valuable technique for the identification of CRT responders (87). Global wasted work and the average wasted work measured at the level of the interventricular septum derived from the echocardiographic LV pressure-volume loops had higher values in CRT responders compared to non-responders, and a significant reduction was observed after CRT implantation, converging towards the values typical of a normal heart (88).

The prognostic value of septal wasted work for the response to CRT may be enhanced by combining it with the LV wall motion

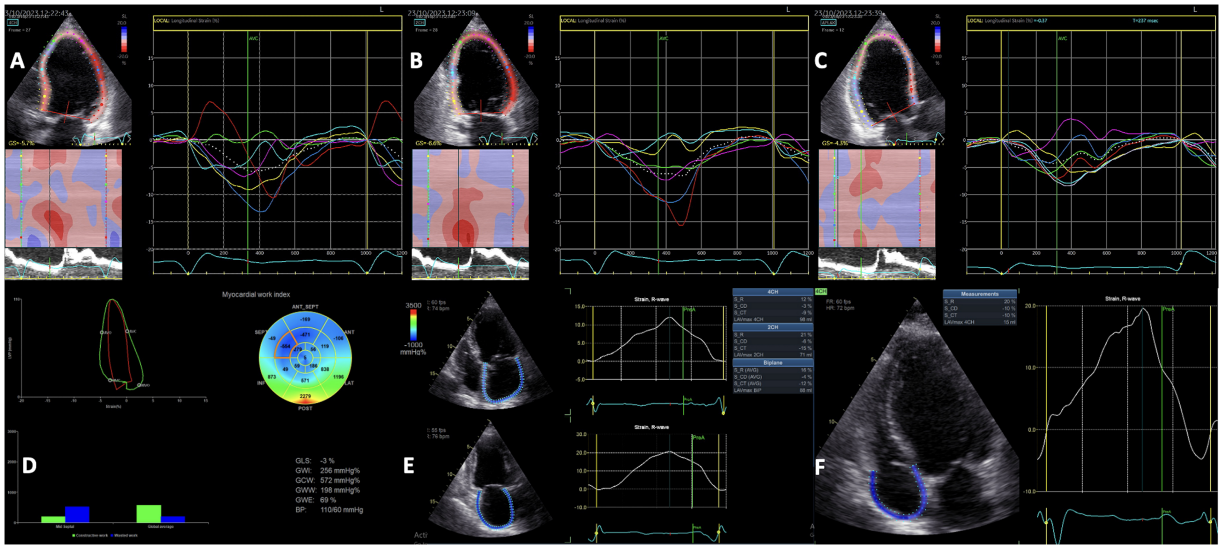

FIGURE 2
Two-dimensional speckle-tracking analysis of segmental left ventricular myocardial deformation showing the intraventricular dyssynchrony in the apical 4-chamber **(A)**, 2-chamber **(B)** and 3-chamber **(C)** views. Myocardial work analysis showing increased GWW, and regional WW at the level of the septum, and low GWI, GCW and GWE **(D)** Left atrial strain analysis **(E)** and Right atrial strain analysis **(F)** showing reduced values in a patient with left ventricular dyssynchrony and left bundle branch block. GCW, global constructive work; GWE, global work efficiency; GWI, global work index.

score. The LV lateral wall to septal work difference alone had predictive value comparable to visual assessments of dyssynchrony, and combining it with septal scar evaluation by CMR significantly enhanced the accuracy of predicting CRT response (89). Finally, an effective parameter for the prediction of long-term reverse remodeling involves examining the redistribution of myocardial work between the septal and lateral LV walls following CRT implantation (90).

While the existing evidence on these echocardiographic parameters may not be robust enough to solely guide treatment decisions, routine analysis of myocardial work parameters should be integrated into the patient selection process because of their demonstrated value in selecting patients that might benefit from CRT, and an integrative approach might enhance the selection of suitable CRT candidates (91).

5.4 Three-dimensional (3D) echocardiography

Due to the intricate spatial orientation of LV myocardial fibers, and its simultaneous contraction in various directions, LV mechanics are recognized as a 3D phenomenon, and 3D echocardiography provides its most accurate evaluation (92–94). Despite the less encouraging outcomes reported in the PROSPECT trial (6), there is a growing interest in employing advanced echocardiography to identify patients who would benefit from CRT (93). The main additional value of 3D echocardiography is that it enables simultaneous comparison of synchrony across LV segments within the same cardiac cycle. An essential parameter derived from 3D echocardiography is the systolic dyssynchrony index (SDI) (95). The SDI represents the standard deviation of the average time intervals necessary for every LV segment to reach their minimum end-systolic volume. Expressed as a percentage of the entire cardiac cycle, this index is useful for comparing patients with different heart rates. Those with normal cardiac function demonstrate well-synchronized segmental function. Importantly, individuals who respond positively to CRT exhibit a significant reduction in SDI, corresponding to decreases in LV end-diastolic volume and increases in EF (96). Apart from SDI, various metrics obtained from 3D speckle-tracking echocardiography — namely, longitudinal strain (Figure 3), radial strain, circumferential strain, and, more recently, area strain — have been proposed for assessing myocardial mechanical dyssynchrony (97).

6 Cardiac magnetic resonance (CMR)

The utilization of cardiovascular magnetic resonance (CMR) imaging for HF evaluation is being used increasingly. This trend reflects the numerous appealing attributes of CMR in contrast to echocardiography, including enhanced tissue characterization, superior spatial resolution, and the absence of imaging limitations related to patient orientation and overlapping structures.

6.1 Tissue scar, myocardial viability and myocardial dyssynchrony evaluation

Evaluating the magnitude and location of the myocardial scar tissue by the use of late gadolinium enhancement (LGE) plays a crucial role (Figure 4), together with the evaluation of different LV

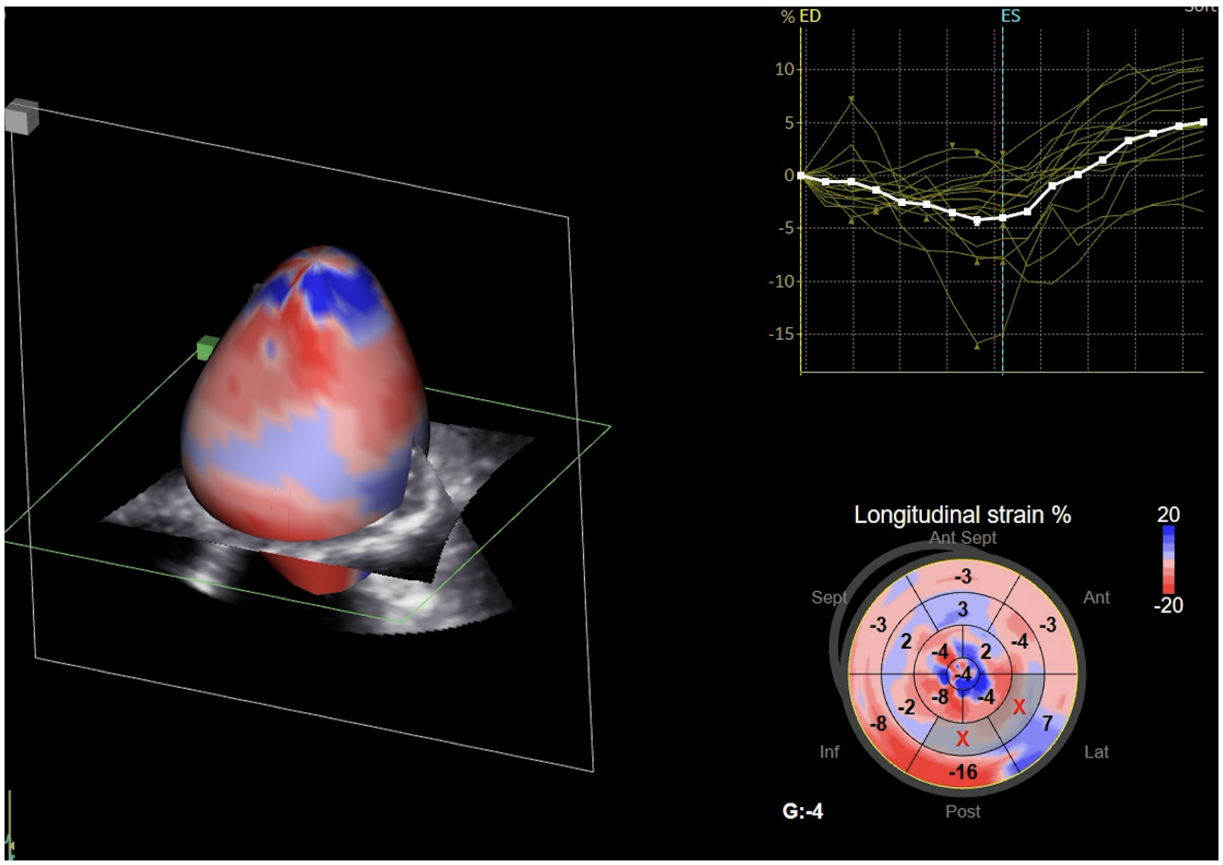

FIGURE 3
Three-dimensional speckle-tracking analysis of left ventricular global longitudinal strain.

contraction patterns (3). The identification and characterization of scar patterns is particularly valuable in predicting the clinical response in LBB pacing for CRT (98).

In patients with nonischemic dilated cardiomyopathy, significant myocardial fibrosis and reduced circumferential dyssynchrony at CMR were independently associated with unfavorable response and long-term events after CRT (99). On the other hand, in patients with ischemic cardiomyopathy, the size and position of the myocardial scar tissue significantly affect the response to CRT in two primary ways. Firstly, placing the LV pacing lead in scarred regions correlates with less clinical and echocardiographic improvements. Secondly, greater scar burden corresponds to reduced residual LV contractility (74). A substantial scar extent (>33%) or high transmurality (>51%) serve as unfavorable predictors for CRT response. Interestingly, lateral wall scarring was less predictive of CRT response than septal scarring. The presence of septal LGE, whether ischemic or non-ischemic, is a robust indicator for predicting non-response and unfavorable long-term outcomes after CRT (77, 100).

Furthermore, because mechanical dyssynchrony parameters are affected by regional scarring, several CMR methods have been developed for an adequate evaluation of dyssynchrony. Endocardial contour tracking software, contraction propagation maps, CMR-tissue synchronization indicesare some of the used sequences and analysis techniques.

This can be explained by the reduction in the typical LBBB -induced septal motion pattern (101) due to the decreased contractility of the lateral wall. The septum is thereby less stretched and SF and ApRock are diminished (102). Recent studies suggest that septal scar evaluation by CMR LGE together with SF visual assessment by CMR cine sequences as a singular imaging modality, together with other parameters such as delayed aortic valve opening measured relative to both end-diastole, and to pulmonic valve opening, or changes in septal-to-LV free-wall curvature ratios provide further insights into mechanical dyssynchrony, and accurately identify responders to CRT, while also reliably predicting long-term survival (103). If septal LGE is absent, the response rate remains outstanding, regardless of the presence or absence of other parameters of dyssynchrony. Conversely, if septal LGE is present without the occurrence of SF, the likelihood of a favorable response to CRT is significantly diminished, and if both septal LGE and SF are present, patients could respond positively to CRT (69).

Finally, integrating scar data with non-contact endocardial mapping to identify regions of slow conduction facilitates the optimization of the hemodynamic response. Furthermore, the combination of scar data with regional contractility patterns proves to be more effective in predicting long-term remodeling after CRT compared to standard echocardiography (104).

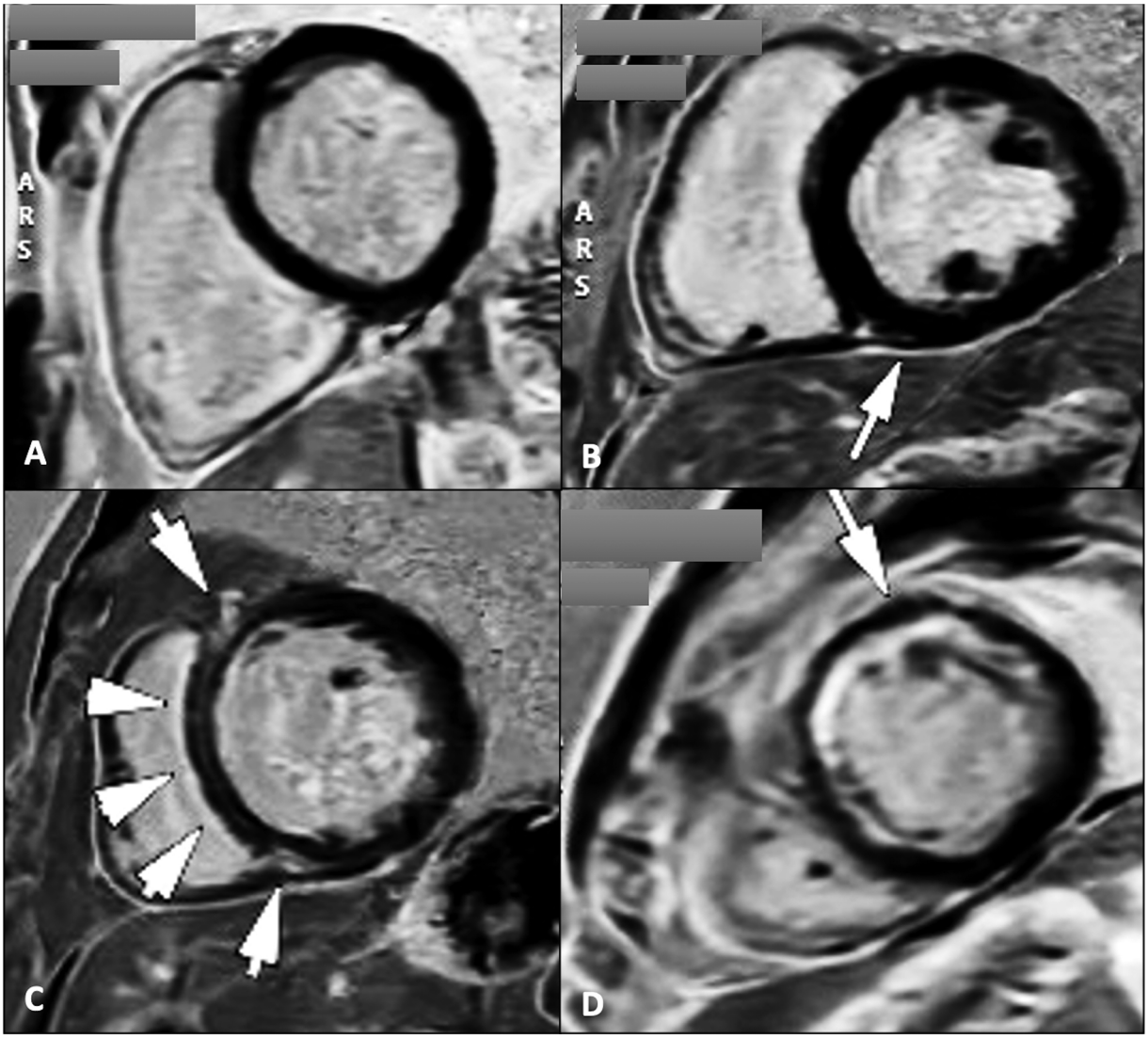

FIGURE 4
Cardiac magnetic resonance late gadolinium enhancement sequences for the assessment of myocardial scar tissue/fibrosis in four patients with dilated cardiomyopathy showing absence of LGE **(A)**; localized LGE at the level of the inferior intraventricular septum on the RV insertion point **(B)**; midwall linear fibrosis at the level of the intraventricular septum commonly known as "septal stripe" LGE, and at the level of the RV insertion points **(C)**; and subendocardial antero-septal and anterior wall LGE **(D)** types B and C LGE pattern are typically found in patients with genetic/idiopathic etiologies of dilated cardiomyopathies, while pattern D suggests an ischaemic etiology. LGE, late gadolinium enhancement; RV, right ventricle.

Accordingly, CMR evaluation plays a crucial role for selecting CRT candidates, predicting cardiac remodeling and patients' outcomes after CRT implantation, additionally identifying the regions that should be avoided during the lead placement process. CMR is useful in establishing the indication for adding an implantable cardiac defibrillator (ICD) to CRT (CRT-D) for primary sudden cardiac death prevention (105), which might be particularly important as demonstrated by the findings from the MADIT-CRT study (106). In patients with mildly symptomatic HFrEF [classified as New York Heart Association (NYHA) class I or II if ischemic, and NYHA class II if non-ischemic], with an LVEF of 30% or lower, and a QRS duration of 130 ms the prophylactic treatment with CRT-D significantly lowers the risk (including mortality) in comparison to solely receiving an ICD (107). Lastly, the importance of using CMR together with cardiac computed tomography for creating detailed anatomical maps together with a thorough understanding of the ventricular anatomy, including the identification of structural abnormalities as part of the pre-procedural planning are crucial for precise lead placement in conduction system pacing (108).

6.2 Other CMR-derived measurements

Apart from myocardial scar and viability evaluation by CMR, greater CMR-derived circumferential uniformity ratio estimate used to quantify LV mechanical dyssynchrony by measuring LV segments contraction and stretch as negative, positive

circumferential strain, respectively (109), was associated with a more favorable response and survival in female HF CRT patients (110). Nonetheless, both LA size and function (reservoir and booster function) (111), as well as RV function (RVEF, with a cut-off value of 55%) (112) predicted CRT response and LV reverse remodeling.

6.3 Four-dimensional (4D) flow CMR

Hemodynamic force (HDF) analysis of LV blood flow is a novel indicator of cardiac function that offers distinctive insights into the relationship between the ventricular movement and the resulting blood flow patterns, identifying HF patients with LBBB who are unlikely to benefit from CRT. Although not commonly used in clinical practice, it offers significant advantages in the comprehensive hemodynamic evaluation since it allows the assessment of complex flow dynamics in all three spatial dimensions over time. LV HDF represent the collective forces exchanged between the blood pool and the surrounding myocardium, which arise from the cumulative pressure gradients within the LV (113). In healthy hearts, LV HDF primarily align in the longitudinal direction, and an elevated ratio of transverse to longitudinal HDF suggests an aberrant blood flow pattern (114). CRT responders have higher inferior-anterior systolic and apex-base diastolic HDF (115).

The short-axis to long-axis 4D filling HDF ratio, an indicator of the deviation of the LV hemodynamic forces from the main flow direction, was higher during the initial diastolic filling phase in patients with dyssynchronous LV relaxation (LBBB patients) compared to age, gender, heart rate, and LV characteristics matched non-LBBB patients (116). However, LV HDF are influenced by conditions that lead to changes in LV inflow directions such as mitral valve dysfunction or prosthetic valve replacement, as well as significant regional wall motion abnormalities resulting from myocardial infarction. Consequently, HDF analysis may offer supplementary insights for the personalized evaluation of patients suitable for CRT.

7 Single-photon emission computed tomography (SPECT)

In cases when CMR is unavailable or contraindicated, SPECT may be used for myocardial scar tissue and viability evaluation in CRT recipients, and their identification has been linked to both CRT response and prognosis. Perfusion defects in the septal and apical segments that arise from relative hypoperfusion in the septal region compared to the lateral wall in the presence of LBBB, and in the absence of coronary artery lesions can also be detected by SPECT (117, 118).

8 Conclusions

A multiparametric evaluation is key for the personalized evaluation of HF patients undergoing CRT, and integrating multimodality cardiac imaging techniques has the potential to improve outcomes and reduce the number of non-responders. Echocardiography remains essential in evaluating cardiac dyssynchrony, with advanced techniques like speckle-tracking echocardiography and three-dimensional echocardiography improving patient selection. Cardiac magnetic resonance imaging provides complementary information on myocardial scar tissue, aiding in predicting CRT response and guiding lead placement. Finally, emerging modalities such as four-dimensional flow CMR offer novel perspectives on LV hemodynamic forces and LV blood flow patterns, potentially further refining the identification of suitable CRT candidates.

Author contributions

F-MS: Conceptualization, Data curation, Funding acquisition, Investigation, Methodology, Supervision, Writing – original draft, Writing – review & editing. D-RH: Conceptualization, Data curation, Investigation, Methodology, Project administration, Supervision, Writing – original draft, Writing – review & editing. C-DH: Conceptualization, Data curation, Funding acquisition, Methodology, Project administration, Resources, Supervision, Writing – original draft, Writing – review & editing. ID: Conceptualization, Data curation, Funding acquisition, Project administration, Supervision, Writing – original draft, Writing – review & editing. CF: Conceptualization, Data curation, Funding acquisition, Investigation, Methodology, Project administration, Supervision, Visualization, Writing – original draft, Writing – review & editing.

Funding

The author(s) declare financial support was received for the research, authorship, and/or publication of this article. The article processing charges were funded by the University of Medicine and Pharmacy of Craiova, Romania.

Conflict of interest

The authors declare that the research was conducted in the absence of any commercial or financial relationships that could be construed as a potential conflict of interest.

Publisher's note

References

1. Glikson M, Nielsen JC, Kronborg MB, Michowitz Y, Auricchio A, Barbash IM, et al. ESC Scientific Document Group. 2021 ESC Guidelines on cardiac pacing and cardiac resynchronization therapy. *Eur Heart J*. (2021) 42(35):3427–520. doi: 10.1093/eurheartj/ehab364. Erratum in: *Eur Heart J*. (2022) 43(17):1651. doi: 10.1093/eurheartj/ehac075

2. McDonagh TA, Metra M, Adamo M, Gardner RS, Baumbach A, Böhm M, et al. 2021 ESC guidelines for the diagnosis and treatment of acute and chronic heart failure. *Eur Heart J*. (2021) 42:3599–726. doi: 10.1093/eurheartj/ehab368

3. Chalil S, Foley PWX, Muyhaldeen SA, Patel KCR, Yousef ZR, Smith REA, et al. Late gadolinium enhancement-cardiovascular magnetic resonance as a predictor of response to cardiac resynchronization therapy in patients with ischaemic cardiomyopathy. *Europace*. (2007) 9:1031–7. doi: 10.1093/europace/eum133

4. Nakai T, Ikeya Y, Kogawa R, Okumura Y. Cardiac resynchronization therapy: current status and near-future prospects. *J Cardiol*. (2022) 79:352–7. doi: 10.1016/j.jjcc.2021.10.021

5. Prinzen FW, Lumens J. Investigating myocardial work as a CRT response predictor is not a waste of work. *Eur Heart J*. (2020) 41:3824–6. doi: 10.1093/eurheartj/ehaa677

6. Chung ES, Leon AR, Tavazzi L, Sun J-P, Nihoyannopoulos P, Merlino J, et al. Results of the predictors of response to CRT (PROSPECT) trial. *Circulation*. (2008) 117:2608–16. doi: 10.1161/CIRCULATIONAHA.107.743120

7. Gorcsan J, Oyenuga O, Habib PJ, Tanaka H, Adelstein EC, Hara H, et al. Relationship of echocardiographic dyssynchrony to long-term survival after cardiac resynchronization therapy. *Circulation*. (2010) 122:1910–8. doi: 10.1161/CIRCULATIONAHA.110.954768

8. Stassen J, Galloo X, Chimed S, Hirasawa K, Marsan NA, Delgado V, et al. Clinical implications of left atrial reverse remodelling after cardiac resynchronization therapy. *Eur Heart J Cardiovasc Imaging*. (2022) 23:730–40. doi: 10.1093/ehjci/jeac042

9. Badran HA, Abdelhamid MA, Ibrahim MT, Abdelmoteleb AM, Zarif JK. Left atrium in cardiac resynchronization therapy: active participant or innocent bystander. *J Saudi Heart Assoc*. (2017) 29:259–69. doi: 10.1016/j.jsha.2017.01.008

10. Layec J, Decroocq M, Delelis F, Appert L, Guyomar Y, Riolet C, et al. Dyssynchrony and response to cardiac resynchronization therapy in heart failure patients with unfavorable electrical characteristics. *JACC Cardiovasc Imaging*. (2023) 16:873–84. doi: 10.1016/j.jcmg.2022.12.023

11. Yu C-M, Sanderson JE, Gorcsan J. Echocardiography, dyssynchrony, and the response to cardiac resynchronization therapy. *Eur Heart J*. (2010) 31:2326–37. doi: 10.1093/eurheartj/ehq263

12. Russo E, Russo G, Cassese M, Braccio M, Carella M, Compagnucci P, et al. The role of cardiac resynchronization therapy for the management of functional mitral regurgitation. *Cells*. (2022) 11(15):2407. doi: 10.3390/cells11152407

13. Lavanya K, Mgbemena ON, Keim SG. Atrio-ventricular dyssynchrony after cardiac resynchronization therapy: an unusual contributor to heart failure symptoms. *Cureus*. (2023) 15(3):e35661. doi: 10.7759/cureus.35661

14. Monge García MI, Jian Z, Hatib F, Settles JJ, Cecconi M, Pinsky MR. Relationship between intraventricular mechanical dyssynchrony and left ventricular systolic and diastolic performance: an *in vivo* experimental study. *Physiol Rep*. (2023) 11(4):e15607. doi: 10.14814/phy2.15607

15. Ahmed MA, Gercek M, Sommer P, Rudolph V, Dumitrescu D, Faber L, et al. Echocardiographic mechanical dyssynchrony predicts long-term mortality in patients with cardiac resynchronisation therapy. *Int J Cardiovasc Imaging*. (2024) 40(1):35–43. doi: 10.1007/s10554-023-02972-1

16. Green PG, Herring N, Betts TR. What have we learned in the last 20 years about CRT non-responders? *Card Electrophysiol Clin*. (2022) 14:283–96. doi: 10.1016/j.ccep.2021.12.019

17. Fornwalt BK, Sprague WW, Bedell P, Suever JD, Gerritse B, Merlino JD, et al. Agreement is poor among current criteria used to define response to cardiac resynchronization therapy. *Circulation*. (2010) 121:1985–91. doi: 10.1161/CIRCULATIONAHA.109.910778

18. Tomassoni G. How to define cardiac resynchronization therapy response. *J Innov Card Rhythm Manag*. (2016) 7:S1–7. doi: 10.19102/icrm.2016.070003

19. Gold MR, Rickard J, Daubert JC, Zimmerman P, Linde C. Redefining the classifications of response to cardiac resynchronization therapy: results from the REVERSE study. *JACC Clin Electrophysiol*. (2021) 7:871–80. doi: 10.1016/j.jacep.2020.11.010

20. Sieniewicz BJ, Gould J, Porter B, Sidhu BS, Teall T, Webb J, et al. Understanding non-response to cardiac resynchronisation therapy: common problems and potential solutions. *Heart Fail Rev*. (2019) 24:41–54. doi: 10.1007/s10741-018-9734-8

21. Cheng YJ, Zhang J, Li WJ, Lin XX, Zeng WT, Tang K, et al. More favorable response to cardiac resynchronization therapy in women than in men. *Circ Arrhythm Electrophysiol*. (2014) 7:807–15. doi: 10.1161/CIRCEP.113.001786

22. Arshad A, Moss AJ, Foster E, Padeletti L, Barsheshet A, Goldenberg I, et al. Cardiac resynchronization therapy is more effective in women than in men: the MADIT-CRT (multicenter automatic defibrillator implantation trial with cardiac resynchronization therapy) trial. *J Am Coll Cardiol*. (2011) 57:813–20. doi: 10.1016/j.jacc.2010.06.061

23. Lee AWC, O'Regan DP, Gould J, Sidhu B, Sieniewicz B, Plank G, et al. Sex-Dependent QRS guidelines for cardiac resynchronization therapy using computer model predictions. *Biophys J*. (2019) 117:2375–81. doi: 10.1016/j.bpj.2019.08.025

24. Cheng A, Gold MR, Waggoner AD, Meyer TE, Seth M, Rapkin J, et al. Potential mechanisms underlying the effect of gender on response to cardiac resynchronization therapy: insights from the SMART-AV multicenter trial. *Heart Rhythm*. (2012) 9:736–41. doi: 10.1016/j.hrthm.2011.12.013

25. Kirubakaran S, Ladwiniec A, Arujuna A, Ginks M, McPhail M, Bostock J, et al. Male gender and chronic obstructive pulmonary disease predict a poor clinical response in patients undergoing cardiac resynchronisation therapy. *Int J Clin Pract*. (2011) 65:281–8. doi: 10.1111/j.1742-1241.2010.02491.x

26. van Stipdonk AMW, Vanbelle S, ter Horst IAH, Luermans JG, Meine M, Maass AH, et al. Large variability in clinical judgement and definitions of left bundle branch block to identify candidates for cardiac resynchronisation therapy. *Int J Cardiol*. (2019) 286:61–5. doi: 10.1016/j.ijcard.2019.01.051

27. Surawicz B, Childers R, Deal BJ, Gettes LS. AHA/ACCF/HRS recommendations for the standardization and interpretation of the electrocardiogram. Part III: intraventricular conduction disturbances A scientific statement from the American Heart Association electrocardiography and arrhythmias committee, council on clinical cardiology; the American College of Cardiology foundation; and the heart rhythm society. *J Am Coll Cardiol*. (2009) 53:976–81. doi: 10.1016/j.jacc.2008.12.013

28. Brignole M, Auricchio A, Baron-Esquivias G, Bordachar P, Boriani G, Breithardt OA, et al. 2013 ESC guidelines on cardiac pacing and cardiac resynchronization therapy. *Eur Heart J*. (2013) 34:2281–329. doi: 10.1093/eurheartj/eht150

29. Strauss DG, Selvester RH, Wagner GS. Defining left bundle branch block in the era of cardiac resynchronization therapy. *Am J Cardiol*. (2011) 107:927–34. doi: 10.1016/j.amjcard.2010.11.010

30. Caputo ML, van Stipdonk A, Illner A, D'Ambrosio G, Regoli F, Conte G, et al. The definition of left bundle branch block influences the response to cardiac resynchronization therapy. *Int J Cardiol*. (2018) 269:165–9. doi: 10.1016/j.ijcard.2018.07.060

31. Cleland JG, Abraham WT, Linde C, Gold MR, Young JB, Claude Daubert J, et al. An individual patient meta-analysis of five randomized trials assessing the effects of cardiac resynchronization therapy on morbidity and mortality in patients with symptomatic heart failure. *Eur Heart J*. (2013) 34:3547–56. doi: 10.1093/eurheartj/eht290

32. Cunnington C, Kwok CS, Satchithananda DK, Patwala A, Khan MA, Zaidi A, et al. Cardiac resynchronisation therapy is not associated with a reduction in mortality or heart failure hospitalisation in patients with non-left bundle branch block QRS morphology: meta-analysis of randomised controlled trials. *Heart*. (2015) 101:1456–62. doi: 10.1136/heartjnl-2014-306811

33. Kligfield P, Gettes LS, Bailey JJ, Childers R, Deal BJ, Hancock EW, et al. Recommendations for the standardization and interpretation of the electrocardiogram: part I: the electrocardiogram and its technology: a scientific statement from the American Heart Association electrocardiography and arrhythmias committee, council on clinical cardiology; the American College of Cardiology foundation; and the heart rhythm society. *Circulation*. (2007) 115:1306–24. doi: 10.1161/CIRCULATIONAHA.106.180200

34. van Stipdonk AMW, Ter Horst I, Kloosterman M, Engels EB, Rienstra M, Crijns HJGM, et al. QRS area is a strong determinant of outcome in cardiac resynchronization therapy. *Circ Arrhythm Electrophysiol*. (2018) 11:e006497. doi: 10.1161/CIRCEP.118.006497

35. Tokavanich N, Prasitlumkum N, Mongkonsritragoon W, Trongtorsak A, Cheungpasitporn W, Chokesuwattanaskul R. QRS area as a predictor of cardiac resynchronization therapy response: a systematic review and meta-analysis. *Pacing Clin Electrophysiol*. (2022) 45:393–400. doi: 10.1111/pace.14441

36. Spartalis M, Tzatzaki E, Spartalis E, Damaskos C, Athanasiou A, Livanis E, et al. The role of echocardiography in the optimization of cardiac resynchronization therapy: current evidence and future perspectives. *Open Cardiovasc Med J*. (2017) 11:133–45. doi: 10.2174/1874192401711010133

37. Steffel J, Robertson M, Singh JP, Abraham WT, Bax JJ, Borer JS, et al. The effect of QRS duration on cardiac resynchronization therapy in patients with a narrow QRS complex: a subgroup analysis of the EchoCRT trial. *Eur Heart J*. (2015) 36:1983–9. doi: 10.1093/eurheartj/ehv242

38. Papadopoulos CH, Kyriakides ZS, Maniotis C, Dymarkowski S, Bogaert J. Noninvasive cardiovascular imaging as a guide to cardiac resynchronization therapy. *Hellenic J Cardiol*. (2015) 56(1):72–84.

39. Pitzalis MV, Iacoviello M, Romito R, Massari F, Rizzon B, Luzzi G, et al. Clinical application of echocardiographic findings cardiac resynchronization therapy tailored by echocardiographic evaluation of ventricular asynchrony. *J Am Coll Cardiol*. (2002) 40(9):1615–22. doi: 10.1016/s0735-1097(02)02337-9

40. Pitzalis MV, Iacoviello M, Romito R, Guida P, De Tommasi E, Luzzi G, et al. Ventricular asynchrony predicts a better outcome in patients with chronic heart failure receiving cardiac resynchronization therapy. *J Am Coll Cardiol*. (2005) 45:65–9. doi: 10.1016/j.jacc.2004.09.058

41. Marcus GM, Rose E, Viloria EM, Schafer J, De Marco T, Saxon LA, et al. Septal to posterior wall motion delay fails to predict reverse remodeling or clinical improvement in patients undergoing cardiac resynchronization therapy. *J Am Coll Cardiol*. (2005) 46:2208–14. doi: 10.1016/j.jacc.2005.05.095

42. Stankovic I, Voigt JU, Burri H, Muraru D, Sade LE, Haugaa KH, et al. Imaging in patients with cardiovascular implantable electronic devices: part 1—imaging before and during device implantation. A clinical consensus statement of the European association of cardiovascular imaging (EACVI) and the European heart rhythm association (EHRA) of the ESC. *Eur Heart J Cardiovasc Imaging*. (2024) 25:E1–E32. doi: 10.1093/ehjci/jead272

43. Stătescu C, Ureche C, Enachi Ş, Radu R, Sascău RA. Cardiac resynchronization therapy in non-ischemic cardiomyopathy: role of multimodality imaging. *Diagnostics*. (2021) 11(4):625. doi: 10.3390/diagnostics11040625

44. Parsai C, Bijnens B, Sutherland GR, Baltabaeva A, Claus P, Marciniak M, et al. Toward understanding response to cardiac resynchronization therapy: left ventricular dyssynchrony is only one of multiple mechanisms. *Eur Heart J*. (2009) 30:940–9. doi: 10.1093/eurheartj/ehn481

45. Cazeau S, Toulemont M, Ritter P, Reygner J. Statistical ranking of electromechanical dyssynchrony parameters for CRT. *Open Heart*. (2019) 6(1): e000933. doi: 10.1136/openhrt-2018-000933

46. Achilli A, Peraldo C, Sassara M, Orazi S, Bianchi S, Laurenzi F, et al. Prediction of response to cardiac resynchronization therapy: the selection of candidates for CRT (SCART) study. *PACE*. (2006) 29:S11–19. doi: 10.1111/j.1540-8159.2006.00486.x

47. Richardson M, Freemantle N, Calvert MJ, Cleland JGF, Luigi T. Predicting outcome in severe heart failure. Who will benefit from device therapy (CRT)? *Eur Heart J*. (2007) 28:1827–34. doi: 10.1093/eurheartj/ehm192

48. Maass AH, Vernooy K, Wijers SC, Van 'T Sant J, Cramer MJ, Meine M, et al. Refining success of cardiac resynchronization therapy using a simple score predicting the amount of reverse ventricular remodelling: results from the markers and response to CRT (MARC) study. *Europace*. (2018) 20:e1–e10. doi: 10.1093/europace/euw445

49. Hamdy RM, Osama H, Fereig HM. Evaluation of cardiac mechanical dyssynchrony in heart failure patients using current Echo-Doppler modalities. *J Cardiovasc Imaging*. (2022) 30:307–19. doi: 10.4250/jcvi.2022.0061

50. Szulik M, Streb W, Lenarczyk R, Stabryła-Deska J, Kowalski O, Kalarus Z, et al. The incremental value of right ventricular indices for predicting response to cardiac resynchronization therapy. *J Am Soc Echocardiogr*. (2011) 24:170–179.e3. doi: 10.1016/j.echo.2010.11.015

51. Bragança B, Trêpa M, Santos R, Silveira I, Fontes-Oliveira M, Sousa MJ, et al. Echocardiographic assessment of right ventriculo-arterial coupling: clinical correlates and prognostic impact in heart failure patients undergoing cardiac resynchronization therapy. *J Cardiovasc Imaging*. (2020) 28:109–20. doi: 10.4250/jcvi.2019.0094

52. Dawood M, Elsharkawy E, Nawar M, Sanhoury M. Right ventricular response to cardiac resynchronization therapy: a three-dimensional and speckle tracking echocardiographic study. *Am J Cardiol*. (2023) 205:150–61. doi: 10.1016/j.amjcard.2023.07.105

53. Stassen J, Galloo X, Hirasawa K, Chimed S, Marsan NA, Delgado V, et al. Right ventricular–pulmonary artery coupling in cardiac resynchronization therapy: evolution and prognosis. *ESC Heart Fail*. (2022) 9:1597–607. doi: 10.1002/ehf2.13857

54. Galli E, Smiseth OA, Aalen JM, Larsen CK, Sade E, Hubert A, et al. Prognostic utility of the assessment of diastolic function in patients undergoing cardiac resynchronization therapy. *Int J Cardiol*. (2021) 331:144–51. doi: 10.1016/j.ijcard.2021.01.046

55. Radu A, Zlibut A, Scarlatescu A, Cojocaru C, Bogdan S, Scafa-Udriște A, et al. Cardiac resynchronization therapy and left atrial remodeling: a novel insight? *Biomedicines*. (2023) 11:1156. doi: 10.3390/biomedicines11041156

56. St John Sutton M, Linde C, Gold MR, Abraham WT, Ghio S, Cerkvenik J, et al. Left ventricular architecture, long-term reverse remodeling, and clinical outcome in mild heart failure with cardiac resynchronization results from the REVERSE trial. *JACC Heart Fail*. (2017) 5(3):169–78. doi: 10.1016/j.jchf.2016.11.012

57. Zand S, Sadeghian H, Kazemisaied A, Ashraf H, Lotfi-Tokaldany M, Jalali A. Predicting factors of echocardiographic super-response to cardiac resynchronization therapy. *J Clin Ultrasound*. (2023) 51:388–93. doi: 10.1002/jcu.23380

58. Lafitte S, Garrigue S, Perron J, Bordachar P, Reuter S, Jaïs P, et al. Improvement of left ventricular wall synchronization with multisite ventricular pacing in heart failure: a prospective study using Doppler tissue imaging. *Eur J Heart Fail*. (2004) 6:203–12. doi: 10.1016/j.ejheart.2003.10.008

59. Bader H, Garrigue S, Lafitte S, Reuter S, Jaïs P, Haïssaguerre M, et al. Intra-left ventricular electromechanical asynchrony. *J Am Coll Cardiol*. (2004) 43:248–56. doi: 10.1016/j.jacc.2003.08.038

60. Bax JJ, Molhoek SG, van Erven L, Voogd PJ, Somer S, Boersma E, et al. Usefulness of myocardial tissue Doppler echocardiography to evaluate left ventricular dyssynchrony before and after biventricular pacing in patients with idiopathic dilated cardiomyopathy. *Am J Cardiol*. (2003) 91:94–7. doi: 10.1016/S0002-9149(02)03009-6

61. Gorcsan J, Abraham T, Agler DA, Bax JJ, Derumeaux G, Grimm RA, et al. Echocardiography for cardiac resynchronization therapy: recommendations for performance and reporting-A report from the American society of echocardiography dyssynchrony writing group endorsed by the heart rhythm society. *J Am Soc Echocardiogr*. (2008) 21:191–213. doi: 10.1016/j.echo.2008.01.003

62. Serri K, Lafitte S, Amyot R, Sauvé C, Roudaut R. Echocardiographic evaluation of cardiac dyssynchrony. *Can J Cardiol*. (2007) 23:303–10. doi: 10.1016/S0828-282X(07)70760-2

63. Bax JJ, Bleeker GB, Marwick TH, Molhoek SG, Boersma E, Steendijk P, et al. Left ventricular dyssynchrony predicts response and prognosis after cardiac resynchronization therapy. *J Am Coll Cardiol*. (2004) 44:1834–40. doi: 10.1016/j.jacc.2004.08.016

64. Yu C-M, Fung JW-H, Chan C-K, Chan Y-S, Zhang Q, Lin H, et al. Comparison of efficacy of reverse remodeling and clinical improvement for relatively narrow and wide QRS complexes after cardiac resynchronization therapy for heart failure. *J Cardiovasc Electrophysiol*. (2004) 15:1058–65. doi: 10.1046/j.1540-8167.2004.03648.x

65. Yu CM, Abraham WT, Bax J, Chung E, Fedewa M, Ghio S, et al. Predictors of response to cardiac resynchronization therapy (PROSPECT) - study design. *Am Heart J*. (2005) 149:600–5. doi: 10.1016/j.ahj.2004.12.013

66. Zweerink A, van Everdingen WM, Nijveldt R, Salden OAE, Meine M, Maass AH, et al. Strain imaging to predict response to cardiac resynchronization therapy: a systematic comparison of strain parameters using multiple imaging techniques. *ESC Heart Fail*. (2018) 5:1130–40. doi: 10.1002/ehf2.12335

67. Yu CM, Fung JWH, Zhang Q, Chan CK, Chan YS, Lin H, et al. Tissue Doppler imaging is superior to strain rate imaging and postsystolic shortening on the prediction of reverse remodeling in both ischemic and nonischemic heart failure after cardiac resynchronization therapy. *Circulation*. (2004) 110:66–73. doi: 10.1161/01.CIR.0000133276.45198.A5

68. Stankovic I, Prinz C, Ciarka A, Daraban AM, Kotrc M, Aarones M, et al. Relationship of visually assessed apical rocking and septal flash to response and long-term survival following cardiac resynchronization therapy (PREDICT-CRT). *Eur Heart J Cardiovasc Imaging*. (2016) 17:262–9. doi: 10.1093/ehjci/jev288

69. Larsen CK, Smiseth OA, Duchenne J, Galli E, Aalen JM, Lederlin M, et al. Cardiac magnetic resonance identifies responders to cardiac resynchronization therapy with an assessment of septal scar and left ventricular dyssynchrony. *J Clin Med*. (2023) 12(22):7182. doi: 10.3390/jcm12227182

70. Bustillo S R, Durán A G, Fernández A C, Mas-Stachurska A, Escalante F, Vallès E, et al. Prognostic value of apical rocking and septal flash after cardiac resynchronization. *REC: CardioClinics*. (2023) 58:25–31. doi: 10.1016/j.rccl.2022.06.002

71. Calle S, Delens C, Kamoen V, De Pooter J, Timmermans F. Septal flash: at the heart of cardiac dyssynchrony. *Trends Cardiovasc Med*. (2020) 30:115–22. doi: 10.1016/j.tcm.2019.03.008

72. Duchenne J, Larsen CK, Cvijic M, Galli E, Aalen JM, Klop B, et al. Mechanical dyssynchrony combined with septal scarring reliably identifies responders to cardiac resynchronization therapy. *J Clin Med*. (2023) 12(18):6108. doi: 10.3390/jcm12186108

73. Ghani A, Delnoy PPHM, Ottervanger JP, Misier ARR, Smit JJJ, Adiyaman A, et al. Association of apical rocking with long-term major adverse cardiac events in patients undergoing cardiac resynchronization therapy. *Eur Heart J Cardiovasc Imaging*. (2016) 17:146–53. doi: 10.1093/ehjci/jev236

74. Galli E, Galand V, Le Rolle V, Taconne M, Wazzan AA, Hernandez A, et al. The saga of dyssynchrony imaging: are we getting to the point. *Front Cardiovasc Med*. (2023) 10:1111538. doi: 10.3389/fcvm.2023.1111538

75. Knappe D, Pouleur A-C, Shah AM, Cheng S, Uno H, Hall WJ, et al. Dyssynchrony, contractile function, and response to cardiac resynchronization therapy. *Circ Heart Fail*. (2011) 4:433–40. doi: 10.1161/CIRCHEARTFAILURE.111.962902

76. Bazoukis G, Thomopoulos C, Tse G, Tsioufis K, Nihoyannopoulos P. Global longitudinal strain predicts responders after cardiac resynchronization therapy—a systematic review and meta-analysis. *Heart Fail Rev*. (2022) 27:827–36. doi: 10.1007/s10741-021-10094-w

77. Delgado V, Van Bommel RJ, Bertini M, Borleffs CJW, Marsan NA, Ng ACT, et al. Relative merits of left ventricular dyssynchrony, left ventricular lead position, and myocardial scar to predict long-term survival of ischemic heart failure patients undergoing cardiac resynchronization therapy. *Circulation*. (2011) 123:70–8. doi: 10.1161/CIRCULATIONAHA.110.945345

78. Risum N, Tayal B, Hansen TF, Bruun NE, Jensen MT, Lauridsen TK, et al. Identification of typical left bundle branch block contraction by strain echocardiography is additive to electrocardiography in prediction of long-term outcome after cardiac resynchronization therapy. *J Am Coll Cardiol*. (2015) 66(6):631–41. doi: 10.1016/j.jacc.2015.06.020

79. van der Bijl P, Khidir MJH, Leung M, Yilmaz D, Mertens B, Ajmone Marsan N, et al. Reduced left ventricular mechanical dispersion at 6 months follow-up after cardiac resynchronization therapy is associated with superior long-term outcome. *Heart Rhythm*. (2018) 15:1683–9. doi: 10.1016/j.hrthm.2018.05.005

80. Lumens J, Tayal B, Walmsley J, Delgado-Montero A, Huntjens PR, Schwartzman D, et al. Differentiating electromechanical from non-electrical substrates of mechanical discoordination to identify responders to cardiac resynchronization therapy. *Circ Cardiovasc Imaging*. (2015) 8(9):e003744. doi: 10.1161/CIRCIMAGING.115.003744

81. Voigt J-U, Lindenmeier G, Exner B, Regenfus M, Werner D, Reulbach U, et al. Incidence and characteristics of segmental postsystolic longitudinal shortening in normal, acutely ischemic, and scarred myocardium. *J Am Soc Echocardiogr*. (2003) 16:415–23. doi: 10.1016/S0894-7317(03)00111-1

82. Beela AS, Manetti CA, Lyon A, Prinzen FW, Delhaas T, Herbots L, et al. Impact of estimated left atrial pressure on cardiac resynchronization therapy outcome. *J Clin Med*. (2023) 12:4908. doi: 10.3390/jcm12154908

83. Galli E, Oger E, Aalen JM, Duchenne J, Larsen CK, Sade E, et al. Left atrial strain is a predictor of left ventricular systolic and diastolic reverse remodelling in CRT candidates. *Eur Heart J Cardiovasc Imaging*. (2022) 23:1373–82. doi: 10.1093/ehjci/jeab163

84. D'Andrea A, Scarafile R, Riegler L, Salerno G, Gravino R, Cocchia R, et al. Right atrial size and deformation in patients with dilated cardiomyopathy undergoing cardiac resynchronization therapy. *Eur J Heart Fail*. (2009) 11:1169–77. doi: 10.1093/eurjhf/hfp158

85. Hădăreanu CD, Hădăreanu DR, Stoiculescu FM, Raicea VC, Târtea GC, Florescu C, et al. The added value of advanced echocardiography for the morpho-functional and prognostic evaluation of the right heart in dilated cardiomyopathy: do not forget about the right atrium. *J Clin Med*. (2024) 13(5):1400. doi: 10.3390/jcm13051400

86. Lim P, Buakhamsri A, Popovic ZB, Greenberg NL, Patel D, Thomas JD, et al. Longitudinal strain delay Index by speckle tracking imaging. *Circulation*. (2008) 118:1130–7. doi: 10.1161/CIRCULATIONAHA.107.750190

87. Kloosterman M, Damman K, Van Veldhuisen DJ, Rienstra M, Maass AH. The importance of myocardial contractile reserve in predicting response to cardiac resynchronization therapy. *Eur J Heart Fail*. (2017) 19:862–9. doi: 10.1002/ejhf.768

88. Bijl P VD, Vo NM, Kostyukevich M V, Mertens B, Ajmone Marsan N, Delgado V, et al. Prognostic implications of global, left ventricular myocardial work efficiency before cardiac resynchronization therapy. *Eur Heart J Cardiovasc Imaging*. (2019) 20:1388–94. doi: 10.1093/ehjci/jez095

89. Aalen JM, Donal E, Larsen CK, Duchenne J, Lederlin M, Cvijic M, et al. Imaging predictors of response to cardiac resynchronization therapy: left ventricular work asymmetry by echocardiography and septal viability by cardiac magnetic resonance. *Eur Heart J*. (2020) 41:3813–23. doi: 10.1093/eurheartj/ehaa603

90. Ilardi F, D'andrea A, D'ascenzi F, Bandera F, Benfari G, Esposito R, et al. On behalf of the Working Group Of Echocardiography of the Italian Society of Cardiology Sic. Myocardial work by echocardiography: principles and applications in clinical practice. *J Clin Med*. (2021) 10(19):4521. doi: 10.3390/jcm10194521

91. Li X, Zhang P, Li M, Zhang M. Myocardial work: the analytical methodology and clinical utilities. *Hellenic J Cardiol*. (2022) 68:46–59. doi: 10.1016/j.hjc.2022.07.007

92. Cai Q, Ahmad M. Left ventricular dyssynchrony by three-dimensional echocardiography: current understanding and potential future clinical applications. *Echocardiography*. (2015) 32:1299–306. doi: 10.1111/echo.12965

93. Muraru D, Niero A, Rodriguez-Zanella H, Cherata D, Badano L. Three-dimensional speckle-tracking echocardiography: benefits and limitations of integrating myocardial mechanics with three-dimensional imaging. *Cardiovasc Diagn Ther*. (2018) 8:101–17. doi: 10.21037/cdt.2017.06.01

94. Kapetanakis S, Kearney MT, Siva A, Gall N, Cooklin M, Monaghan MJ. Real-time three-dimensional echocardiography. *Circulation*. (2005) 112:992–1000. doi: 10.1161/CIRCULATIONAHA.104.474445

95. Yu H, Yu W, Cheuk DKL, Wong SJ, Chan GCF, Cheung Y. New three-dimensional speckle-tracking echocardiography identifies global impairment of left ventricular mechanics with a high sensitivity in childhood cancer survivors. *J Am Soc Echocardiogr*. (2013) 26:846–52. doi: 10.1016/j.echo.2013.04.018

96. Spartalis M, Tzatzaki E, Spartalis E, Damaskos C, Athanasiou A, Livanis E, et al. Pathophysiology and current evidence for detection of dyssynchrony. *Cardiol Res*. (2017) 8:179–83. doi: 10.14740/cr598w

97. Al Saikhan L, Park C, Hughes AD. Reproducibility of left ventricular dyssynchrony indices by three-dimensional speckle-tracking echocardiography: the impact of sub-optimal image quality. *Front Cardiovasc Med*. (2019) 6:149. doi: 10.3389/fcvm.2019.00149

98. Chen Z, Ma X, Gao Y, Wu S, Xu N, Chen F, et al. Cardiac magnetic resonance-derived myocardial scar is associated with echocardiographic response and clinical prognosis of left bundle branch area pacing for cardiac resynchronization therapy. *Europace*. (2023) 25(11):euad326. doi: 10.1093/europace/euad326

99. Song Y, Chen X, Yang K, Dong Z, Cui C, Zhao K, et al. Cardiac MRI–derived myocardial fibrosis and ventricular dyssynchrony predict response to cardiac resynchronization therapy in patients with nonischemic dilated cardiomyopathy. *Radiol Cardiothorac Imaging*. (2023) 5(5):e220127. doi: 10.1148/ryct.220127

100. Chan L, Suever J, Fornwalt B, Clement-Guinaudeau S, D'Andrea A, Del Viscovo L, et al. Presence of transmural posterolateral scar by LGE MRI is associated with non-response to CRT. *J Cardiovasc Magn Reson*. (2011) 13:P256. doi: 10.1186/1532-429X-13-S1-P256

101. Atabekov TA, Khlynin MS, Mishkina AI, Batalov RE, Sazonova SI, Krivolapov SN, et al. The value of left ventricular mechanical dyssynchrony and scar burden in the combined assessment of factors associated with cardiac resynchronization therapy response in patients with CRT-D. *J Clin Med*. (2023) 12(6):2120. doi: 10.3390/jcm12062120

102. Gallard A, Hubert A, Smiseth O, Voigt J-U, Le Rolle V, Leclercq C, et al. Prediction of response to cardiac resynchronization therapy using a multi-feature learning method. *Int J Cardiovasc Imaging*. (2021) 37:989–98. doi: 10.1007/s10554-020-02083-1

103. Revah G, Wu V, Huntjens PR, Piekarski E, Chyou JY, Axel L. Cardiovascular magnetic resonance features of mechanical dyssynchrony in patients with left bundle branch block. *Int J Cardiovasc Imaging*. (2016) 32:1427–38. doi: 10.1007/s10554-016-0925-x

104. McDonagh TA, Metra M, Adamo M, Gardner RS, Baumbach A, Böhm M, et al. Corrigendum to: 2021 ESC guidelines for the diagnosis and treatment of acute and chronic heart failure: developed by the task force for the diagnosis and treatment of acute and chronic heart failure of the European Society of Cardiology (ESC) with the special contribution of the heart failure association (HFA) of the ESC. *Eur Heart J*. (2021) 42:4901–4901. doi: 10.1093/eurheartj/ehab670

105. Koshy AO, Swoboda PPP, Gierula J, Witte KK. Cardiac magnetic resonance in patients with cardiac resynchronization therapy: is it time to scan with resynchronization on? *Europace*. (2019) 21:554–62. doi: 10.1093/europace/euy299

106. Hsu JC, Solomon SD, Bourgoun M, McNitt S, Goldenberg I, Klein H, et al. Predictors of super-response to cardiac resynchronization therapy and associated improvement in clinical outcome. *J Am Coll Cardiol*. (2012) 59:2366–73. doi: 10.1016/j.jacc.2012.01.065

107. Pouleur A-C, Knappe D, Shah AM, Uno H, Bourgoun M, Foster E, et al. Relationship between improvement in left ventricular dyssynchrony and contractile function and clinical outcome with cardiac resynchronization therapy: the MADIT-CRT trial. *Eur Heart J*. (2011) 32:1720–9. doi: 10.1093/eurheartj/ehr185

108. Richter S, Gebauer R, Ebert M, Ludueña CM, Scheller D, Lucas J, et al. Electroanatomical mapping–guided left bundle branch area pacing in patients with structural heart disease and advanced conduction abnormalities. *Europace*. (2023) 25:1068–76. doi: 10.1093/europace/euac232

109. Ramachandran R, Chen X, Kramer CM, Epstein FH, Bilchick KC. Singular value decomposition applied to cardiac strain from MR imaging for selection of optimal cardiac resynchronization therapy candidates. *Radiology*. (2015) 275:413–20. doi: 10.1148/radiol.14141578

110. Bivona DJ, Tallavajhala S, Abdi M, Oomen PJA, Gao X, Malhotra R, et al. Cardiac magnetic resonance defines mechanisms of sex-based differences in outcomes following cardiac resynchronization therapy. *Front Cardiovasc Med*. (2022) 9:1007806. doi: 10.3389/fcvm.2022.1007806

111. Ma X, Chen Z, Song Y, Wang J, Yang S, Yu S, et al. CMR feature tracking-based left atrial mechanics predicts response to cardiac resynchronization therapy and adverse outcomes. *Heart Rhythm*. (2024) 21(8):1354–62. doi: 10.1016/j.hrthm.2024.03.028

112. Manca P, Cossa S, Matta G, Scalone A, Tola G, Schintu B, et al. Right ventricular function assessed by cardiac magnetic resonance predicts the response to resynchronization therapy. *J Cardiovasc Med*. (2020) 21(4):299–304. doi: 10.2459/JCM.0000000000000931

113. Domenichini F, Pedrizzetti G. Hemodynamic forces in a model left ventricle. *Phys Rev Fluids*. (2016) 1:083201. doi: 10.1103/PhysRevFluids.1.083201

114. Vallelonga F, Airale L, Tonti G, Argulian E, Milan A, Narula J, et al. Introduction to hemodynamic forces analysis: moving into the new frontier of cardiac deformation analysis. *J Am Heart Assoc*. (2021) 10(24):e023417. doi: 10.1161/JAHA.121.023417

115. Pola K, Roijer A, Borgquist R, Ostenfeld E, Carlsson M, Bakos Z, et al. Hemodynamic forces from 4D flow magnetic resonance imaging predict left ventricular remodeling following cardiac resynchronization therapy. *J Cardiovasc Magn Reson*. (2023) 25(1):45. doi: 10.1186/s12968-023-00955-8

116. Eriksson J, Zajac J, Alehagen U, Bolger AF, Ebbers T, Carlhäll C-J. Left ventricular hemodynamic forces as a marker of mechanical dyssynchrony in heart failure patients with left bundle branch block. *Sci Rep*. (2017) 7:2971. doi: 10.1038/s41598-017-03089-x

117. Pergola V, Cameli M, Mattesi G, Mushtaq S, D'Andrea A, Guaricci AI, et al. Multimodality imaging in advanced heart failure for diagnosis, management and follow-up: a comprehensive review. *J Clin Med*. (2023) 12:7641. doi: 10.3390/jcm12247641

118. Abdellatif YA, Onsy AM, Eldemerdash SEH, Rayan MM, Abu Shouk HM, Badran HA. Prediction of cardiac resynchronization therapy response using quantitative gated myocardial perfusion imaging. *J Innov Card Rhythm Manag*. (2023) 14:5313–21. doi: 10.19102/icrm.2023.14014

frontiers | Frontiers in Cardiovascular Medicine

TYPE Original Research
PUBLISHED 10 February 2025
DOI 10.3389/fcvm.2025.1461744

OPEN ACCESS

EDITED BY
Dominik Buckert,
Ulm University Medical Center, Germany

REVIEWED BY
Mark Gallagher,
St George's University Hospitals NHS Foundation Trust, United Kingdom
Maxim Avanesov,
University Medical Center Hamburg-Eppendorf, Germany

*CORRESPONDENCE
Yanjing Wang
✉ Wangyanjing@jlu.edu.cn

RECEIVED 09 July 2024
ACCEPTED 24 January 2025
PUBLISHED 10 February 2025

CITATION
Pan Y, Zeng H, Liu X, Fu X, Pan L and Wang Y (2025) Anatomical characteristics of mitral isthmus and its spatial relationship with the esophagus in patients undergoing atrial fibrillation ablation using CT angiography. Front. Cardiovasc. Med. 12:1461744. doi: 10.3389/fcvm.2025.1461744

Anatomical characteristics of mitral isthmus and its spatial relationship with the esophagus in patients undergoing atrial fibrillation ablation using CT angiography

Yilin Pan[1,2], Hong Zeng[1], Xin Liu[1], Xiaohang Fu[1], Liyuan Pan[1] and Yanjing Wang[3]*

[1]Department of Cardiology, China-Japan Union Hospital of Jilin University, Changchun, China, [2]Department of Critical Care Medicine, Beijing Anzhen Hospital, Capital Medical University, Beijing, China, [3]Department of Radiology, China-Japan Union Hospital of Jilin University, Changchun, China

Background: This study examines the anatomical characteristics of the mitral isthmus (MI) and its spatial relationship with the esophagus in patients undergoing atrial fibrillation ablation, using cardiovascular computed tomographic angiography (CTA). Understanding this relationship is crucial to minimize the risk of esophageal injuries during ablation procedures.

Methods: The investigation included 300 participants, divided into 200 subjects in the experimental group undergoing atrial fibrillation ablation and 100 in the control group. Detailed CTA scans were used to assess the MI's structure and proximity to the esophagus, employing various measurements like the MI's endocardial length, depth, and its relation to adjacent esophageal anatomy.

Results: The study revealed significant differences in the MI's length and distance measurements between the experimental and control groups, with the former showing greater dimensions, potentially influencing ablation strategies. A substantial proportion of patients exhibited close proximity or direct contact between the MI and the esophagus, emphasizing the importance of pre-procedural imaging in identifying risks for esophageal damage.

Conclusions: Pre-procedural cardiovascular CTA provides essential insights into the MI's anatomical details and its relation to the esophagus, aiding in the customization of ablation strategies to enhance procedural safety and efficacy. The findings highlight the significance of tailored imaging assessments to mitigate esophageal injury risks in atrial fibrillation ablation.

KEYWORDS

atrial fibrillation, ablation, mitral isthmus, esophageal injury, CT angiography

Abbreviations

AF, atrial fibrillation; AEF, atrio-esophageal fistula; CTA, computed tomographic angiography; EAT, epicardial adipose tissue; HDL-C, high-density lipoprotein cholesterol; ICC, intraclass correlation coefficient; LA, left atrium; LDL-C, low-density lipoprotein cholesterol; LIPV, left inferior pulmonary vein; MI, mitral isthmus; PFA, pulsed-field ablation; TC, total cholesterol; TG, triglycerides.

1 Introduction

Atrial fibrillation (AF) is the most prevalent clinical arrhythmia (1). Catheter ablation has emerged as a standard and effective treatment strategy for AF, demonstrating marked superiority over antiarrhythmic drugs in improving clinical symptoms, and enhancing the overall quality of life (2–6).

For patients with persistent AF, the guidelines recommend performing pulmonary vein isolation and considering additional ablation targeting the sustaining substrate of AF (7, 8). The mitral isthmus (MI), located between the left inferior pulmonary vein (LIPV) and the mitral annulus, is a prevalent site for additional linear ablation in AF cases. Given the proximity of the MI region to crucial anatomical structures such as the esophagus, pulmonary arteries and airways, understanding its unique anatomical and morphological variations is imperative.

Atrio-esophageal fistula (AEF) is a rare but severe complication associated with AF radiofrequency ablation procedures. The incidence of AEF is reported to be between 0.1% and 0.04% per ablation procedure (9, 10). However, its manifestation is almost universally fatal, with mortality rates nearing 100% (11, 12). The pivotal element contributing to esophageal injury is the anatomical proximity between the esophagus and the left atrium (LA). Due to this intimate anatomical relationship, ablative energy may permeate the left atrial muscle, causing detrimental effects on the esophageal wall (10). When performing additional linear ablation of the MI—which initiates at the mitral annulus and terminates near the posterior wall of the LA, adjacent to the LIPV—the risk of esophageal injury is significantly increased due to the close spatial relationship between the MI and the esophagus.

Currently, left atrial computed tomographic angiography (CTA) is routinely used in preoperative assessments for patients scheduled for AF ablation. This study used CTA to examine the anatomical details of the MI and its spatial relationship with the adjacent esophagus in patients undergoing AF ablation. The aim was to enhance the understanding of the MI ablation line and its anatomical interrelation with the adjacent esophagus before AF ablation. This enhanced insight might assist operators in choosing appropriate ablation techniques and energy settings, ultimately aimed at minimizing the risk of postoperative esophageal injury complications.

2 Methods

2.1 Patient selection and criteria

This study encompassed 200 patients consecutively enrolled between July 2020 and December 2021 in the Cardiovascular Department of China-Japan Union Hospital of Jilin University. All participants in the experimental group (AF group) underwent radiofrequency ablation. The control group comprised 100 non-AF individuals who also underwent CTA.

The following are the exclusion criteria for the patients:

(1) Patients with esophageal tumors or other conditions that could lead to significant esophageal dilation or thickening.
(2) Patients with a dilated esophagus, defined as an esophageal diameter greater than 20 mm at any level on CTA. To avoid normal variations in the esophageal lumen, such as those caused by recent food or liquid intake, all patients were instructed to fast for at least 6 h before undergoing CTA.
(3) Patients with pulmonary vein anomalies, including common pulmonary veins or pulmonary veins with three or more branches, as identified by CTA.

The study was approved by the Ethics Committee of the China-Japan Union Hospital of Jilin University (approval number: 2023122704), and conducted in accordance with the Declaration of Helsinki. Confidentiality of patient data was strictly maintained throughout the research.

2.2 Data acquisition and analysis

The study employed a third-generation dual-source CT (SOMATOM Force, Siemens, Germany), incorporating both respiratory and electrocardiogram gating. A retrospective electrocardiogram-gated scanning approach was deployed, using iohexol (Omnipaque, 370; 100 ml, GE Healthcare Inc., USA) as the contrast medium. Patients were positioned supine and interfaced with a dual-barrel high-pressure injector. For scan localization, patients were aligned foot-first with arms elevated, holding their breath. The positioning line was established 1.0 cm above the tracheal bifurcation to the cardiac diaphragmatic surface. The high-pressure injector facilitated the intravenous administration of 70 ml of the contrast agent through the right cubital vein at a flow rate of 4.5 ml/s, followed by a 50-ml flush of normal saline at a consistent rate. The region of interest was determined at the LA's level, using an intelligent tracking system to initiate scanning upon detecting a CT attenuation shift to 100 HU.

The scanning parameters comprised a slice thickness of 0.625 mm, dual-energy scanning tube voltages of 90 and Sn150 kV, an effective current of 280 mAs, a tube rotation time of 0.33 s, and a pitch ranging from 0.16 to 0.2.

Data measurements were performed by an independent observer with over 10 years of training and experience in interpreting CTA images. To assess the reliability of the measurements, inter-observer and intra-observer reproducibility were evaluated as follows:For inter-observer reproducibility, a second experienced independent observer performed repeated measurements on the same 30 patients' CTA images, using the same methods and measurement standards. For intra-observer reproducibility, the same observer performed a second round of measurements on the same images to assess consistency over time. Multiple pivotal parameters were diligently assessed for meticulous quantification of the MI. The subsequent sections delineate the specialized methods employed for these precise measurements:

(1) easurement of MI endocardial length:

The exact distance of the MI endocardial length was quantified by measuring the distance (in millimeters) from the bottom of the LIPV to the MI.

(2) easurement of MI linear distance:

Employing a consistent plane as used in the initial measurement, the linear extension of the MI was ascertained (in millimeters).

(3) Measurement of MI depth:

The depth of the MI was determined by measuring the distance (in millimeters) from the specified point on the line from the second measurement to the profoundest endocardial point of the MI.

Depths ≤2 mm characterized the MI as linear, whereas depths >2 mm designated the MI as curved, based on clinical observation and anatomical experience (Figure 1).

A ridge-shaped MI is identified when the endocardial contour prominently extends along a vertical line, forming a slender band on the surface. Conversely, the pouch-shaped morphology comprises the vestibule and the pouch, enhancing the granularity of the anatomical characterization of the MI, as depicted in Figure 2.

The spatial measurements of the MI were meticulously captured using the post-processing techniques of multiplanar reformation and volume rendering facilitated by CT, aiming to assess its proximity to the surrounding esophagus. The measurements were systematically recorded at three strategic locations: the intersection of the upper end of the MI and the LIPV (Level 1), the midpoint of the MI (Level 2), and the level of the mitral annulus (Level 3) (Figure 3). Cross-sectional and sagittal images, as illustrated in Figure 4, were utilized to accurately determine the proximity of the MI to the esophagus at these levels, providing a detailed assessment of their spatial relationship.

The measurements were made to ascertain the minimal spatial distances between the esophagus and the LIPV. Based on these measurements, patients were stratified into two risk groups according to the proximity of the esophagus to the LIPV: a high-risk group (distance from the esophagus to the LIPV < 5 mm) and a low-risk group (distance from the esophagus to the LIPV ≥ 5 mm). To further analyze the impact of age, patients were also stratified into two subgroups based on age: age ≤65 years and age >65 years.

2.3 Statistical analysis

IBM SPSS Statistics 25.0 was utilized for statistical analyses. Continuous variables underwent normality assessment using the Kolmogorov–Smirnov test. Data adhering to normal distribution were presented as mean ± standard deviation ($x \pm S$), with group comparisons via independent-sample or Welch's t tests. Non-normal continuous data were expressed as median[M (P_{25}, P_{75})], analyzed using the Mann–Whitney U test. Categorical data, reported as frequencies or proportions, were evaluated using chi-square, corrected chi-square, or Fisher's exact tests. Pearson's coefficient analyzed correlations in normally distributed bivariate data, while Spearman's coefficient was applied to non-normal variables. A p value <0.05 was considered statistically significant. Both inter-observer and intra-observer reproducibility were evaluated using the intraclass correlation coefficient (ICC), with

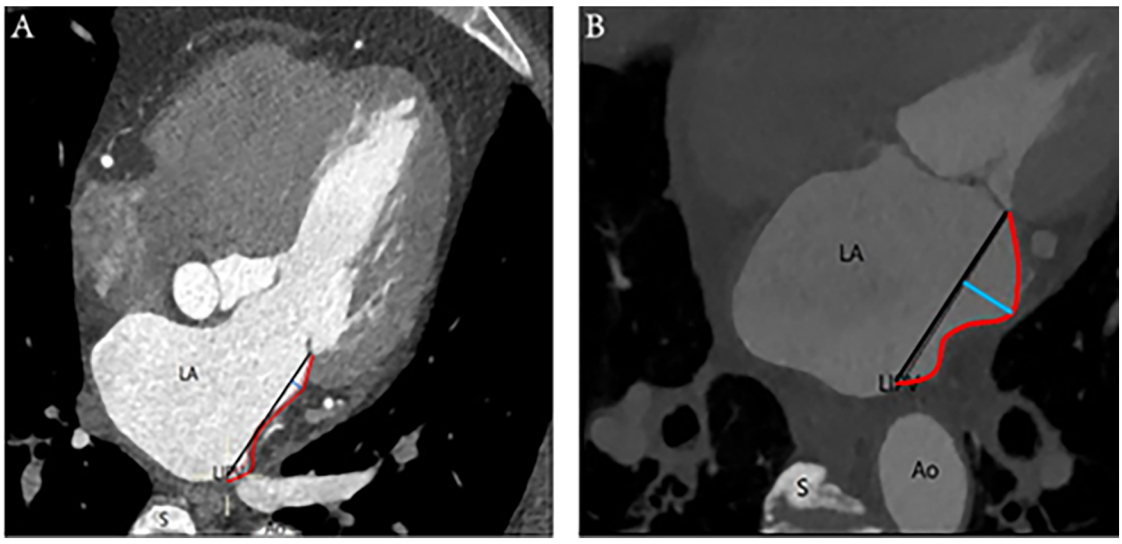

FIGURE 1
Linear and curved MI: **(A)** On the left is an illustration of a linear-shaped MI, whereas **(B)** on the right is a depiction of a curved-shaped MI. The annotations are as follows: Ao, aorta; LA, left atrium; LIPV, left inferior pulmonary vein; S, spine; red curve, distance of MI; black straight line, length of MI; blue straight line, depth of MI.

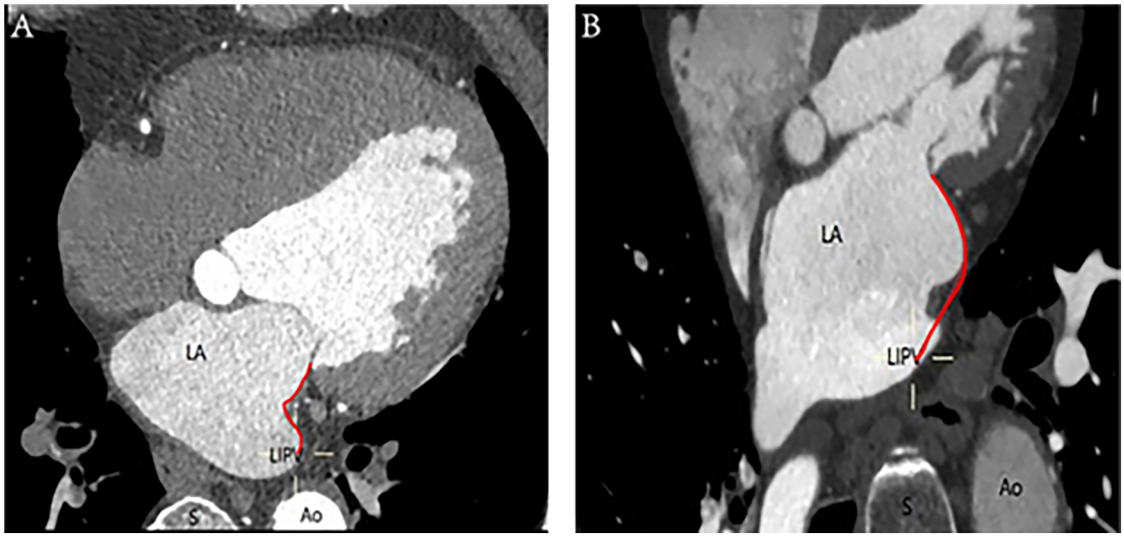

FIGURE 2
Ridge-shaped and pouch-shaped MI: **(A)** The left image depicts a ridge-shaped MI, whereas **(B)** the right image illustrates a pouch-shaped MI. The annotations are as follows: Ao, aorta; LA, left atrium; LIPV, left inferior pulmonary vein; S, spine; red curve, distance of MI.

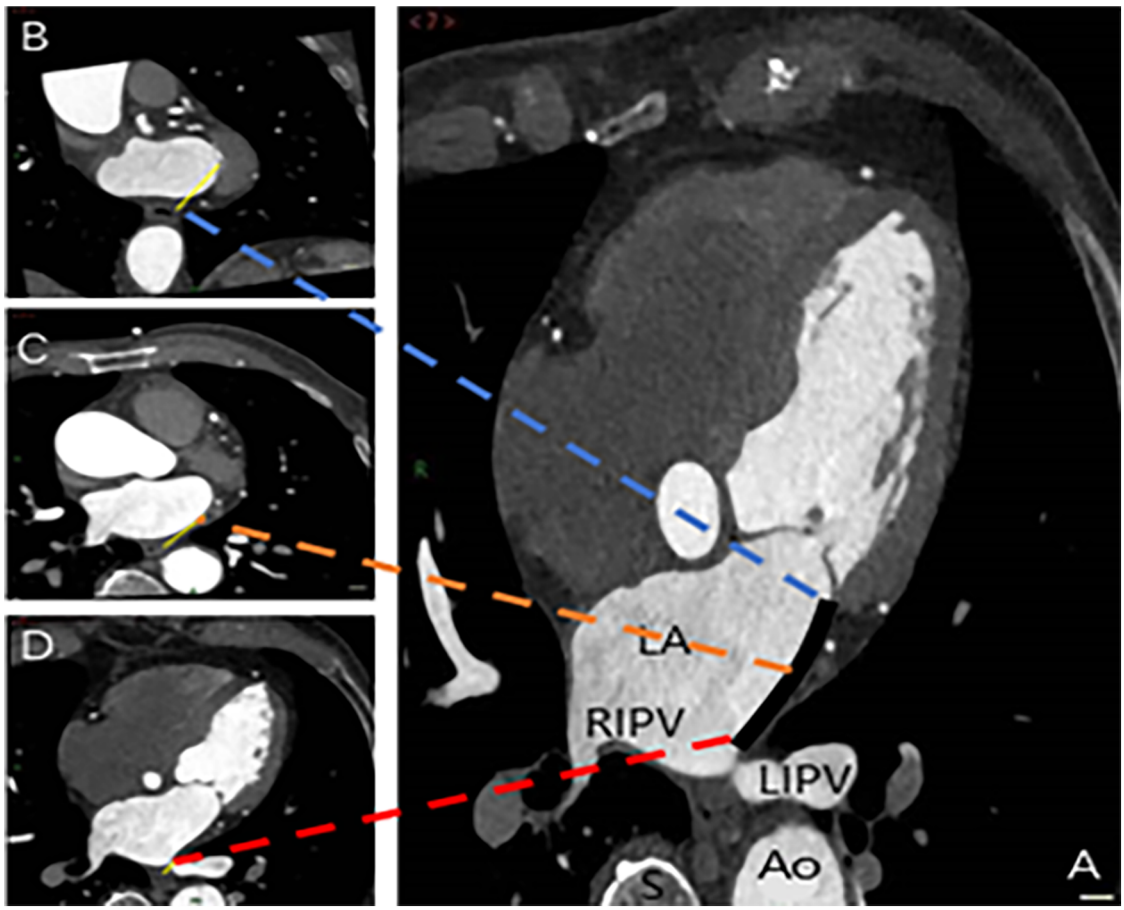

FIGURE 3
Spatial measurements of MI and its proximity to the esophagus. The measurements were taken at three key locations: Level 1 (intersection of the upper end of MI and LIPV) in image D, Level 2 (midpoint of MI) in image C, and Level 3 (level of the mitral annulus) in image B. The annotations are as follows: Ao, aorta; LA, left atrium; LIPV, left inferior pulmonary vein; RIPV, right inferior pulmonary vein; S, spine; black solid line, MI distance measurement; yellow solid line, distance from the three levels to the esophagus.

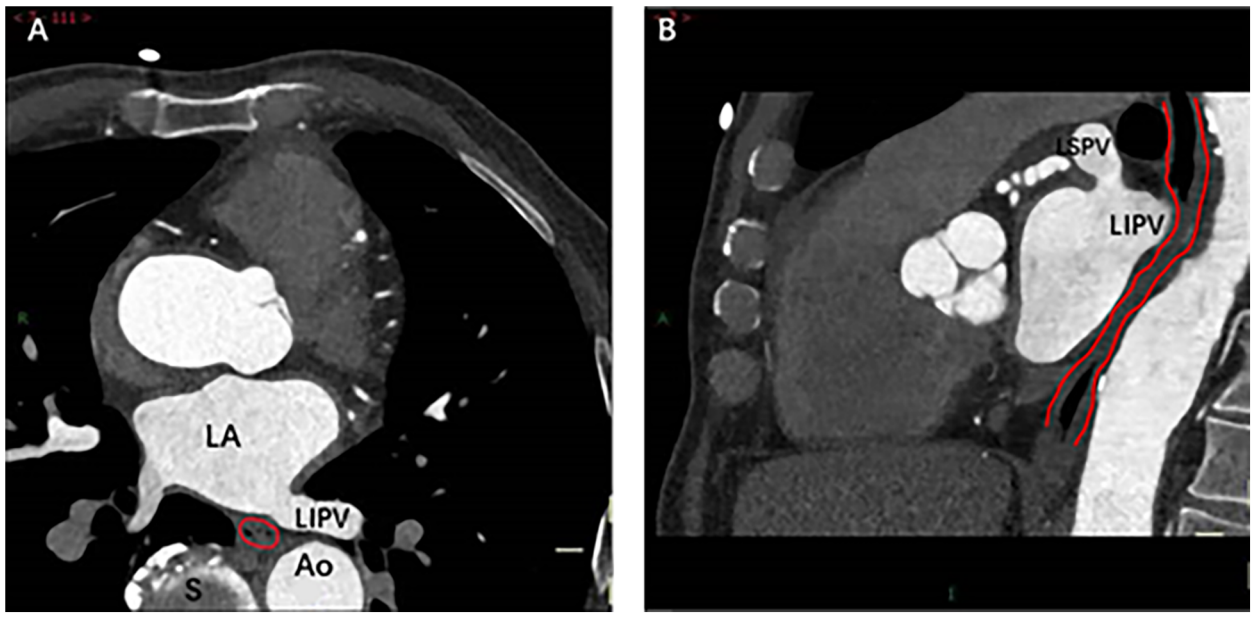

FIGURE 4
Spatial relationship between MI and esophagus. The cross-sectional (A) and sagittal (B) images show direct contact between the bottom of the left lower pulmonary vein and the esophagus (indicated by red lines). Right image: As the esophagus descends, the spatial distance between it and MI gradually increases. Ao, Aorta; LA, left atrium; LIPV, Left lower pulmonary vein; LSPV, Left superior pulmonary vein; S, spine.

ICC values ≥0.75 indicating good agreement between the observers.

3 Results

3.1 Patient characteristics

The study included 300 participants divided into 2 groups: 200 in the AF group and 100 in the control group. A comparison between the AF and control groups revealed no statistically significant differences in demographic and clinical characteristics such as age, sex distribution, history of smoking, alcohol consumption, hypertension, diabetes, and coronary artery disease ($p > 0.05$ for all variables). Likewise, laboratory parameters such as triglycerides (TG), total cholesterol (TC), and low-density lipoprotein cholesterol (LDL-C) exhibited no statistically significant differences between the two groups ($p > 0.05$ for all parameters) (Table 1).

TABLE 1 Comparison of general information between two groups of patients.

	AF group	Control group	*P*
n	200	100	–
Age (year)	62.63 ± 10.22	61.20 ± 14.24	0.370
Sex (men, %)	125 (62.5)	52 (52.0)	0.081
Smoking (cases, %)	60 (30.0)	32 (32.0)	0.723
Alcohol consumption (cases, %)	33 (16.5)	11 (11.0)	0.204
Hypertension (cases, %)	86 (43.0)	54 (54.0)	0.072
Diabetes (cases, %)	32 (16.0)	16 (16.0)	>0.999
Coronary heart disease (cases, %)	92 (46.0)	57 (57.0)	0.072
TG (mmol/L)	1.31 (0.97–1.78)	1.36 (1.06–2.44)	0.097
TC (mmol/L)	4.42 (3.62–5.16)	4.40 (3.75–5.26)	0.659
LDL-C (mmol/L)	2.56 (1.95–3.28)	2.69 (2.09–3.28)	0.345

3.2 Reproducibility testing

The ICC analysis revealed that the intra-observer ICC values for the MI-related anatomical measurements and the three esophageal distance measurements ranged from 0.943 to 0.995, while the inter-observer ICC values ranged from 0.937 to 0.981 (Table 2).

3.3 Imaging results

3.3.1 Comparison of Mi structure and morphology between the two groups

Both the length and distance of the MI were significantly greater in the AF group than in the control group (length: 42.17 ± 9.52 mm vs. 36.45 ± 8.28 mm, $p < 0.001$; distance: 39.20 ± 8.40 mm vs. 34.06 ± 7.35 mm, $p < 0.001$). However, the depths of the MI in both groups did not exhibit a significant difference [3.91 (1.95–6.20) mm in the AF group and 4.25 (2.57–7.14) mm in the control group, $p = 0.105$].

In terms of MI morphology, 27% of participants in the AF group exhibited linear-type MIs and 73% showed curvilinear-type MIs. In comparison, these proportions were 22% and 78%, respectively, in the control group. The distribution of ridge- and

TABLE 2 Reproducibility of MI anatomical measurements and esophageal distances.

Measurement	Intra-Observer ICC	Inter-Observer ICC
MI Endocardial length	0.976	0.975
MI Linear length	0.973	0.981
MI Depth	0.992	0.978
Level 1	0.995	0.947
Level 2	0.982	0.980
Level 3	0.943	0.937

TABLE 3 Comparison of MI structure and morphology between the two groups.

	AF group	Control group	*P*
MI length (mm)	42.17 ± 9.52	36.45 ± 8.28	<0.001
MI distance (mm)	39.20 ± 8.40	34.06 ± 7.35	<0.001
MI depth (mm)	3.91 (1.95,6.20)	4.25 (2.57,7.14)	0.105
Linear-type MI (cases, %)	50 (25.0)	22 (22.0)	0.566
Curved-type MI (cases, %)	150 (75.0)	78 (78.0)	
Ridge-shaped MI (cases, %)	44 (22.0)	18 (18.0)	0.420
Pouch-shaped MI (cases, %)	156 (78.0)	82 (82.0)	

pouch-type MIs also did not differ significantly between the two groups, with $p > 0.05$ in all comparisons (Table 3).

3.3.2 Comparison of MI and esophagus spatial distance based on LIPV distance and age

In this study, patients were divided into high-risk and low-risk groups based on the proximity of the esophagus to the LIPV. Each group was further stratified by age (≤65 years and >65 years).

In the high-risk group, patients aged ≤65 years had a significantly greater minimal spatial distance between the MI and the esophagus at Level 1 in the AF group compared to the control group [AF group: 3.82 (2.46, 4.31) mm vs. control group: 2.67 (1.82, 3.70) mm, $p = 0.018$]. However, no significant differences were observed at Level 2 and Level 3 [Level 2: 21.15 (18.38, 24.84) mm vs. 19.49 (17.55, 23.24) mm, $p = 0.277$; Level 3: 34.20 ± 6.31 mm vs. 31.99 ± 5.76 mm, $p = 0.132$]. In patients aged >65 years, no significant differences were found between the AF group and control group at any of the levels [Level 1: AF group: 3.10 ± 1.02 mm vs. control group: 3.29 ± 1.09 mm, $p = 0.555$; Level 2: 22.13 ± 6.60 mm vs. 23.02 ± 6.10 mm, $p = 0.610$; Level 3: 34.87 ± 8.07 mm vs. 35.65 ± 5.52 mm, $p = 0.682$].

In the low-risk group, patients aged ≤65 years showed no significant differences in the minimal spatial distance between the MI and the esophagus at Level 1 [AF group: 10.36 (6.71, 14.43) mm vs. control group: 7.61 (5.96, 11.95) mm, $p = 0.103$], Level 2 [AF group: 26.1 (22.33, 31.10) mm vs. control group: 24.78 (21.44, 31.22) mm, $p = 0.559$], or Level 3 [AF group: 37.92 ± 8.44 mm vs. control group: 37.16 ± 7.95 mm, $p = 0.658$]. For patients aged >65 years, the AF group had a smaller minimal spatial distance at Level 1 compared to the control group, but this difference was not statistically significant [AF group: 7.92 (5.79, 13.23) mm vs. control group: 10.74 (7.67, 13.71) mm, $p = 0.225$]. No significant differences were found at Level 2 [AF group: 27.43 ± 7.89 mm vs. control group: 28.58 ± 7.79 mm, $p = 0.578$] or Level 3 [AF group: 40.29 ± 9.84 mm vs. control group: 38.21 ± 6.59 mm, $p = 0.311$] (Table 4).

4 Discussion

This study aimed to explore the anatomical characteristics of the MI and its spatial relationship with the esophagus in patients undergoing AF ablation using cardiovascular CTA. The main findings of this study were as follows: (1) Patients with AF exhibited a significantly longer MI length and greater MI distance compared to controls, which could increase procedural complexity during ablation; (2) A notable proportion of patients had a minimal spatial distance of less than 5 mm between the MI and the esophagus, particularly in the high-risk group, emphasizing the importance of pre-procedural imaging; (3) Younger patients (≤65 years) in the high-risk group demonstrated a significantly greater distance at Level 1 compared to controls, possibly influenced by epicardial adipose tissue (EAT). These findings are further elaborated and discussed below.

TABLE 4 Comparison of spatial distance between esophagus and LIPV across different age groups and measurement levels in AF and control patients.

Group	Age	Measurement level	AF group	Control group	*P*
High-risk	≤65	Level 1	3.82 (2.46,4.31)	2.67 (1.82,3.70)	0.018
		Level 2	21.15 (18.38,24.84)	19.49 (17.55,23.24)	0.277
		Level 3	34.20 ± 6.31	31.99 ± 5.76	0.132
	>65	Level 1	3.10 ± 1.02	3.29 ± 1.09	0.555
		Level 2	22.13 ± 6.60	23.02 ± 6.10	0.610
		Level 3	34.87 ± 8.07	35.65 ± 5.52	0.682
Low-risk	≤65	Level 1	10.36 (6.71,14.43)	7.61 (5.96,11.95)	0.103
		Level 2	26.1 (22.33,31.10)	24.78 (21.44,31.22)	0.559
		Level 3	37.92 ± 8.44	37.16 ± 7.95	0.658
	>65	Level 1	7.92 (5.79,13.23)	10.74 (7.67,13.71)	0.225
		Level 2	27.43 ± 7.89	28.58 ± 7.79	0.578
		Level 3	40.29 ± 9.84	38.21 ± 6.59	0.311

4.1 Analysis of the characteristics of MI structure and morphology

This study assessed the endocardial length of the MI in two distinct groups: the AF and control groups, yielding a mean length of 42.17 ± 9.52 mm and 36.45 ± 8.28 mm, respectively. The linear distance of the MI was determined to be 39.20 ± 8.40 mm in the AF group and 34.06 ± 7.35 mm in the control group, aligning closely with the findings of Wittkampf et al. (13), who reported an analogous MI length of 35 ± 7 mm in a cadaveric anatomical study. In the present study, the AF group demonstrated an enhanced MI length and linear distance compared with the control group. Complementary observations of Scherr et al. (14) suggested that the MI length acted as a determinant independent risk factor, obstructing the attainment of a definitive bidirectional conduction block amid ablation procedures. This indicated that patients with AF possessing extended MI segments might experience protracted ablation periods and an escalation in procedural intricacies, necessitating thoughtful strategic planning and execution.

A significant finding of this study based on the measurements of MI depth was as follows: a modest proportion of MIs was linear type, irrespective of the presence of AF, whereas a substantial majority (>75%) exhibited curvilinear configurations. The prevalence of curvilinear MIs was due to their non-flat endocardial surfaces, complicating the attainment of optimal catheter–target contact during ablation. Furthermore, most patients (>78%) displayed a pouch-like morphology, contrasting with a ridge-like structure. Pouch-like configurations, forming concave atrial vestibules and recesses, posed potential hindrances to effective catheter–tissue contact during ablation, escalating the risk of catheter entrapment. Yokokawa et al. (15) confirmed these findings, illustrating increased challenges in achieving a complete bidirectional block when the pouch-like MI depth exceeded 10 mm. These observations underscored the critical influence of the distinct anatomical features of the MI on procedural complexity and success.

4.2 Analysis of the spatial relationship between the MI and the esophagus

In a detailed comparative analysis of patients in the high-risk group, those aged <65 years exhibited a significantly greater minimal spatial distance between the upper border of the MI and the LIPV junction (Level 1) compared to the control group. This finding suggests that for younger patients in the high-risk group, the proximity of the esophagus to the LIPV may be notably altered in patients with AF, potentially contributing to a greater distance at Level 1. A conceivable explanation for the extended distance at Level 1 in patients with AF is the presence of EAT. Previous studies, including those by Le Jemtel et al. (16)and Ahn et al. (17), have highlighted EAT volume as a significant intrinsic risk factor for AF, with pronounced left atrial (LA) and EAT volumes identified in patients with AF.

The accumulation of EAT in AF patients may create additional mechanical separation between the MI and the esophagus, resulting in a greater distance at Level 1 compared to those without AF. This phenomenon is less pronounced at Level 2 and Level 3, where the inherent distances between the MI and the esophagus are greater, making it less likely for EAT to cause a notable effect. Although this hypothesis provides a plausible explanation for the observed findings, further research is necessary to explore the complex relationship between AF and EAT. More comprehensive studies could help clarify whether EAT directly contributes to the altered spatial relationships observed in the high-risk AF patients, particularly those under the age of 65.

In some patients, the MI measurement points near the upper border of the LIPV were found to be less than 5 mm from the esophagus, placing these tissues at high risk of thermal injury during ablation. Given this close anatomical proximity, careful consideration of tailored ablation strategies is essential to minimize complications and enhance procedural safety.

Several practical approaches can be employed to enhance procedural safety in these cases. Modifying ablation parameters is essential, as studies suggest that reducing ablation power (<25–30 W) and shortening lesion duration (<20 s) can significantly lower the risk of esophageal injury (18, 19). Alternatively, high-power short-duration protocols (e.g., 40–50 W for 5–15 s) produce more controlled and superficial lesions, reducing thermal penetration (19). Recent advancements in esophageal protection techniques also highlight the potential of thermal control devices. For instance, the IMPACT study demonstrated that using the ensoETM thermal control device during ablation procedures significantly reduced the incidence of esophageal thermal injuries without affecting procedural efficacy or duration (20). This finding underscores the importance of incorporating esophageal protection measures, such as active cooling, into procedural planning to minimize complications and improve patient outcomes. Alternative energy modalities, such as cryoablation and pulsed-field ablation (PFA), also show promise in reducing esophageal complications (21, 22). PFA, in particular, uses non-thermal mechanisms to induce tissue necrosis and has been shown to be safer for the esophagus in both preclinical and early clinical studies (23). Additionally, intraoperative esophageal temperature monitoring with probes provides real-time feedback to adjust energy delivery when necessary, while esophageal cooling systems can help maintain the esophageal wall temperature below the injury threshold (24, 25). Despite these benefits, challenges such as probe positioning or potential mechanical injury must also be considered (26).

Integrating these strategies with individualized planning and patient selection can minimize esophageal injury risks and improve outcomes in high-risk patients. This study translates anatomical findings into actionable guidance for interventional cardiologists managing complex ablation cases.

5 Limitations

This study had certain limitations. First, the retrospective design of the study may limit the generalizability of the results

and the applicability of the findings to clinical practice. Second, due to the lack of detailed intraoperative data, such as ablation power and duration, and patient outcome data, the clinical implications of these findings, particularly in terms of risk stratification or the practical application of CTA-based measurements before pulmonary vein ablation, remain unclear. Future research will integrate these data to better understand the relationship between mitral isthmus characteristics and ablation difficulty and assess whether these findings can contribute to improving procedural safety and efficacy. Third, potential confounders in the CTA-based measurements, such as variations in esophageal distension, vertebral changes, and anatomical differences, could have introduced biases. Finally, CTA has limitations in accurately measuring very thin structures like the myocardial thickness of the mitral isthmus, and we plan to explore this further using Cardiovascular Magnetic Resonance in future studies.

6 Conclusions

Cardiovascular CTA has equipped interventional physicians with a detailed understanding of the anatomical characteristics of MI ablation lines in patients with AF and their spatial relationship with the adjacent esophagus, before beginning ablation procedures. This invaluable insight has facilitated the meticulous selection of personalized ablation protocols and energy parameters, consequently reducing the potential risks and complications associated with esophageal injuries.

Data availability statement

The original contributions presented in the study are included in the article/Supplementary Material, further inquiries can be directed to the corresponding authors.

Ethics statement

The studies involving humans were approved by Ethics Committee of the China-Japan Union Hospital of Jilin University. The studies were conducted in accordance with the local legislation and institutional requirements. The ethics committee/institutional review board waived the requirement of written informed consent for participation from the participants or the participants' legal guardians/next of kin because The study was exempted from written informed consent due to its retrospective nature, minimal risk, and the use of anonymized data.

Author contributions

YP: Conceptualization, Data curation, Investigation, Resources, Software, Writing – original draft. HZ: Funding acquisition, Methodology, Project administration, Resources, Supervision, Validation, Writing – review & editing. XL: Data curation, Validation, Writing – original draft. XF: Methodology, Visualization, Writing – original draft. LP: Writing – original draft. YW: Supervision, Validation, Writing – review & editing.

Funding

The author(s) declare financial support was received for the research, authorship, and/or publication of this article. This research was funded by the Jilin Provincial Natural Science Foundation, grant number 20200201332JC. The grant provider did not participate in the design, execution, or reporting of the study.

Conflict of interest

The authors declare that the research was conducted in the absence of any commercial or financial relationships that could be construed as a potential conflict of interest.

Publisher's note

References

1. Brundel B, Ai X, Hills MT, Kuipers MF, Lip GYH, de Groot NMS. Atrial fibrillation. *Nat Rev Dis Primers*. (2022) 8:21. doi: 10.1038/s41572-022-00347-9

2. Parameswaran R, Al-Kaisey AM, Kalman JM. Catheter ablation for atrial fibrillation: current indications and evolving technologies. *Nat Rev Cardiol*. (2021) 18:210–25. doi: 10.1038/s41569-020-00451-x

3. Sohns C, Fox H, Marrouche NF, Crijns H, Costard-Jaeckle A, Bergau L, et al. Catheter ablation in end-stage heart failure with atrial fibrillation. *N Engl J Med*. (2023) 389:1380–9. doi: 10.1056/NEJMoa2306037

4. Al-Kaisey AM, Parameswaran R, Bryant C, Anderson RD, Hawson J, Chieng D, et al. Atrial fibrillation catheter ablation vs medical therapy and psychological distress: a randomized clinical trial. *JAMA*. (2023) 330:925–33. doi: 10.1001/jama.2023.14685

5. Alhassan HA, Kainat A, Donohue J, Baumgartner SJ, Akunor H, Saba S, et al. Safety of catheter ablation therapy for atrial fibrillation in cardiac amyloidosis. *J Am Heart Assoc*. (2023) 12:e029339. doi: 10.1161/JAHA.122.029339

6. Davong B, Adeliño R, Delasnerie H, Albenque JP, Combes N, Cardin C, et al. Pulsed-field ablation on mitral isthmus in persistent atrial fibrillation: preliminary data on efficacy and safety. *JACC Clin Electrophysiol*. (2023) 9:1070–81. doi: 10.1016/j.jacep.2023.03.021

7. Yang G, Zheng L, Jiang C, Fan J, Liu X, Zhan X, et al. Circumferential pulmonary vein isolation plus low-voltage area modification in persistent atrial fibrillation: the STABLE-SR-II trial. *JACC Clin Electrophysiol*. (2022) 8:882–91. doi: 10.1016/j.jacep.2022.03.012

8. Mulder MJ, Kemme MJB, Allaart CP. Radiofrequency ablation to achieve durable pulmonary vein isolation. *Europace*. (2022) 24:874–86. doi: 10.1093/europace/euab279

9. Deneke T, Nentwich K, Halbfaß P, Sommer P. There is glory in prevention!-atrio-esophageal fistula and atrial fibrillation ablation. *Europace*. (2021) 23:491–3. doi: 10.1093/europace/euaa417

10. Barbhaiya CR, Kumar S, Guo Y, Zhong J, John RM, Tedrow UB, et al. Global survey of esophageal injury in atrial fibrillation ablation: characteristics and outcomes of esophageal perforation and fistula. *JACC Clin Electrophysiol*. (2016) 2:143–50. doi: 10.1016/j.jacep.2015.10.013

11. Jehaludi A, Heist EK, Giveans MR, Anand R. Retrospective review of 65 atrioesophageal fistulas post atrial fibrillation ablation. *Indian Pacing Electrophysiol J*. (2018) 18:100–7. doi: 10.1016/j.ipej.2018.02.002

12. Han HC, Ha FJ, Sanders P, Spencer R, Teh AW, O'Donnell D, et al. Atrioesophageal fistula: clinical presentation, procedural characteristics, diagnostic investigations, and treatment outcomes. *Circ Arrhythm Electrophysiol*. (2017) 10:e005579. doi: 10.1161/CIRCEP.117.005579

13. Wittkampf FH, van Oosterhout MF, Loh P, Derksen R, Vonken EJ, Slootweg PJ, et al. Where to draw the mitral isthmus line in catheter ablation of atrial fibrillation: histological analysis. *Eur Heart J*. (2005) 26:689–95. doi: 10.1093/eurheartj/ehi095

14. Scherr D, Derval N, Sohal M, Pascale P, Wright M, Jadidi A, et al. Length of the mitral isthmus but not anatomical location of ablation line predicts bidirectional mitral isthmus block in patients undergoing catheter ablation of persistent atrial fibrillation: a randomized controlled trial. *J Cardiovasc Electrophysiol*. (2015) 26:629–34. doi: 10.1111/jce.12667

15. Yokokawa M, Sundaram B, Garg A, Stojanovska J, Oral H, Morady F, et al. Impact of mitral isthmus anatomy on the likelihood of achieving linear block in patients undergoing catheter ablation of persistent atrial fibrillation. *Heart Rhythm*. (2011) 8:1404–10. doi: 10.1016/j.hrthm.2011.04.030

16. Le Jemtel TH, Samson R, Ayinapudi K, Singh T, Oparil S. Epicardial adipose tissue and cardiovascular disease. *Curr Hypertens Rep*. (2019) 21:36. doi: 10.1007/s11906-019-0939-6

17. Ahn J, Shin SY, Shim J, Kim YH, Han SJ, Choi EK, et al. Association between epicardial adipose tissue and embolic stroke after catheter ablation of atrial fibrillation. *J Cardiovasc Electrophysiol*. (2019) 30:2209–16. doi: 10.1111/jce.14154

18. Tilz RR, Chun KR, Metzner A, Burchard A, Wissner E, Koektuerk B, et al. Unexpected high incidence of esophageal injury following pulmonary vein isolation using robotic navigation. *J Cardiovasc Electrophysiol*. (2010) 21:853–8. doi: 10.1111/j.1540-8167.2010.01742.x

19. Winkle RA, Mohanty S, Patrawala RA, Mead RH, Kong MH, Engel G, et al. Low complication rates using high power (45–50 W) for short duration for atrial fibrillation ablations. *Heart Rhythm*. (2019) 16:165–9. doi: 10.1016/j.hrthm.2018.11.031

20. Leung LWM, Bajpai A, Zuberi Z, Li A, Norman M, Kaba RA, et al. Randomized comparison of oesophageal protection with a temperature control device: results of the IMPACT study. *Europace*. (2021) 23:205–15. doi: 10.1093/europace/euaa276

21. Moreira W, Manusama R, Timmermans C, Ghaye B, Philippens S, Wellens HJ, et al. Long-term follow-up after cryothermic ostial pulmonary vein isolation in paroxysmal atrial fibrillation. *J Am Coll Cardiol*. (2008) 51:850–5. doi: 10.1016/j.jacc.2007.08.065

22. Koruth JS, Kuroki K, Kawamura I, Brose R, Viswanathan R, Buck ED, et al. Pulsed field ablation versus radiofrequency ablation: esophageal injury in a novel porcine model. *Circ Arrhythm Electrophysiol*. (2020) 13:e008303. doi: 10.1161/CIRCEP.119.008303

23. Cochet H, Nakatani Y, Sridi-Cheniti S, Cheniti G, Ramirez FD, Nakashima T, et al. Pulsed field ablation selectively spares the oesophagus during pulmonary vein isolation for atrial fibrillation. *Europace*. (2021) 23:1391–9. doi: 10.1093/europace/euab090

24. Redfearn DP, Trim GM, Skanes AC, Petrellis B, Krahn AD, Yee R, et al. Esophageal temperature monitoring during radiofrequency ablation of atrial fibrillation. *J Cardiovasc Electrophysiol*. (2005) 16:589–93. doi: 10.1111/j.1540-8167.2005.40825.x

25. Arruda MS, Armaganijan L, Di Biase L, Rashidi R, Natale A. Feasibility and safety of using an esophageal protective system to eliminate esophageal thermal injury: implications on atrial-esophageal fistula following AF ablation. *J Cardiovasc Electrophysiol*. (2009) 20:1272–8. doi: 10.1111/j.1540-8167.2009.01536.x

26. Cummings JE, Schweikert RA, Saliba WI, Burkhardt JD, Brachmann J, Gunther J, et al. Assessment of temperature, proximity, and course of the esophagus during radiofrequency ablation within the left atrium. *Circulation*. (2005) 112:459–64. doi: 10.1161/CIRCULATIONAHA.104.509612

frontiers | Frontiers in Cardiovascular Medicine

TYPE Original Research
PUBLISHED 27 February 2025
DOI 10.3389/fcvm.2025.1462263

OPEN ACCESS

EDITED BY
Matthias Renker,
Kerckhoff Clinic, Germany

REVIEWED BY
Fabiana Isabella Gambarin,
Fondazione Salvatore Maugeri, Veruno (IRCCS), Italy
Giulia Iannaccone,
Catholic University of the Sacred Heart, Italy
Cristina Tudoran,
Victor Babes University of Medicine and Pharmacy, Romania

*CORRESPONDENCE
Dengfeng Gao
✉ gaomedic@mail.xjtu.edu.cn

RECEIVED 09 July 2024
ACCEPTED 14 February 2025
PUBLISHED 27 February 2025

CITATION
Liu C, Ma Y, Qiao S, Li K, Qi M, Gu C, Zhang L, Wei J and Gao D (2025) Impact of self-reported SARS-CoV-2 antibody positivity on cardiac structure and function: findings from UK Biobank CMR cohort.
Front. Cardiovasc. Med. 12:1462263.
doi: 10.3389/fcvm.2025.1462263

Impact of self-reported SARS-CoV-2 antibody positivity on cardiac structure and function: findings from UK Biobank CMR cohort

Chang Liu[1], Yao Ma[1], Shiyuan Qiao[1], Kexin Li[1], Mengyao Qi[1], Chunyu Gu[1,2], Lanxin Zhang[1,2], Jia Wei[1] and Dengfeng Gao[1]*

[1]Department of Cardiology, The Second Affiliated Hospital of Xi'an Jiaotong University, Xi'an, China, [2]Department of Radiology, Affiliated Hospital of Shaanxi University of Chinese Medicine, Xianyang, China

Background: SARS-CoV-2 antibody positivity, whether due to natural infection or vaccination, is known to be associated with specific cardiac and vascular damage, yet its impact on cardiac structure and function in prospective cohorts remains incompletely understood.
Objective: We aimed to assess cardiac changes in the UK Biobank cohort among individuals with self-reported seropositive results for SARS-CoV-2 antibodies.
Methods: UK Biobank participants with self-reported serological results for SARS-CoV-2 antibodies, who underwent their first cardiac magnetic resonance (CMR) scan after 2019 were included. Cardiac changes potentially associated with SARS-CoV-2 antibody positivity were assessed, with measurements of left ventricular (LV) parameters, including volume, dimensions, wall thickness, myocardial mass, cardiac output (CO), and cardiac index (CI), manually extracted from the CMR images. Propensity score matching (PSM) was used to pair seropositive and seronegative individuals. Native T1 was used to assess the within-subject changes in seropositive individuals. Logistic regression was performed to assess the association between SARS-CoV-2 antibody status and the incidence of LV hypertrophy.
Results: A total of 720 participants were included, with 453 individuals self-reporting as SARS-CoV-2 antibody positive. After PSM, 261 participants remained in each group. Over an average follow-up period of 110 days, significant decreases in CO and CI were observed in the paired participants. Additionally, native T1 values appeared to be elevated in seropositive participants (852.77 ± 53.55 ms vs. 860.01 ± 47.81 ms, $P = 0.012$). Logistic regression analysis in the overall cohort indicated an association between SARS-CoV-2 antibody positivity and an increased risk of LV hypertrophy, with an adjusted odds ratio of 3.257 [95% CI (1.036–10.239), $P = 0.043$].
Conclusions: Our findings suggest subtle cardiac changes associated with SARS-CoV-2 antibody positivity within approximately hundred days. SARS-CoV-2 antibody positivity appeared to be associated with an increased risk of LV hypertrophy. However, these results are exploratory, and further longitudinal studies with extended follow-up are needed to better understand the long-term cardiac impact of SARS-CoV-2 antibody positivity.

KEYWORDS

UK Biobank, COVID-19, cardiovascular magnetic resonance cohort, native T1, left ventricular hypertrophy

1 Introduction

As the Coronavirus disease 2019 (COVID-19) pandemic persists worldwide, Severe Acute Respiratory Syndrome Coronavirus 2 (SARS-CoV-2) not only targets the respiratory system through the angiotensin-converting enzyme 2 receptor (1), but also inflicts damage on cardiovascular system, leading to myocardial injury (2).

Concurrently, the numerous sequelae of SARS-CoV-2 infection have led to a significant increase in cardiovascular adverse events, highlighting the crucial need for ongoing monitoring and management of cardiovascular health in patients recovering from COVID-19 (3–7). Moreover, there have been reports of cardiac side effects following COVID-19 vaccination, including myocarditis and pericarditis, particularly in younger individuals. These adverse events further highlight the importance of monitoring cardiac health not only in those infected with SARS-CoV-2 but also in vaccinated individuals (8, 9).

Cardiovascular magnetic resonance (CMR) examination serves as an essential and valuable tool for assessing myocardial structure and cardiac function. Advanced CMR techniques such as native T1 mapping, extracellular volume (ECV) fraction, and late gadolinium enhancement (LGE) enable the detection of subtle changes in myocardial tissue. The American College of Cardiology, the European Society of Cardiology, and the Society for Cardiovascular Magnetic Resonance have collectively acknowledged the value of CMR in evaluating the structural and functional repercussions of SARS-CoV-2 infection (10, 11).

Long COVID, characterized by persistent symptoms and long-term complications following acute SARS-CoV-2 infection, has also been associated with significant cardiovascular issues (12). The UK Biobank conducted a monthly follow-up survey for COVID-19 patients within its cohort. From May to November 2020, among the 10,878 COVID-19 patients surveyed, a subset exhibited symptoms suggestive of cardiovascular involvement, including shortness of breath (4.30%), wheezing (2.21%), chest pain (1.84%), nausea (1.93%), and increased fatigue (10.08%). Of these patients, 3.37% required medical intervention for COVID-19-related symptoms, and 0.21% required hospitalization.

A cross-sectional study of CMR parameters in SARS-CoV-2 seropositive patients from the UK Biobank cohort revealed that, beyond traditional cardiovascular risk factors, pre-existing adverse CMR phenotypes may be associated with susceptibility to COVID-19 (13). With the gradual release of subsequent CMR examinations conducted after 2019 for repeat imaging visits by the UK Biobank, we are now able to investigate whether there are any subtle changes in CMR parameters among participants with self-reported positive SARS-CoV-2 antibody test results.

2 Methods

2.1 Study design and participants

The UK Biobank established a population-based cohort study, recruiting 502,357 participants aged 39 to 70 years at baseline from 2006 to 2010. Among these, 69,902 participants underwent at least one long axis heart CMR scan(data field 20208), while a total of 5,154 participants completed a first repeat CMR scan, and 811 of these participants had their initial CMR scan after January 1, 2019. Participants for this study were selected based on having both initial and follow-up CMR scans and at least one SARS-CoV-2 antibody test result.

To ensure representative and unbiased results, we selected participants who had completed their first CMR scan after January 1, 2019, and whose antibody test results were available between the initial and follow-up scans. The participant selection process is illustrated in Figure 1. This selection process ensured that the study cohort included individuals who had both pre- and post-SARS-CoV-2 antibody test result data.

Additionally, 201,890 participants had at least one self-reported SARS-CoV-2 antibody test result (data field 27,981), of which 720 participants' first antibody test result was obtained between the initial and follow-up CMR scans.

Among the 453 seropositive participants, 392 had experimental shortened Modified Look-Locker Inversion Recovery (shMOLLI) sequence images (data field 20,214). After performing 1:1 propensity score matching (PSM), 261 participants were retained in both the SARS-CoV-2 antibody positive and negative groups.

A list of International Classification of Disease (ICD) codes used to define baseline diseases is provided in Supplementary Table S1 (data field 41,270).

2.2 SARS-CoV-2 antibody test

Participants were initially categorized as positive or negative based on self-reported results using the Fortress Rapid Test kit or AbC-19TM Rapid Test kit between February 2021 and July 2021. These antibody results were collected over two rounds during this six-month period. The data were subsequently compiled and made available by the UK Biobank Participant Resource Centre. For the analysis, the first available result for each participant was used to determine whether they tested positive for SARS-CoV-2 antibodies. The antibody results obtained in this manner were collected at least one year after the initial CMR scan of the imaging follow-up cohort included in the study.

2.3 CMR scanning protocol and cardiac parameters

The UK Biobank plans to recall approximately 100,000 participants for a comprehensive CMR examination as part of their multi-organ, multi-modality imaging visit (14). The CMR protocol was previously described in detail, and in summary, all steady-state free precession cine imaging of CMR long axis images were conducted using a 1.5 Tesla scanner, with no MR-contrast enhancement for safety reasons (15). CMR image analysis was performed by two radiologists specializing in MRI and one cardiovascular specialist using cvi42 image post-processing software (Version 5.11, Circle Cardiovascular Imaging Inc., Calgary, Canada). Manual contouring was employed to extract left ventricular

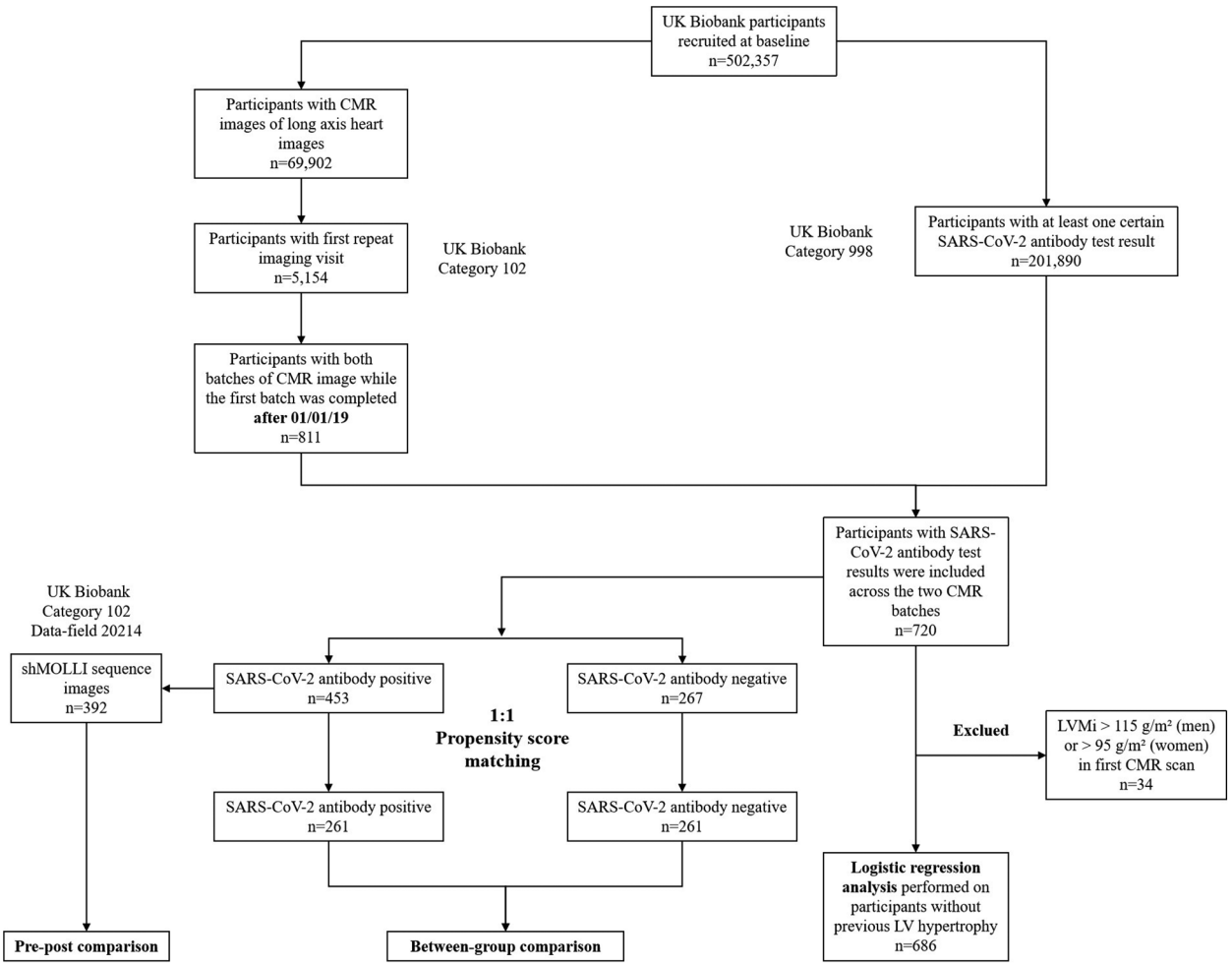

FIGURE 1
Flow chart of participant selection and experimental procedures.

volumes, myocardial mass, and dimensions during both end-diastolic and end-systolic phases from the long axis images. LV myocardial native T1 was manually extracted from the experimental shMOLLI sequence on a mid-ventricular short-axis image.

Our focus was on various LV parameters, including left ventricular end-diastolic volume (LVEDV), end-systolic volume (LVESV), stroke volume (LVSV), ejection fraction (LVEF), cardiac output, cardiac index, left ventricular mass (LVM), end-diastolic dimension (Dd), end-systolic dimension (Ds), posterior wall thickness (PWT), relative wall thickness (RWT), left ventricular mass index (LVMi), left ventricular global function index (LVGFi), left ventricular mass volume ratio (LVMVR) on long axis heart images, and myocardial native T1 on short axis shMOLLI sequence images. LV hypertrophy was defined as LVMi greater than 115 g/m^2 (for men) and 95 g/m^2 (for women).

For the imaging analysis, CMR parameters were extracted from the first and repeat CMR tests for all 5,154 participants in a single batch. Analysts were blinded to participants' SARS-CoV-2 antibody status and personal information to prevent bias. To ensure consistency, an intra-class correlation coefficient (ICC) analysis was conducted between the three observers on the first 2,000 cases, demonstrating excellent internal consistency with all ICC values exceeding 0.75. The results for the remaining cases were obtained through consensus among the three observers, with the final analysis completed by the cardiovascular specialist.

2.4 Statistics analysis

Statistical analysis was conducted using Python 3.9.13. Continuous variables were presented as mean (standard deviation) or median (interquartile range), while categorical variables were expressed as percentages. The normality distribution was assessed using the Kolmogorov–Smirnov test. Baseline characteristics and CMR parameters were compared using the two-sample *t*-test for normally distributed variables or the Wilcoxon rank-sum test for non-normally distributed variables, and the chi-square test for categorical variables.

We employed PSM to randomly select a matched control participant for each seropositive participant. The PSM caliper value was set at 0.05. The PSM considered factors including age, sex, ethnity, TDI (Townsend Deprivation Index), height, weight,

BMI (Body Mass Index), BSA (Body Surface Area), SBP (Systolic Blood Pressure), DBP (Diastolic Blood Pressure), current smoking, current drinking, self-reported history of hypertension, hyperlipidemia, diabetes, asthma, and other cardiovascular diseases. Paired *t*-tests were performed after PSM.

Logistic regression analysis was performed to evaluate the association between SARS-CoV-2 antibody status and the incidence of LV hypertrophy in the overall study population, with adjustment for relevant covariates. Participants with LV hypertrophy detected in their initial CMR scan were excluded from further analysis. Model 1 comprised a univariate analysis, Model 2 incorporated adjustments for age, sex, ethnity, TDI, height, weight, BMI, BSA, SBP, DBP. Model 3 was further adjusted for a history of hypertension, cardiovascular disease, and diabetes. A P-value < 0.05 was considered statistically significant.

3 Results

3.1 Characteristics of study participants

With the gradual release of subsequent CMR examinations conducted after 2019 for repeat imaging visit by the UK Biobank, we are now able to investigate the variations in CMR parameters among participants with different SARS-CoV-2 antibody status. A total of 720 participants were included, of which 453 self-reported as SARS-CoV-2 seropositive. All participants underwent their initial CMR imaging after 2019, followed by subsequent CMR examinations after the detection of SARS-CoV-2 antibody results. Table 1 presents the clinical characteristics of the study participants. Significant differences in age were observed between the two groups. After 1:1 PSM, 261 participants remained in each group. The clinical characteristics post-matching, stratified by SARS-CoV-2 antibody results, are presented in Table 2. Following PSM, no significant differences were observed between the groups in terms of other baseline characteristics, except for vaccination status. The median interval between the date of SARS-CoV-2 antibody testing and the follow-up CMR examination was 109 days for the seropositive group and 112 days for the seronegative group.

3.2 Cardiac parameters of initial and follow-up CMR cohort

After 1:1 PSM, seropositive participants exhibited lower LVEDV, LVESV, LVEDVi, LVESVi, Dd, and Ds during the

TABLE 1 Baseline characteristics of study participants.

Baseline characteristics	SARS-CoV-2 antibody positive n = 453	SARS-CoV-2 antibody negative n = 267	P value
Age (year)	52 (11)	50 (12)	0.001[b]
Male (%)	49.4	45.9	0.361[c]
TDI	−1.97 (4.60)	−1.95 (4.27)	0.629[b]
Weight (kg)	77.69 (13.55)	77.76 (14.88)	0.944[a]
Height (cm)	170.81 (9.39)	171.55 (9.20)	0.307[a]
BMI (kg/m^2)	1.88 (0.21)	1.89 (0.23)	0.744[a]
BSA (m^2)	1.9 (0.2)	1.9 (0.2)	0.782[a]
SBP (mmHg)	139 (18)	139 (20)	0.491[b]
DBP (mmHg)	78 (11)	78 (11)	0.716[b]
Days interval (day)	128 (109)	120 (108)	0.553[b]
Vaccinated (%)	81.8	61.7	<0.001[c]
Ethnity			
White (%)	92.5	90.3	0.311[c]
Other ethnicities (%)	7.5	9.7	–
Life-style			
Current Smoking (%)	39.1	40.1	0.790[c]
Current drinking (%)	94.9	94.0	0.600[c]
Self-reported diseases			
Hypertension (%)	13.7	12.4	0.611[c]
High Cholesterol (%)	7.7	6.4	0.496[c]
Diabetes mellitus (%)	5.3	5.2	0.975[c]
Asthma (%)	6.0	6.0	0.986[c]
Cardiac diseases (%)	6.8	8.6	0.384[c]

Continuous variables were summarized using means and standard deviations or medians and interquartile ranges, categorical variables were summarized using percentages.
Ab, antibody; TDI, townsend deprivation score; BMI, body mass index; BSA, body surface area; SBP, systolic blood pressure; DBP, diastolic blood pressure.
[a]Two-sample *T*-test.
[b]Wilcoxon rank sum test.
[c]chi square test.

TABLE 2 Baseline characteristics of study participants after 1:1 propensity score matched with SARS-CoV-2 antibody test result.

Baseline characteristics	SARS-CoV-2 antibody positive n = 261	SARS-CoV-2 antibody negative n = 261	P-value
Age (year)	51 (11.5)	50 (12)	0.628[b]
Male (%)	47.5	49.0	0.726[c]
TDI	−2.20 (4.68)	−1.95 (4.23)	0.972[b]
Weight (kg)	77.67 (13.73)	77.70 (14.85)	0.986[a]
Height (cm)	170.84 (9.41)	171.43 (9.22)	0.471[a]
BMI (kg/m^2)	1.88 (0.21)	1.89 (0.23)	0.843[a]
BSA (m^2)	1.9 (0.2)	1.9 (0.2)	0.782[a]
SBP (mmHg)	139 (18)	139 (19)	0.608[b]
DBP (mmHg)	78 (11)	78 (11)	0.614[b]
Days interval (day)	109 (115)	120 (107)	0.522[b]
Vaccinated (%)	77.3	62.4	<0.001[c]
Ethnity			
White (%)	92.0	92.3	0.871[c]
Other ethnicities (%)	8.0	7.7	–
Life-style			
Current Smoking (%)	37.9	39.5	0.719[c]
Current drinking (%)	93.9	94.3	0.853[c]
Self-reported diseases			
Hypertension (%)	11.9	11.9	1.000[c]
High Cholesterol (%)	5.7	5.7	1.000[c]
Diabetes Mellitus (%)	4.2	5.4	0.539[c]
Asthma (%)	5.7	6.1	0.853[c]
Cardiac diseases (%)	8.0	7.3	0.742[c]

Continuous variables were summarized using means and standard deviations or medians and interquartile ranges, categorical variables were summarized using percentages.
Abbreviations as in Table 1.
[a]Paired *T*-test.
[b]Wilcoxon rank sum test.
[c]Chi square test.

initial CMR scan compared to the negative group. These differences persisted during the subsequent CMR test, with seropositive participants still showing lower LVEDV, LVESV, LVEDVi, and LVESVi (Table 3).

In all seropositive participants, significant reductions were observed in LV parameters, including CO and CI following the onset of antibody positivity (mean ± SD: CO 5.38 ± 1.30 L/min vs. 5.09 ± 1.24 L/min, $P < 0.001$; CI 2.85 ± 0.58 L/min/m^2 vs. 2.60 ± 0.66 L/min/m^2, $P < 0.001$, see Table 3 and Figure 2). However, a similar declining trend was evident in the negative group (median (IQR): CO 5.33 (1.74) L/min vs. 4.92 (1.60) L/min, $P = 0.002$; CI 2.83 (0.81) L/min/m^2 vs. 2.65 (0.67) L/min/m^2, $P = 0.003$).

Additionally, in overall seropositive participants ($n = 392$), myocardial native T1 was found to be increased after antibody positivity (mean ± SD: 852.77 ± 53.55 ms vs. 860.01 ± 47.81 ms, $P = 0.012$, Supplementary Table S2, Figure 3).

3.3 Variation of cardiac parameters over the interval period

Our investigation aimed to determine whether there were significant changes in cardiac structure and function between SARS-CoV-2 seropositive and seronegative groups over time. We analyzed cardiac parameters from consecutive CMR examinations and calculated the rate of change by dividing the difference between the two CMR measurements by the initial CMR measurement, and expressed as a percentage. We then calculated the interval between the two scans, ultimately deriving the annualized rate of change for the CMR parameters, enabling standardized comparisons.

As shown in Table 4, both SARS-CoV-2 seropositive and seronegative groups exhibited reductions in cardiac function parameters such as LVEF, LVGFi, CO, and CI, as well as increases in cardiac structural parameters such as PWT, RWT, LVM, LVMI, and LVMVR. These results indicate significant changes in these cardiac parameters over an average interval of approximately one hundred days. However, despite similar trends in both groups, the differences between them did not reach statistical significance.

3.4 Association between SARS-CoV-2 antibody positivity and LV hypertrophy incidence

Considering the observed increase in average myocardial native T1 levels following the onset of antibody positivity, indicative of a potential trend towards myocardial fibrosis, we utilized LVMi, a direct indicator derived from CMR imaging, to assess the occurrence of LV hypertrophy.

After excluding 34 participants (17 men and 17 women) who demonstrated LV hypertrophy at their initial CMR examination, logistic regression analysis revealed that SARS-CoV-2 antibody positivity was associated with an increased odds ratio (OR) for the incidence of new LV hypertrophy. The univariate analysis showed an OR of 2.517 [95% CI:

TABLE 3 Comparison of LV parameters in initial and subsequent follow-up CMR examinations between PSM-processed SARS-CoV-2 antibody positive and negative groups.

LV parameters	Group A (Initial, positive)	Group B (Subsequent, positive)	Group C (Initial, negative)	Group D (Subsequent, negative)	*P*-value			
					A/B (Intra-group)	C/D (Intra-group)	A/C (Inter-group)	B/D (Inter-group)
LVEDV (ml)	116.94 (26.67)	116.45 (29.03)	122.95 (38.69)	117.95 (39.67)	0.680	0.313*	0.007	0.041
LVESV (ml)	30.11 (11.21)	31.08 (13.45)	32.30 (16.83)	31.41 (18.87)	0.133	0.853*	0.004	0.036
LVEDVi (ml/m^2)	61.99 (11.83)	61.84 (13.22)	65.47 (12.33)	64.73 (13.04)	0.802	0.508	0.001	0.011
LVESVi (ml/m^2)	16.01 (5.66)	16.52 (6.78)	17.30 (8.29)	17.16 (8.63)	0.130	0.969*	0.002	0.027
LVSV (ml)	86.83 (20.16)	85.49 (20.36)	88.82 (27.68)	87.25 (26.06)	0.152	0.199*	0.068	0.145
LVEF (%)	74.46 (6.87)	73.98 (7.20)	73.51 (7.44)	73.09 (9.51)	0.270	0.519*	0.106	0.110
CO (l/min)	5.38 (1.30)	5.09 (1.24)	5.33 (1.74)	4.92 (1.60)	<0.001	0.002*	0.746	0.787
CI (l/min/m^2)	2.85 (0.58)	2.60 (0.66)	2.83 (0.81)	2.65 (0.67)	<0.001	0.003*	0.667	0.558*
LVM (g)	150.82 (53.45)	145.29 (56.64)	153.35 (55.81)	152.03 (60.09)	0.977*	0.778*	0.322	0.380*
Dd (mm)	50.87 (5.24)	50.96 (5.43)	52.18 (5.21)	51.68 (5.35)	0.742	0.280	0.003	0.096
Ds (mm)	28.34 (4.38)	28.40 (4.56)	29.23 (4.66)	29.22 (4.63)	0.769	0.974	0.012	0.052*
PWT (mm)	10.23 (1.98)	10.41 (1.97)	10.36 (3.06)	10.11 (2.44)	0.105	0.461*	0.612	0.428
RWT	0.39 (0.10)	0.40 (0.13)	0.39 (0.13)	0.39 (0.11)	0.522*	0.969*	0.257*	0.136
LVMi (g/m^2)	78.91 (19.08)	79.85 (19.46)	82.24 (20.61)	81.35 (21.54)	0.978*	0.811*	0.156*	0.163*
LVGFi	0.40 (0.06)	0.39 (0.06)	0.40 (0.06)	0.39 (0.08)	0.095	0.440*	0.780	0.704
LVMVR	1.30 (0.32)	1.29 (0.39)	1.26 (0.31)	1.23 (0.33)	0.976	0.850*	0.082	0.146*

Group A—Initial batch of SARS-CoV-2 antibody positive participants; Group B—Subsequent batch of SARS-CoV-2 antibody positive participants; Group C—Initial batch of SARS-CoV-2 antibody negative participants; Group D—Subsequent batch of SARS-CoV-2 antibody negative participants. Independent variables was calculated as means and standard deviation or median and interquartile range.

LVEDV, left ventricular end-diastolic volume; LVESV, left ventricular end-systolic volume; LVSV, left ventricular stroke volume; LVEF, left ventricular ejection fraction; CO, cardiac output; CI, cardiac index; Dd, end-diastolic dimension; Ds, end-systolic dimension; PWT, posterior wall thickness; RWT, relative wall thickness; LVM, left ventricular mass; LVGFi, left ventricular global function index; LVMVR, left ventricular mass-volume ratio.

*Indicates results from the Wilcoxon test.

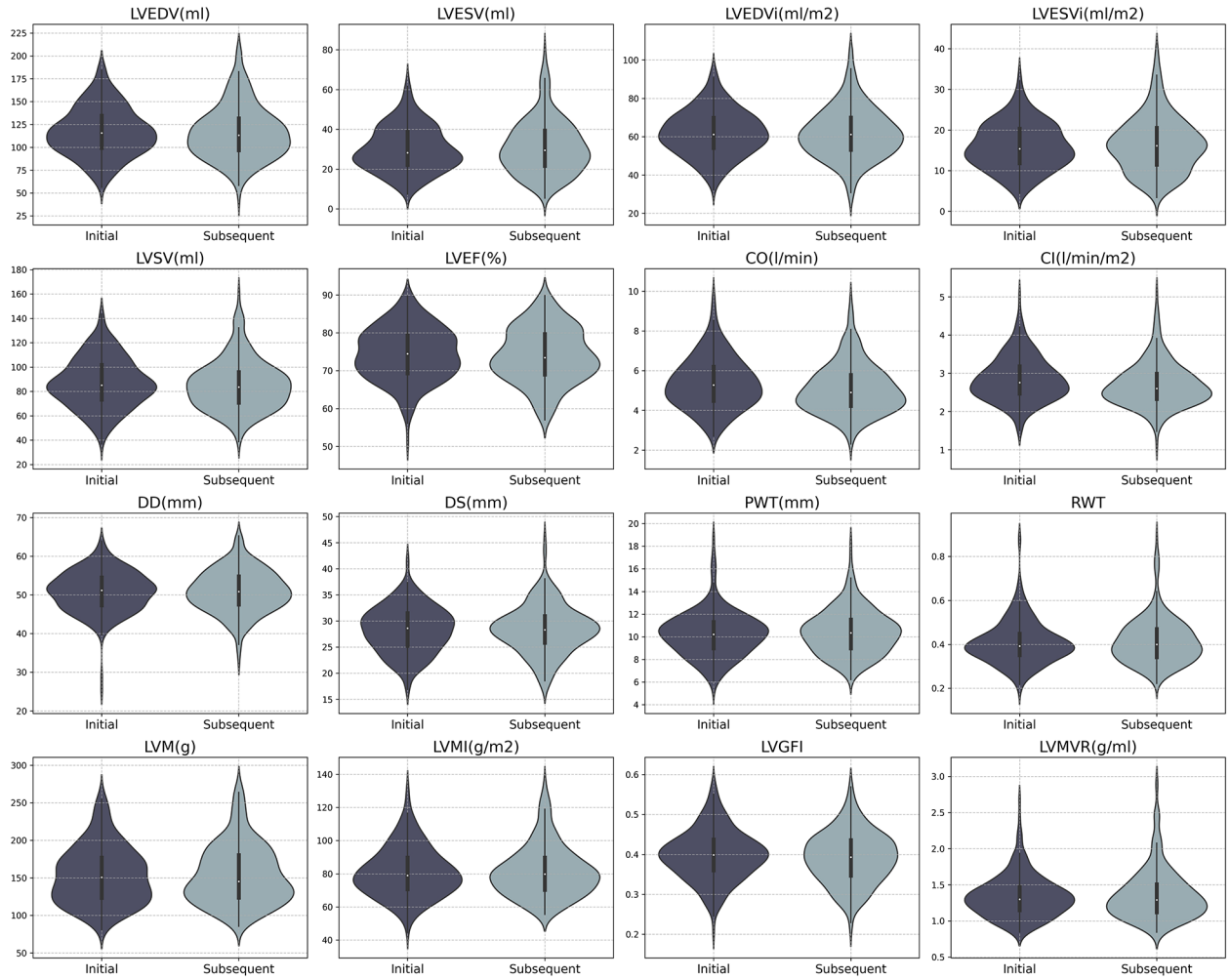

FIGURE 2
Distribution of CMR parameters in initial and subsequent batches for SARS-CoV-2 antibody positive participants. LVEDV, left ventricular end-diastolic volume; LVESV, left ventricular end-systolic volume; LVSV, left ventricular stroke volume; LVEF, left ventricular ejection fraction; CO, cardiac output; CI, cardiac index; Dd, end-diastolic dimension; Ds, end-systolic dimension; PWT, posterior wall thickness; RWT, relative wall thickness; LVM, left ventricular mass; LVGFi, left ventricular global function index; LVMVR, left ventricular mass-volume ratio.

(0.838–7.566), $P = 0.100$]. Model 2 adjusting for confounders resulted in an OR of 3.257 [95% CI: (1.036–10.239), $P = 0.043$]. Further adjustment for baseline comorbidities yielded an OR of 2.866 [95% CI: (0.907–9.057), $P = 0.073$]. Detailed results are provided in Table 5.

4 Discussion

4.1 Main findings

In this study, we investigated a cohort of participants who underwent CMR examinations both before and after SARS-CoV-2 antibody testing. Our findings revealed a decrease in CO and CI among participants with positive SARS-CoV-2 antibody status. Although a similar declining trend was observed in the seronegative group, no significant differences were evident in the inter-group comparison of changes in CMR parameters over time. After 1:1 PSM, we found no significant association between SARS-CoV-2 antibody status and the status of LV structure or pumping function. Despite finding subtle intra-group changes, the annual change rates of all LV parameters did not show significant differences between the SARS-CoV-2 seropositive and seronegative groups. This suggests that within the average interval of approximately one hundred days, SARS-CoV-2 antibody positivity might not induce substantial changes in LV structure or function detectable through CMR.

Additionally, we observed an elevation in myocardial native T1 in seropositive participants, indicating a potential impact of SARS-CoV-2 antibody positivity on myocardial fibrosis over a period of approximately 110 days. Logistic regression analysis further revealed that SARS-CoV-2 antibody positivity was associated with an increased risk of LV hypertrophy, with an adjusted odds ratio of 3.257.

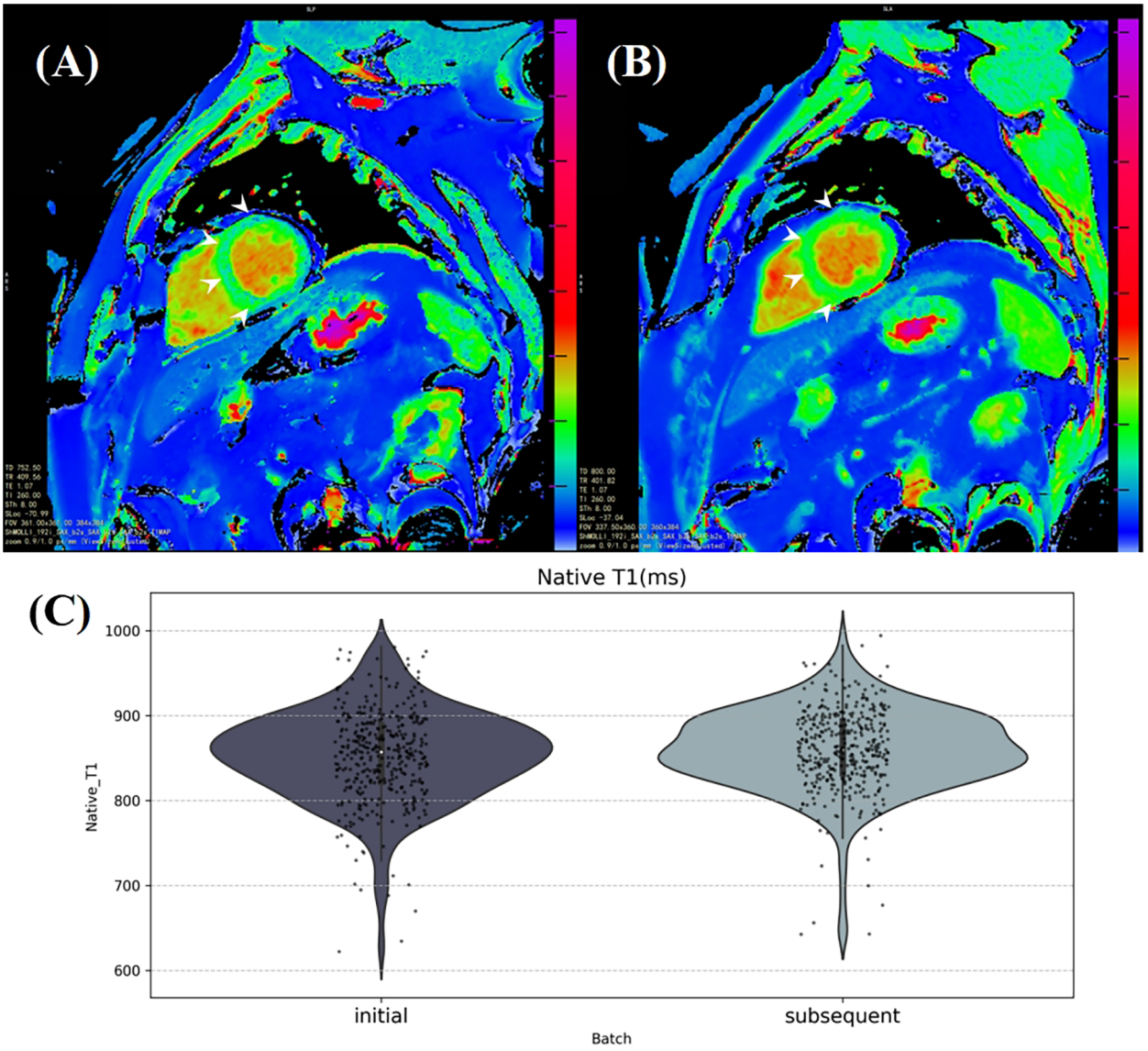

FIGURE 3
The average myocardial native T1 was calculated from a manually labeling region in a mid-ventricular short axis slice on the T1 mapping. (A) and (B) illustrate a significant increase in myocardial native T1, particularly in the interventricular septum area (white arrows), in a healthy 53-year-old male participant 185 days after SARS-CoV-2 antibody turned positive. (C) The violin plot shows the distribution of average myocardial native T1 in the initial and subsequent CMR batches of SARS-CoV-2 antibody positive participants.

4.2 Integration into the literature

Our findings align with previous studies reporting cardiovascular sequelae following SARS-CoV-2 infection. For instance, a study involving 148 COVID-19 patients with elevated troponin levels found that 19% had myocardial infarction, with 66% of these cases occurring in individuals without prior coronary disease (16). Similarly, Huang et al. (17) reported elevated LV global T1 and ECV in COVID-19 patients compared to healthy controls, although no significant differences in LV structure or pumping function were observed. These studies, however, were limited to post-infection CMR examinations and primarily included participants with moderate to severe COVID-19, lacking self-comparisons before and after infection.

Follow-up studies at three and six months post-infection have shown gradual improvements in certain cardiopulmonary indicators, such as right ventricular EDV, right ventricular EF, T1, LGE, and peak VO2. However, symptoms like decreased exercise tolerance and muscle fatigue persisted without significant improvement (18). A multi-center prospective cohort study involving 182 COVID-19 patients at three and twelve months follow-ups reported no significant changes in left or right ventricular structure and function, suggesting that cardiac impairments may be reversible in some cases (19). Notably, these

TABLE 4 Annual change rates on CMR parameters of the two groups.

LV parameters	SARS-CoV-2 antibody positive $n = 261$	SARS-CoV-2 antibody negative $n = 261$	*P*-value
LVEDV (%)	−0.795 (16.336)	−1.005 (15.365)	0.801*
LVESV (%)	1.468 (45.363)	0.677 (47.174)	0.796*
LVEDVi (%)	0.007 (18.062)	−1.035 (14.637)	0.472
LVESVi (%)	−0.213 (9.962)	−0.039 (11.252)	0.843
LVSV (%)	0.007 (18.062)	−1.035 (14.637)	0.472
LVEF (%)	−0.213 (9.962)	−0.039 (11.252)	0.843
CO (%)	−3.554 (19.193)	−4.704 (17.560)	0.458
CI (%)	−3.403 (19.237)	−4.494 (17.130)	0.490
LVM (%)	1.067 (12.189)	0.317 (9.552)	0.423
Dd (%)	0.561 (9.421)	−0.719 (7.089)	0.072
Ds (%)	0.984 (13.188)	0.638 (13.619)	0.766
PWT (%)	3.431 (18.345)	1.517 (18.867)	0.228
RWT (%)	4.100 (22.906)	3.059 (21.952)	0.586
LVMi (%)	1.178 (11.768)	0.596 (9.261)	0.512
LVGFi (%)	−0.410 (16.940)	−0.471 (15.848)	0.966
LVMVR (%)	3.219 (20.825)	2.607(17.140)	0.723

Abbreviations as in Table 3.
*Indicates results from the Wilcoxon test.

TABLE 5 Logistic regression analysis of the association between SARS-CoV-2 antibody positivity and the incidence of new LV hypertrophy.

SARS-CoV2 antibody status	OR (95% CI)	*P*-value
Univariate	2.517 (0.838–7.566)	0.100
Adjusted for Confounders	3.257 (1.036–10.239)	0.043
Fully Adjusted	2.866 (0.907–9.057)	0.073

Confounders: age, sex, ethnity, TDI, height, weight, BMI, SBP, DBP.
Fully Adjusted: Confounders + baseline comorbidities including hypertension, cardiovascular diseases and diabetes.

studies did not find significant differences in LV parameters during the observation period as well, with potential COVID-19-related effects primarily observed on several right ventricular metrics (20).

In contrast to these studies, our research benefits from the availability of baseline CMR data, allowing us to directly compare cardiac parameters before and after SARS-CoV-2 antibody testing. This unique design minimizes confounding effects and provides a clearer picture of the cardiac impacts associated with SARS-CoV-2 antibody positivity. However, our findings differ from some previous reports, possibly due to the shorter follow-up period and the inclusion of both naturally infected and vaccinated individuals in the seropositive group. This heterogeneity may have diluted the observed differences in cardiac structural and functional changes between seropositive and seronegative individuals.

Given the limitation of the UK Biobank CMR protocol, native T1 values represent one of the most precise indicators available for assessing myocardial changes. A recent study from the UK Biobank CMR cohort found that higher native myocardial T1 was associated with various diseases, such as heart failure, nonischemic cardiomyopathies, atrial fibrillation, stroke, and diabetes (21). Our observation of elevated native T1 in seropositive participants supports the hypothesis that SARS-CoV-2 antibody positivity may contribute to myocardial fibrosis, although further studies using T2 STIR or LGE imaging are needed to exclude the possibility of acute myocarditis-induced myocardial edema as a confounding factor.

The CardioCOVID-Gemelli study investigated the relationship between COVID-19 vaccination status and myocardial injury, finding that vaccination had a protective effect against myocardial injury in elderly individuals (OR: 0.57, 95% CI: 0.34–0.94; $P = 0.03$) but was an independent risk factor in younger individuals (OR: 4.44, 95% CI: 1.28–15.34, $P = 0.02$) (22). While our study did not specifically differentiate between natural infection and vaccination, the observed increase in LVMi suggests that SARS-CoV-2 antibody positivity may accelerate cardiac remodeling.

Unlike most observational COVID-19 studies, which lack baseline cardiac data, our study is the first to utilize two sets of CMR images, including examinations before and after SARS-CoV-2 antibody test, from the UK Biobank cohort. Specifically, we selected participants who underwent their initial CMR examinations after 2019 but before their SARS-CoV-2 exposure to minimize the confounding effects of other factors on cardiac data. This approach allows us to explore the association between SARS-CoV-2 antibody status and variations in LV structure and function over an average interval of 110 days. By comparing direct LV parameters across different serological immune states, we provide a unique perspective on the cardiac impacts of SARS-CoV-2 antibody positivity.

Furthermore, our findings showed reductions in cardiac parameters such as LVEF, CO, and CI, as well as increases in cardiac structural parameters like LVMi, LVESVi, Ds, PWT, and LVMVR, in both SARS-CoV-2 antibody-positive and antibody-negative groups. These changes may reflect the natural cardiac remodeling process that occurs over time, particularly given the approximately 100-day interval between the initial and follow-up CMR scans. This suggests that both groups experienced alterations in cardiac function and structure during this period, regardless of antibody status. The observed reductions in cardiac function and increases in structural measures could indicate early signs of cardiac remodeling that may be independent of SARS-CoV-2 exposure.

4.3 Limitation

Several limitations should be acknowledged. First, SARS-CoV-2 antibody positivity was determined using serological antibody tests, but positive results could not differentiate between natural infection and successful vaccination, which may have different effects on cardiac structure and function. Similarly, negative antibody results could not distinguish between uninfected individuals and those with a non-responsive vaccination. Second, our study required a second CMR scan to assess cardiac changes after a clear positive or negative antibody test result, leading to potential participant loss for those who only had baseline images available. The average follow-up period of approximately 100 days may not be long enough to fully capture the long-term cardiovascular effects of COVID-19.

Additionally, due to safety and practical considerations, the UK Biobank CMR protocol did not include enhanced CMR imaging, such as T2 STIR sequences, LGE, and ECV analyses. As a result, we could not exclude the possibility that myocardial edema contributed to the observed Native T1 changes. Finally, since all raw images were obtained from the UK Biobank, the CMR follow-up examinations were part of a general survey, and specific clinical indications for these examinations were not available.

Furthermore, while an ICC analysis showed good consistency between the three observers, the varying experience levels of the observers could have introduced some bias. This potential variability is acknowledged as a limitation.

5 Conclusion

Our findings suggest subtle cardiac changes associated with SARS-CoV-2 antibody positivity over an approximately 100-day period, including decreases in CO and CI, an increase in myocardial native T1, and a potential risk of LV hypertrophy. However, no significant differences were observed in LV structure and function between the seropositive and seronegative groups. These results are exploratory, and further studies with longer follow-up are needed to clarify the long-term cardiovascular effects of SARS-CoV-2 antibody positivity.

Data availability statement

The datasets presented in this article are not readily available because the raw imaging data and non-imaging participant characteristics are available from the UK Biobank. Requests to access the datasets should be directed to http://www.ukbiobank.ac.uk/register-apply.

Ethics statement

The studies involving humans were approved by the National Health Service National Research Ethics Service on June 17, 2011 (Ref 11/NW/0382) and extended on June 18, 2021 (Ref 21/NW/0157). This study complies with the Declaration of Helsinki, and written informed consent was obtained from all participants. The studies were conducted in accordance with the local legislation and institutional requirements. The participants provided their written informed consent to participate in this study.

Author contributions

CL: Methodology, Software, Visualization, Writing – original draft, Writing – review & editing. YM: Data curation, Resources, Writing – review & editing. SQ: Investigation, Resources, Writing – review & editing. KL: Conceptualization, Investigation, Writing – review & editing. MQ: Data curation, Investigation, Resources, Writing – review & editing. CG: Data curation, Software, Visualization, Writing – review & editing. LZ: Data curation, Software, Visualization, Writing – review & editing. JW: Formal Analysis, Writing – review & editing. DG: Conceptualization, Funding acquisition, Resources, Supervision, Writing – review & editing.

Funding

The author(s) declare financial support was received for the research, authorship, and/or publication of this article. National Natural Science Foundation of China, 81872563. Key Science and Technology Program of Shaanxi Province, 2022SF-078.

Acknowledgements

We are grateful to all the participants of UK Biobank and all the people involved in building the large biobank. This work was carried out based on the large population of the CMR cohort from the UK Biobank and conducted under the access application 68722. You may get more details about the biobank and the CMR images may be acquired on the UK Biobank website: https://www.ukbiobank.ac.uk.

Conflict of interest

The authors declare that the research was conducted in the absence of any commercial or financial relationships that could be construed as a potential conflict of interest.

Publisher's note

Supplementary material

The Supplementary Material for this article can be found online at: https://www.frontiersin.org/articles/10.3389/fcvm.2025.1462263/full#supplementary-material

References

1. Walls AC, Park YJ, Tortorici MA, Wall A, McGuire AT, Veesler D. Structure, function, and antigenicity of the SARS-CoV-2 spike glycoprotein. *Cell*. (2020) 181(2):281–292.e6. doi: 10.1016/j.cell.2020.02.058

2. Shi S, Qin M, Shen B, Cai Y, Liu T, Yang F, et al. Association of cardiac injury with mortality in hospitalized patients with COVID-19 in Wuhan, China. *JAMA Cardiol*. (2020) 5(7):802–10. doi: 10.1001/jamacardio.2020.0950

3. Shi S, Qin M, Cai Y, Liu T, Shen B, Yang F, et al. Characteristics and clinical significance of myocardial injury in patients with severe coronavirus disease 2019. *Eur Heart J*. (2020) 41(22):2070–9. doi: 10.1093/eurheartj/ehaa408

4. Ayoubkhani D, Khunti K, Nafilyan V, Maddox T, Humberstone B, Diamond I, et al. Post-COVID syndrome in individuals admitted to hospital with COVID-19: retrospective cohort study. *Br Med J*. (2021) 372:n693. doi: 10.1136/bmj.n693

5. Inciardi RM, Adamo M, Lupi L, Cani DS, Di Pasquale M, Tomasoni D, et al. Characteristics and outcomes of patients hospitalized for COVID-19 and cardiac disease in Northern Italy. *Eur Heart J*. (2020) 41(19):1821–9. doi: 10.1093/eurheartj/ehaa388

6. Chatrath N, Kaza N, Pabari PA, Fox K, Mayet J, Barton C, et al. The effect of concomitant COVID-19 infection on outcomes in patients hospitalized with heart failure. *ESC Heart Fail*. (2020) 7(6):4443–7. doi: 10.1002/ehf2.13059

7. Alvarez-Garcia J, Lee S, Gupta A, Cagliostro M, Joshi AA, Rivas-Lasarte M, et al. Prognostic impact of prior heart failure in patients hospitalized with COVID-19. *J Am Coll Cardiol*. (2020) 76(20):2334–48. doi: 10.1016/j.jacc.2020.09.549

8. Scholkmann F, May CA. COVID-19, post-acute COVID-19 syndrome (PACS, "long COVID") and post-COVID-19 vaccination syndrome (PCVS, "post-COVIDvac-syndrome"): similarities and differences. *Pathol Res Pract*. (2023) 246:154497. doi: 10.1016/j.prp.2023.154497

9. Patone M, Mei XW, Handunnetthi L, Dixon S, Zaccardi F, Shankar-Hari M, et al. Risks of myocarditis, pericarditis, and cardiac arrhythmias associated with COVID-19 vaccination or SARS-CoV-2 infection. *Nat Med*. (2022) 28(2):410–22. doi: 10.1038/s41591-021-01630-0

10. Rudski L, Januzzi JL, Rigolin VH, Bohula EA, Blankstein R, Patel AR, et al. Multimodality imaging in evaluation of cardiovascular complications in patients with COVID-19: JACC scientific expert panel. *J Am Coll Cardiol*. (2020) 76(11):1345–57. doi: 10.1016/j.jacc.2020.06.080

11. Task Force for the management of COVID-19 of the European Society of Cardiology. ESC Guidance for the diagnosis and management of cardiovascular disease during the COVID-19 pandemic: part 2-care pathways, treatment, and follow-up. *Eur Heart J*. (2022) 43(11):1059–103. doi: 10.1093/eurheartj/ehab697

12. Raman B, Bluemke DA, Lüscher TF, Neubauer S. Long COVID: post-acute sequelae of COVID-19 with a cardiovascular focus. *Eur Heart J*. (2022) 43(11):1157–72. doi: 10.1093/eurheartj/ehac031

13. Raisi-Estabragh Z, McCracken C, Cooper J, Fung K, Paiva JM, Khanji MY, et al. Adverse cardiovascular magnetic resonance phenotypes are associated with greater likelihood of incident coronavirus disease 2019: findings from the UK Biobank. *Aging Clin Exp Res*. (2021) 33(4):1133–44. doi: 10.1007/s40520-021-01808-z

14. Petersen SE, Matthews PM, Bamberg F, Bluemke DA, Francis JM, Friedrich MG, et al. Imaging in population science: cardiovascular magnetic resonance in 100,000 participants of UK Biobank—rationale, challenges and approaches. *J Cardiovasc Magn Reson*. (2013) 15(1):46. doi: 10.1186/1532-429X-15-46

15. Petersen SE, Matthews PM, Francis JM, Robson MD, Zemrak F, Boubertakh R, et al. UK Biobank's cardiovascular magnetic resonance protocol. *J Cardiovasc Magn Reson*. (2016) 18:8. doi: 10.1186/s12968-016-0227-4

16. Kotecha T, Knight DS, Razvi Y, Kumar K, Vimalesvaran K, Thornton G, et al. Patterns of myocardial injury in recovered troponin-positive COVID-19 patients assessed by cardiovascular magnetic resonance. *Eur Heart J*. (2021) 42(19):1866–78. doi: 10.1093/eurheartj/ehab075

17. Huang L, Zhao P, Tang D, Zhu T, Han R, Zhan C, et al. Cardiac involvement in patients recovered from COVID-2019 identified using magnetic resonance imaging. *J Am Coll Cardiol Img*. (2020) 13(11):2330–9. doi: 10.1016/j.jcmg.2020.05.004

18. Cassar MP, Tunnicliffe EM, Petousi N, Lewandowski AJ, Xie C, Mahmod M, et al. Symptom persistence despite improvement in cardiopulmonary health—insights from longitudinal CMR, CPET and lung function testing post-COVID-19. *EClinicalMedicine*. (2021) 41:101159. doi: 10.1016/j.eclinm.2021.101159

19. Øvrebotten T, Myhre P, Grimsmo J, Mecinaj A, Trebinjac D, Nossen MB, et al. Changes in cardiac structure and function from 3 to 12 months after hospitalization for COVID-19. *Clin Cardiol*. (2022) 45(10):1044–10. doi: 10.1002/clc.23891

20. Tudoran C, Tudoran M, Lazureanu VE, Marinescu AR, Cut TG, Oancea C, et al. Factors influencing the evolution of pulmonary hypertension in previously healthy subjects recovering from a SARS-CoV-2 infection. *J Clin Med*. (2021) 10(22):5272. doi: 10.3390/jcm10225272

21. Raisi-Estabragh Z, McCracken C, Hann E, Condurache D-G, Harvey NC, Munroe PB, et al. Incident clinical and mortality associations of myocardial native T1 in the UK Biobank. *J Am Coll Cardiol Img*. (2023) 16(4):450–60. doi: 10.1016/j.jcmg.2022.06.011

22. Montone RA, Rinaldi R, Masciocchi C, Lilli L, Damiani A, La Vecchia G, et al. Vaccines and myocardial injury in patients hospitalized for COVID-19 infection: the CardioCOVID-Gemelli study. *Eur Heart J Qual Care Clin Outcomes*. (2025) 11(1):59–67. doi: 10.1093/ehjqcco/qcae016

Frontiers in
Cardiovascular Medicine

Innovations and improvements in cardiovascular treatment and practice

Focuses on research that challenges the status quo of cardiovascular care, or facilitates the translation of advances into new therapies and diagnostic tools.

Discover the latest Research Topics

See more →

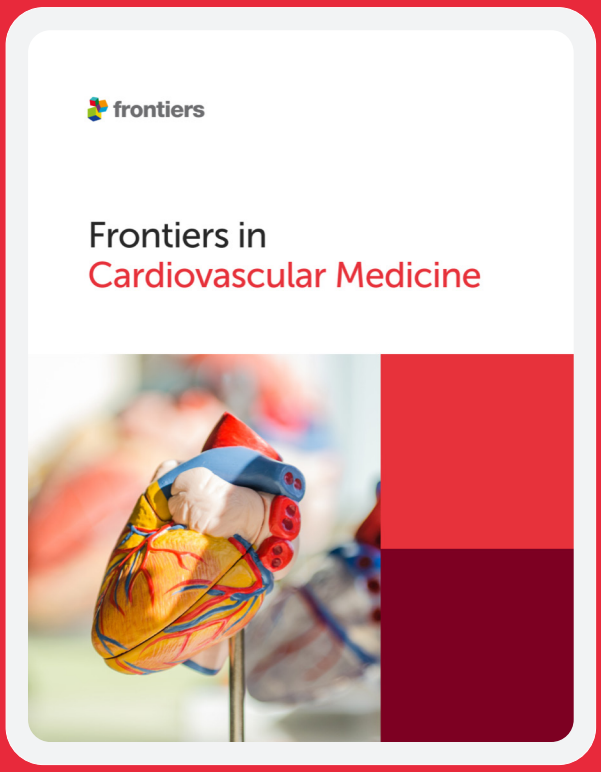

Frontiers

Avenue du Tribunal-Fédéral 34
1005 Lausanne, Switzerland
frontiersin.org

Contact us

+41 (0)21 510 17 00
frontiersin.org/about/contact